Photon Detection by Converter Layers using a Micro-Pattern Gaseous Detector

Katrin Elisabeth Penski

München 2024

Photon Detection by Converter Layers using a Micro-Pattern Gaseous Detector

Katrin Elisabeth Penski

Dissertation
an der Fakultät für Physik
der Ludwig–Maximilians–Universität
München

vorgelegt von
Katrin Elisabeth Penski
aus München

München, den 08.10.2024

Erstgutachter: Prof. Dr. Otmar Biebel
Zweitgutachter: Prof. Dr. Wolfgang Dünnweber
Tag der mündlichen Prüfung: 14.11.2024

Zusammenfassung

Mikrostrukturierte Gasdetektoren (MPGDs) weisen eine hervorragende räumliche und zeitliche Auflösung und eine hohe Ratenfestigkeit auf, sind kostengünstig und skalierbar. Sie werden in Experimenten wie ATLAS zur Spurrekonstruktion geladener Teilchen eingesetzt. Aufgrund der niedrigen Ordnungszahl ($Z < 20$) und Dichte des Standard-Detektorgases weisen MPGDs eine geringe Detektionseffizienz für Photonen auf. In der medizinischen Diagnostik, wie Bildgebung oder PET, ist eine effiziente Photonendetektion mit hoher räumlicher Auflösung entscheidend. Um die Vorteile von MPGDs für die Photonendetektion zu nutzen, soll diese Arbeit ihre Photonendetektionseffizienz verbessern und gleichzeitig präzise Positionsinformationen liefern. Dazu wird ein GEM-Detektor (Gaseous Electron Multiplier) genutzt, eine Art von MPGDs.
Der Wechselwirkungsquerschnitt von Photonen nimmt bei Materialien mit höherem Z im keV-Energiebereich zu, in dem der photoelektrische Effekt dominiert. Das neuartige Konzept besteht darin, Konverterschichten mit höherem Z im Driftbereich des GEM-Detektors in einer gestapelten Konfiguration senkrecht zu seiner Ausleseebene anzuordnen. Dies ermöglicht die Verwendung mehrerer Schichten, von denen jede die Wechselwirkungswahrscheinlichkeit erhöht. Die Konverterschichten bestehen aus einem isolierenden Trägermaterial mit Kupferstreifen ($Z = 29$) und werden exemplarisch mit 59,5 keV Photonen untersucht. Die aus dem Konvertermaterial in das Gas austretenden Photoelektronen werden durch ein elektrisches Feld nach unten in den aktiven Bereich des GEM-Detektors geleitet, wo ihre 2D-Position bestimmt wird. Wenn aus dieser 2D-Position die Interaktionsposition auf der Konverterschicht mit hoher Genauigkeit eindeutig reproduziert werden kann, ermöglicht dies die Rekonstruktion der Richtung der Punktquelle.
Es werden senkrechte und geneigte Anordnungen mit je 5 Konverterschichten verwendet, wobei mit der geneigten Konfiguration Methoden zur Positionsrekonstruktion untersucht werden. Mit detaillierten Simulationen (Geant4, ANSYS und Garfield++) werden die physikalischen Prozesse in den Schichten und im Detektor analysiert. Simulation und Messung zeigen eine gute Übereinstimmung der Elektronenbewegung bei verschiedenen elektrischen Feldern, der deponierten Ladung und der Detektionseffizienz unter Verwendung von Konverterschichten mit unterschiedlicher Dicke und Isoliermaterialien. Durch Materialoptimierung wird die Detektionseffizienz im Vergleich zu einem Aufbau ohne Schichten um den Faktor 2 auf $(1{,}38 \pm 0{,}21)\,\%$ verbessert, wobei dünne Isolationsschichten bevorzugt werden.
Die ablaufenden Interaktionsprozesse der Simulation zeigt: anstatt der direkten Detektion des in Kupfer erzeugten Photoelektrons, ist der dominante detektierte Effekt die Emission eines 8 keV Photons, das durch die Elektronenumordnung nach dem photoelektrischen Effekt entsteht. Dieses Photon interagiert mit dem Gas und erzeugt ein Elektron-Ionen-Paar. Das detektierte Elektron enthält keine Informationen über die anfängliche Interaktionsposition oder die Richtung der Punktquelle, da das 8 keV Photon isotrop emittiert wird.
In dieser Arbeit wird die Detektionseffizienz für Photonen durch Materialoptimierung der Konverterschichten verbessert und ein detailliertes Verständnis ihrer Funktion geschaffen.

Die Detektionseffizienz des GEM-Detektors mit Konverterschichten für 511 keV-Photonen, wie sie bei der PET entstehen, wird mittels Koinzidenzmessung mit Szintillationsdetektoren bestimmt. Die Photonenkonversionseffizienz mit 9 Konverterschichten ist 0,31 %, welche dem erwarteten Wert entspricht und etwa doppelt so hoch ist verglichen ohne Schichten.

Im Rahmen dieser Arbeit wurde darüber hinaus noch eine Elektronikuntersuchung durchgeführt. Für das High-Luminosity-Upgrade des LHC Speicherrings am CERN werden die Ausleseelektronik der MDT-Kammern (Monitored Drift Tube) im ATLAS-Detektor ausgetauscht, um eine einwandfreie Funktionalität bei den erhöhten Kollisionsraten zu gewährleisten. Dies umfasst den neuen Amplifier-Shaper-Discriminator-Chip (ASD2). Seine Leistung wird untersucht und ein Testverfahren entwickelt, um die leistungsstärksten ASD2-Chips für die Integration zu ermitteln.

Abstract

Micro-Pattern Gaseous Detectors (MPGDs) have an excellent spatial and temporal resolution. They are high rate capable, cost-effective and scalable. Therefore, they are used in experiments like ATLAS for tracking of charged particles. Due to the low atomic number ($Z < 20$) and density of the standard detector gas, MPGDs exhibit a poor detection efficiency for photons. For many applications in medical physics, like imaging or PET, an efficient photon detection with high spatial resolution is essential. To exploit the advantages of MPGDs for photon detection, this thesis aims to improve their photon detection efficiency while providing precise position information using a GEM (Gaseous Electron Multiplier) detector, a type of MPGDs. The photon interaction cross-section increases for higher-Z materials in the keV energy range, where the photoelectric effect dominates. The novel approach is to arrange the converter layers in the drift region of the GEM detector in a stacked configuration perpendicular to its readout plane. This allows for multiple layers, each increasing the photon interaction probability. The converter layers are made of an insulating carrier material with copper strips ($Z = 29$) on both sides. The photon conversion is investigated exemplarily using a 59.5 keV X-ray source. Photoelectrons exiting the converter material into the gas are guided downwards by an electric field into the active area of the GEM detector, providing 2D position. In case this 2D position allows for the interaction position on the converter layer to be unambiguously reproduced with high accuracy, the direction of a point source can be reconstructed.
Both, perpendicular and tilted configurations using 5 converter layers are investigated, whereby the tilted configuration is used for studying position reconstruction methods. A detailed simulation, including Geant4, ANSYS and Garfield++, is established to understand the physical processes in the converter layers and the detector. Simulation and measurement provide good agreement regarding the electron drift under various conditions of the electric guiding field, the deposited charge and detection efficiency when using converter layers of varying thickness and insulating materials. By optimizing the material properties, the detection efficiency is improved by a factor of 2 to $(1.38 \pm 0.21)\%$ compared to having no layers, with thin insulating material layers being favorable.
The analysis of the simulation results shows the interaction processes influencing the detection efficiency. Instead of directly detecting the photoelectrons produced in copper, 8 keV photons are emitted due to electron rearrangement following the photoelectric effect. This photon interacts with the gas creating an electron-ion pair. Unfortunately, the detected electrons carry no more information about the initial interaction position or the direction of the point source, since the 8 keV photon is emitted isotropically.
This work improves the detection efficiency for photons by material optimization of the converter layers and provides a detailed understanding of their working principle.

The detection efficiency for 511 keV photons, like in PET, in the GEM detector with converter layers is measured using a coincidence measurement setup including scintillation detectors. A 511 keV photon conversion efficiency of 0.31 % is determined with 9 converter layers, which is similar to the expected value from the simulation and about twice as high compared to a setup without converter layers.

Beyond that, new front-end electronics for the ATLAS detector was investigated. For the High Luminosity upgrade of the LHC, the readout electronics of the Monitored Drift Tube (MDT) chambers in the ATLAS detector will be replaced to ensure flawless performance at the increased collision rates. This includes a new Amplifier-Shaper-Discriminator (ASD2) chip. Its performance is investigated, and a testing procedure is developed to identify the best-performing ASD2 chips for the integration.

Contents

Chapter 1

Introduction and Motivation

Micro-Pattern Gaseous Detectors (MPGDs) have been studied for approximately 40 years and are well-known particle detectors that are widely used for various purposes. They provide several advantages: very good temporal and spatial resolution, high rate stability, large-scale capability as well as cost efficiency, for example by using abundant materials. A few applications of MPGDs are presented in chapter 1.1. In general, MPGDs are used to detect electrically charged particles, but not necessarily electrically neutral particles such as photons, as their detection efficiency is low for those. In this thesis a novel technique to improve the detection efficiency for photons in MPGDs including a 3D position reconstruction is developed and investigated.

1.1 Applications of Micro-Pattern Gaseous Detectors

The invention of the Multi-Wire Proportional Chamber (MWPC) by Charpak [Charpak, 1969] in 1968 marked a significant achievement in the field of particle detection and tracking and formed the beginning of intensive research in the area of gas ionization devices. Based on this invention, Micro-Pattern Gaseous Detectors (MPGDs) emerged. MPGDs belong to the group of gas filled detectors with a planar micro-pattern readout structure. Currently, there are two well-studied examples of MPGDs: MICRO MEsh GAseous Structure (Micromegas) [Giomataris et al., 1996] and Gaseous Electron Multiplier (GEM) [Sauli, 1997] detectors. Both detectors are based on the same working principle: an ionizing particle interacts with the gas inside the detector generating electrons, which are then multiplied by gas amplification due to a high electric field. While this gas amplification in the Micromegas detector works by applying a high electric field between an anode and a micro-mesh, it is realized in the GEM detector by applying the high electric field across a thin foil with holes (see chapter 3). Further developments of the original Micromegas detector are the floating strip Micromegas detector and the resistive type Micromegas detector, for which further information can be found in [Bortfeldt, 2014; Klitzner, 2019] and [Alexopoulos et al., 2011] respectively. Since these particle detectors have been intensively studied, since they work reliably and show various advantages such as e.g. high-rate capability and an excellent resolution, they are used in various High Energy Physics (HEP) experiments.
The two detector techniques, Micromegas and GEM, are components of ATLAS (A Toroidal LHC ApparatuS) [The ATLAS Collaboration, 2008] and CMS (Compact Muon Solenoid) [The CMS Collaboration, 2008], two HEP experiments of the LHC (Large Hadron Collider) at LHC (Conseil Européen pour la Recherche Nucléaire). In the last upgrade phase, the New Small Wheel (NSW) [Kawamoto et al., 2013] has been incorporated in the ATLAS detector, as shown in figure 1.1. One component of the NSW are Micromegas detectors in the size of

several square meters [Herrmann, 2019]. They are used for muon precision tracking. At the same time, the CMS detector was upgraded by installing GEM detectors for precise muon tracking [Colaleo et al., 2015]. In the next upgrade phase, the readout electronics of the Monitored Drift Tube (MDT) chambers, which are part of the ATLAS muon spectrometer as shown in figure 1.1, is replaced. This topic is covered in this thesis as well (see chapter 10).

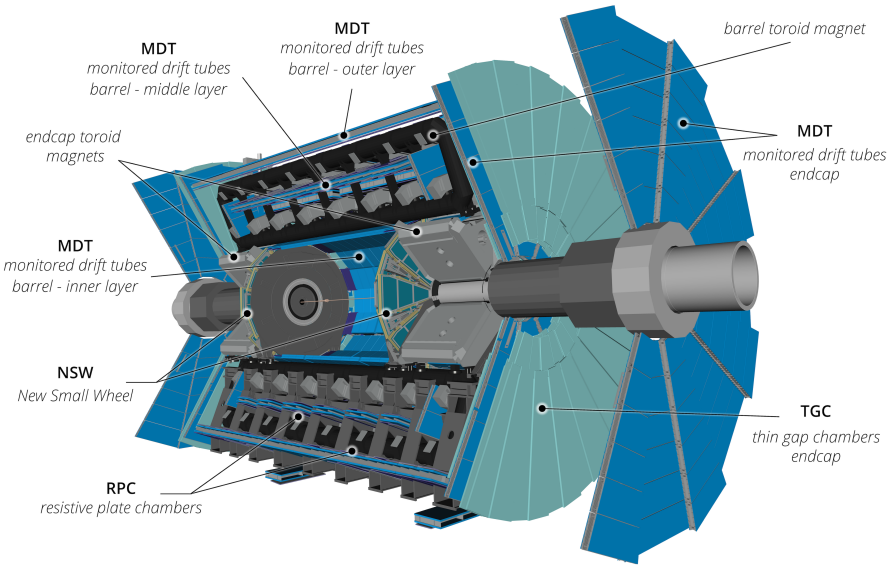

Figure 1.1: View of the ATLAS detector, a multi-purpose detector system at the LHC. It consists of various detector subsystems, all of them having different functions and specializations to detect certain particles and extract information such as e.g. their trajectory and energy. Here in particular the muon systems are indicated, such as the NSW, which includes Micromegas detectors The MDT chambers are in chapter 10. Figure taken from [The ATLAS Collaboration, 2023].

Due to the reliable operation of these two detector types, they are constantly under investigation to cover additional areas of application and to improve the technology. The combination of the Micromegas and GEM detectors lead to the newly μ-Resistive WELL (RWELL) [Bencivenni et al., 2015] or the Segmented GEM Readout (SGR) detector [Jagfeld, 2023]. Additionally, there are other promising developments such as the Cherenkov Ring Imaging MPGDs [Rinnagel, 2023], which aims to reconstruct a known particle's momentum by measuring its Cherenkov cone. Many other applications of MPGDs can be found in [Francke and Peskov, 2014].
In this work, the MPGDs (here a GEM detector is used) are further developed by the novel approach of inserting converter layers to improve the detection efficiency of photons. Furthermore, the application aims to enable an imaging application as used in the medical field.

1.2 Detectors for Medical Applications

In addition to HEP, particle detectors have a wide range of applications in various fields, such as medical physics. One of the main areas of application is medical imaging, as for example Computed Tomography (CT) or Positron Emission Tomography (PET), both of which are introduced here. Important requirements for the detectors are the efficient detection of photons in order to minimize the radiation dose for the patient and excellent spatial resolution.

1.2.1 Medical Imaging

The discovery of X-rays in 1895 by Röntgen [Röntgen, 1895] in combination with the first captured image using this radiation, represents the starting point for X-ray imaging in medical diagnostics. The basic concept of medical imaging is introduced here, following [Schlegel et al., 2018] and [Seeram, 2023] if not stated differently.
X-ray imaging is a widely available technique in medical diagnostics. Due to intensive research and rapid technical progress in detector development as well as computer technology, nowadays advanced imaging techniques such as CT or Magnetic Resonance Imaging (MRI) are available and complement the existing methods. In contrast to CT, MRI does not use X-rays. Instead, MRI is based on the detection of hydrogen spin flips using resonances in magnetic fields, from which images are produced [Weishaupt et al., 2006].
For X-ray imaging the use of a screen is still a common method of this so-called projection radiography, as it offers high image quality, simple imaging technology and a favorable cost-benefit ratio. The basic concept of radiography is shown in figure 1.2.

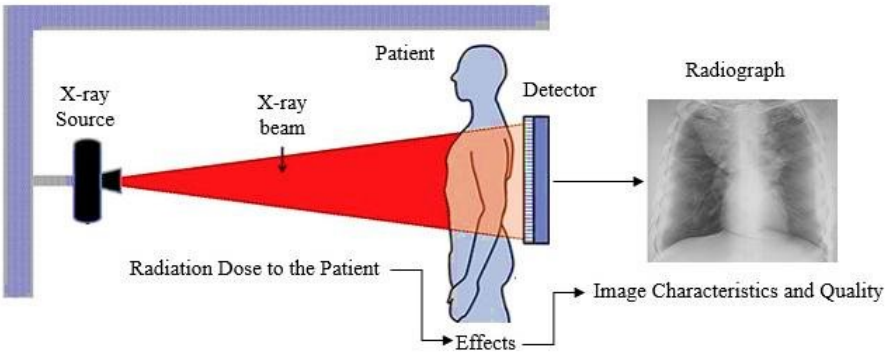

Figure 1.2: To produce a 2D X-ray image of a patient, the part of the patient to be examined is placed between an X-ray source and a detector. Due to the different absorption properties of e.g. bones and soft tissue, the different parts of the body are visible on the X-ray image, making e.g. broken bones visible. Illustration taken from [Isola et al., 2021].

The patient is irradiated and either a radiographic film or a digital detector is utilized to visualize the inner structure of the body. Particularly in industrialized countries, digital radiography processes find increasing usage. These digital detectors have to fulfill high requirements, e.g. high image quality in terms of resolution, contrast and homogeneity, high efficiency for the detection of X-rays to ensure a low dose requirement as well as a fast response time. Depending on the medical application, there are various systems that are specifically adapted to the area of the body to be diagnosed. As this is a relatively complex topic, two examples with different requirements are given here: digital radiography and mammography as a specialized X-ray imaging technique. In addition to the references listed above, further information is extracted from [Bushberg et al., 2011]. One adjustable parameter is the X-ray energy, which is defined by the X-ray tube voltage. Depending on the body part, a range between 50–120 kV is typically set for X-ray imaging. While, for example, 55 kV is needed for the bone imaging of the wrist, the scan of the lung anatomy requires 120 kV to reduce the conspicuity of the ribs. For mammography, on the other hand, lower energies are necessary in order to detect breast anomalies, which are abnormalities of the soft tissues. Therefore, a typical operation voltage below 40 kV is set.
For both applications, digital radiography and mammography, Flat-Panel Detector (FPD)s are used for particle detection. These detectors are solid-state detectors and it is distinguished between indirect and direct FPDs. In the latter case, the conversion of X-rays into an electrical

charge occurs directly in a photoconductor, which is commonly made of amorphous selenium. Due to this direct conversion and the detector design, there is almost no lateral spread of electrons, resulting in high spatial resolution. Furthermore, it provides a high conversion efficiency for photons with energies below 40 keV and is therefore used for mammography.
In indirect FPDs the X-rays are first converted into light in a scintillator (typically made of cesium iodide or gadolinium oxysulfide). It is coupled to an amorphous silicon photodiode array, where the light is converted to an electrical charge. For the energy range of radiographic imaging introduced above, these indirect FPDs show a higher quantum efficiency than direct ones. In indirect FPDs made of CsI phosphor this conversion efficiency is at around 80 % for 70 kV and 50 % for 120 kV photons. At these energies, direct FPDs made from amorphous selenium have a 10–15 % lower conversion efficiency. For this reason, indirect detectors are used in this area. In both types of FPDs, the signal is digitized and processed, resulting in the desired image.
While the previously introduced technologies provide 2D images, with a CT scan a 3D image of the inner structure of the body is possible. The basic principle is the same as presented above, but in a CT scan the images are taken from various angles around the body. The patient is lying on a table, which is moving into a cylinder, called gantry. In this gantry the X-ray source and the detectors are located, which are rotating around the patient measuring the absorption. Afterwards, the measurement results are processed by a computer and a 3D image is reconstructed by applying a tomographic reconstruction algorithm. In addition, the CT is a powerful tool for detecting cancer, e.g. with regard to treatment planning [Bortfeld, 2006] or for simultaneous application with PET to ensure high spatial resolution (see chapter 1.2.2).
This introduction to medical imaging shows that the detectors have to fulfill three main requirements: they have to be sensitive to photons with an energy from 15–120 keV, offer a high spatial resolution as well as a high photon detection efficiency for the specific energy in order to minimize the exposure time for the patient.

1.2.2 Positron Emission Tomography

PET is another imaging technique in nuclear medicine. Compared to CT (see chapter 1.2.1), it has a poor position resolution, but the main advantage of PET is the visualization of metabolic processes. Therefore, it is used to detect early signs of cancer, the heart function or the brain condition [Valk et al., 2006].
The imaging procedure starts with the injection of a radioactive tracer into the patient's body (normally into the vein). 18F-Fluorodeoxyglucose (FDG) is a typically used radiotracer to detect cancer. It is a radioactively tagged sugar [Miele et al., 2008], consequently it accumulates at body parts where a lot of energy is burned. Since a growing tumor also needs much energy, meaning sugar, FDG will also gather high activity there.
In the radioactive decay of the radionuclide, a positron is emitted as visualized in figure 1.3. It nearly directly annihilates with an electron in the surrounding tissue, creating a back-to-back 511 keV photon pair. In order to detect this photon pair, the PET scanner consists of detectors arranged in a ring around the patient, as shown in figure 1.4. In modern scanners these detectors are silicon photo-multipliers, which consist of an array of hundreds or thousands of integrated single-photon avalanche-diodes. They are very sensitive for photon detection. If a photon pair is detected within a coincidence time window and along a straight line where the annihilation happened (the so called Linie of Response (LoR), see figure 1.4), the signal is processed [Agrawal et al., 2021].

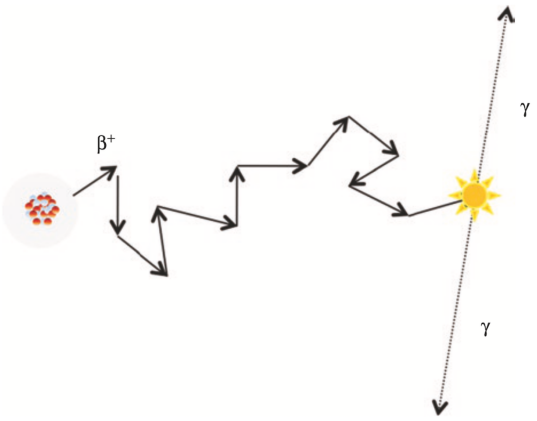

Figure 1.3: In the nuclear decay of the radiotracer a positron (β^+) is created, which interacts with the surrounding atoms until it annihilates with an electron. In this process two 511 keV photons are emitted in opposite directions. Figure taken from [Agrawal et al., 2021].

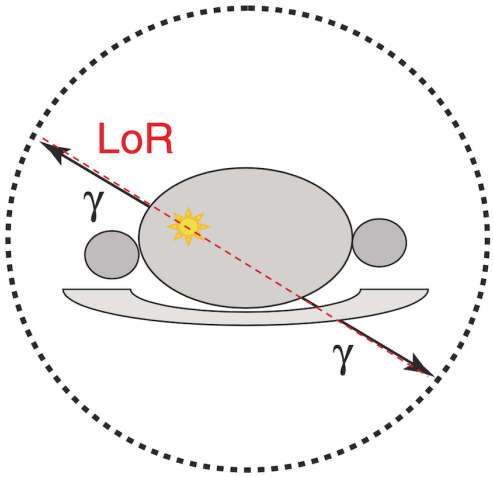

Figure 1.4: To detect the photon pair from figure 1.3, the PET scanner is made of detectors forming a ring around the patient. The detected coincident event lies on a straight line (LoR). Figure taken from [Agrawal et al., 2021].

By collecting data over some time, all LoRs are used to reconstruct the original tracer distribution. In the resulting image unusual bright spots indicate cancer, as shown in figure 1.5. For a better determination of the cancer's position, parallel to the PET scan a CT scan is performed [Li et al., 2018].

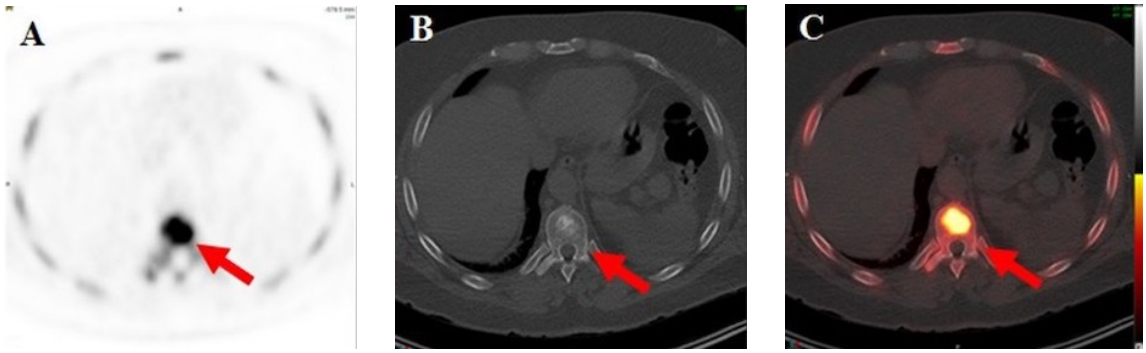

Figure 1.5: These images show a metastatic prostate cancer, which is indicated by the red arrows. The FDG PET scan (A) has a poor position resolution, which is solved by a simultaneous CT scan (B). By combining both techniques (C) an abnormal high radiotracer activity is measured, indicating prostate cancer. Figures taken from [Li et al., 2018], adapted.

In addition to cancer detection, there are other applications for PET scans. FDG can also be used as tracer for brain PET scans, e.g., to distinguish the Alzheimer's diseases from other reasons for dementia [Marcus et al., 2014].

1.2.3 Challenges: MPGDs for Medical Applications

In HEP experiments such as ATLAS, MPGDs are mostly used to determine the trajectory of a charged particle with high spatial resolution. However, for both medical applications presented in the previous sections, a detector with good spatial resolution and highly efficient

photon detection is essential. Especially the last aspect is not fulfilled by MPGDs, as they are filled with gas, which has low density and low atomic number Z, resulting in a lower photon attenuation than the solid-state FPDs. Nevertheless, MPGDs exhibit several other advantages: they offer excellent spatial [Flierl, 2018] and temporal resolution [Maerschalk, 2016], are scalable over large areas [Herrmann, 2019], provide high rate capability without aging effects [Fallavollita et al., 2020] and are cost-effective [Fukuda et al., 2011]. In order to exploit these advantages of MPGDs over FPDs, it is essential to increase the photon conversion in MPGDs and thereby achieve a very good spatial resolution, as these are the main requirements for imaging and PET. Thus, these are the main topics of this thesis.

1.3 On the Content of this Thesis

This thesis aims to improve the photon detection efficiency in MPGDs while obtaining complete position information. All measurements are performed with triple-GEM detectors, which are one kind of MPGDs.
Due to the low density of the active gas volume of GEM detectors, they exhibit only a poor detection efficiency for electrically neutral particles. For photons, the detection via the photoelectric effect can be increased by using a solid converter cathode made of high-Z materials [Flierl, 2014]. The novel approach is to introduce many converter layers into the drift region of a triple-GEM detector. These layers are arranged in a stacked configuration, oriented perpendicular to the GEM readout. This configuration enables the use of multiple layers, as illustrated in figure 1.6. X-rays emitted from a point source interact with one of the converter layers, creating electrons. When the electrons exit the material into the surrounding gas, they can be guided downwards into the active area of the GEM detector by a special electric field configuration. If from the measured 2D GEM position the interaction position on the converter layer can be evidently reproduced with high accuracy, the intensity profiles on the different layers allow for the reconstruction of the direction of the point source. This is a very ambitious task and this thesis is an investigation of the feasibility of this approach.

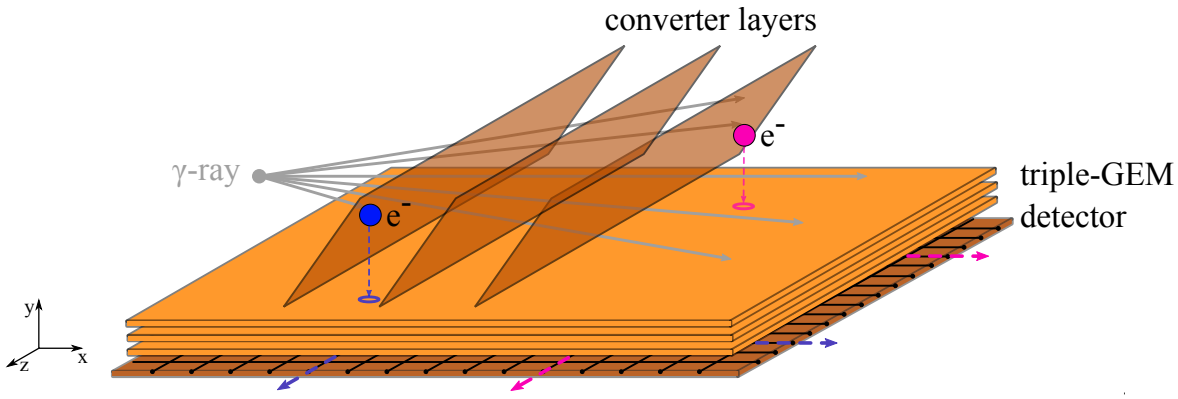

Figure 1.6: The photons enter the gaseous volume of a triple GEM detector. Multiple converter layers are placed in its drift region, perpendicular to the GEM readout. Therefore, the photon interaction probability increases with each additional converter layer. When photons interact with the converter layers, electrons are produced. If these electrons enter the detector gas, they are guided into the active area, maintaining their position information. The position information is provided by the readout structure. After the electron amplification by the triple-GEM detector, they reach the readout area. This readout structure consists of strips in the x- and z-directions, as shown in the sketch. By reading out these strips, the ones seeing a signal from the electrons are identified and a 2D position is determined. The novel concept investigated in this work is the introduction of converter layers into the GEM detector to increase the photon conversion probability while achieving a complete 3D position reconstruction. Sketch not to scale.

The material and thickness of the converter layers is a crucial parameter, as it strongly influences the photon conversion probability. Therefore, the investigation of the material is a main part of this thesis. In addition, it is aimed to achieve a complete 3D position reconstruction, which includes the additional reconstruction of the y-position. Furthermore, two different photon energies are investigated: The majority of the measurements are performed with 59.5 keV photons, which are in the typical energy range of medical imaging (see chapter 1.2.1). In addition, 511 keV photons are analyzed, as used in PET (see chapter 1.2.2).

Overall, the following topics are covered in this thesis:

- The theoretical principles are introduced in chapter 2. This includes all the fundamental physical processes relevant to this work, such as the interaction of particles with matter, focusing on photons, and the movement of charged particles in an electric field.

- In chapter 3 the structure and functionality of the GEM detector, which is used here for the measurements, is explained and first simulation results regarding its performance are presented.

- The different methods applied in this thesis are described in chapter 4 including the various simulation programs, the detector readout electronics and the signal analysis that provides a 2D position on the readout anode.

- In chapter 5 the focus lies on the introduction of the converter layers, the measurement setup and the simulation procedure. First measurements with the converter layers are performed with 59.5 keV photons to study the photoelectric effect, which provides a known electron energy and range simplifying the analysis. Furthermore, the particle source is available. This energy is within the energy range for digital radiography (see chapter 1.2.1). In particular, the consideration of various measured quantities and their comparison with the simulation results is highlighted.

- The influence of the environmental parameters on the detector performance is analyzed in chapter 6. A method is developed to compensate for the pressure fluctuations by changing the detector operating parameters.

- In order to enable imaging or PET, a complete 3D position reconstruction of the particle is required when using converter layers. While the x- and z-positions are given by the readout structure, the y-position is more complex to determine. The main aspect of chapter 7 is the investigation of the y-position, which is examined using simulations.

- The proper material and the dimensions of the converter layers are decisive parameters for a high photon conversion probability and therefore have to be optimized. These parameters are investigated in chapter 8 using different converter layer types. In an initial study the 59.5 keV absorption behavior of the converter layers is investigated using a Germanium detector. Additional simulations enable the underlying physical processes to be investigated in order to understand the impact of the converter layers on the detector performance and additionally the working principle of the converter layer. In addition, the detection efficiency of 59.5 keV photons is determined when using solid converter layers.

- In addition to 59.5 keV photons, the detector performance is investigated for 511 keV photons, as they are used for PET (see chapter 1.2.2). Thus, chapter 9 aims to determine the efficiency of the GEM detector for 511 keV photons. For this purpose, a coincidence setup with scintillators is introduced.

- Furthermore, this thesis covers the implementation of a testing procedure and analysis method for the new ASD2 chips. The ASD chip is part of the readout electronics of the MDT chamber (see figure 1.1), which will be replaced in Phase-II upgrade. Therefore, this new ASD2 chips are necessary. The results are presented in chapter 10.

At this point, it should already be noted that for all diagrams shown in this thesis with data points where no error is visible, the error of the displayed data points is smaller than the size of the markers.

Chapter 2

Theoretical Background

In this chapter, the various interaction processes of different particles with matter are introduced. While charged particles are directly detectable due to their electromagnetic interaction with the detector, electrically neutral particles such as photons are detected indirectly by charged particles, which are created in the interaction processes [Kleinknecht, 2005]. Since the aim of this thesis is the detection of photons, their interaction with matter is described in more detail in chapter 2.2, focusing on the investigated energies of 59.5 keV (used in chapter 5 to chapter 8) and 511 keV (used in chapter 9).
The basic detector principle works as follows: In all considered photon interaction processes, an electron-ion pair is created in the detector gas by ionization. For all measurements performed in this thesis, the detector is filled with an Ar:CO_2 93:7 vol. % gas mixture. The created charges in the gas are separated by a low electric field and the electrons drift (see chapter 2.3.1) to the amplification region. There, the number of electrons is multiplied by a strong electric field (see chapter 2.3.2) to obtain a detectable signal, which is measurable at the readout anode. The complete functionality of the used GEM detector, which belongs to the MPGDs, is explained in chapter 3.

2.1 Charged Particle Interaction with Matter

Charged particles interact with a medium almost completely through the electromagnetic force. Non-relativistic charged particles with $m >> m_e$ interact by ionization. At relativistic energies, the Cherenkov effect, transition radiation and, at very high energies, bremsstrahlung occur [Kleinknecht, 2005]. For the purposes of this thesis, the creation of electron-ion pairs by ionization, when the charged particles interact with the gas of MPGDs, is the dominant process. The average energy loss of heavy charged particles (particles with masses $m_0 >> m_e$) per unit length was first properly calculated by Bethe [Bethe, 1930] and Bloch [Bloch, 1933], taking quantum mechanics into account. It is known as the Bethe-Bloch formula and with all corrections equals as follows [Particle Data Group et al., 2022]

$$-\left\langle \frac{dE}{dx} \right\rangle = 4\pi N_A r_e^2 m_e c^2 z^2 \frac{Z}{A} \frac{1}{\beta^2} \left[\frac{1}{2} \ln \frac{2m_e c^2 \beta^2 \gamma^2 T_{max}}{I^2} - \beta^2 - \frac{\delta(\beta\gamma)}{2} \right] \tag{2.1}$$

with N_A the Avogadro's number, r_e the classical electron radius, m_e the electron mass, c the speed of light, z the charge number of the incident particle, Z the atomic number of the absorber, $\beta = \frac{v}{c}$ the particle velocity v divided by the speed of light c, γ the Lorentz factor $\gamma = \frac{1}{\sqrt{1-\beta^2}}$, T_{max} the maximum possible energy that can be transferred to an electron in a single collision, I the mean excitation energy and $\delta(\beta\gamma)$ the Fermi density effect correction

to ionization energy loss [Fermi, 1940]. More information about equation 2.1 and its different terms can be found in [Particle Data Group et al., 2022].

The ionization process comprises two different components: primary and secondary ionization. In primary ionization, the electrons and ions are produced directly by the incident radiation. If the primary electron gains a sufficiently large energy, it can generate further electron-ion pairs, which is known as secondary ionization. These secondary electrons can continue ionizing, creating electron-ion pairs, until the energy is no longer adequate for ionization [Leo, 1995]. Another secondary ionization mechanism is the Penning effect [Penning, 1927]. In this process, a gas atom is in a metastable excited state where the de-excitation to the ground state by the emission of a photon is suppressed. Instead, de-excitation is caused by the collision of the excited atom with another gas atom, which is then ionized.

2.2 Photon Interaction with Matter

Since photons are electrically neutral and massless, their interaction behavior is very different from the one of charged particles. If a photon beam of an intensity I_0 interacts with matter, it is exponentially attenuated. After traversing a distance x in the material, the remaining intensity $I(x)$ is described by the Lambert-Beer law [Lambert, 1760; Beer, 1852]:

$$I(x) = I_0 \cdot e^{-\mu x} \tag{2.2}$$

Instead of the attenuation coefficient μ (in units of cm^{-1}), the mass-attenuation coefficient μ/ρ (in units of $\mathrm{cm}^2\,\mathrm{g}^{-1}$) is often used. It includes the medium's density ρ and consequently shows a characteristic behavior depending on the absorber material. The mass-attenuation coefficient μ/ρ for copper as a function of the photon energy E_γ is shown in figure 2.1. The dominant interaction process depends on the photon energy E_γ and is described in the following sections.

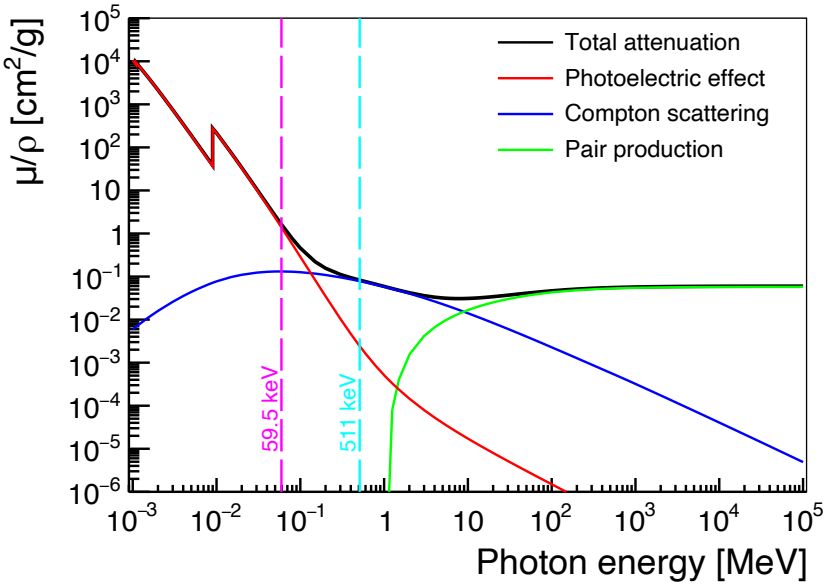

Figure 2.1: Mass-attenuation coefficient μ/ρ for different photon energies in copper. The contributions for the different photon-matter-interaction processes are shown: photoelectric effect, Compton scattering and pair production (in the nuclear field). Additionally, the used photon energies are indicated. For 59.5 keV photons (chapter 5 to chapter 8) the photoelectric effect is dominant while for 511 keV photons (chapter 9) it is Compton scattering. Data extracted from [Berger et al., 2010].

The mass-attenuation coefficient μ/ρ is directly related to the total cross-section σ per atom according to the following equation [Leo, 1995]:

$$\frac{\mu}{\rho} = \sigma \cdot \frac{N_\mathrm{A}}{A} \tag{2.3}$$

with Avogadro's number N_A and the molar mass A. Following [Leo, 1995], for materials containing various compounds, the total mass-attenuation coefficient is the sum of the individual mass-attenuation coefficients of each compound according to equation 2.3, weighted by a specific weight fraction w_i

$$\frac{\mu}{\rho} = \sum_i w_\mathrm{i} \cdot \frac{\mu_\mathrm{i}}{\rho_\mathrm{i}} \tag{2.4}$$

The weight fraction w_i is the mass of one compound divided by the total mass of the complete mixture. equation 2.3 has shown that the mass-attenuation coefficient is directly proportional to the cross-section σ, which is a measure of the photon interaction probability in matter. As indicated in figure 2.1, the total cross-section σ per atom is the sum of the individual cross-sections σ_photo (photoelectric effect, see equation 2.7), σ_c (Compton effect, see equation 2.12) and σ_pair (pair creation, see equation 2.15):

$$\sigma = \sigma_\mathrm{photo} + Z \cdot \sigma_\mathrm{c} + \sigma_\mathrm{pair} \tag{2.5}$$

In order to include the number of electrons per atom Z for the Compton cross-section[1], it is multiplied by Z [Leo, 1995]. The photon-matter interaction is a statistical process and is described by these interaction probabilities. As already shown in figure 2.1, the probability of a process occurring depends on the photon energy E_γ and the material. Since the photoelectric and Compton effects are the dominant effects for the photon energies considered in this thesis, these are examined in more detail in the following.

The attenuation coefficient differs for various materials. For completeness, the linear mass attenuation coefficients μ for copper (Cu), argon (Ar), carbon dioxide (CO_2) and Polyimide (PI) are listed in Table 2.1 for 60 keV photons[2]. In addition, the mean free path $\lambda = 1/\mu_{total}$ is given, which defines the average distance a particle travels before interacting with the material. At $x = \mu$, the beam intensity I_0 (see equation 2.2) is reduced by a factor of e.

Material	μ_photo		μ_C		μ_total	λ
	value [cm^{-1}]	fraction	value [cm^{-1}]	fraction	value [cm^{-1}]	value [mm]
Cu	12.1	91 %	1.2	9 %	13.3	0.75
PI	0.01	4 %	0.23	96 %	0.24	41.67
Ar	5.0×10^{-4}	68 %	2.4×10^{-4}	32 %	7.4×10^{-4}	13.5×10^{3}
CO_2	0.3×10^{-4}	9 %	3.1×10^{-4}	91 %	3.4×10^{-4}	29.4×10^{3}

Table 2.1: The total linear attenuation coefficient μ_total and its contributions from the Photoelectric effect and Compton Scattering are compared for four different materials for 60 keV photons. Pair creation does not contribute at this energy and the contribution from Rayleigh scattering is neglected. The solid and gaseous materials differ in terms of the linear absorption coefficient μ_total and the mean free path λ by around 4 orders of magnitude. Data extracted from [Berger et al., 2010].

[1] While the atomic number Z is already included in the respective cross-sections for the photoelectric effect and pair creation, this is not the case for the Compton effect. For this reason, the atomic number has to be included in equation 2.5 for σ_c only.

[2] PI is a plastic with the chemical formula $C_{22}H_{10}O_5N_2$ (see chapter 8.2.3).

2.2.1 Photoelectric Effect

If $E_\gamma < 100\,\mathrm{keV}$, the photoelectric effect is the dominant interaction process in copper [Kleinknecht, 2005]. The incident photon is entirely absorbed by an atomic electron, transferring its complete energy. In case the photon energy E_γ is larger than the binding energy of the electron W, the atom is ionized and a free photoelectron is created, carrying an energy of [Einstein, 1905]

$$T = E_\gamma - W \tag{2.6}$$

The sharp edge in figure 2.1 at about 10 keV is the so-called K-edge, which is associated with the K-shell electrons of an atom. The required photon energy E_γ is high enough to release electrons from this K-shell. At lower photon energies, the binding energy of the electrons dominates, which leads to a drop in the mass-attenuation coefficient [Leo, 1995], resulting in the K-edge.
For the photoelectric effect the cross-section σ_{photo} per atom is defined by

$$\sigma_{\mathrm{photo}} = \sqrt{32}\alpha^4 Z^5 \epsilon^{-3.5} \sigma_{\mathrm{Th}} \tag{2.7}$$

with the fine-structure constant $\alpha \approx 1/137$, the atomic number Z, the reduced photon energy $\epsilon = E_\gamma/(m_e c^2)$ and the Thomson cross-section $\sigma_{\mathrm{Th}} = \frac{8}{3}\pi r_e^2$ with the classical electron radius r_e [Kleinknecht, 2005; Leo, 1995]. equation 2.7 shows with $\sigma_{\mathrm{photo}} \sim Z^5$ a strong dependence of the photon interaction probability on the material[3]. Due to this strong correlation, high-Z materials are particularly favorable for the detection of photons.
Although in an interaction process the created photoelectron is not emitted in the same direction as the incident photon, it shows a particular angular distribution. Using the wave equations of electrons and considering relativistic approaches, Sauter derived the following equation describing the angular distribution of the photolecetrons [Davisson and Evans, 1952]

$$\begin{aligned} J(\theta,\beta) = \mathrm{const}\cdot\beta^2\sin^2\theta\Bigg(&\frac{(1-\beta^2)^{\frac{1}{2}}}{(1-\beta\cos\theta)^4} - \frac{(1-(1-\beta^2)^{\frac{1}{2}})}{2(1-\beta^2)^{\frac{1}{2}}(1-\beta\cos\theta)^3} \\ &+ \frac{2(1-(1-\beta^2)^{\frac{1}{2}})}{4(1-\beta^2)(1-\beta\cos\theta)^3}\Bigg) \end{aligned} \tag{2.8}$$

with the normalization factor *const*, the relativistic velocity β and the angle of the photoelectron θ, which is relative to the incident photon direction. Due to the strong dependence on $(1-\beta\cos\theta)^4$ or $(1-\beta\cos\theta)^3$ in the denominator of this equation, it is shown that with increasing photon energy, the photoelectrons are emitted more in the forward direction. In order to understand the behavior of this equation in more detail, it is visualized in figure 2.2.

[3] The Z^5 dependence of the photoelectric cross-section is typically observed for high atomic number materials, such as copper and results from the quantum mechanical description of the photon-electron interaction. It is defined by the general interaction of light with charged particles using perturbation theory, whereby a single light quantum is absorbed creating a transition of the unperturbed system. The photon cross-section with the corresponding Z dependence is derived from the resulting matrix element of the single quantum absorption and the two electron wave functions (of the electron in the K-shell and in the continuous spectrum). More details with calculation can be found in [Heitler, 1984]

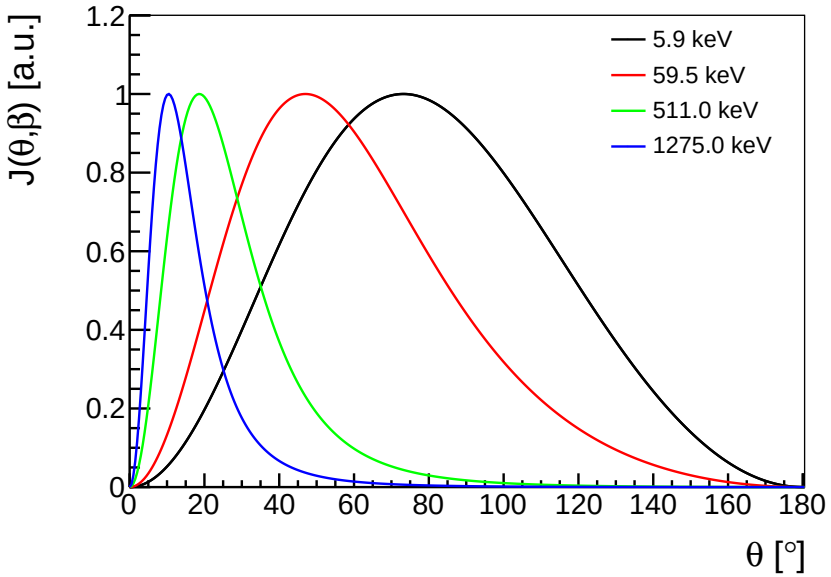

Figure 2.2: Visualization of equation 2.8, which describes the angular distribution of the created photoelectrons with respect to the photon direction for various incident energies. The curves are normalized to the maximum. With increasing photon energy the distribution's width gets smaller and the maximum shifts to smaller angles, indicating a more forward direction of the emitted photoelectron. For the 59.5 keV photons, about 84 % are emitted at an angle $\theta < 90°$ and 16 % at $\theta > 90°$.

If the energy of the photoelectron in the gaseous detectors is high enough, it can interact with the detector medium and cause secondary ionization according to chapter 2.1, producing electron-ion pairs. The same applies to the electrons produced in the interaction processes presented next.
In all measurements with 59.5 keV photons (from chapter 5 up to and including chapter 8) where copper is used as interaction material, the photoelectric effect is dominant, but Compton scattering can additionally occur (see Table 2.1). For the photoelectric effect in copper, the 59.5 keV photons interact predominantly with the K-shell electrons, which have a binding energy of about 9.0 keV [Thompson et al., 2001]. The resulting photoelectron has an energy of 50.5 keV (see equation 2.6).

2.2.2 Compton Effect

For higher photon energies E_γ between 100 keV and 2 MeV the Compton effect dominates (see figure 2.1 or [Kleinknecht, 2005]), where a photon scatters inelastically at a single electron and parts of the photon's energy is transferred to the target electron. Although the electron is bound in the material, for photon energies $E_\gamma >> E_B$, where E_B is the electron's binding energy, the electron is considered as essentially free particle [Leo, 1995]. Considering energy and momentum conservation, the scattering angle of the photon θ can be derived

$$\cos\theta = 1 - \frac{2}{(1+\gamma)^2 \tan^2\phi + 1} \tag{2.9}$$

as well as the scattering angle of the electron ϕ

$$\cot\phi = (1+\gamma)\tan\frac{\theta}{2} \tag{2.10}$$

using $\gamma = h\nu/m_e$ [Leo, 1995]. Both scattering angles, θ and ϕ, are defined with respect to the

direction of the incident photon beam. The differential cross-section of a photon scattered from a free electron is described by the Klein-Nishina formula [Klein and Nishina, 1929], which is derived from quantum electrodynamics:

$$\frac{d\sigma}{d\Omega} = \frac{r_e^2}{2}\frac{1}{(1+\gamma(1-\cos\theta))^2}\left(1+\cos^2\theta+\frac{\gamma^2(1-\cos\theta)^2}{1+\gamma(1-\cos\theta)}\right) \tag{2.11}$$

with the classical electron radius r_e. Integrating the Klein-Nishina formula over $d\Omega$ provides the total cross-section per electron for Compton scattering, which is defined as follows

$$\sigma_c = 2\pi r_e^2\left(\frac{1+\gamma}{\gamma^2}\left(\frac{2(1+\gamma)}{1+2\gamma}-\frac{1}{\gamma}\ln(1+2\gamma)\right)+\frac{1}{2\gamma}\ln(1+2\gamma)-\frac{1+3\gamma}{(1+2\gamma)^2}\right) \tag{2.12}$$

σ_c contributes to the total cross-section in equation 2.5.
In addition, the energy distribution of the Compton recoil electrons can be derived from the Klein-Nishina formula (equation 2.11), which results in [Leo, 1995]

$$\frac{d\sigma}{dT} = \frac{\pi r_e^2}{m_e c^2\gamma^2}\cdot\left(2+\frac{s^2}{\gamma^2(1-s)^2}+\frac{s}{1-s}\left(s-\frac{2}{\gamma}\right)\right) \tag{2.13}$$

with the energy T and $s = T/h\nu$. This equation is visualized in figure 2.3 for two different photon energies. The maximum energy T_{max} that a recoil electron can receive is given by [Leo, 1995]

$$T_{max} = h\nu\left(\frac{2\gamma}{1+2\gamma}\right) \tag{2.14}$$

and identifiable in the energy distribution as a clear edge (the so-called Compton edge).

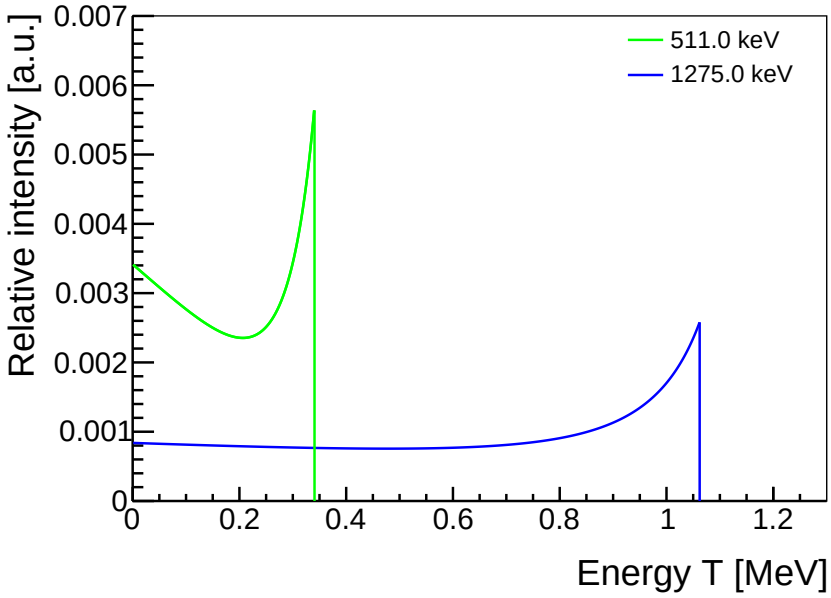

Figure 2.3: Energy distribution of the Compton recoil electrons according to equation 2.13 (in arbitrary units) for the two photon energies investigated in chapter 9. The sharp edge, known as Compton edge, marks the maximum energy an electron can obtain and is defined by equation 2.14. For the 511 keV photons the Compton edge lies at 340.7 keV, while for 1275 keV photons it is at 1062.5 keV. This energy distribution is easy to measure with dedicated particle detectors and is therefore an interesting parameter.

2.2.3 Pair Production

The third interaction process of photons with matter, shown in figure 2.1, is pair formation, which was discovered in 1933 [Blackett and Occhialini, 1933]. In this process, a photon generates an electron-positron pair. Therefore, the photon requires at least twice the rest mass energy of the electron-positron pair, which is $2 \cdot 511\,\mathrm{keV} = 1.022\,\mathrm{MeV}$, but becomes dominant for $E_\gamma > 2\,\mathrm{MeV}$ [Kleinknecht, 2005]. Due to energy and momentum conservation, a third body, typically the nucleus, is essential for the interaction [Leo, 1995] to occur. Consequently, the cross-section per nucleus for pair production depends on the number of electrons surrounding the nucleus, as they influence the effective electric field of the nucleus. This effect is referred to as screening [Leo, 1995]. For the situation without screening with $1 < \epsilon < 137Z^{-1/3}$, the cross-section is given by [Kleinknecht, 2005]

$$\sigma_{\mathrm{pair}} = r_\mathrm{e}^2 4\alpha Z^2 \left(\frac{7}{9} \ln(2\epsilon) - \frac{109}{54} \right) \tag{2.15}$$

using the same variables introduced in equation 2.7.

2.3 Charge Movement in Electric Fields

In MPGDs an external electric field influences the movement of electrons and ions in the gas.

2.3.1 Charged Particle Drift in Gases

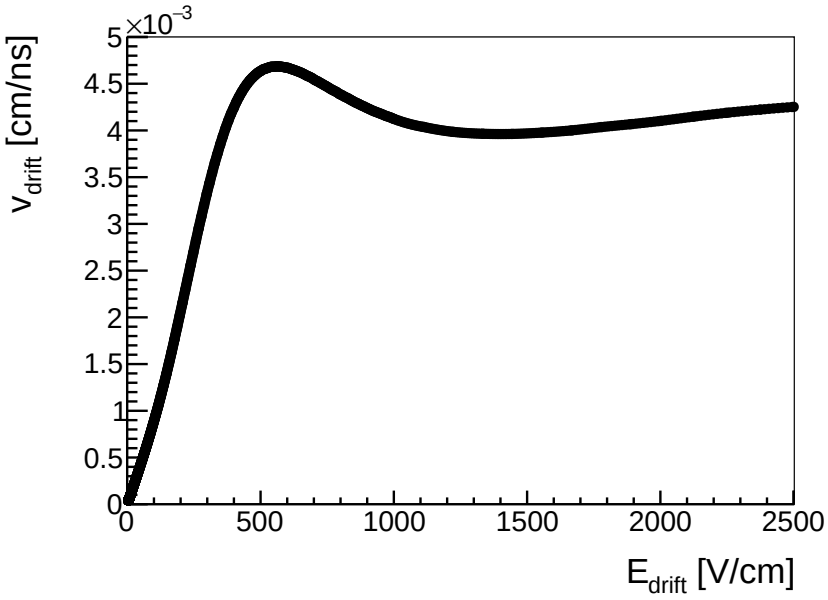

Figure 2.4: Simulated electron drift velocity as a function of the electric drift field E_{drift} for an Ar:CO_2 93:7 vol. % gas mixture. The maximum drift velocity $\vec{v}_{\mathrm{drift}}$ is reached for $|\vec{E}_{\mathrm{drift}}| \approx 550\,\mathrm{V\,cm^{-1}}$. It is simulated with MAGBOLTZ (see chapter 4.1.3) at a temperature $T = 20\,^\circ\mathrm{C}$ and pressure $p = 1000\,\mathrm{mbar}$.

For low electric fields $\mathcal{O}(|\vec{E}|) \lesssim 10^3\,\mathrm{V\,cm^{-1}}$ charged particles follow the electric field lines. While the positively charged ions move towards the cathode, the electrons drift towards the anode. Due to the electric field, both experience an acceleration that increases their drift

velocity $\vec{v}_{\text{drift}}$. The drift velocity for electrons in gas (here Ar:CO_2 93:7 vol. %) as a function of the electric field is shown in figure 2.4. Collisions with other gas atoms lead to a limitation of the drift velocity, resulting in a plateau in figure 2.4 at around $550\,\text{V}\,\text{cm}^{-1}$.
Due to their heavier mass, ions have a lower drift velocity. Mathematically, the drift velocity $\vec{v}_{\text{drift}}$ and the electric field $\vec{E}$ are related by the mobility μ. According to [Kleinknecht, 2005], for ions it is given by

$$\vec{v}^{+}_{\text{drift}} = \mu^{+}\vec{E}\frac{p_0}{p} \tag{2.16}$$

and depends on the reduced electric field $\vec{E}/p$ with the gas pressure p and the normal pressure p_0.
For the measurements performed in this thesis, the electric drift field is chosen such that it results in the maximum electron drift velocity. For the gas mixture Ar:CO_2 93:7 vol. % it is reached at about $|\vec{E}_{\text{drift}}| \approx 550\,\text{V}\,\text{cm}^{-1}$.

2.3.2 Gas Amplification Process

Since the amount of electrons created in an interaction process (see chapter 2.1 and chapter 2.2) is too small to be directly measurable, the signal is usually amplified. In MPGDs this is realized by gas amplification at high electric fields $\mathcal{O}(|\vec{E}|) = 10^4$–$10^5\,\text{V}\,\text{cm}^{-1}$. Consequently, an electron gains enough energy between two collisions with gas atoms to ionize another gas atom. This leads to an electron avalanche [Townsend, 1910]. In this process the number of electrons $N(x)$ increases by $\mathrm{d}N$ after drifting a distance $\mathrm{d}x$:

$$\mathrm{d}N = N(x)\alpha(x)\,\mathrm{d}x \tag{2.17}$$

where α is the first Townsend coefficient. α describes the ionization probability per path length and is therefore defined by $\alpha = 1/\lambda$ with λ being the mean free path of an electron. The total number of electrons is then

$$N = N_0 \exp\left(\int \alpha(x)\,\mathrm{d}x\right) \tag{2.18}$$

with the initial number of electrons N_0 and the Townsend coefficient $\alpha(x)$, which in general depends on the the electric field and the gas. In order to solve the Townsend equation, there are several empirical parametrizations like the one from Rose and Korff [Rose and Korff, 1941] or the one used here [Marić et al., 2005]

$$\alpha = A_0 n \exp\left(-\frac{B_0 n}{E}\right) \tag{2.19}$$

with the two parameters $A_0 = k_{\text{B}}A$ and $B_0 = k_{\text{B}}B$, which include the gas constants A and B as well as the Boltzmann constant k_{B}, the electric field E and the particle density n. Inserting the ideal gas law [Clapeyron, 1834] in the form $n = \frac{p}{k_{\text{B}}T}$, with pressure p and temperature T, into equation 2.19 results in

$$\alpha = \frac{Ap}{T}\exp\left(-\frac{Bp}{ET}\right) \tag{2.20}$$

Nowadays, there are computer models providing the Townsend coefficient value and taking various parameters like gas ionization and excitation into account. Finally, using equation 2.18 and equation 2.20, the amplification factor is described by

$$M = \frac{N}{N_0} = \exp\left(\frac{Ap}{T}\exp\left(-\frac{Bp}{ET}\right)x\right) \tag{2.21}$$

This equation allows theoretically a limitless exponential increase of gas multiplication. In reality it is limited to $M < 10^8$ or $\alpha x < 20$, which is known as the Raether limit [Raether, 1964]. In order to understand this effect, the different detector operation regions and their influence on the detector performance have to be considered. These can be seen in figure 2.5 and the crucial regions are discussed here, following [Leo, 1995].

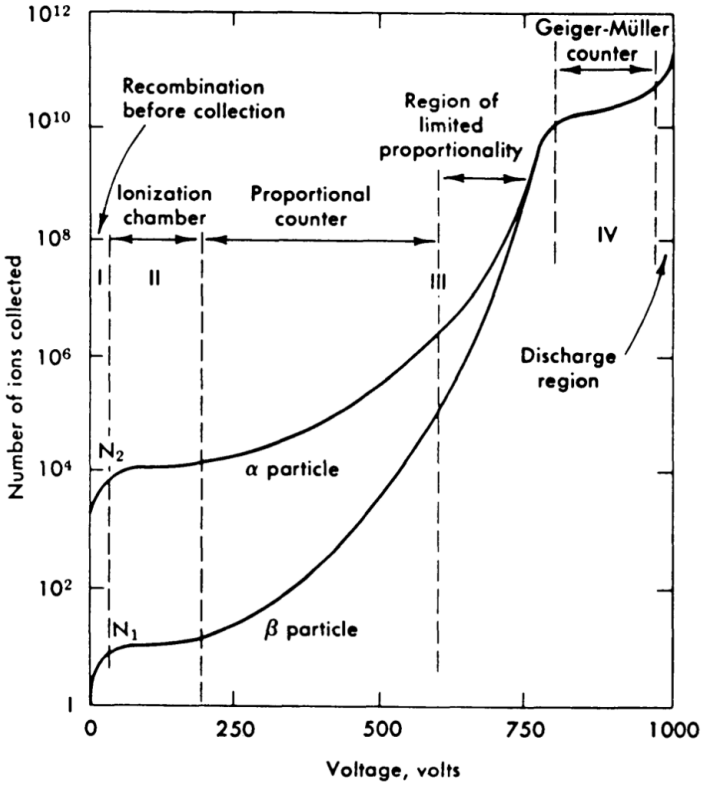

Figure 2.5: Depending on the applied voltage, the detector exhibits different operation regions. The MPGDs used here work as proportional counter, where the detected charge is directly proportional to initial deposited charge by the incoming particle (here shown for α and β particles). Figure taken from [Melissinos, 1966].

Due to gas ionization, an electron-ion pair is created. For a sufficient electric field this electron-ion pair is separated and recombination is prevented. The electron drifts to the anode while the ion moves to the cathode. The detectors used here are operated in the proportional counter region. The electrons are amplified according to equation 2.18, whereby the detected charge is directly proportional to the initial ionization. By further increasing the voltage, the region of limited proportionality is reached. Since ions have a lower mobility than electrons, a space charge is created influencing the effective electric field. If the voltage is increased further, the discharge region is reached in which a conductive plasma is created between the anode and cathode. A continuous breakdown occurs independent of the radiation. This is the Raether limit and has to be avoided as it can damage the detector.

Chapter 3

GEM Detector

In 1997 Fabio Sauli invented the GEM detector [Sauli, 1997], which belongs to the MPGDs. The functionality and performance of GEM detectors has been investigated intensively and is well known. It is high rate capable up to about 6 kHz cm^{-2} without loss in performance [Bianco et al., 2021]. In addition, it has an excellent spatial and temporal resolution of less than 100 µm [Flierl, 2018] and 5 ns [Maerschalk, 2016], respectively.
All measurements in this thesis are carried out with a GEM detector. Its structure, functional principle and the complete detection mechanism are presented in this chapter.

3.1 Working Principle

The basic working principle of a GEM detector as used in this thesis is shown in figure 3.1. An incoming photon interacts with the cathode via one of the interaction processes presented in chapter 2.2, depending on the initial photon energy. When the produced electron exits the cathode, it enters the detector gas, which is a gas mixture of Ar:CO_2 93:7 vol. %.

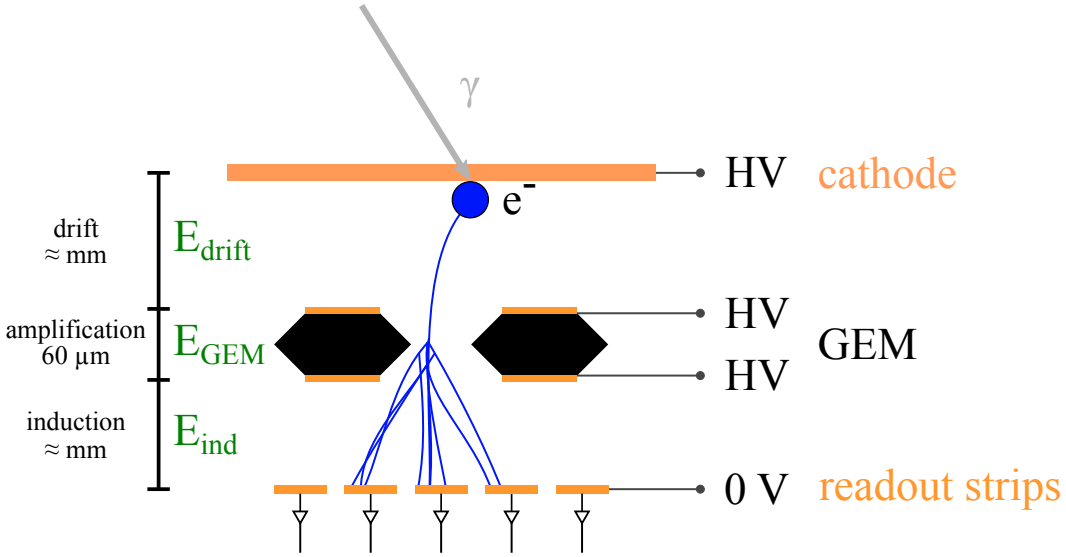

Figure 3.1: Schematic sketch (not in scale) of the working principle of a GEM detector: The photon interacts with the cathode and creates an electron. It enters the drift region, where it is guided to the GEM foil by the electric field $\vec{E}_{\text{drift}}$. In the GEM foil, the electrons are amplified by a strong electric field $\vec{E}_{\text{GEM}}$, creating an electron avalanche. Afterwards, $\vec{E}_{\text{ind}}$ guides the electrons to the readout strips. This charge movement induces a signal on the readout strips.

In total, the GEM detector is divided into three regions, which are indicated in figure 3.1:

- After exiting the cathode, the electron enters the drift region of the GEM detector. Due to the electric field $|\vec{E}_{\text{drift}}| = 550\,\text{V}\,\text{cm}^{-1}$ (see chapter 2.3.1), the electron drifts downward to the GEM foil, guided by the electric field.
- In the amplification region, the number of electrons is multiplied by a strong electric field $\mathcal{O}(|\vec{E}_{\text{GEM}}|) = 10^4\text{–}10^5\,\text{V}\,\text{cm}^{-1}$, as explained in chapter 2.3.2. The detector is operated in the proportional regime.
  The key component in the amplification stage are GEM foils (see chapter 3.2). By applying a voltage difference between the top and bottom side of the GEM foil, strong electric fields are created in the holes in which electron multiplication occurs.
- After amplification, the electrons reach the induction region between the GEM foil and the readout strips on the anode. A low electric field $\mathcal{O}(|\vec{E}_{\text{ind}}|) \approx 3\,\text{kV}\,\text{cm}^{-1}$ is applied between the GEM foil and the anode, guiding the electrons to the anode. The electron movement induces an electrical signal on the readout strip of the anode.

3.2 GEM Foil

3.2.1 Structure

As mentioned in chapter 3.1, the gas amplification processes (see chapter 2.3.2) is realized in a GEM foil. The GEM foils used here have the size $10 \times 10\,\text{cm}^2$. They consist of a 50 µm thick insulating Kapton [Dupont, 2024] layer, coated with 5 µm copper on both sides. By a lithography process [Oliveira, 2023] a periodic hole structure is etched in the foil. A Scanning Electron Microscopy (SEM) picture of a GEM foil can be seen in figure 3.2.

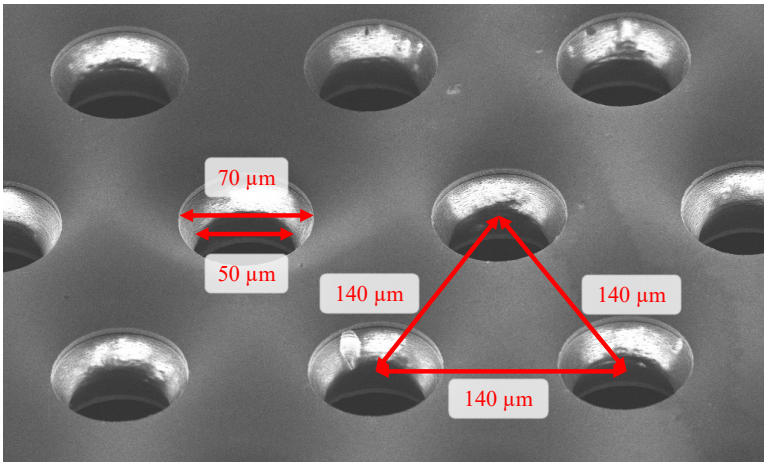

Figure 3.2: SEM picture [provided by Julius Kühne, internal communication] of a GEM foil: A periodic hole structure with a pitch of 140 µm is etched in the foil. The holes have a double-cone shape with an inner diameter of 50 µm and an outer diameter of 70 µm. Since Kapton is an insulator, a voltage difference between both copper sides can be applied, leading to a high electric field inside the holes of a GEM foil.

Applying a voltage difference of about $\Delta U_{\text{GEM}} = 300\,\text{V}$ between the top and bottom copper layer leads to an electric field of about $50\,\text{kV}\,\text{cm}^{-1}$ inside the GEM holes. Consequently, the resulting electric field in the GEM foil is high enough for gas amplification as described in

chapter 2.3.2. The typical gain achieved when applying $\Delta U_{\mathrm{GEM}} = 300\,\mathrm{V}$ is around 20 per GEM foil.

3.2.2 Simulation

In order to visualize and understand the occurring physical processes, the GEM foil is simulated. The simulated electric field configuration as well as the resulting electron avalanche are shown in figure 3.3 and figure 3.4, respectively.
A detailed description and verification of this simulation can be found in Appendix A. While the electric field configuration is provided by the ANSYS (see chapter 4.1.2), the electron amplification is simulated with Garfield++ (see chapter 4.1.4). For all simulations in this chapter a voltage difference $\Delta U_{\mathrm{GEM}} = 280\,\mathrm{V}$ between the top and bottom side of one GEM foil is applied, since it is used for the measurements performed in this thesis[1].

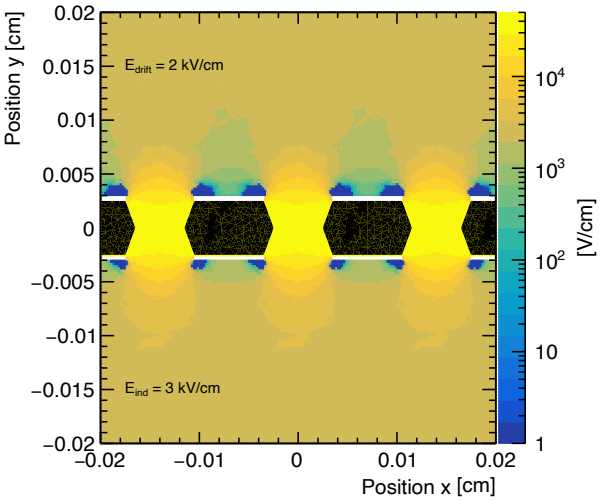

Figure 3.3: Simulated electrical field inside the GEM hole: By applying a voltage difference of $\Delta U_{\mathrm{GEM}} = 280\,\mathrm{V}$ between the top and bottom copper side, an electric field of about $50\,\mathrm{kV\,cm^{-1}}$ is achieved. In addition, a drift field $\vec{E}_{\mathrm{drift}} = 2\,\mathrm{kV\,cm^{-1}}$ and induction field $\vec{E}_{\mathrm{ind}} = 3\,\mathrm{kV\,cm^{-1}}$ is applied.

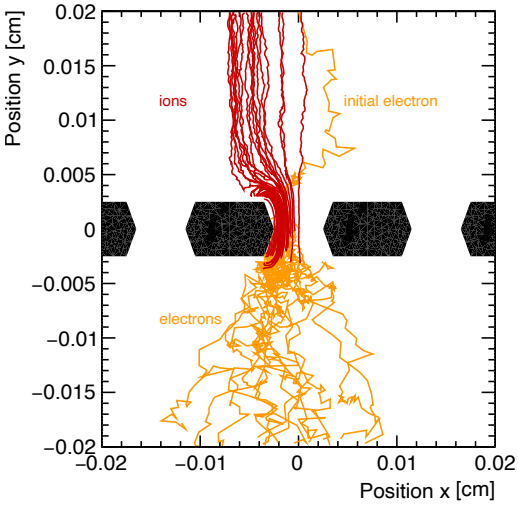

Figure 3.4: Simulated electron avalanche of one initial electron entering a GEM hole: Due to the high electric field shown in figure 3.3 an electron avalanche is created. The movement of the electrons is visualized in orange and that of the ions in red. Not all electrons can exit the GEM hole but are e.g. absorbed by the Kapton layer. The ions move upwards or are absorbed by the GEM foil.

The simulation illustrates the operating principle of the GEM foil: Following $\vec{E}_{\mathrm{drift}}$, the initial electron drifts to the GEM foil (see figure 3.4), where it is multiplied by the high electric field $\mathcal{O}(|\vec{E}_{\mathrm{GEM}}|) = 50\,\mathrm{kV\,cm^{-1}}$ in the hole (see figure 3.3). This leads to an electron avalanche and the production of ions. The ions move upwards or are absorbed by the GEM foil due to the electric field configuration, while the electrons are directed further downwards by $\vec{E}_{\mathrm{ind}}$.

A measure for the electron amplification is the effective gas gain, which is defined as

$$g_{\mathrm{eff}} = \frac{\text{number of detected electrons}}{\text{number of initial electrons}} \tag{3.1}$$

[1] It should be noted here that the applied GEM voltage depends on various factors, such as the particle source or environmental influences, and has to be adjusted accordingly (see chapter 5.5.3 and chapter 6)

Since only detected electrons are considered and therefore electron losses are included, the effective gas amplification is a measurable quantity. The simulated effective gas amplification is shown in figure 3.5. As expected from equation 2.21, the gas amplification increases exponentially with higher GEM voltage. The simulation cannot describe the amplification correctly, which leads to discrepancies between measurement and simulation (see Appendix A). In order to achieve agreement between simulation and measurement, the simulation is corrected by a factor of 2.25 [Janssens, 2019]. This correction is considered in the corrected effective gas gain $g_{\text{eff,corr}}$, which is further used to correctly describe the gas amplification in the GEM detector.

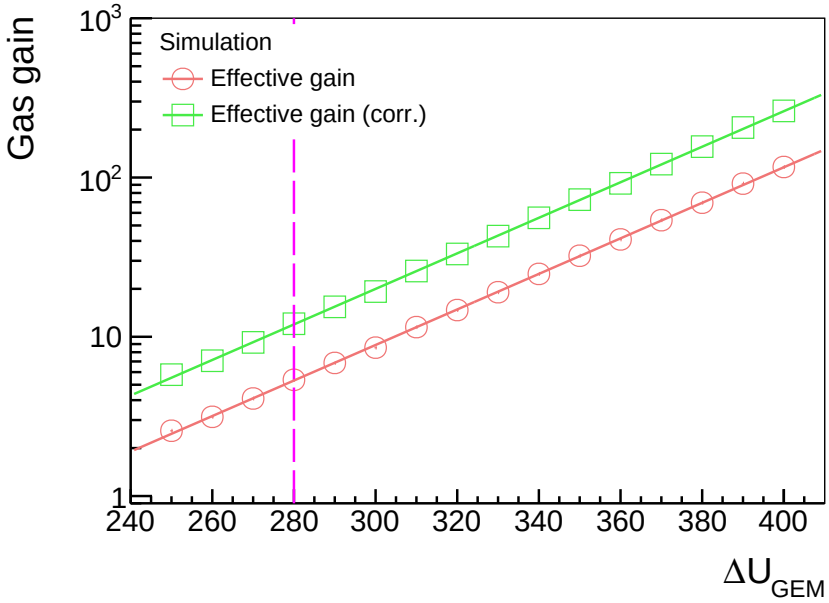

Figure 3.5: Exponential increase of the simulated effective gas gain with ΔU_{GEM}. For the GEM voltage ΔU_{GEM} = 280 V, used for the measurements in this thesis and indicated by the pink dashed line, the simulated effective gas gain is 5.4 and the corrected one 12.1 for a single GEM foil, a factor 2.25 higher.

Applying a GEM voltage of ΔU_{GEM} = 280 V results in an amplification of $g_{\text{eff,corr}}$ = 12.1 for a single-GEM foil, $g_{\text{eff,corr}}$ = 20 is reached at ΔU_{GEM} = 300 V.

3.3 Triple-GEM Detector

3.3.1 Structure

The gas amplification by a single-GEM foil is typically insufficient to obtain a measurable signal. The option to increase the GEM voltage ΔU_{GEM} is only theoretically possible, discharges occur which damage the foil. A more reliable solution is stacking several GEM foils. Here, all measurements are performed with a triple-GEM detector, which should provide an amplification[2] of about $12^3 = 1728$ when using ΔU_{GEM} = 280 V, according to chapter 3.2.2. In total, three GEM foils (see chapter 3.2) are placed in a gas-tight aluminum housing that serves as a Faraday cage. A schematic sketch of a triple-GEM detector is shown in figure 3.6.

[2] For ΔU_{GEM} = 300 V this results in a gas amplification of 20^3 = 8000 for a triple-GEM detector.

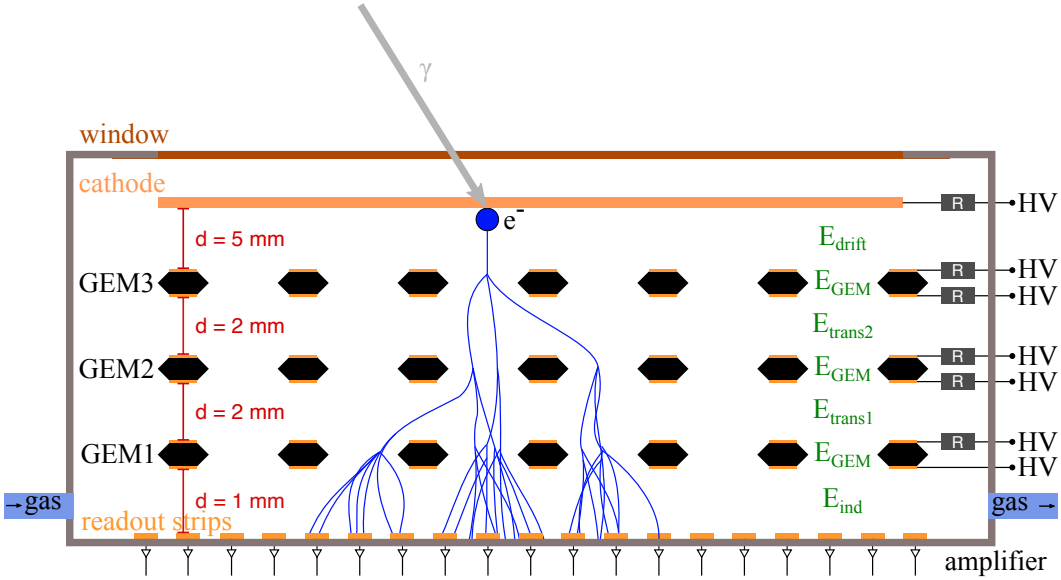

Figure 3.6: Sketch of a triple-GEM detector (not to scale): A photon enters the detector through a window and an electron is generated by an interaction process with the cathode. Due to the electric field $\vec{E}_{\text{drift}}$, the electron drifts from the cathode into the amplification region where the GEM foils are located. The electrons are multiplied, generating an electron avalanche and thus a measurable signal. This signal is read out at copper strips on the anode, using APV25 front-end electronics.

Through an aluminum-coated Kapton window, a photon (X-ray) enters the detector. If the photon interacts for instance with the cathode or the gas, an electron-ion pair is produced. The working principle is identical as described in chapter 3.1: due to the electric field $\vec{E}_{\text{drift}}$, the electron drifts towards the amplification region where three GEM foils are stacked. In each foil electron multiplication occurs. The transfer of the multiplied electrons to the next GEM foil is achieved by an additional electric field $\mathcal{O}(|\vec{E}_{\text{trans}}|) = 2\,\text{kV}\,\text{cm}^{-1}$. Between the last GEM foil and the anode $\vec{E}_{\text{ind}}$ is applied, guiding the electrons towards the anode. The electron movement induces an electrical signal on the readout strip of the anode.

This readout anode consists of a Printed Circuit Board (PCB) with two insulated layers of copper strips arranged perpendicularly, providing 2D position of the particle. Each layer consists of 256 copper strips. As the two strip layers are arranged on top of each other, they experience a different amount of induced charge, which would lead to different pulse heights on both layers. This effect is counteracted by different strip widths. While the upper strips have a width of 80 µm, the lower strips have a width of 320 µm, guaranteeing a homogeneous pulse height distribution for both layers. The strip pitch[3] is 400 µm for both layers. The strips are connected via a Panasonic connector[4], which establishes the connection to the readout electronics (see chapter 4.2).

The detector is constantly flushed with a gas mixture of argon (Ar) and carbon dioxide (CO_2): Ar:CO_2 93:7 vol. %. Noble gases are preferred for the gas amplification process in proportional counters because they fulfill several requirements, such as high amplification, good proportionality, high rate capability and a low working voltage [Leo, 1995]. Due to its low cost, Ar is typically used, but in combination with a polyatomic gas. Otherwise, the UV photons from the deexcitation cause further ionization in the detector. The polyatomic gas, here CO_2, quenches these UV photons and also the secondary emission caused by positive

[3] In this thesis the pitch is defined as the distance between identical points in adjacent units of the periodic structure.
[4] AXK6SA3677YG

ions reaching the cathode [Korff and Present, 1944]. For this reason, CO_2 is referred to as a quencher. In addition, the detector is operated with overpressure to ensure that no oxygen or humidity enters through leaks. Even small amounts of oxygen change the amplification process and consequently the measurement results.

In order to guide the electrons from the cathode to the anode, the cathode and the GEM foils are connected to a negative High-Voltage (HV) supply, whereby the highest negative voltage is applied to the cathode while the anode is grounded. Apart from the bottom side of the GEM1 foil (see figure 3.6), a resistor R is installed for every other HV connection in line to reduce the noise of the power supply. The bottom side of the GEM1 foil provides the trigger signal (see chapter 4.2).

The strength of the electric fields depends on the distances between the various components in the detector (see figure 3.6). The GEM foils are framed, with a total frame height of 1.35 mm (including the GEM foil of 60 µm). In addition, spacers with a height of 0.8 mm are placed between two adjacent GEM foils as well as the GEM1 foil and anode. The distance is necessary to ensure proper drift conditions, which are also required for induction. This results in an effective distance of 1.5 mm between the GEM and anode and 2.1 mm between two adjacent GEM foils.

3.3.2 Simulation

As for the single-GEM foil, the configurations of the electric field and the avalanche process are simulated for a triple-GEM detector, using the simulation from Appendix A. Here, the dimensions (see chapter 3.3.1) and voltages (see Table 5.1) from the real measurement setup are taken. The resulting simulated electric field configuration can be seen in figure 3.7 and the electron avalanche in figure 3.8.

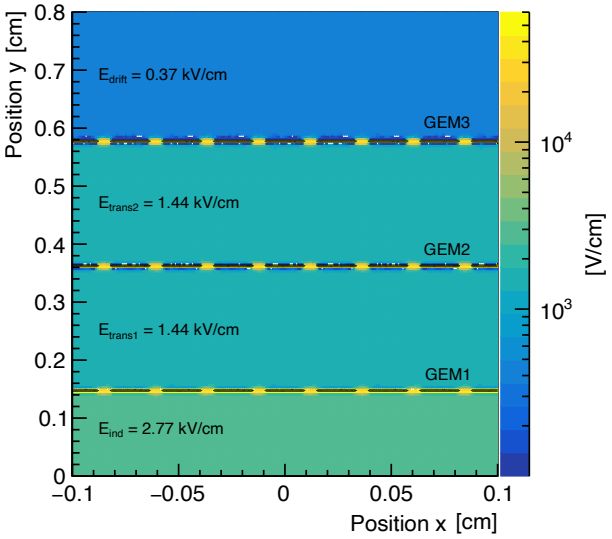

Figure 3.7: Simulated electric field of a triple GEM detector for drift, amplification and induction region. The values and dimensions used correspond to those of the real measurement setup with $\Delta U_{\mathrm{GEM}} = 280\,\mathrm{V}$.

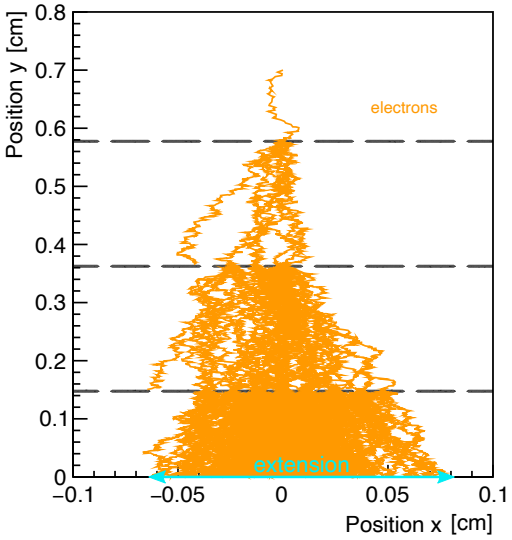

Figure 3.8: Using the electric field configuration of the triple GEM detector from figure 3.7, a single electron multiplication is simulated. Although some electrons are for example absorbed by the subsequent GEM foils, an electron avalanche is created with a specific gas gain and an extension of about 0.15 cm in x-dimension.

While an electric field of $\mathcal{O}(|\vec{E}_{\mathrm{GEM}}|) = 50\,\mathrm{kV\,cm^{-1}}$ is required for electron amplification, the electric fields for the drift, transfer and induction region are lower. According to the simulation they range between $\mathcal{O}(|\vec{E}|) = 0.5\text{–}3\,\mathrm{kV\,cm^{-1}}$ (see figure 3.7). The resulting effective gas gain (see equation 3.1) for a triple-GEM detector is shown in figure 3.9 together with the corrected effective gas gain.

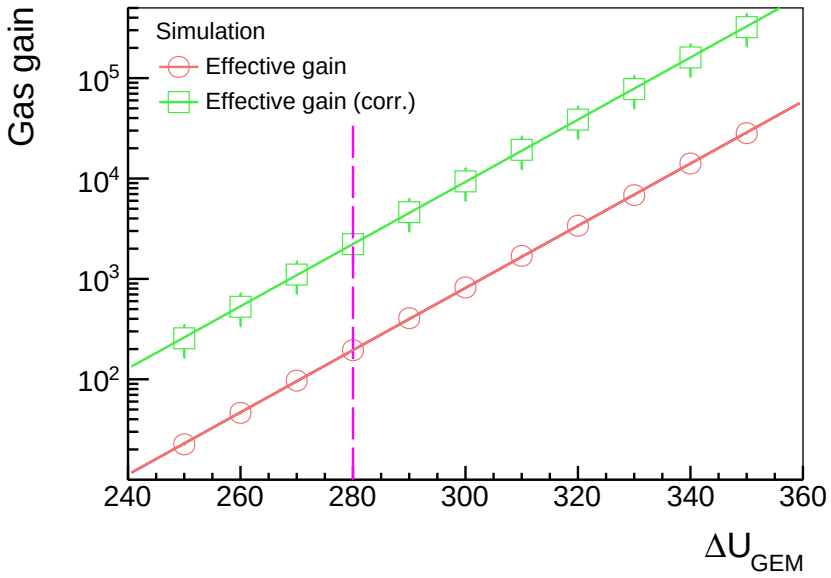

Figure 3.9: For a triple-GEM detector with the electric fields from figure 3.7 and $\Delta U_{\mathrm{GEM}} = 280\,\mathrm{V}$, an effective gas gain of 195 and corrected effective gas gain of 2220 is simulated. The gas gain increases exponentially. An exponential function is fit to the corrected gas gain, with the extracted fit parameters being included in equation 3.2.

For the applied GEM voltage of 280 V, a corrected effective gas gain of $g_{\mathrm{eff,corr}} = 2220$ is achieved. Due to a different drift and induction field compared to the single-GEM foil simulation (see chapter 3.2.2), $g_{\mathrm{eff,corr}}$ is higher than the predicted value $12^3 = 1728$ from the single-GEM simulation.

The exponential increase of the corrected gas gain in figure 3.9 is described by the following equation[5]:

$$g_{\mathrm{eff,corr}} = \exp(-(12.27 \pm 1.04) + (0.0713 \pm 0.0034)\Delta U_{\mathrm{GEM}}) \tag{3.2}$$

where the parameters are extracted from an exponential fit.

When using $\Delta U_{\mathrm{GEM}} = 280\,\mathrm{V}$, in the amplification process of a triple GEM detector an average number of 2220 secondary electrons is produced from an initial electron. These electrons reach the readout anode, where they are combined to a charge-cluster. As indicated in figure 3.8, this charge-cluster has an extension of about 0.15 cm, shown here for the x-dimension, which is further analyzed.
The gas amplification is a stochastic process that leads to a variation in the number of produced secondary electrons and hence to different charge-cluster extensions. In total 5000 events are simulated, each containing one initial electron. The resulting distribution of the charge-cluster extension can be seen in figure 3.10. A Gaussian function is fit to provide the mean value μ and the sigma value of the distribution.

[5] All exponential functions used for fitting in this thesis have the form $y(x) = \exp(const + slope \cdot x)$.

For ΔU_{GEM} = 280 V the mean charge-cluster expansion is μ = 1.4 mm. The number of strips hit on the readout anode can be estimated from this value, when considering the readout strip pitch of 0.4 mm (see chapter 3.3.1). This corresponds to 1.4 mm/0.4 mm = 3.5 hit strips. In addition, the sigma value of the Gaussian fit σ = 0.4 mm is equivalent to the pitch size and thus to one strip. For ΔU_{GEM} = 280 V, the majority of charge-clusters therefore have an extension of 3.5 ± 1 strips. For other ΔU_{GEM} values, the results are shown in figure 3.11.

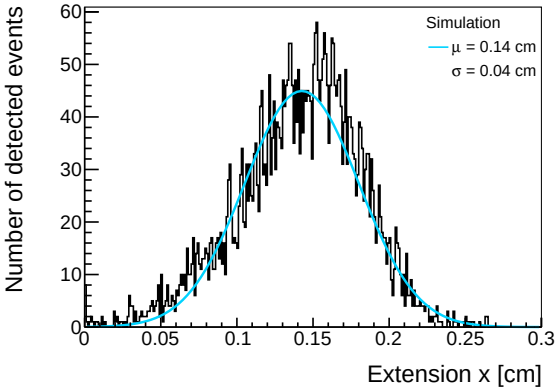

Figure 3.10: Due to the broadening of the electron avalanche, as shown in figure 3.8, an extended area of the anode is hit by electrons. For ΔU_{GEM} = 280 V, the extension in x-direction is shown here for 5000 events, each containing one initial electron. A Gaussian function is fit.

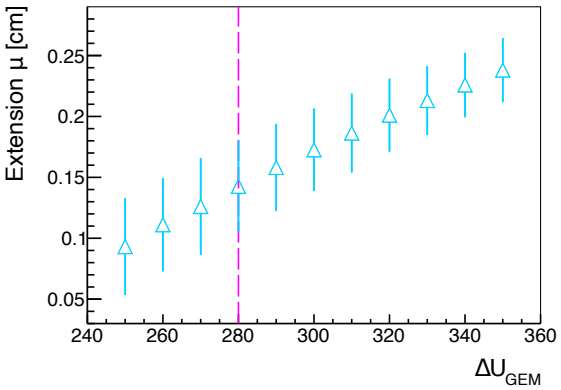

Figure 3.11: This Gaussian fit is performed for various ΔU_{GEM} and the resulting mean cluster extensions μ and corresponding σ values are summarized here. While the mean extension μ of the charge-cluster increases linearly, the width of the distribution σ decreases with higher ΔU_{GEM}.

Chapter 4

Methods

4.1 Simulation Packages

Simulations are carried out using various packages, each specialized in a different field, with the aim of understanding the underlying physical processes in the detector and validating the measurement results.

4.1.1 Geant4

GEometry ANd Tracking (Geant) is a software framework developed at CERN and is used for many HEP experiments such as ATLAS or CMS. Geant4 simulates the interaction of particles with matter using Monte Carlo Methods [Agostinelli et al., 2003]. As the name indicates, both the geometry of the experiment and the tracking of the particles are taken into account. First, the experimental setup is modeled, including the proper dimensions and materials of the various detector components. Then, for tracking purposes, the interaction of particles with the material is simulated, including different physical processes and interactions. Information about the created particles, like e.g. the particle type, position, energy and creation process is provided. Despite the standard processes, which are automatically included, three models are added.
The Geant4 physics list QGSP-BERT-HP is the most recommended model for HEP and is used in ATLAS [Wright and Incerti, n.d.]. Its main purpose is to simulate the interaction of hadrons with matter. Therefore, it contains the quark-gluon string model (QGS) for high energies and the Bertini cascade model (BERT) and a high-precision neutron model (HP). Furthermore, it contains standard electromagnetic processes. Since it provides various standard models and is recommended, it is implemented in the used Geant4 simulation. For the 59.9 keV photons, the inclusion of this model has no significant influence on the results, but for the 511 keV photons it improves the performance of the simulation.
In this thesis the interaction of photons with matter is simulated. The photon interaction in gas in Geant4 is described by the G4PAIPhotonModel (Photo Absorption Ionization Photon Model), which has been explicitly added to Geant4 for the simulation of gaseous detectors [Pfeiffer et al., 2019].
Additionally, the package G4EmLivermorePhysics is included. Since it is specialized on electromagnetic processes and models, some processes are implemented more precisely compared to the QGSP-BERT-HP model, especially at low energies. G4EmLivermorePhysics is very reliable and precisely validated [Ivanchenko et al., 2011].
In the interaction processes of photons with matter (see chapter 2.2) electrons are created. Various information such as the position, momentum, energy, conversion process of these

electrons is extracted from Geant4 and passed onto other simulation programs.

4.1.2 ANSYS

With the software ANalysis SYStem (ANSYS) [ANSYS, Inc., 2022] the electric field configuration in the detector is simulated. It is a Finite Element Analysis (FEA) software. The basic FEA procedure in ANSYS is described in [Thompson and Thompson, 2017]: Using the Mechanical ANSYS Parametric Design Language (APDL) interface, a 3D-model of the detector is created including element types and material properties. In the next step, the geometry is meshed, creating a finite element model. Here, the applied voltages are defined as constraints. ANSYS solves the problem and provides the corresponding electric fields, e.g. of the triple-GEM detector (see figure 3.8) or the converter layers in the detector (see figure 5.22). These resulting electric fields are extracted and further used in Garfield++.

4.1.3 MAGBOLTZ

Using MAGBOLTZ [Biagi, 1995], the transport properties of charged particles in gas are simulated. The drift gas properties are calculated by a numerical integration of the Boltzmann transport equation. The electron drift depends on various material properties, such as energy loss, excitation levels, cross-section, density and more. All this data is available in a large database, which MAGBOLTZ uses to simulate the path of the electrons in a specific gas mixture. Parameters such as the drift velocity (see chapter 2.3.1) or the Townsend avalanche coefficient (see chapter 2.3.2) are then provided. For the simulations carried out here, the electron drift in a certain gas mixture under the influence of an electric field is analyzed.

4.1.4 Garfield++

Garfield++ [Alsamak et al., 2023] is a toolkit specially developed for simulating semiconductor and gaseous detectors, with a focus on the latter. Four main simulation purposes are implemented for gaseous detectors: the ionization process of an incident fast-charged particle, the influence of an electric field, the transport mechanism in the gas and the signal of the readout electronics [Schindler, 2023]. In Garfield++, the ionization is calculated directly with the package High Energy ElectroDynamics (HEED) [Smirnov, 2005]. In addition, simple electric fields can be calculated in Garfield++, but more complex fields have to be imported for example from ANSYS (see chapter 4.1.2). For the electron movement in gas MAGBOLTZ (see chapter 4.1.3) is used, which includes the electron drift in an electric field (see figure 5.28) or the amplification process (see figure 3.8).
Moreover, the ion movement can be simulated, but is not investigated in this work, nor are the readout electronics. Since the photon interaction is simulated more precisely in Geant4 and the electric field in ANSYS, these parts of the simulation are carried out with these packages and the information is imported into Garfield++. Only the electron drift and amplification under the influence of the electric field is simulated.

4.2 GEM Detector Readout Electronics

The GEM detector readout is performed using a Scalable Readout System (SRS) [Martoiu et al., 2013] of the RD51 collaboration [Pinto, 2010]. It was designed to find a general solution for different readout requirements including e.g. a common chip link interface and large scalability.

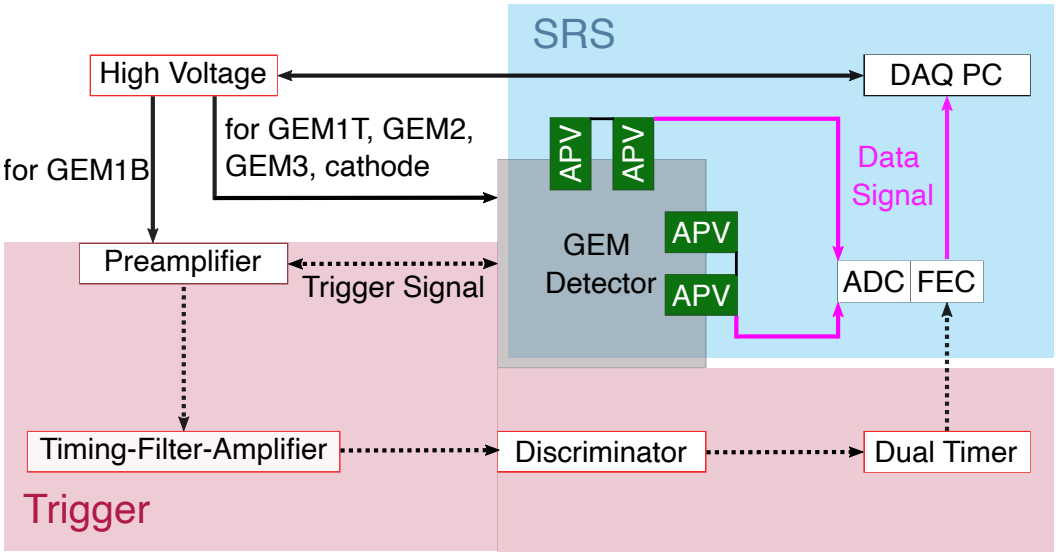

Figure 4.1: In this sketch the DAQ setup is visible, including the SRS and trigger logic. The bottom side of GEM1 foil (see figure 3.6) provides the trigger signal (dashed line), which is further processed by the different components of the readout electronics. When the trigger signal reaches the FEC card, the detector is read out. Therefore, the data signal (pink line), which was sent from the APV25 boards to the ADC, is forwarded to the PC.

The readout electronics logic for the detector can bee seen in figure 4.1. It is employed as trigger and Data AcQuisition (DAQ) system for all measurements performed in this thesis with a GEM detector. The high voltage for the GEM foils and the cathode is provided by a power supply [CAEN, 2023e,d] and is controlled by a computer software [CAEN, 2023c]. Only the bottom side of the lowest GEM foil (GEM1B) is connected to a preamplifier [Ortec, 2002]. Since the electrons drift to the anode, a signal is induced on this GEM foil side. This is used as trigger. This preamplified signal is shaped and smoothed by a Timing-Filter-Amplifier [Ortec, 1969]. In the Constant Fraction Discriminator (CFD) [CAEN, 2023a] a threshold value is set that prevents the measurement of noise, since only a signal that exceeds this threshold value is further processed. For this purpose, the CFD converts the signal into a rectangular trigger pulse (Nuclear Instrumentation Standard (NIM)). The Dual Timer [CAEN, 2023b] extends the duration of the pulse and sends it to the Front End Concentrator (FEC), where it is utilized as trigger for the SRS.
The SRS consists of various components, but the readout chain starts with a front-end Application-Specific Integrated Circuit (ASIC) chip. These ASICs are designed to meet the requirements of the specific detector system. For the GEM detector the APV25 front-end electronics is used [Raymond et al., 2000].

Figure 4.2 shows an APV25 hybrid board [French et al., 2001]. Originally, the ASIC was developed for the CMS silicon tracker. Each of the 128 channels of the chip amplifies and shapes the raw signal from the detector. The output is sampled at the 40 MHz Large Hadron Collider (LHC) bunch crossing frequency, resulting in time bins of 25 ns. For this setup 24

of these time bins are sampled to reconstruct the pulse shape. For pulse heights above 1600 ADC counts[1] an APV25 channels start saturating [Bhopatkar et al., 2017].

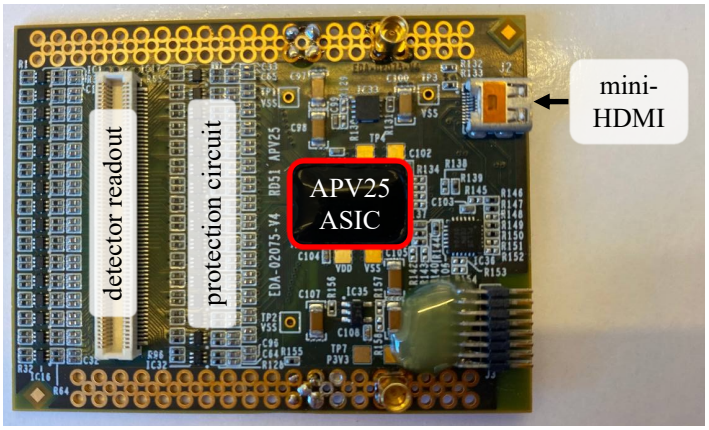

Figure 4.2: Photo of a master APV25 hybrid board, highlighting the protection circuit, the adapter for mounting this board on a detector and the mini-HDMI connector for linking to the SRS. The ASIC is hidden behind the black top-globbing protection.

In order to protect the APV25 chip against discharges, which can occur in the detector and lead to high currents, it is placed on a hybrid board with a special protection circuit. Additionally, these boards provide the connection from the detector to the Analog to Digital Converter (ADC) (see figure 4.1). There are two types of hybrid boards: the master and slave boards. For the GEM detector readout a configuration with two master-slave pairs is chosen. Each pair of master and slave boards is connected with a flat ribbon cable, while the powering and data transfer to the ADC is provided by an HDMI cable connected to the master APV25 hybrid board. In the ADC the analog signal is digitized and forwarded to the connected FEC card. The FEC card controls the front-end electronics and forms an interface to the DAQ PC. If the FEC then also receives a trigger, the detector is read out and the data is sent to the DAQ PC with an Ethernet cable, where it is processed, stored and further analyzed.

4.3 Readout Software and Signal Analysis

For the data taking and processing special software is required, which is introduced in this section.

4.3.1 Readout Software

The data sent from the FEC card to the DAQ PC (see figure 4.1) needs to be recorded. Therefore, the software Micromegas DAQ (mmdaq) [Byszewski, 2012] is used. When recording data with mmdaq, a certain baseline offset, the pedestal, is subtracted for all readout strips per time bin. If the pulse height of a strip is considerably higher than the noise level of that strip, it is considered as hit and the signal on the corresponding strip is saved for each event during the measurement. Once a measurement has been finished, the data is saved as a root file for further analysis.

[1] The exact value is slightly different for each APV25 and is determined experimentally.

For more information on the data analysis software see [Flierl, 2018]. The basic principles are summarized here.

4.3.2 Signal Shape Evaluation

In order to reconstruct various parameters about the measured particles, like e.g. their positions, the collected data has to be analyzed. First, the signal and its shape on the readout strips have to be evaluated. Figure 4.3 shows a typical single strip signal.

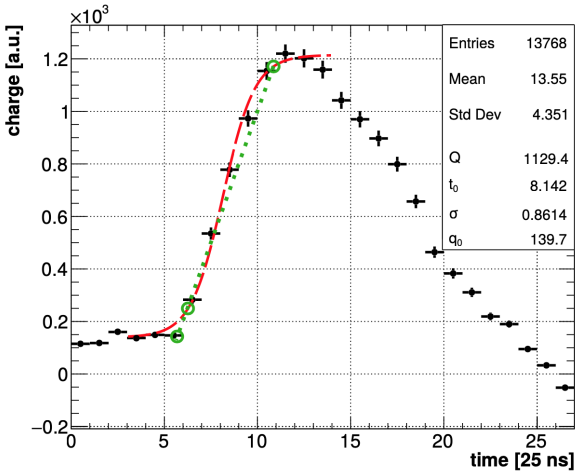

Figure 4.3: A characteristic single strip signal from a GEM detector has a fast rise-time and a slow drop. An inverse Fermi function (equation 4.1) is fit to the data points (red function). In green the extrapolated start timing of the signal is indicated. Figure taken from [Flierl, 2018].

To extract the physically relevant information, which is mostly provided by the rise of the signal, an inverse Fermi function is fit:

$$q(t) = \frac{Q}{1 + e^{\frac{t-t_0}{\sigma}}} + q_0 \tag{4.1}$$

with the maximum charge Q, the point of inflection t_0 which is used as strip time information, a measure for the rise time σ and the offset from the baseline q_0. Since the detector is a proportional counter (see chapter 2.3.2), Q is proportional to the complete energy deposited in the drift area.

4.3.3 Charge-Cluster Reconstruction

So far, only the measured signal on a readout strip has been considered. However, due to the amplification process of the electrons in the GEM foil (see chapter 3.2) and charge sharing between the strips, it is extremely unlikely that only one strip is hit per event. Instead, only one hit strip indicates noise. A full event signal is determined by grouping the single adjacent hit strips (see chapter 4.3.2) to one charge-cluster. There are four conditions which have to be fulfilled for charge-cluster reconstruction:

- At least three neighboring strips have to be hit.
- Only a single strip gap is allowed.

- The deposited charge per strip q_{strip} has to exceed 60 adc channels to be considered in the reconstruction process.
- The total charge collected by these strips $Q_{\text{cluster}} = \sum_{\text{strips}} q_{\text{strip}}$ in the charge-cluster has to be larger than 300 adc channels channels.

Every charge-cluster corresponds to one single particle interaction in the detector.

4.3.4 Position Reconstruction

The position of this charge-cluster is determined by the center of the charge, which is known as the centroid method. This method allows for a position reconstruction by weighting the position of each strip x_{strip} with the deposited charge q_{strip} leading to the charge weighted mean hit position:

$$\vec{x}_{\text{cen}} = \frac{\sum_{\text{strips}} \vec{x}_{\text{strip}} \cdot q_{\text{strip}}}{\sum_{\text{strips}} q_{\text{strip}}} \tag{4.2}$$

where $\vec{x}$ contains the coordinates of the readout plane, namely the x- and z-coordinate and q_{strip} is the charge collected at the corresponding strip.

Chapter 5

Converter Layers for Photon Detection

5.1 Simulation: Motivation

The novel idea of this project is the improvement of the photon conversion efficiency[1] in a triple-GEM detector by inserting multiple solid converter layers. There are two main aspects regarding the photon-matter interaction (see chapter 2.2), which are the inspiration behind this approach.
On the one hand, the density ρ of a solid material is much higher than that of gas. As the attenuation coefficient μ is proportional to the density ρ (see equation 2.3), this leads to a higher photon attenuation in a solid material compared to gaseous media. Specifically for 60 keV photons, the main detector gas argon exhibits an attenuation coefficient[2] of $\mu_{\mathrm{Ar}} = 7.4 \times 10^{-4}\,\mathrm{cm}^{-1}$. In copper it is $\mu_{\mathrm{Cu}} = 13.3\,\mathrm{cm}^{-1} \approx 18 \times 10^{3}\mu_{\mathrm{Ar}}$, which is 4 orders of magnitude higher. According to equation 2.2, this results in stronger photon absorption in copper, for example by a factor of 773 for $x = 5\,\mathrm{mm}$ material thickness.
On the other hand, for the photoelectric effect, which is the dominant process for the photon energies investigated here (see figure 2.1), the cross section σ_{photo} is proportional to Z^5 (see equation 2.7). Consequently, a solid material with a high atomic number Z increases the photon interaction probability.
Therefore, solid converter layers with high-Z coating are preferable.

This idea is further motivated in figure 5.1. The cases shown in green and pink have been simulated using Geant4.
There are 5 configurations with an increasing number of stacked layers reaching from 0 to 4 layers (green). In addition, 4 tilted layers are simulated (pink). All layers are made of 20 µm thick copper, they are placed in a GEM detector and are irradiated with 50 keV photons, as shown in figure 5.1 on the left. With each additional stacked layer the conversion probability enhances by about 0.3 %. For this specific simulated setup with 4 stacked layers and 4 tilted layers, both provide roughly the same photon conversion probability of about 1.5 %. The simulation confirms the fundamental concept of utilizing multiple solid converter layers, preferable with high-Z coating, to increase the detection efficiency of photons in a

[1] In this thesis the conversion efficiency $\varepsilon_{\mathrm{conversion}}$ includes the interaction and extraction probability, meaning $\varepsilon_{\mathrm{conversion}} = \varepsilon_{\mathrm{interaction}} \cdot \varepsilon_{\mathrm{extraction}}$.
$\varepsilon_{\mathrm{interaction}}$ is the photon-matter interaction probability, where an electron is created. In a gaseous detector, only electrons in the detector gas can be detected. If the electron is not produced directly in the gas but in another material, the extraction probability $\varepsilon_{\mathrm{extraction}}$ from this material into the gas has to be considered.
[2] For the calculation data from [Berger et al., 2010] is used. The same values are presented in Table 2.1.

GEM detector.

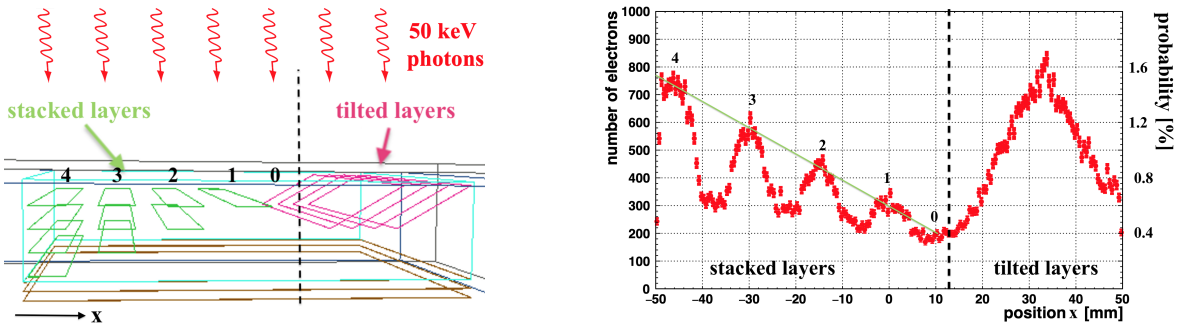

Figure 5.1: In a Geant4 simulation the detector setup is irradiated with 50 keV photons (left) and the results are shown in the right figure. In the detector, 0 to 4 stacked layers and 4 tilted layers consisting of 20 µm thick copper are simulated. With each layer, the number of produced electrons reaching the gas increases. Both configurations with 4 stacked and 4 tilted layers provide a equivalent number of created electrons with respect to the x-extension of the layers and thus a similar photon conversion probability (right), [Penski, 2020].

5.2 Theoretical Working Principle

For an efficient photon detection as well as a high electron guiding efficiency, multiple converter layers are arranged perpendicular to the GEM foils, as shown in figure 5.2.

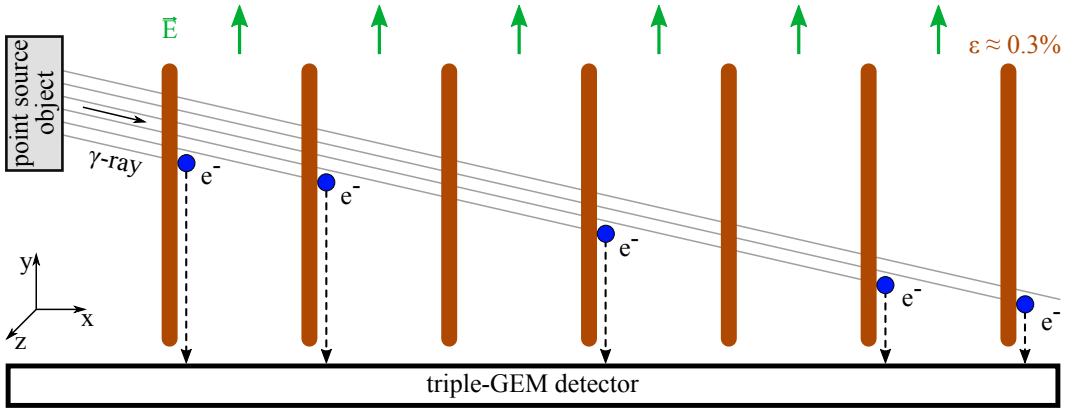

Figure 5.2: A point source object is emitting photons, which interact with the converter layers. By inserting multiple converter layers, the photon conversion probability increases. In the interaction process an electron is created, which has to be guided to the amplification and readout area of the triple-GEM detector. This is achieved by introducing an electric guiding field $\vec{E}$ in y-direction. These converter layers replace the cathode in the triple-GEM detector.

A particle source emits keV X-ray photons, which interact with the converter layers according to the processes introduced in chapter 2.2, creating electrons. As simulated in chapter 5.1 the probability of an interaction in combination with an electron extraction is about 0.3 % using one 20 µm thick copper layer and 50 keV photons. In order to increase the photon conversion probability, multiple of these layers are placed inside the triple-GEM detector, replacing the cathode (see figure 1.6).
For the detection of the electrons, they have to drift to the amplification region of the triple-GEM detector. Therefore, an electric guiding field $\vec{E}$ between two layers is mandatory. It is realized by a structured converter layer design (introduced in chapter 5.3.1), to which a

voltage gradient in y-direction is applied (introduced in chapter 5.3.2) resulting in an electric field in this direction. The basic concept of the electric guiding field is also illustrated in figure 5.2. After amplification, the signal is read out and the x- and z-position of the particle is provided by the 2D readout structure of the GEM detector.

This setup aims for optimizing the following aspects, which are covered in this thesis:

- Electric guiding field: The electric guiding field is responsible for guiding the electrons from the drift region, where the converter layers are located, into the amplification region of the GEM detector, as shown in figure 5.2. This electric field influences the electron drift and thus the performance of the detector. A configuration has to be found where the number of detected electrons is maximized, which means a high electron guiding efficiency has to be achieved (see chapter 5.5.4).

- Material optimization: The material composition and its properties like the layer thickness, influence the photon conversion probability and the number of extracted electrons. In the end, a setup is desirable where the photons have a high detection efficiency. Thus, in addition to the high guiding efficiency, the photon conversion and electron extraction efficiency has to be investigated. This material optimization process is described in chapter 8 for photons with an energy of 59.5 keV. Additionally, the detection efficiency of 511 keV photons is investigated in chapter 9.

- Position reconstruction: As shown in figure 5.2 the 2D position of the particle is given by the GEM detector readout, providing the x- and z-coordinate. For the reconstruction of the 3D position of the particle, the setup has to be modified. The position reconstruction method is implemented in chapter 7.

5.3 Converter Layers

5.3.1 Design

The converter layers used in this thesis are custom-designed double-sided PCBs (Printed Circuit Boards). A PCB consists of an insulating material with conductive lines etched on both sides. Figure 5.3 shows a picture of the converter layer design.
The converter layer has an active area of 100 mm × 20.6 mm, which refers to the part of the PCB covered with copper strips. In total there are 25 copper strips, each with a width of 400 µm. They are arranged at a distance of 400 µm, as visible in the top picture of figure 5.3. Neighboring strips are connected with 22 MΩ Surface Mount Device (SMD) resistors in order to minimize the drawn current. Both outer copper strips are connected to contact pads, where the voltage difference ΔU_y (see figure 5.4) is applied. The distance from the edge of the outer most copper strip to the end of the insulating material is 500 µm.
The copper strip design of figure 5.3 is identical for the front and back side of the layer. In addition, the same layer design is utilized for all converter layers investigated in this thesis, in particular in chapter 8, where various converter layer types are examined. These types differ in the thickness of the copper strips and the insulation material as well as the insulator material.

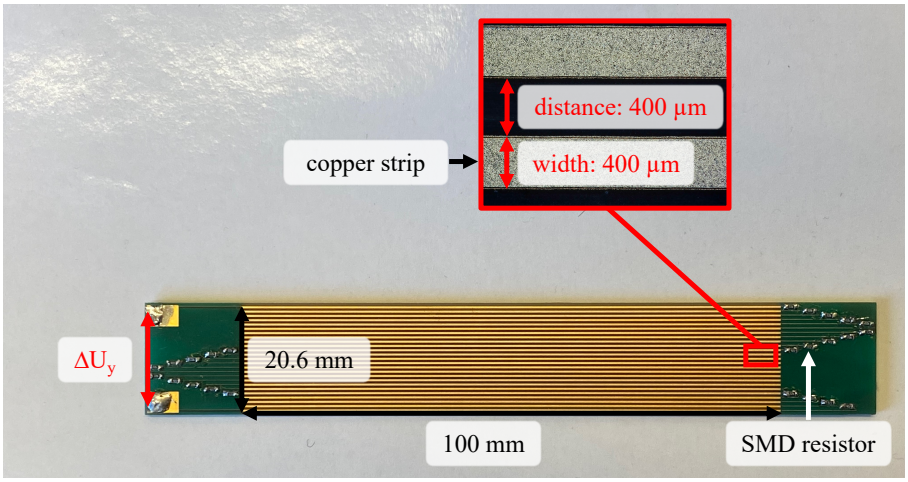

Figure 5.3: A converter layer is a PCB made of an insulating carrier material with a height of 20.6 mm and copper strips with a length of 100 mm in order to cover the complete active GEM foil area. The neighboring copper strips are connected via 22 MΩ SMD resistors and the outer most ones have a contact pad to apply the voltage difference ΔU_y. As visible on the enlarged image of the copper strips, they are arranged at a pitch of 800 µm.

For a proof of concept the main focus of this work is the detection of photons with an energy of 59.5 keV. The converter layer design fulfills the following requirements:

- For the investigated photon energy of 59.5 keV, the photoelectric effect dominates in copper (see figure 2.1), thus the photon interaction probability σ is approximated by $\sigma \approx \sigma_{\text{photo}}$ (see equation 2.5). As σ_{photo} scales with Z^5 (see equation 2.7), high-Z materials are preferred. Copper has an atomic number of $Z = 29$, which is higher than that of the main detector gas argon with $Z = 18$. Therefore, copper provides a higher cross-section and the use of copper-coated converter layers increases the photon interaction probability. Compared to other materials like gold with $Z = 79$, it is comparatively cheap, industrially available and therefore well suited for an initial proof of concept.

- An electric field (here in the y-direction) is necessary to guide the electrons created during the conversion process down to the amplification area. This guiding field is created by a voltage difference that decreases linearly from top to bottom. In contrast to a single copper plate (see figure 5.1), this requirement is met with the copper strip design, as a voltage gradient is realized (see figure 5.3).

- The use of several bare copper strips, which are connected to each other via resistors, also meets the previous requirements. However, mounting these single strips in the detector is more complicated, and therefore the use of a carrier material is preferred. The insulating material of a PCB serves as a carrier material for the copper strips and enables a simple installation in the detector.
  In order to realize the electron drift by the electrical guiding field, copper strips have to be on both sides of the insulating carrier material. Additionally, more copper is available for the photons to interact with. As shown in figure 2.2, the majority of the photo-electrons are emitted in forward direction, but there is still a small proportion that is emitted backwards and is therefore additionally detectable.

A double-sided PCB fulfills all these requirements and is therefore chosen as converter layer. In this chapter the performance of one specific converter layer type is investigated including

the comparison to simulation results. This converter layer type[3] has an insulating material thickness of 1520 µm and a copper thickness of 35 µm, while the insulating material is Flame Retardant (FR)4 (for more information, see chapter 8.2).

5.3.2 Electric Guiding Field

All applied voltages, which influence the resulting electric guiding field $\vec{E}_{\text{res}}$ of the converter layer, are presented in figure 5.4.

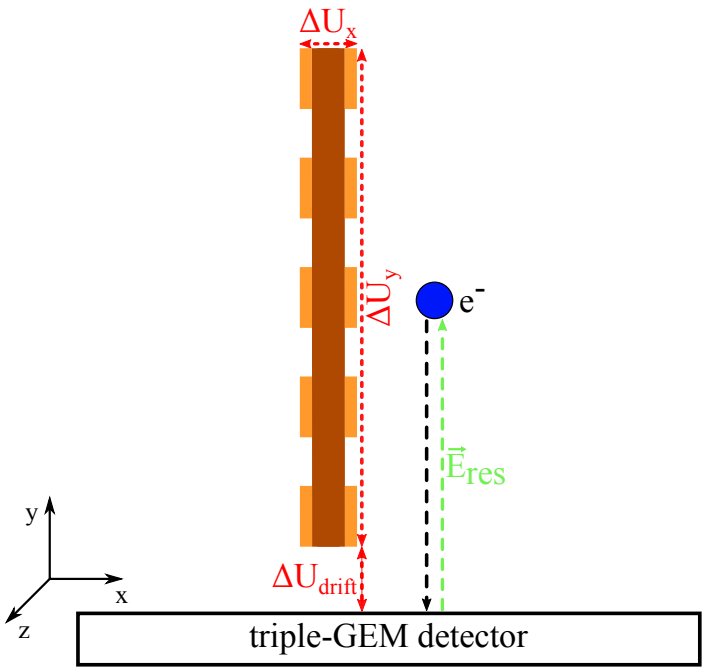

Figure 5.4: Three different voltage differences influence the resulting electric field $\vec{E}_{\text{res}}$: ΔU_{y} between the top and bottom copper strip, ΔU_{x} between the two copper sides of the PCB and ΔU_{drift} between the lowest copper strip and top GEM foil. The electron moves anti-parallel to $\vec{E}_{\text{res}}$. The resulting electric field $\vec{E}_{\text{res}}$ does not have to be perpendicular to the GEM foils, as indicated here.

There are three voltage differences with respect to the converter layer that influence the electric guiding field and thus the electron drift:

- ΔU_{y}: It is applied between the upper and lower copper strip of a converter layer and ensures the electron drift in y-direction. For detection, the electron has to be guided downwards to the triple-GEM detector. ΔU_{y} is also indicated in figure 5.3.
- ΔU_{x}: This voltage difference is applied between the copper strip sides of one PCB. It influences the electron drift in x-direction.
- ΔU_{drift}: To guide the electrons from the bottom of the converter layer to the top GEM foil of the triple-GEM detector, the voltage difference ΔU_{drift} is applied.

The main purpose of the applied voltage configuration is to ensure an efficient electron guiding to the amplification region of the GEM detector. Therefore, a voltage combination has to be found that influences the electric guiding field such that the electron guiding efficiency is

[3] Due to the dimensions, this converter layer type is referred to as 1520 + 35 in the following.

maximized.

Negative voltages are applied to the converter layers to guide the electrons to the amplification region. In order to better understand the definition of the applied voltage differences ΔU_y and ΔU_x, a detailed description including examples can be found in figure 5.5.

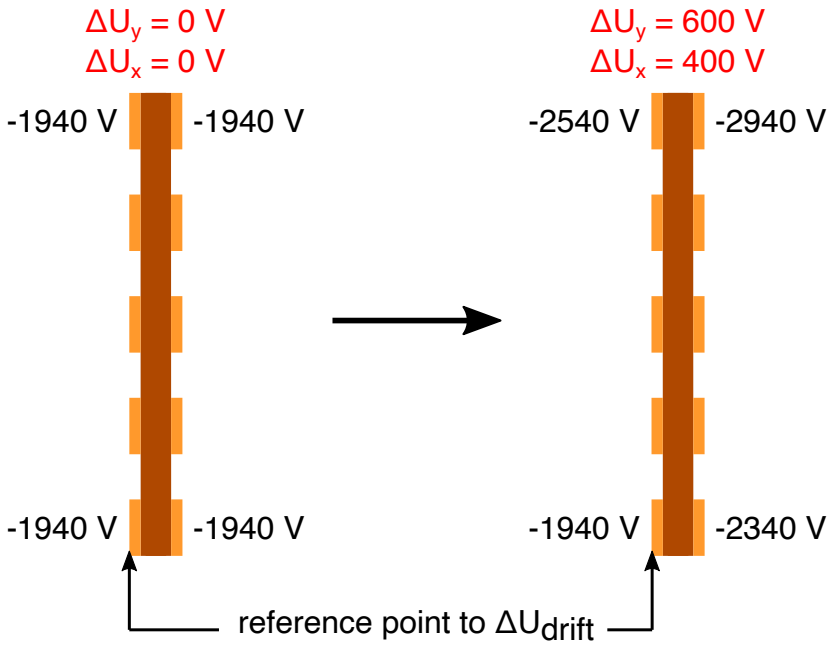

Figure 5.5: For a better understanding of the introduced voltage definitions, two examples are illustrated here. For the perpendicular setup the bottom left strip of one converter is set as reference point to ΔU_{drift} and is kept constant (here at −1940 V).
Left setup: When applying $\Delta U_y = 0$ V and $\Delta U_x = 0$ V, all other copper strips have the some potential of −1940 V.
Right setup: Due to $\Delta U_y = 600$ V, at the upper left strip the voltage −2540 V is applied. The voltage difference $\Delta U_x = 400$ V increases the absolute voltage at the strips on the right side by 400 V. As a result, −2340 V is applied to the lower right strip and −2940 V to the upper right strip.
Other combination (not shown here): For the voltage combination $\Delta U_y = 600$ V and $\Delta U_x = -400$ V, the voltages applied to the left copper strips are identical to the ones shown in the right setup. But due to $\Delta U_x = -400$ V, −1540 V is applied to the lower right strip and −2140 V to the upper right strip.

As an example, the resulting equipotential distribution for the voltage combination $\Delta U_y = 600$ V and $\Delta U_x = 0$ V of the converter layers is shown in figure 5.23.

5.4 Measurement

5.4.1 Setup

A picture of the measurement setup can be seen in figure 5.6. The converter layers presented in chapter 5.3.1, consisting of a 1520 µm thick FR4 insulator layer, are incorporated perpendicularly into the triple-GEM detector (see chapter 3.3.1).
In total 5 of these layers are installed in the drift region, replacing the cathode. An additional spacer with a height of 2 mm is placed between the top GEM foil and the bottom edge of the converter layer to prevent sparks. The adjacent converter layers have a distance of 11.2 mm. The exact dimensions of the mount can be viewed in Appendix B. The cut-outs for insert-

ing the layers are slightly larger, as the resistors increase the total thickness of the layers. This setup is irradiated with a radioactive Americium-241 (^{241}Am) source with an activity of 370 kBq that is positioned in the source holder and emits photons (for more information, see chapter 5.4.2).

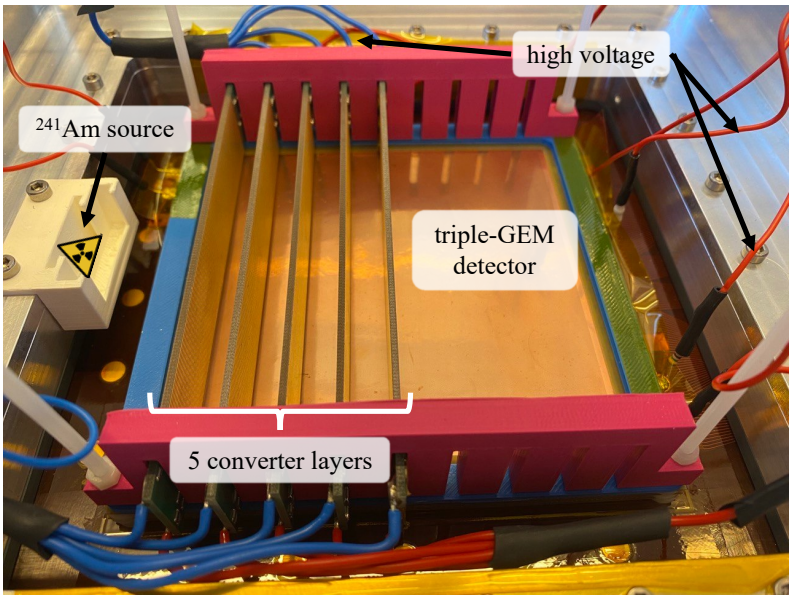

Figure 5.6: In the GEM detector 5 converter layers are placed perpendicularly. Using high voltage cables the proper voltages are applied to the GEM foils and the converter layers. A radioactive point source (not shown) is placed in the source holder on the left in order to irradiate the converter layers.

In this chapter the voltages of Table 5.1 are applied, following the naming scheme of figure 3.6 and figure 5.4. These applied voltages provide a good working point for this GEM detector setup, as discussed later in chapter 5.5.3. For the triple-GEM detector the corresponding electric fields[4] are listed.

Variable	Value
ΔU_{ind}	400 V
$\vec{E}_{\text{ind}}$	2.77 kV cm^{-1}
$\Delta U_{\text{trans1,2}}$	300 V
$\vec{E}_{\text{trans1,2}}$	1.44 kV cm^{-1}
$\Delta U_{\text{GEM1,2,3}}$	280 V
$\vec{E}_{\text{GEM1,2,3}}$	56 kV cm^{-1}
ΔU_{drift}	100 V
$\vec{E}_{\text{drift}}$	0.37 kV cm^{-1}
ΔU_{x}	0 V
ΔU_{y}	600 V

Table 5.1: Applied voltages and corresponding electric fields for the triple-GEM detector and drift region used for measurements performed in this chapter, providing electron drift, amplification and transport. The corresponding electric field of the triple-GEM detector is visualized in figure 3.7 and of the converter layer setup in the GEM detector in figure 5.24.

[4] They result from calculations with the exact dimensions of the detector setup presented in chapter 3.3.1. Example: The drift region has a size of $d_{\text{drift}} = 2\,\text{mm} + \frac{1.35\,\text{mm}}{2} \approx 2.7\,\text{mm}$ (2 mm spacer introduced above and 1.35 mm GEM frame). This results in an electric field of $|\vec{E}_{\text{drift}}| = \frac{100\,\text{V}}{2.7\,\text{mm}} = 0.37\,\text{kV cm}^{-1}$.

For the various perpendicular converter layer structures investigated in chapter 8, the basic measurement setup described here is the same despite minor adjustments regarding the layer mounting. For completeness, the applied voltages for the GEM foils are listed in Appendix C including the environmental conditions for all measurements performed in this thesis.

5.4.2 Americium-241 Particle Source

For the test measurements discussed in this thesis, an Americium-241 (^{241}Am) particle source is used. The relevant information about this source is summarized here, while more detailed information can be found in [Terada et al., 2016]. ^{241}Am decays via an α-decay to ^{237}Np with a half-life of 432 years:

$$^{241}_{95}\mathrm{Am} \longrightarrow {}^{237}_{93}\mathrm{Np} + {}^{4}_{2}\alpha^{2+} + \gamma(59.5\,\mathrm{keV}) \tag{5.1}$$

The created α particles have energies between 5400 keV to 5600 keV. Additionally, a gamma ray with an energy of about 59.5 keV is emitted with a probability of around 36 %. In the other cases there is deexcitation emission of γ-rays, conversion electrons, Auger electrons and X-rays [Denecke, 1987]. Since the radioactive material is embedded in a plastic sheet, which absorbs all α- particles, and all other decay-products are negligible [Ziegler, 2010], the 59.5 keV photons are the dominant emission product and are utilized for measurements. It is a point source with an activity of roughly 370 kBq, leading to an 59.5 keV emission rate of $0.36 \cdot 370\,\mathrm{kBq} = 133\,\mathrm{kBq}$ in 4π.

5.5 Measurement Results

The measurements, performed with the setup and voltages introduced in the previous section, focus on understanding the basic working principle and performance of a triple-GEM detector when incorporating the 1520 µm FR4 layers with 35 µm Cu strips on both sides. Five of these layers are irradiated with 59.5 keV photons.

5.5.1 2D Position Reconstruction

The 2D hit distribution on the anode is shown in figure 5.7. Each hit corresponds to one charge-cluster, from which the x- and z-position is determined by the centroid method (see chapter 4.3.4). In the area where the converter layers are located, events are detected over the complete z-dimension and up to $x \approx 15$ mm. This shows that the basic concept of electron guiding works as intended. Due to the electric field configuration and the resulting electron drift, no electrons reach the region with $x > 15$ mm. As can be seen in the hit distribution, peaks occur between the converter layers.
To investigate this in more detail, the profile of this hit distribution is shown in figure 5.8. The position of the converter layers is visible as a dip in the intensity because of their thickness resulting in the formation of peaks between the layers. The peak height decreases with increasing distance from the source. There are two reasons for this: Firstly, the initial photon intensity I_0 decreases according to the inverse square law with $I = I_0/r^2$, where r is the distance from the source. This principle was first postulated by [Newton, 1846]. Secondly, the intensity decreases exponentially due to a non-negligible photon absorption in the thick FR4 insulating layer according to the Lambert-Beer law (see equation 2.2). The absorption behavior of the converter layer is further investigated in chapter 8.3. These two effects overlap and lead to the observed attenuation.

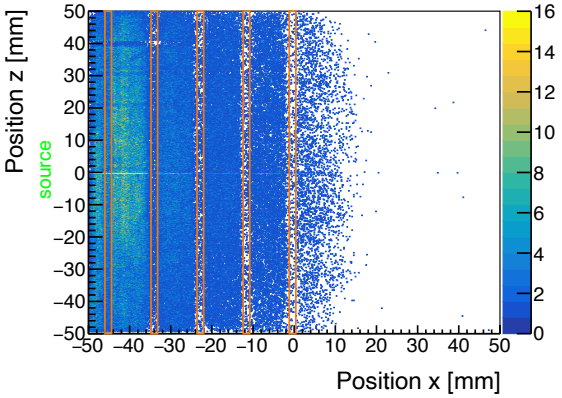

Figure 5.7: There are more hits between the converter layers (orange box), showing that the electrons are extracted and guided downwards from the converter layers and hence are detectable.

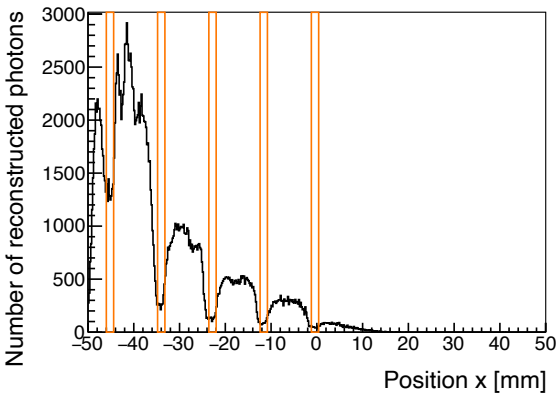

Figure 5.8: Profile of the hit distribution from figure 5.7 with the orange boxes marking the position of the layers. The peaks between the layers are clearly distinguishable and decrease with increasing x-value, due to the greater distance to the particle source and the photon absorption by the converter layers.

5.5.2 Cluster Information

Besides the position, additional information about this reconstructed charge-cluster is extracted and presented in this section. For each trigger signal (see figure 4.1) a specific number of charge-clusters is reconstructed, which is shown in figure 5.9. A reconstructed cluster fulfills all requirements presented in chapter 4.3.3.

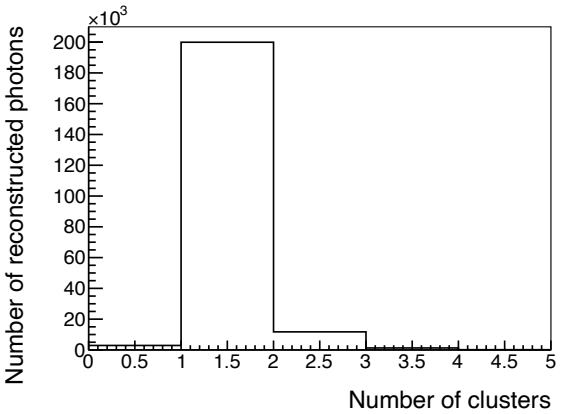

Figure 5.9: With each trigger signal, a certain number of charge-clusters is reconstructed. In around 90 % of the cases, a single charge-cluster is reconstructed, i.e. usually one charge-cluster is generated by a photon interaction.

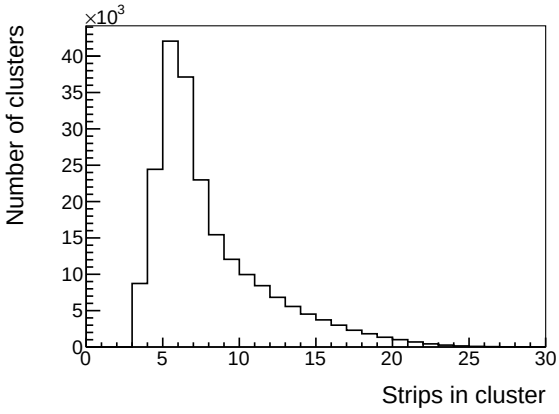

Figure 5.10: Due to the electron drift, ionization and amplification process, the charge is deposited on multiple neighboring strips. In x-direction mainly 5–6 strips are hit, with a tail of up to 24 strips.

A single cluster is reconstructed in the majority of cases. A zero-cluster reconstruction indicates noise coupled to the detector or failed clustering. If two or more clusters are detected, the charge-cluster with the highest charge is further analyzed. As motivated in chapter 3.3, this charge-cluster has a certain extension in x- and z-direction, whereby the former can be seen in figure 5.10. Most of the clusters have a size of 5–6 strips, but some can reach a size of up to 24 strips.

When simulating the amplification process of an electron in a triple-GEM detector, an extension of about 3 ± 1 strips is observed in figure 3.10. Thus, compared to this simulation result, more strips are hit in the measurement. This behavior indicates that the electron-cluster[5] already has a certain extension before the amplification process due to the ionization process of the primary electron. The charge per charge-cluster measured by the APV25 is shown in figure 5.11. This cluster charge distribution has a main peak at approximately 2900 adc channels. The tail of the distribution extends to about 16 000 adc channels, resulting in a peak-tail ratio of $r_{\mathrm{pt}} = 16000/2900 = 5.5$.

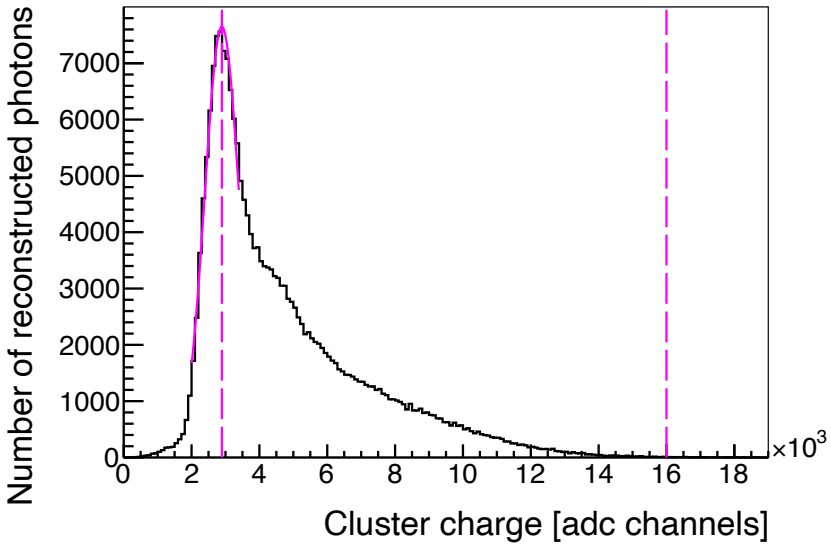

Figure 5.11: A Gaussian function is fit to the main peak of the measured cluster charge distribution. The resulting mean value of the fit is at 2900 adc channels, which is highlighted by the first dashed pink line. The second line marks the end of the distribution at about 16 000 adc channels. In addition, a second peak appears at about 4500 adc channels, which blurs with the tail of the main peak. These measurements are performed with the 1520 µm FR4 converter layers with 35 µm copper strips, whereby $\Delta U_{\mathrm{x}} = 0\,\mathrm{V}$ and $\Delta U_{\mathrm{y}} = 600\,\mathrm{V}$ are applied. $\Delta U_{\mathrm{GEM}} = 280\,\mathrm{V}$ is set.

The number of detected electrons per charge-cluster are estimated from this measured cluster charge distribution. According to [Gnanvo et al., 2012], the charge of 1 adc channel of the APV25 corresponds to roughly 232 electrons. Considering the dominant peak at 2900 adc channels, the most probable number of electrons in the charge-cluster N_{cc} is

$$N_{\mathrm{cc}} = 2900\,\text{adc channels} \cdot 232\,\text{electrons adc channel}^{-1} = 672\,800\,\text{electrons} \tag{5.2}$$

Taking the simulated effective gas gain for a triple-GEM detector from equation 3.2 and accounting for the influence of pressure[6], the effective gas gain for this particular detector configuration is $g_{\mathrm{eff,corr}} = 2858$. Thus, the number of electrons before the amplification process in the electron-cluster N_{ec} is estimated as

$$N_{\mathrm{ec}} = \frac{672\,800\,\text{electrons}}{2858} = 235\,\text{electrons} \tag{5.3}$$

This calculation shows that a primary electron mainly forms an electron-cluster through gas ionization, in which approximately 235 electrons are contained. The mean energy for an

[5] If the created electron enters the gas, it typically causes secondary ionization. A certain number of electrons is produced, which are summarized into an electron-cluster. If this cluster is detected after the amplification process, it is defined as charge-cluster.

[6] This correlation is discussed in chapter 6 and the full calculation is given in Appendix C.

electron-ion pair creation is 26.5 eV in an Ar:CO_2 93:7 vol. % gas mixture[7]. If the photon loses all of its energy in the ionization process in gas, the creation of 59 500 eV/26.5 eV = 2245 electrons is expected, which is the maximum number of electrons an electron-cluster can contain. The most probable number of 235 electrons per electron-cluster, forming the peak in the distribution, is about 10 times smaller. These values are compared within this chapter. These electrons are then amplified and detected in the charge-cluster. It should be noted that in particular the simulated amplification has a certain error and is therefore only a rough estimation. But it is an important parameter for verifying the simulation and is therefore used in this chapter. The origin of the peaks in figure 5.11 is examined in chapter 8.

5.5.3 GEM Detector Working Point

The measurements are carried out with a GEM voltage of ΔU_{GEM} = 280 V. This voltage is justified here, as the decisive parameters that are influenced by the GEM voltage have now been introduced. The previous section demonstrates that the reconstructed charge-clusters exhibit a certain extension and charge. In particular, the measured charge is influenced by the GEM voltage. If the voltage ΔU_{GEM} is too high, the amplification is strong enough that the APV25 begins to saturate (see chapter 4.2).
In order to parameterize this quantity, the strip of a charge-cluster that detects the highest charge is determined. This resulting highest strip charge per cluster is shown in figure 5.12. At ΔU_{GEM} = 290 V, the majority of the strips of the APV25 are saturated. The fraction of saturated strips is shown for the different GEM voltages in figure 5.13 (right axis). The trigger rate (left axis) is shown in the same figure. It is the number of measured and processed trigger signals and with at least one reconstructed charge-cluster per second. In this work, it is an important measure for characterizing the performance of the converter layers.

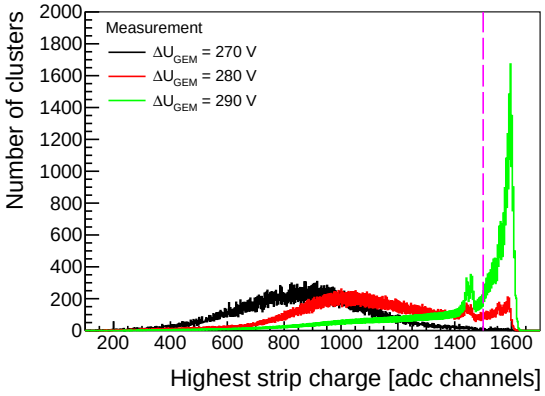

Figure 5.12: The highest strip charge per cluster shifts to higher values for increasing ΔU_{GEM}. The pink line at 1500 adc channels marks the threshold at which the APV25 channel reaches complete saturation. Some begin to saturate earlier, resulting in a slight peak before the pink line. For ΔU_{GEM} = 290 V, the majority of the clusters have at least one saturated strip. Therefore, the detector is operated at lower GEM voltages.

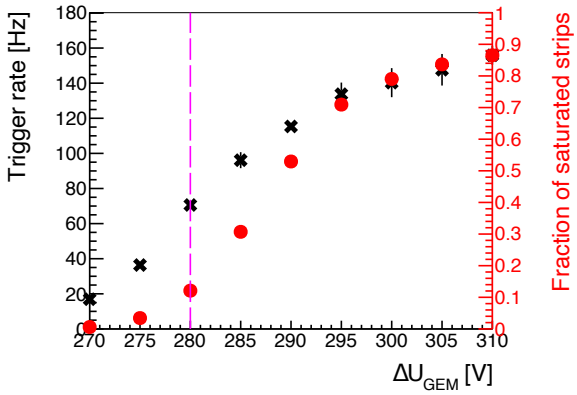

Figure 5.13: The trigger rate is shown in black as a function of ΔU_{GEM}. For higher ΔU_{GEM} it increases due to stronger gas amplification, resulting in more clusters falling below the threshold value and being detected. As a result, the detected cluster charge increases and thus also the ratio of saturated strips, which is shown in red. For an optimized detector performance, the number of saturated strips has to be low (here below 10 %) while maintaining a sufficient trigger rate. This is achieved by ΔU_{GEM} = 280 V (pink line).

[7] The mean energy for an electron-ion pair creation in Ar is 26 eV and in CO_2 33 eV [Leo, 1995], resulting in $0.93 \cdot 26\,\mathrm{eV} + 0.07 \cdot 33\,\mathrm{eV} = 26.5\,\mathrm{eV}$ for the used gas mixture.

With the proper GEM voltages of the setup, it has to be ensured that this GEM voltage is high enough to measure electron-clusters with a low charge. Since the cluster charge (see figure 5.11) for $\Delta U_{\mathrm{GEM}} = 280\,\mathrm{V}$ shows a smooth curve without abrupt cuts especially for low values, the applied voltage is sufficient to detect all clusters. In addition, the APV25 operates at $\Delta U_{\mathrm{GEM}} = 280\,\mathrm{V}$ in their dynamic range outside the saturated range and a reasonable trigger rate is achieved. Therefore, the measurements are performed with $\Delta U_{\mathrm{GEM}} = 280\,\mathrm{V}$. Furthermore, a low noise level is obtained by the appropriate threshold value setting of the discriminator (see chapter 4.2), which is not described in more detail here.
In general, the voltages need to be adjusted for different setups or particle sources. Since the different parameters influence each other, they have to be optimized in order to achieve an ideal detector performance.

5.5.4 Voltage Influence on the Converter Layer Performance

Up to now, all measurements with the converter layers have been performed with a fixed voltage configuration of $\Delta U_{\mathrm{x}} = 0\,\mathrm{V}$ and $\Delta U_{\mathrm{y}} = 600\,\mathrm{V}$. The influence of these voltages, which have been introduced in figure 5.4, on the measured parameters is analyzed here. As motivated in chapter 5.2, a voltage configuration has to be determined that maximizes the number of electron-clusters that are guided towards the triple-GEM.
The influence on the cluster charge for a fixed ΔU_{x} and variable ΔU_{y} is shown in figure 5.14 and on the number of strips per charge-cluster in figure 5.15. In both cases, an increase of 10–15 % is observed from $\Delta U_{\mathrm{y}} = 0\,\mathrm{V}$ to $\Delta U_{\mathrm{y}} = 600\,\mathrm{V}$. Thus, the number of electrons per cluster, which is guided downwards and is detected, increases. This indicates a higher guiding efficiency for the electrons within one electron-cluster. In addition, the total number of detected charge clusters increases with a higher ΔU_{y}. As the distributions are normalized to the same measurement time, more photons are detected in the same time interval.

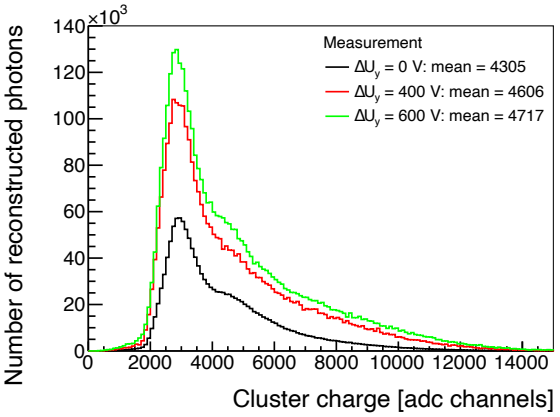

Figure 5.14: Measured cluster charge normalized to the measurement time: With increasing ΔU_{y}, the distribution shape of the deposited charge in the detector remains unchanged and the number of reconstructed photons increases. But with higher ΔU_{y} the mean cluster charge increases by 10 %.

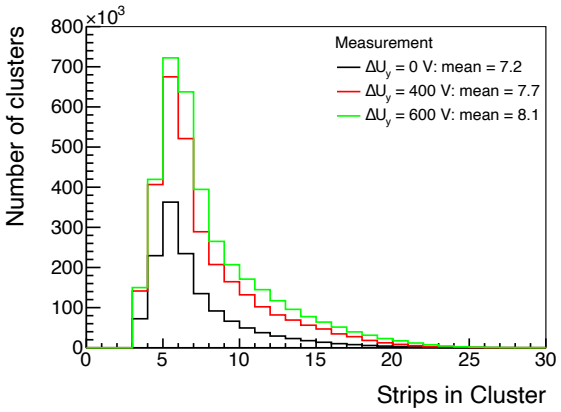

Figure 5.15: Measured number of strips per cluster normalized to the measurement time: The number of reconstructed photons with a higher ΔU_{y} increases. In addition, the mean number of strips per reconstructed charge-cluster size is slightly increasing by 15 %.

The trigger rate is shown as a function of ΔU_{y} in figure 5.16. As expected, the trigger rate increases with higher ΔU_{y} as more electron-clusters are guided downwards due to a stronger electric field. The saturation of the trigger rate starts at around $\Delta U_{\mathrm{y}} = 600\,\mathrm{V}$. Thus, it is a good working point for the converter layers, because the guiding efficiency reaches its maxi-

mum there. This ΔU_y voltage scan characterizes the converter layers regarding their guiding and conversion efficiency and is therefore used in chapter 8 as a comparison parameter to determine the performance of the various layers.

Figure 5.17 shows the influence of ΔU_x on the trigger rate, where ΔU_y = 600 V is kept constant. For this measurement, the voltage at the lower left copper strip is fixed by ΔU_{drift} while the voltage at the lower right strip is changed by ΔU_x (see figure 5.4). The maximum trigger rate is reached at ΔU_x = 0 V and decreases asymmetrically for larger or smaller ΔU_x values. Using simulation, the equipotential distribution and the electron drift are visualized at the end of chapter 5.7.3, explaining the asymmetric behavior. To maximize the guiding efficiency for the perpendicular arranged converter layers, ΔU_x = 0 V and ΔU_y = 600 V form the best voltage combination.

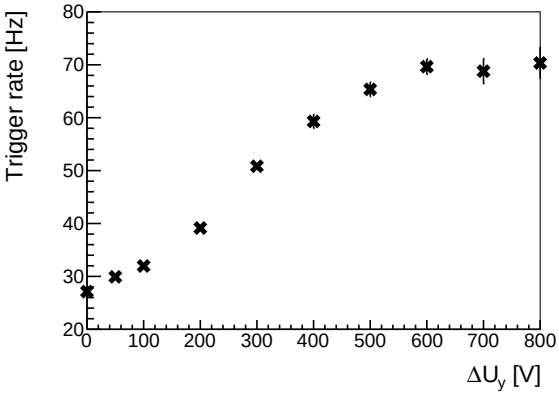

Figure 5.16: As ΔU_y increases, the trigger rate becomes higher and begins to saturate at ΔU_y = 600 V at around 70 Hz, which is a good voltage operating point for the layers. ΔU_x = 0 V remains constant in this measurement.

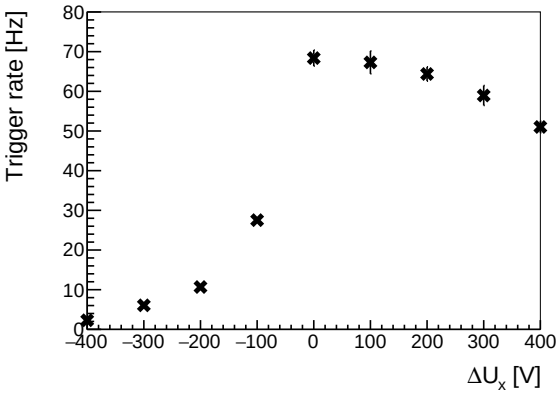

Figure 5.17: The ΔU_x voltage is varied while ΔU_y = 600 V is kept constant. Due to the resulting electric field the maximum trigger rate is achieved for ΔU_x = 0 V and drops asymmetrically by changing the voltage difference.

5.6 Simulation Principle

In order to understand the underlying physical processes of the measurements and layer performance, several linked simulations are performed. In this section, the simulation principle with the various simulation programs is introduced, including the presentation of some simulation results. Afterwards, a direct comparison between simulation and measurement is discussed in chapter 5.7. The same simulation flow is applied in the other chapters in this thesis.

5.6.1 Geant4: Photon-Detector Interaction

The software framework Geant4 (see chapter 4.1.1) is used to simulate the photon interaction in the detector. All crucial components with the correct dimensions and material composition are included in the design of the detector geometry to simulate the real detector setup as accurately as possible. The resulting simulation setup is shown in figure 5.18.
In Geant4, the aluminum detector housing is simulated, which contains the gas volume. This gas volume has a height of 50 mm and a square base area of 161 mm × 161 mm. It is centered around the origin of the coordinate system, whereby the volume ranges from $y = -25$ mm to y = 25 mm. Three GEM foils are placed in this gas volume. Each of them is approximated by a 50 µm thick Kapton foil with 5 µm copper on both sides. The gas volume contains a

further gas volume, which is referred to as the active gas volume. The active gas volume has the same base area as the GEM foils and is slightly higher than the converter layers. It contains 5 converter layers (see figure 5.18). These converter layers are made of 1520 µm FR4 as insulating material[8] and 35 µm thick copper strips on both sides (see chapter 5.3.1). Although the simulated interaction processes occur in the entire structure, only the electrons that reach the active gas region are processed further. Due to these dimensions of the active gas volume, only the electrons that are in principle detectable are considered. Both gas volumes consist of an Ar:CO_2 93:7 vol. % gas mixture as utilized in the measurement.

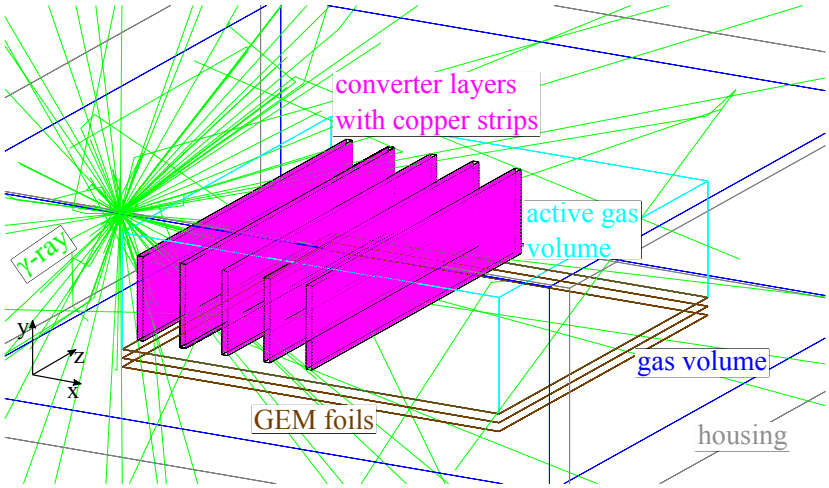

Figure 5.18: The crucial components of the detector are implemented for the Geant4 simulation setup. The detector as used in Geant4 consists of an aluminum housing filled with gas. Inside the gas volume are three GEM foils, while the converter layers are located in a separate active gas volume. They consist of the insulating material and 25 copper strips on each side. The γ-source emits 59.5 keV photons isotropically, as indicated by the green lines. Only electrons reaching the active gas volume are considered.

The setup is irradiated with a point source that emits 59.5 keV photons isotropically in 4π and is positioned centered to the layers at $y = -6.9$ mm (see figure 5.19). All Geant4 simulations are performed with 10×10^6 initial photons, where about 1.5×10^6 photons enter the active gas volume. These photons have the possibility to interact with the converter layers or the gas. The software considers all physical interaction possibilities of the photons with the materials based on the packages presented in chapter 4.1.1, including the interaction processes from chapter 2.2.
When an electron is produced in an interaction process, Geant4 tracks the particle. Secondary ionization processes are included, but as soon as an electron reaches the active gas volume, the tracking is stopped and further interactions are neglected. Instead, all information such as position, momentum and energy of the electron is saved and further processed in Garfield++[9]. The resulting position of the electrons when they enter the active gas volume is shown in figure 5.19. Many electrons are located close to the converter layers, indicating that they have been created there and have subsequently emerged from the material. The high amount of electrons at the edge of the active gas volume originate mainly from interactions outside the active volume, where the electrons afterwards enter the active gas volume. The expected decrease in the number of electrons with increasing x-value, which is explained in chapter 5.5.1, is also observable here.

[8] The exact composition of the FR4 material for the simulations carried out in this chapter can be found in Appendix D.
[9] As recommended in [Pfeiffer et al., 2019], the gas ionization is therefore not simulated in Geant4 but in Garfield++, as this program describes the process more accurately.

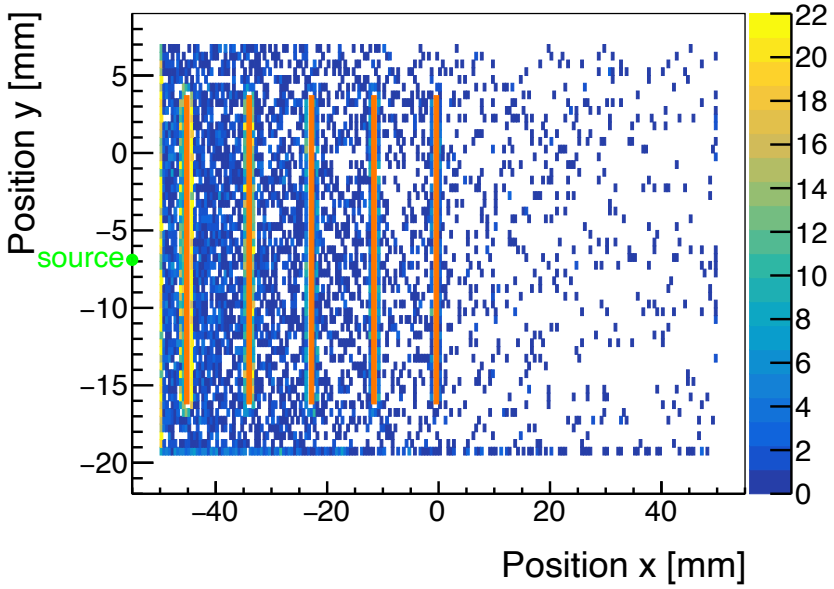

Figure 5.19: As soon as an electron reaches the active gas volume in Geant4, its position is extracted and further interactions for this electron is neglected. The extracted x- and y-positions are shown here, with the orange boxes illustrating the position of the converter layers. If the electron is created outside the active gas volume and enters it afterwards, its position is directly taken leading to a high number of electrons at the edge of this volume. Additionally, many electrons are located close to the converter layers. The number of electrons between the layers decreases as the x-position increases. The green point indicates the y-position of the γ-source.

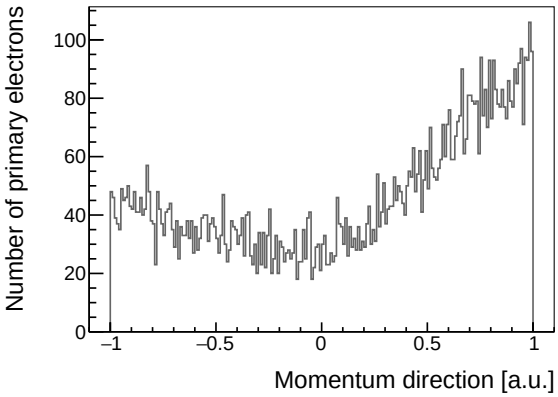

Figure 5.20: The electrons have a momentum direction: If only the x-component and thus the x-axis are considered, then +1 corresponds to a photo-electron emission in the pure forward direction along this axis, while −1 indicates complete backscattering. For a high proportion of electrons, the forward emission dominates.

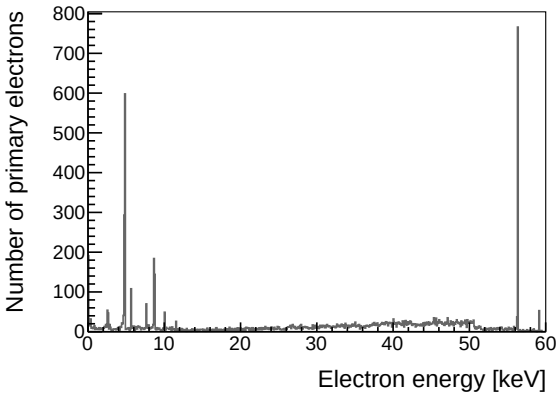

Figure 5.21: Simulated electron energy when the electrons enter the active gas volume. The Compton edge forms at around 50 keV. At certain energies peaks are created, which arise from the photoelectric effect. In particular, the dominant peak at about 4.8 keV is further discussed in the course of this chapter.

In addition, each electron has a momentum direction. The x-momentum direction is shown in figure 5.20. Since the photoelectric effect dominates at this photon energy in copper (see figure 2.1), the photoelectrons are mainly emitted at an angle of $45°^{+80°}_{-35°}$ with respect to the initial photon direction (see figure 2.2). For these electrons a peak between 0 and 1 is expected in figure 5.20 as well as some electrons being emitted in backward direction. However, the simulated distribution differs, with a dominant emission in the forward direction (+1). As anticipated, some electrons are emitted in the backward direction. But complete

backscattering also occurs (−1), which is contrary to expectation. This difference may arise because in figure 5.20 the momentum of the photoelectrons is displayed after entering the gas and not directly after the photon interaction, so some photoelectrons can have changed their direction, e.g. due to collisions. In addition, some electrons are created by Compton scattering in the gas (see Table 2.1), which overlays with the expected momentum direction from the photoelectrons.
The corresponding energy distribution of the electrons can be seen in figure 5.21. Discrete energy peaks form under a small continuous background. The origin of the different peaks is analyzed in more detail in chapter 8.5.1.

5.6.2 ANSYS: Electric Field Configuration

As described in chapter 5.2, an electric field is necessary to guide the electrons to the amplification and readout area. Therefore, a voltage difference is applied between the strips, as introduced in figure 5.4. For the simulation, the corresponding electric field is provided by ANSYS (see chapter 4.1.2). The relevant detector parts are designed in ANSYS using the sizes and material properties of the real components. This includes the converter layers with the individual copper strips. However, the housing is simulated with its entire height (larger than in Geant4). It is grounded (edges are set to 0 V). It should be noted here that the embedding of the housing, including grounding and the usage of the voltages applied in reality, has a strong influence on the resulting electric field and thus the electron movement, which cannot be neglected. The resulting complete distribution of the equipotential lines is shown in figure 5.22.

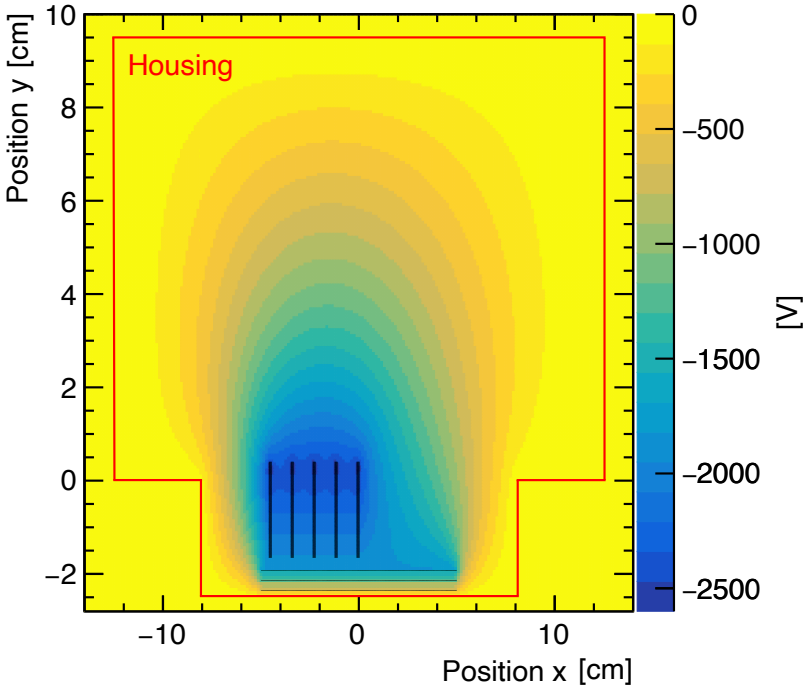

Figure 5.22: In ANSYS the distribution of the equipotential lines within the housing is simulated. It is created by the voltages applied to the converter layers ($x \in [-5, 0]$cm) and GEM foils ($y \approx -2$ cm). The housing, visualized here by the red lines, is grounded while the voltages from Table 5.1 are applied to the other components. The position of the GEM foils and converter layers is indicated by the black lines parallel and perpendicular to x, respectively.

The GEM foils are approximated as simple layers without a hole structure. On the one hand,

the hole structure has no influence on the performance of the converter layers (see [Penski, 2020]) and on the other hand, the simulation of the entire amplification process it too time consuming. Consequently, the influences of the gas amplification in the GEM foils are included afterwards by applying previous simulation results from chapter 3.3.

While the setup is built up completely in the x- and y-dimensions, it is simplified in z-direction. Only a small z-extension is simulated in ANSYS, which is extended in Garfield++ using periodic boundary conditions. For a detailed visualization of the equipotential lines between the converter layers, this image segment is shown enlarged in figure 5.23. These equipotential lines are perpendicular to the converter layers for $\Delta U_\mathrm{x} = 0\,\mathrm{V}$. Since the electrons move perpendicular to the equipotential lines, the maximum number of electrons are guided downwards and detected for $\Delta U_\mathrm{x} = 0\,\mathrm{V}$. This has already been demonstrated in the measurement result presented in figure 5.17. The exact electron drift is discussed in more detail in figure 5.28.

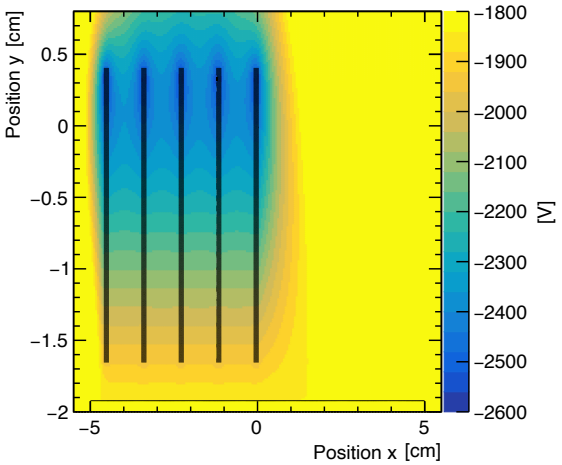

Figure 5.23: In ANSYS, the following voltages are applied to the copper strips of the perpendicularly arranged converter layers, which are shown in black here: $\Delta U_\mathrm{drift} = 100\,\mathrm{V}$ is applied between the top GEM foil, indicated by the horizontal black line, and the bottom of the layers. In addition, $\Delta U_\mathrm{y} = 600\,\mathrm{V}$ and $\Delta U_\mathrm{x} = 0\,\mathrm{V}$ is used. The electrons drift perpendicular to the resulting equipotential lines.

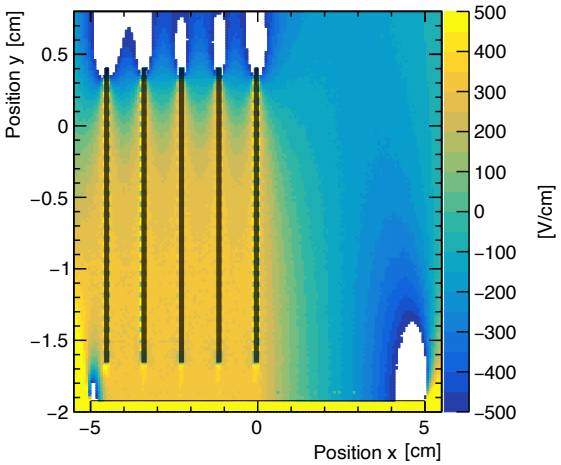

Figure 5.24: Electric field configuration for the equipotential distribution of figure figure 5.23. The y-component of the corresponding electric field is shown. By applying $\Delta U_\mathrm{y} = 600\,\mathrm{V}$ over the layer height of about 2 cm, an electric field of $300\,\mathrm{V\,cm^{-1}}$ between the layers is created. The values for the white areas are outside the range displayed here.

In figure 5.24 the corresponding electric field can be seen. Although the electric field between the layers is non-homogeneous, it has a field strength of around $300\,\mathrm{V\,cm^{-1}}$ when applying $\Delta U_\mathrm{y} = 600\,\mathrm{V}$. For 25 copper strips this leads to a voltage difference of

$$\Delta U_\mathrm{strip} = \frac{600\,\mathrm{V}}{24} = 25\,\mathrm{V} \tag{5.4}$$

between two neighboring strips and an electric near field of

$$E_\mathrm{strip\ (near)} = \frac{25\,\mathrm{V}}{400\,\mu\mathrm{m}} = 625\,\mathrm{V\,cm^{-1}} \tag{5.5}$$

for a strip distance of 400 µm (see figure 5.3). When considering the strip pitch of 800 µm, it results in a far electric field of

$$E_{\text{strip (far)}} = \frac{25\,\text{V}}{800\,\mu\text{m}} = 312.5\,\text{V}\,\text{cm}^{-1} \tag{5.6}$$

For the near and far electric field, the electric field strength is not in the range of the gas amplification and therefore only influences the electron drift.
The total electric field in y-direction is shown in figure 5.24. It includes the field between the layers and the drift region, with the respective heights $h_{\text{layer}} = 2\,\text{cm}$ and $h_{\text{drift}} = 0.27\,\text{cm}$. The field between the layers is about $300\,\text{V}\,\text{cm}^{-1}$, resulting in an electron drift velocity of about $v_{\text{layer}} = 3.5 \times 10^{-3}\,\text{cm}\,\text{ns}^{-1}$ according to figure 2.4. In combination with the drift field of approximately $|\vec{E}_{\text{drift}}| = 370\,\text{V}\,\text{cm}^{-1}$ (see Table 5.1) with a corresponding drift velocity of around $v_{\text{drift}} = 3.6 \times 10^{-3}\,\text{cm}\,\text{ns}^{-1}$, the total drift time for an electron that starts in the upper area of a converter layer is approximated by

$$\begin{aligned}
\Delta t_{\text{totaldrift}} &= \Delta t_{\text{y}} + \Delta t_{\text{drift}} \\
&= \frac{h_{\text{layer}}}{v_{\text{layer}}} + \frac{h_{\text{drift}}}{v_{\text{drift}}} \\
&= \frac{2\,\text{cm}}{3.5 \times 10^{-3}\,\text{cm}\,\text{ns}^{-1}} + \frac{0.27\,\text{cm}}{3.6 \times 10^{-3}\,\text{cm}\,\text{ns}^{-1}} \\
&= 571\,\text{ns} + 75\,\text{ns} = 646\,\text{ns}
\end{aligned} \tag{5.7}$$

The exact electron drift in this electric field is simulated in Garfield++. Therefore, all information about the electric field is exported from ANSYS to Garfield++.

5.6.3 Garfield++: Gas Ionization and Electron Drift

Gas ionization processes as well as the electron drift are simulated using Garfield++ (see chapter 4.1.4), including the Penning effect with $r_{\text{p}} = 0.42$ for the gas mixture of Ar:CO_2 93:7 vol. % (see [Şahin et al., 2014]). In the simulation the temperature is set to 293.5 K and the pressure to 750 Torr. 10 000 events are imported from Geant4. All results presented here are for a voltage combination of $\Delta U_{\text{y}} = 600\,\text{V}$ and $\Delta U_{\text{x}} = 0\,\text{V}$ and the corresponding electric field configuration is provided by ANSYS (see figure 5.23). The information about the position (see figure 5.19), momentum (see figure 5.20) and energy (see figure 5.21) of the electrons is imported from Geant4 into Garfield++. These primary electrons have just entered the active gas volume and possess sufficiently high energy for secondary ionization in the gas according to chapter 2.1, resulting in the creation of secondary electrons.
This process is simulated in Garfield++ and the resulting number of secondary electrons per primary electron is shown in figure 5.25. From the calculations in chapter 5.5.2, a maximum number of 2245 secondary electrons per electron-cluster and a dominant peak at 235 secondary electrons are expected. These values are consistent with the simulation result in figure 5.25, which shows a tail of up to approximately 2300 electrons and a peak at 190 electrons.

All secondary electrons originating from the same ionization process are combined into one electron-cluster. As expected from the measured charge-cluster extension in figure 5.10, the electron-cluster has a certain extension in all dimensions (see figure 5.26). About 75 % of the electron-clusters have an extension[10] of less than 5 mm. The converter layers have a distance

[10] The extension of the electron clusters corresponds to the maximum size of the cluster. Due to collisions with the gas atoms, the electron drift does not occur in a straight line, but in a zigzag motion. This can be seen, for example, in figure 3.4 for the drift of the initial electron to the GEM hole. Therefore, the distance the electron moves is usually greater than the given extension.

of 11 mm. As most electron clusters have a smaller extension, the gas ionization process is not interrupted by the subsequent converter layers. Only some ionization processes are influenced by the distance between the converter layers, limiting the cluster extension and producing a peak at about 11 mm in figure 5.26.

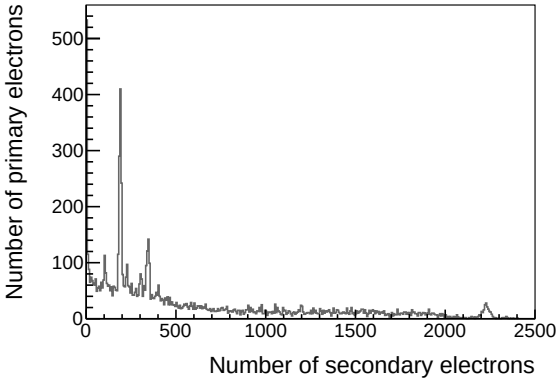

Figure 5.25: The ionization process of the primary electron in the gas is simulated in Garfield++. A primary electron produces the number of secondary electrons shown here. There is a dominant peak at 190 electrons, which corresponds to a primary electron energy of 4.8 keV (see figure 5.27). The tail of the distribution reaches up to 2300 electrons.

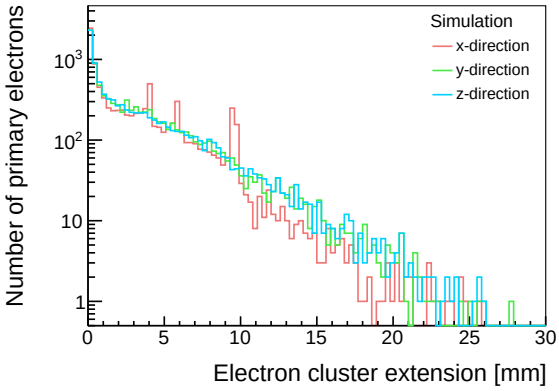

Figure 5.26: The extension of the electron-clusters in x-, y- and z-direction reach up to 25 mm. In x-direction there are different peaks due to geometric aspects, the most dominant one at about 11 mm, which corresponds to the converter layer distance.

Thus, a primary electron with a specific energy generates secondary electrons in the gas ionization process. The correlation between the energy of the primary electron and the number of secondary electrons can be seen in figure 5.27. The proportionality suggests that the peak in the energy distribution in figure 5.21 and the peak in the number of secondary electrons in figure 5.25 are correlated.

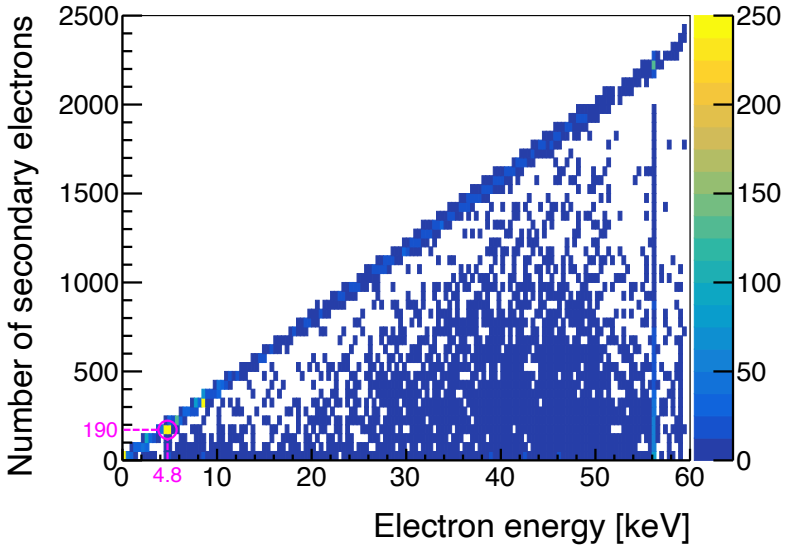

Figure 5.27: Correlation diagram between the primary electron energy and the number of secondary electrons: The peak in the energy spectrum at around 4.8 keV is responsible for the creation of 190 electrons, which is highlighted in pink here. Since the maximum number of electrons generated during ionization is limited by the energy of the primary electron, the diagonal line is created. Gas ionization is a statistical process, therefore fewer electrons are generated in some cases.

A 4.8 keV electron produces mainly 190 electrons. This reasonably corresponds to the average ionization energy in the gas mixture used, which is 4800 eV/26.5 eV ≈ 181 electrons. For all primary electron energies E_{primary}, the maximum number of secondary electrons per electron-cluster can be approximated by $E_{\text{primary}}[\text{eV}]/26.5\,\text{eV}$. This leads to a linear correlation between the primary electron energy and the maximum number of secondary electrons, resulting in a diagonal in figure 5.27. Since gas ionization is a statistical process, also less secondary electrons are produced, causing the entries below the diagonal. In addition, photopeaks are observed at specific energies.

After the ionization, the electron drift under the influence of the electric field from figure 5.24 is simulated in Garfield++. In a first study, the electron drift is investigated without the implementation of the Geant4 results. For this purpose, the electrons are uniformly distributed over the entire height between the converter layers and have an initial kinetic energy of 0.1 eV, excluding secondary ionization. The resulting electron drift is shown in figure 5.28. While most electrons drift downwards, some drift in the upward direction (positive y-direction) and are consequently not detectable. This effect is only described in the simulation if the grounded housing from figure 5.22 is taken into account. If the electron passes below the detection limit of $y = -1.9\,\text{cm}$, it is considered detected. Electron losses occur due to the configuration of the electric field. For example, electrons produced in the upper area of the converter layers are guided upwards. Other electrons are absorbed by the converter layers. In both cases, the electrons are not detectable.

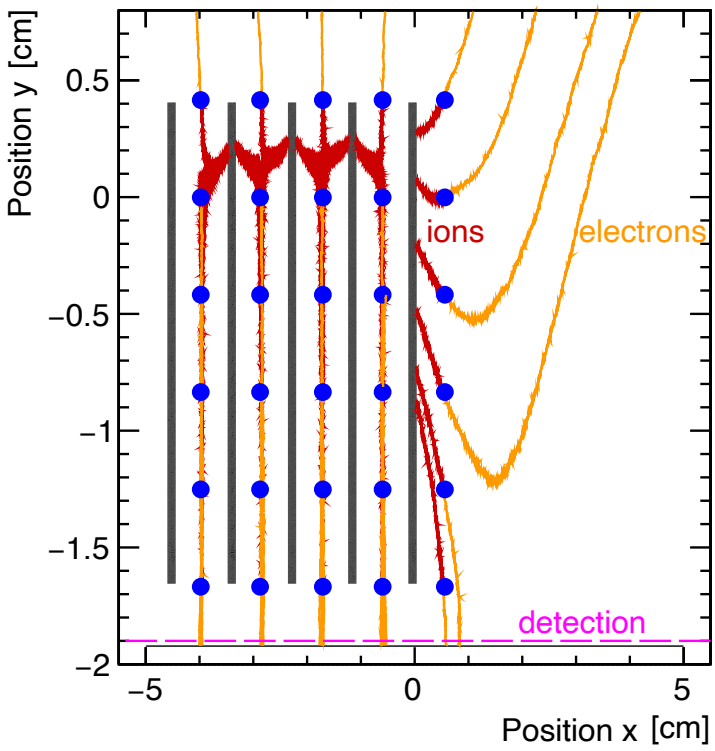

Figure 5.28: The electron drift is visualized for the electric field configuration from figure 5.24. Exemplary, 6 electrons are placed in the middle of two layers with varying y-position (indicated by the blue points). Since the electric field between the layers is parallel in x-direction, the majority of the electrons drift down on a straight line, while the ones placed at $y \approx 0.4\,\text{cm}$ drift upwards. The electrons placed at $x \approx 0.5\,\text{cm}$ show a wider drift-range in x-direction due to the electric field configuration. Electrons at $x \approx 0.5\,\text{cm}$ and $y > -0.8\,\text{cm}$ drift in upward direction. If the electron reaches $y < -1.9\,\text{cm}$ (marked in pink), the electron is counted as detected.

When including the Geant4 results in the Garfield++ simulation, electrons that originate from an electron-cluster and are detected are combined into a charge-cluster. A clustering algorithm has been developed for the charge-cluster characterization in order to simulate similar cuts as in the measurement (see chapter 4.3.3). Since neither the GEM amplification nor the readout strips are included in this simulation, their influence has to be taken into account subsequently. In the simulation, a charge-cluster has to contain at least 30 electrons to be counted. In addition, a time cut of 600 ns is performed after the detection of the first electron of an electron-cluster. Thus, only the electrons that are detected within this time interval are further processed. This corresponds to the APV25 readout time of 24 time bins, whereby one time bin corresponds to 25 ns (see chapter 4.2).
To approximate the readout structure, i.e. the copper strips on the readout anode, the x- and z-extension of the charge cluster is divided into strips with a size of 400 µm in the simulation, which corresponds to the strip pitch. A strip is included in the cluster if it is hit by at least 6 electrons. The amplification of an electron by a triple-GEM detector leads to an average extension of about 1.4 mm, as shown in figure 3.10, which corresponds to about 3 strips. For larger clusters, a gap of 1 strip is permitted, otherwise several clusters are formed. If there are several clusters, the cluster with the highest charge is chosen. The mean charge-cluster position is determined by the charge-weighted position and the resulting simulated hit distribution is shown in figure 5.29.

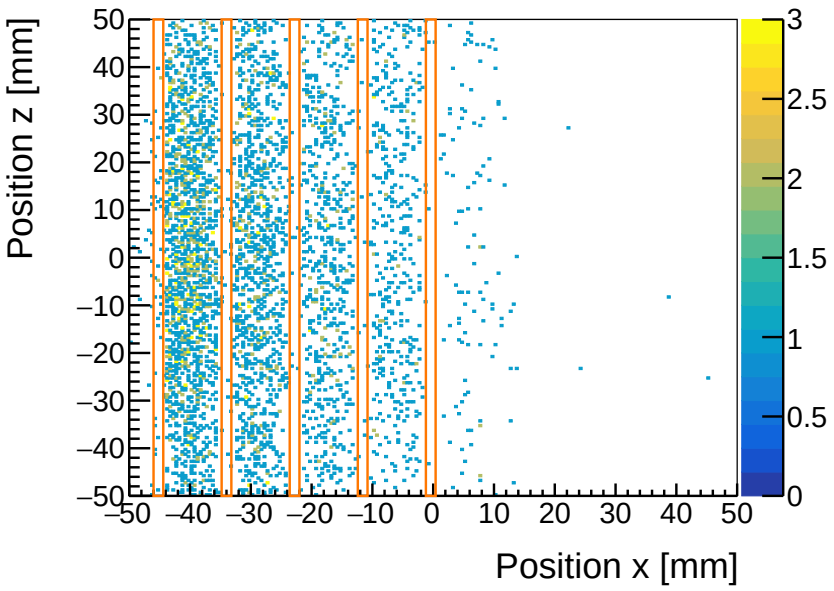

Figure 5.29: Simulated hit distribution: For each charge cluster, the x- and z-position is determined similarly to the measurement. The orange boxes indicate the layer position. As suggested by the measurement (see figure 5.7) and by the simulated electron drift (see figure 5.28), only events between the converter layers are detected. In addition, the number of hits decreases with increasing x-position and thus greater distance from the particle source by $1/r^2$.

From this simulation flow, which includes Geant4, ANSYS and Garfield++, and the post-processing of the resulting simulation data to account for the GEM gain, readout anode structure and clustering, several measurable quantities are extracted, which are compared directly with measurement results in chapter 5.7.

5.6.4 Limitations of Simulation

Each of the simulation packages has certain limitations. Although these will become apparent in the course of the thesis when analyzing the simulation results and comparing them with measurements, they are highlighted here to provide a better first understanding and assessment.
The detector setup is modeled in both Geant4 and ANSYS, with the focus on the crucial components. The converter layer mount, for example, is not included. These non-simulated components have no great influence on the results because they are located outside the active gas volume, but can lead to small discrepancies. In addition, all components are perfectly aligned in the simulations, whereas in the measurement setup deviations can occur, e.g. due to small bends of the converter layers or the positioning of components in the detector.
In Geant4 the photon interaction and electron extraction depends on the material composition and thickness, which are only known to a certain extent. This aspect is considered in more detail in chapter 8.2. In addition, the movement of electrons inside the various materials is simulated without the influence of an electric field, which leads to deviations.
The electric field simulated in ANSYS provides the correct fields for different voltages, as it accurately describes the electron drift when imported into Garfield++. However, as will be shown later (see figure 8.19), the fields do not change with variations in material or thickness. Furthermore, the z-dimension of the field is extended in Garfield++ by using periodic boundary conditions. As a result, the influence of the housing in the z-direction is not included. However, this approach is necessary as otherwise the number of mesh-nodes imported into Garfield++ exceeds its limits.
In Garfield++, various effects are not taken into account in some processes, although these do occur in reality. Firstly, the electron drift is carried out for each electron individually and not for the entire electron-cluster at the same time. As a result, the influence of the electrons on each other is neglected. Secondly, although the ion movement can be simulated, the recombination of the ions with the electrons cannot. Thus, in the simulation, the electrons have optimal drift conditions and can reach the detection region after a certain time, as long as the electric field permits. In addition, if the ions accumulate on the copper strips, they can weaken the effective electric field, which is not described in the simulation. Finally, the number of electrons generated is influenced by the penning effect, which is partially included in the parameter r_{p}. Especially for the simulation of gas amplification in the GEM foils, it is reported that the Penning effect in Garfield++ does not perfectly describe the experimental data [Azevedo et al., 2016]. This phenomenon can lead to deviations in the ionization and amplification as well.
All of these effects result in discrepancies between simulation and measurement results. Nevertheless, simulations are able to provide a better understanding of the occurring physical processes. For this purpose, it is first examined whether simulation and measurement provide similar results within the limits described here.

5.7 Comparison: Simulation and Measurement Results

In this section, the measurement and simulation results are compared. If not stated otherwise, the voltage configuration of ΔU_y = 600 V and ΔU_x = 0 V is used in this section. For all measurements, the converter layers consisting of 1520 µm FR4 with 35 µm copper strips (label: 1520 + 35) are installed in the triple-GEM detector.

5.7.1 2D Position Reconstruction

Comparing the measured and simulated reconstructed cluster position in x- and z-direction of figure 5.7 and figure 5.29, respectively, reveals a similar behavior. In figure 5.30 the x-profile of both distributions is superimposed.
Simulation and measurement show the same result in terms of the reconstructed photon position and absorption behavior. As discussed in chapter 5.5.1, the peaks decrease with increasing distance from the source. The measured decrease is stronger, indicating higher absorption. Different material compositions can cause this behavior, for example in the FR4 insulating layer, which has a more sophisticated structure (see chapter 8.2.4). Nevertheless, a reasonable agreement between measurement and simulation is achieved.

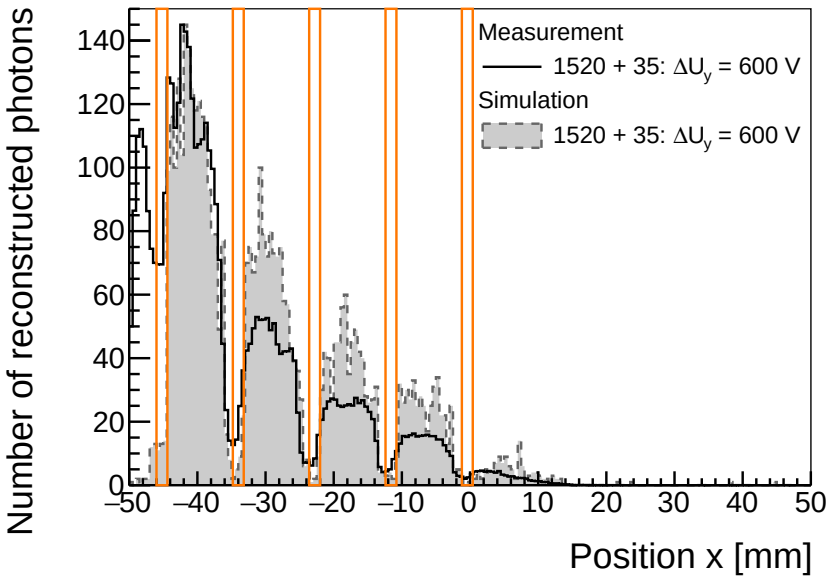

Figure 5.30: The profile of the reconstructed cluster position in the x-direction for the simulation and the measurement are superimposed with respect to the highest value. The orange boxes indicate the layer position. For both, the height of the peaks between the layers decreases with increasing x-value, whereby the measured height decrease is about a factor of 1.6 larger. Both distributions end at about x = 14 mm, indicating that the electron drift in this region is accurately described by the simulation. In the measurement, there is an additional peak in front of the first layer that is not simulated. This effect can be caused by differences between simulation and measurement with regard to the grounded housing or other grounded objects.

5.7.2 Cluster Information

The detected electrons form at least one charge-cluster per reconstructed photon[11]. For comparison, the clustering method from chapter 4.3 is applied for the measurement and from

[11] For a better comparison only the non-zero clusters are considered.

chapter 5.6.3 for the simulation.
The number of reconstructed clusters per trigger (in the measurement) or detected photons (in the simulation) is shown in figure 5.31. The simulation and measurement results look similar: In more than 90 % a single cluster is created and rarely up to four clusters are formed. Consequently, the interaction of a photon with subsequent detection mainly results in the creation of a single charge-cluster. If several clusters are detected per event, the charge-cluster with the highest charge is processed further in simulation and measurement.

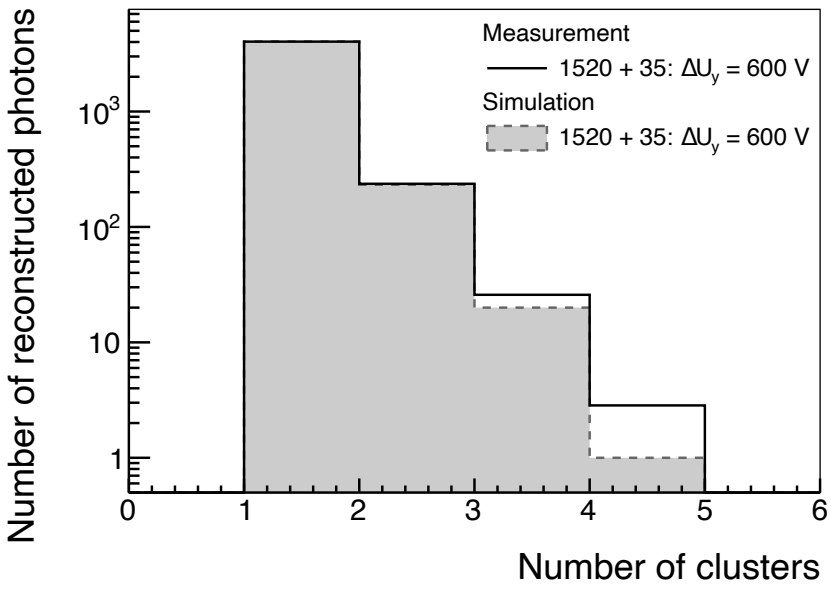

Figure 5.31: For comparing the simulated and measured number of charge-clusters, both are scaled to the same integral and only the non-zero clusters are presented. For reconstructed photons with ≥ 2 clusters, there is a total difference of about 30 clusters between simulation and measurement. Due to the logarithmic y-axis and almost 4000 entries for 1 reconstructed cluster, the difference of 30 clusters resulting from normalization is not visible there. Both show an excellent agreement, whereby one cluster per interaction is mostly produced.

While in the measurement the deposited charge is measured in units of adc channels from the APV25 chip, in the simulation the charge is indicated by the number of detected secondary electrons of an electron-cluster. The former is shown in figure 5.11 and the latter in figure 5.32. As described in chapter 5.5.2, both quantities are convertible into each other. According to equation 5.3, the dominant measured peak at about 2900 adc channels corresponds to about 235 electrons. The simulated main peak at 190 electrons in figure 5.32 is close to this value, taking into account the uncertainties in the simulation regarding the number of secondary electrons generated (see chapter 5.6.4) and the gas gain (see Appendix A), which have a strong influence on this prediction. Therefore, the simulated and measured peak values show good agreement.
The simulated main peak at 190 electrons is narrower than the measured one at 2900 adc channels. The reason for this difference is that the simulation result in figure 5.32 does not fully simulate the gas amplification in the triple- GEM detector. Since the gas amplification is a stochastic process, it leads to a broadening of the peak.
For the simulation, the peak-tail ratio is $r_{\mathrm{pt}} = 1850/190 = 9.7$. It is higher compared to the measured value 5.5. Since the highest peak has the same position in the simulation and in the measurement, this difference arises from the larger tail in the simulation. It indicates that more clusters with a higher charge are formed in the simulation than actually measured.

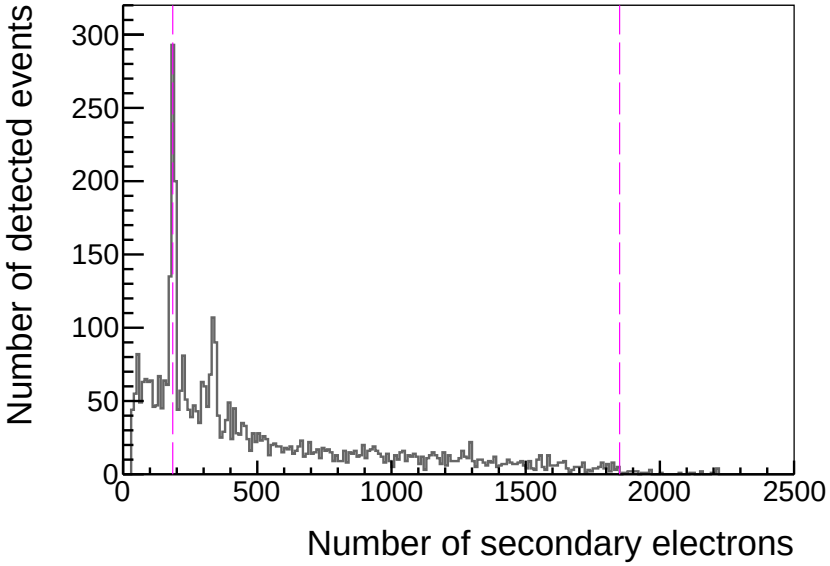

Figure 5.32: In the simulation, the deposited charge is displayed using the number of secondary electrons per detected electron-cluster. The highest peak is at about 190 electrons, with a tail ending at about 1850 electrons. Both values are marked by dashed pink lines. The simulated cluster charge can be determined by considering the corrected effective gas gain (see equation 3.2).

In addition, the extension of the simulated charge-cluster is determined, meaning the number of strips hit, as measured in figure 5.10. The simulations regarding the extension of the electron clusters after detection and the extension due to the amplification process are performed separately. This requires the combination of the electron-cluster extension (see figure 5.26) with the extension due to the gas amplification in the triple-GEM detector (see figure 3.10). Therefore, the number of strips hit is calculated from the distribution in figure 3.10, as described for the clustering algorithm in chapter 5.6.3. Figure 5.33 shows the resulting number of strips. For each electron-cluster the number of hit strips is calculated and corrected by the extension due to the amplification from figure 5.33, considering the proper ratios.

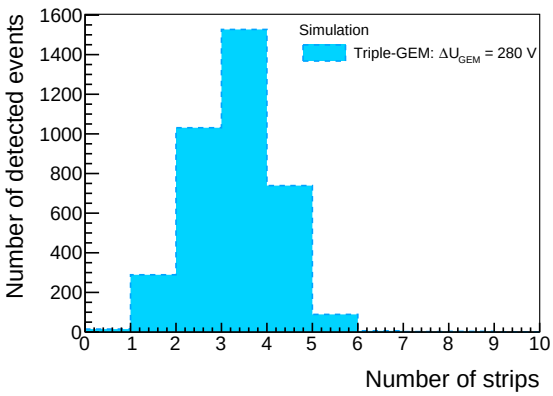

Figure 5.33: Due to the electron amplification in a triple-GEM detector, the resulting charge cluster has a certain extension, as introduced in figure 3.10. This extension is here converted to the number of strips hit. Mainly 2–4 strips are hit.

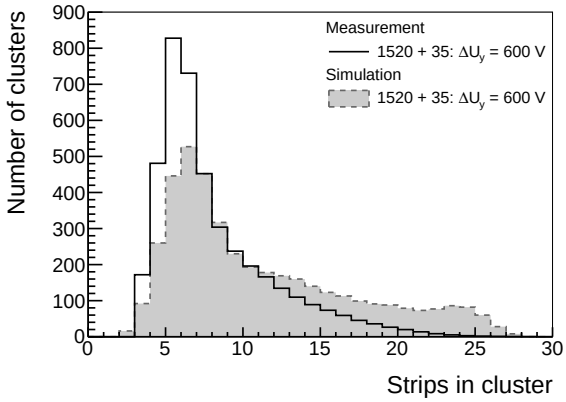

Figure 5.34: By combining the electron-cluster extension and the extension due to the gas amplification, the number of strips hit per charge-cluster is simulated. Compared to the measurement (normalized to the integral) there are more larger clusters, but for both the most probable value is 5–6 strips.

The final simulated charge-cluster extension is shown together with the measurement in figure 5.34. Both provide a similar distribution with a peak at about 5–6 strips for the measurement and 5–7 strips for the simulation. However, more larger clusters are simulated than measured.

For both, the cluster charge and its extension, simulation and measurement give a good agreement. But there are more larger clusters with a higher charge in the simulation than expected from the measurement, indicated by the more pronounced tails. One reason for these longer tails in the simulation could be the neglect of recombination as well as the optimal drift conditions for the electrons (see chapter 5.6.4). Especially during the amplification process in the GEM foil, many ions are produced that recombine with late-arriving electrons, preventing these electrons from being detected in the measurement. These losses are not considered in the simulation correctly and lead to more detected electrons. In addition, the effects of the detector and the readout electronics are not taken into account, including charge threshold effects in the readout electronics and the clustering algorithm (see chapter 4.3.3).

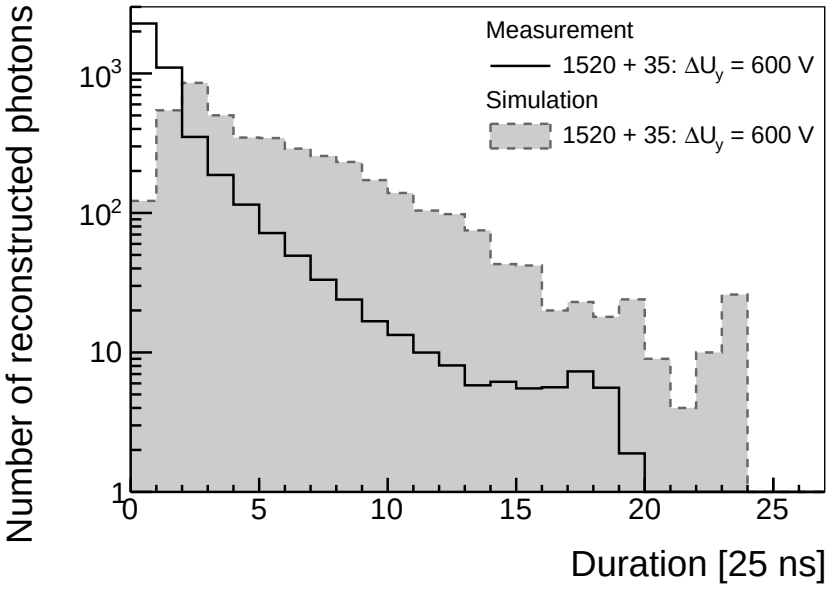

Figure 5.35: The duration, which is defined here as the time difference between the first and the last hit strip of a charge-cluster, tends to be smaller in the measurement than in the simulation. Here, 1 time bin corresponds to 25 ns. Differences can arise mainly due to the hardware electronic cuts, which are not fully included in the simulation, or differences in the data analysis between simulation and measurement, in particular the clustering. This may result in different start times and thus the observed offset of 2 time bins for the maximum values. The duration has been extracted from the measurement using the analysis from [Vogel, 2024].

In figure 5.35, the duration between the first and last strip hit per charge-cluster is compared. Since the generated electron-cluster has a certain height, meaning extension in the y-dimension, as shown in figure 5.26, the corresponding electrons arrive at different times when they are detected. While the distribution for the simulation is limited to 24 time bins corresponding to the hardware electronics cuts (see chapter 5.6.3), the distribution ends at 20 time bins[12] for the measurement. In addition, the distribution reaches its maximum at a duration in the range of 0–25 ns in the measurement, while it peaks in the range of 50–75 ns in the simulation. Thus, the measured duration is slightly shorter than the simulated duration. This behavior is caused either by differences in the y-extension during the creation processes

[12] For a successful signal fit of the inverse Fermi function (see figure 4.3), a time window is set. As a result, less than the 24 time bins are accounted for.

of the electron-cluster or, as described above, by losses that are not considered in the simulation. Since the latter point is consistent with the previous differences between simulation and measurement, it seems more likely.
To summarize, the simulated detected charge-clusters contain more electrons, are larger and have a longer duration than in the measurement. This is due to the ideal conditions and neglect of various real physical effects in the simulation. Considering these factors, simulation and measurement show a good agreement regarding the cluster properties.

5.7.3 Voltage Influence on Trigger Rate and Guiding Efficiency

The applied voltages and the resulting electric field configurations influence the trigger rate. To investigate this, different ΔU_y and ΔU_x voltages are simulated. Only the voltages applied to the converter layers are simulated, with the GEM detector voltages remaining constant.
The simulation exceeds its ability to accurately represent the processes occurring under the real measurement conditions. In the simulation, various effects are not taken into account (see chapter 5.6.4), leading to almost ideal drift conditions of the electron in the gas between the layers. Consequently, most of the electrons are guided downwards, also for large drift times. In the simulation, the electrons can reach drift times of more than 2000 ns, which is much higher than estimated in equation 5.7, where an electron needs a maximum of 646 ns to drift down from the highest point of the layer to the amplification region when applying ΔU_y = 600 V. For this reason, a time cut of 700 ns is introduced in the simulation. It is slightly higher than the maximum required drift time of the electron and thus counteracts the ideal drift conditions in the simulation.
In order to demonstrate the influence of this time cut, three different time cut values are presented for the ΔU_y-scan in figure 5.36. For each time cut value the corresponding data points are normalized to ΔU_y = 0 V.

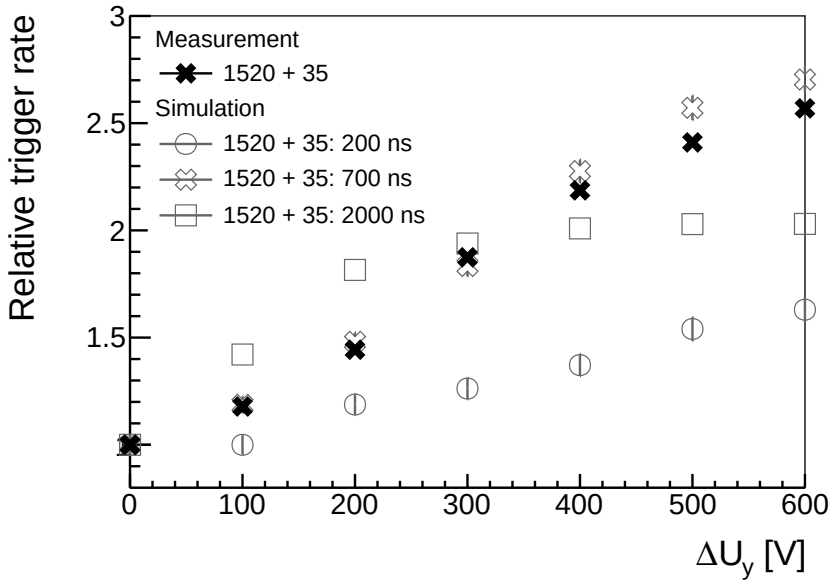

Figure 5.36: The simulated and measured trigger rate are each normalized to ΔU_y = 0 V. ΔU_x = 0 V remains constant. Various time cuts are shown for the simulation, which allow the electron a certain time to drift. For a simulated time cut of 700 ns, the simulated relative trigger rate shows good agreement with the measured values. For both, the trigger rate increases by a factor of 2.7. The normalization to ΔU_x = 0 V leads to a smaller increase for an allowed drift time of 2000 ns, since at ΔU_x = 0 V a large fraction of the electrons is already detected, leading to an early and low saturation.

Due to the long allowed drift time of 2000 ns, the majority of electrons are already detected at 0 V, which leads to a smaller increase at higher voltages and a saturation at around 300 V. For short allowed drift times of 200 ns, in particular the electron-clusters produced at large y-values, meaning the top of the converter layer furthest away from the amplification region, at are not detected. This prevents saturation of the trigger rate and only a maximum relative trigger rate of 1.6 at 600 V is achieved. With a permitted drift time cut of 700 ns, which is the most reasonable[13] as discussed above, simulation is in good agreement with the measurement. Both provide the same relative trigger rate for various ΔU_y, which reaches its maximum of 2.7 at $\Delta U_\mathrm{y} = 600\,\mathrm{V}$.
A higher voltage ΔU_y results in a stronger electrical fields between the converter layers, especially with regard to the y-component. For this reason, additional electron-clusters, which are created at larger y-positions, are detected at higher voltages. This results in an increase in the trigger rate.

From the simulation, the guiding efficiency is extracted, which is defined as follows

$$\varepsilon_\mathrm{guiding} = \frac{\text{number of detected electron-clusters}}{\text{number of created electron-clusters}} \tag{5.8}$$

and is shown in figure 5.37. According to the simulation, a maximum guiding efficiency of 67 % is reached. Thereby, only electrons between the converter layers are considered, meaning primary electrons that are created between $-42.5\,\mathrm{mm} < x < -0.4\,\mathrm{mm}$ (see figure 5.19) and thus experience the force of the electric field. Losses are caused by the time cut of 700 ns, electrons that drift upwards or being absorbed by the layer.

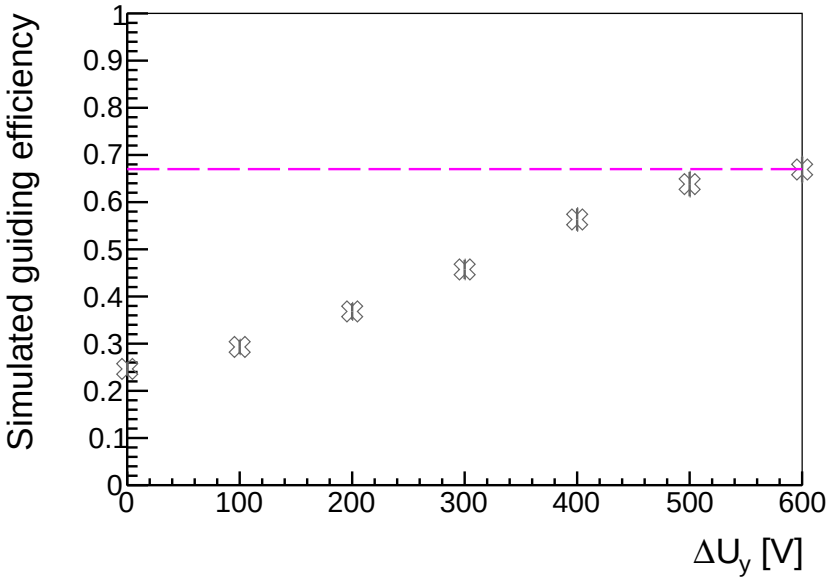

Figure 5.37: Simulated guiding efficiency for the 1520 + 35 converter layers: With higher ΔU_y the guiding efficiency increases, reaching its maximum of 67 % at $\Delta U_\mathrm{y} = 600\,\mathrm{V}$.

The ΔU_x voltage scan introduced in chapter 5.5.4 is simulated and compared with the corresponding measurement result in figure 5.38. The maximum trigger rate and thus the maximum guidance efficiency is achieved for $\Delta U_\mathrm{x} = 0\,\mathrm{V}$. For lower and higher ΔU_x values, the trigger rate decreases asymmetrically. Simulating the resulting equipotential distribution and the corresponding electron drift provides an explanation for the asymmetric behavior.

[13] This time cut is applied for all simulations in this thesis and has also been used for the previously presented simulation results in this chapter.

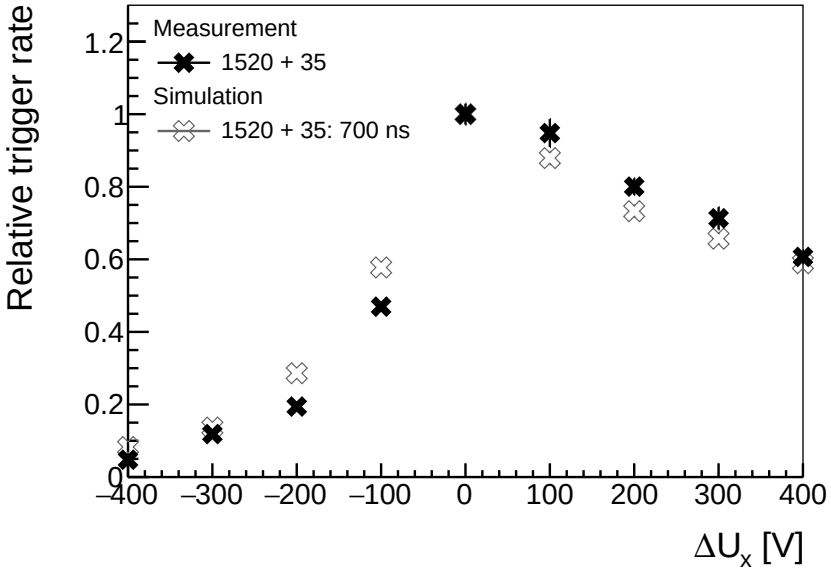

Figure 5.38: Variation in ΔU_x with constant $\Delta U_y = 600\,V$ using a time cut of 700 ns: The trigger rate is normalized to $\Delta U_x = 0\,V$. Simulation and measurement show a good agreement.

For simulation and measurement the voltage at the lower left copper strip is fixed by ΔU_{drift} while the voltage at the lower right strip is changed by ΔU_x, which is shown for $\Delta U_x = -400\,V$ (see figure 5.39) and $\Delta U_x = 400\,V$ (see figure 5.40).

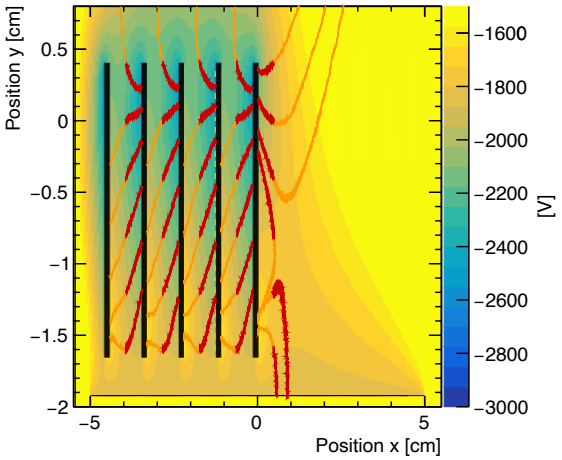

Figure 5.39: Equipotential distribution and electron drift for $\Delta U_x = -400\,V$: The voltage at the lower left copper strip is fixed by ΔU_{drift} and the voltage at the lower right strip is adapted. By using $\Delta U_x = -400\,V$, an absolute lower voltage is applied to the right strips compared to the left strips of a layer. As a result the electrons (orange) drift in negative x-direction towards the copper strips on the right side of the layer, where they are absorbed. None of the electrons created between the converter layers are guided towards the GEM foil for amplification, leading to a relative trigger rate close to 0 in figure 5.38. The ion movement is visualized in red. $\Delta U_y = 600\,V$ is set.

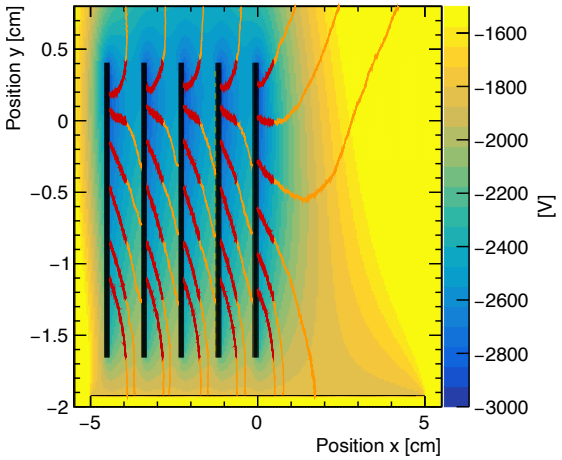

Figure 5.40: Equipotential distribution and electron drift for $\Delta U_x = 400\,V$: As described in figure 5.39, the voltage on the right copper strips of a layer is changed, here by $\Delta U_x = 400\,V$. This leads to absolute higher voltages on the right strips compared to the left strips and the electrons are drifting in positive x-direction. Electrons with an initial y-position $< -1.2\,cm$ are detected, while the others are absorbed by the converter layers. As a result, the number of detected electrons is smaller than for $\Delta U_x = 0\,V$ but higher than for $\Delta U_x = -400\,V$, where no electrons are detected, causing the asymmetric behavior in figure 5.38. $\Delta U_y = 600\,V$ is set.

With variations of ΔU_x, the equipotential lines are no longer parallel to the GEM foil, but are slightly tilted. As a result, the electrons are guided towards the layers and absorbed, reducing the relative trigger rate (see chapter 5.5.4). While for $\Delta U_x = -400\,\mathrm{V}$ all electrons created between the layers are absorbed, for $\Delta U_x = 400\,\mathrm{V}$ some are guided downwards and are detected, causing the asymmetric decrease in figure 5.38.

For both, the ΔU_y and the ΔU_x voltage scan, a good agreement between measurement and simulation is achieved after implementing a justified time cut. This provides a good description of the influence of the electric field on the electron drift. For this setup, a guiding efficiency of $\varepsilon_{\mathrm{guiding}} = 67\,\%$ is achieved.

5.8 Photon Detection Efficiency

For the following simulation, the absolute trigger rate is taken into account. Up to now only the relative trigger rate has been analyzed. From chapter 5.4.2 it is known that the ^{241}Am particle source emits $133 \times 10^3\ \frac{\mathrm{photons}}{\mathrm{s}}$ in 4π. In the simulation, 10×10^6 photons are emitted from the point source in 4π, this being 75 times the measured activity. The normalized values (to $\frac{\mathrm{photons}}{\mathrm{s}}$) are compared to the measured trigger rate in figure 5.41. Simulation and measurement show good agreement. A maximum trigger rate of 70–80 Hz at $\Delta U_y = 600\,\mathrm{V}$ (see figure 5.16) is achieved with these converter layers.

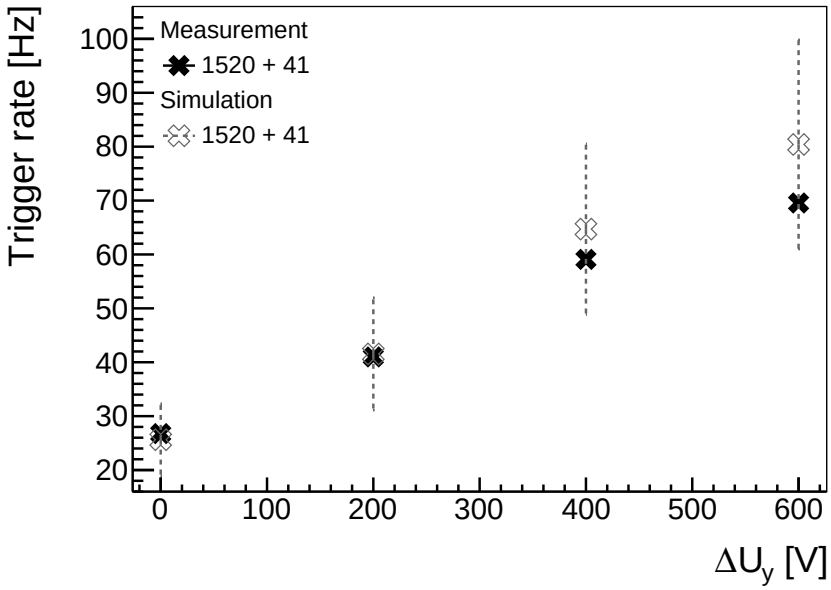

Figure 5.41: The trigger rates of simulation and measurement show good agreement. At $\Delta U_y = 600\,\mathrm{V}$, the simulated trigger rate of 80 Hz is slightly higher than the measured one (70 Hz), but they agree within the indicated error.

Due to the good agreement, it is justified to estimate the detection efficiency of the GEM detector for 59.5 keV photons with 1520 + 35 converter layers on the basis of the simulation results. The detection $\varepsilon_{\mathrm{detection}}$ efficiency is defined as

$$\varepsilon_{\mathrm{detection}} = \varepsilon_{\mathrm{conversion}} \cdot \varepsilon_{\mathrm{guiding}} \tag{5.9}$$

with the guiding efficiency[14] $\varepsilon_{\text{guiding}}$ from equation 5.8 and the conversion efficiency $\varepsilon_{\text{conversion}}$, which is defined as

$$\varepsilon_{\text{conversion}} = \frac{\text{number of created electron-cluster}}{\text{number of photons in active gas}} \tag{5.10}$$

and therefore includes the interaction and extraction probability. Only the photons that enter the active gas volume and are able to interact with the detector gas or converter layers are considered. Of the 10×10^6 simulated photons emitted by the source, 1.27×10^6 photons enter the active gas volume. For the detector with converter layers, this results in a conversion efficiency of $\varepsilon_{\text{conversion}} = 0.69\,\%$. In comparison, the conversion efficiency without converter layers is 0.58 %. The conversion probability for the GEM detector with $1520 + 35$ converter layers is therefore slightly higher, but similar. For the detection efficiency with converter layers, this results in

$$\begin{aligned} \varepsilon_{\text{detection}} &= \varepsilon_{\text{conversion}} \cdot \varepsilon_{\text{guiding}} \\ &= 0.0069 \cdot 0.67 \\ &= 0.0046 = 0.46\,\% \end{aligned} \tag{5.11}$$

The detection efficiency of $\varepsilon_{\text{detection}} = 0.46\,\%$ with the $1520 + 35$ converter layers is of the same order of magnitude as the conversion efficiency of the 59.5 keV photons in gas, whereby the guiding efficiency is not taken into account in the latter case.
The influence of the different materials on photon absorption is examined in more detail in chapter 8. For an initial assessment of the detection efficiency some of the results are used here. Considering 5 converter layers consisting of 1520 µm FR4 and 35 µm thick copper strips on both sides, about 56 % 59.5 keV photons are absorbed (see figure 8.13). This comprises about 22 % in copper (see figure 8.12) and the remaining 34 % in FR4. Since the conversion probability is 0.69 %, which also includes interactions directly in the gas, only about 1.2 % of all electrons produced in the converter layer can exit from FR4 and copper, or about 3 % if the detected electrons originate only from copper. A large fraction of produced electrons cannot leave the material and is not detected.The high absorption and low extraction of the $1520 + 35$ layers lead to a similar photon conversion efficiency compared to gas. Therefore, improvements in material and material thickness are essential to achieve an improved photon detection efficiency.

The aim is to gain a better understanding of the material influences and interaction processes as well as to further increase the detection efficiency by optimizing the material of the converter layers, which is investigated in chapter 8.

5.9 Summary of Converter Layers in GEM Detectors

The detection efficiency of photons via the photoelectric effect can be increased by a solid converter layer made of high-Z materials. In this approach, converter layers are introduced in a triple-GEM detector to increase the detection efficiency of photons. They replace the cathode and are arranged perpendicularly in the detector. The photoelectric effect dominates at the analyzed photon energy of 59.5 keV. By stacking several converter layers, which is possible due to the vertical arrangement, the interaction probability is increased by each additional

[14] Since the electric field is only present in the range $-42.5\,\text{mm} < x < -0.4\,\text{mm}$, which has been used to determine the guiding efficiency in figure 5.37, this position cut is applied for this calculation as well.

layer. The converter layers used here consist of an insulating carrier material with copper strips (PCB), more specifically a 1520 µm FR4 layer with 35 µm thick copper strips on both sides.
When the electron produced by the photoelectric effect leaves the copper, it enters the detector gas and produces secondary electrons through ionization. The electrons are guided through an optimized electric guiding field to the amplification and readout area of the GEM detector. This guiding field is realized by a certain voltage configuration of ΔU_{x} and ΔU_{y}, which are applied to the converter layers.
This new detection principle with converter layers works as intended regarding the electron drift by the electric guiding field and electron detection between the converter layers. Furthermore, a simulation procedure consisting of Geant4 (for the simulation of the photon-matter interaction), ANSYS (for the simulation of the electric field) and Garfield++ (for the simulation of gas ionization and electron drift) is introduced. The comparable parameters from measurements and simulation, considering the different limitations, show a good agreement. This includes the hit distribution, charge-cluster information (detected charge, extension and duration) as well as the ΔU_{x} and ΔU_{y} voltage scans.
This chapter provides the initial principles and understanding of the measurement results and simulation procedure. A detection efficiency of 0.46 % is determined. The aim is to further improve this detection efficiency by optimizing the converter layers to reduce the absorption of non-detectable photons.

Chapter 6

Impact of Environmental Conditions on the Performance of GEM Detectors

The reproducibility of the measurement results is of great importance to verify the measurement procedure and achieve reliable and comparable results. Following equation 2.20, the gas gain of the GEM detector is influenced by environmental parameters such as the temperature T and pressure p. These parameters therefore affect the operation of the detector [Thorpe and Vahsen, 2023].
In order to characterize the influence of the various converter layers on the detector performance and its photon detection efficiency, it is essential that the measurement is independent of these external factors. Therefore, in this section the environmental parameters are analyzed with regard to their influence on the trigger rate.

6.1 Gas Humidity

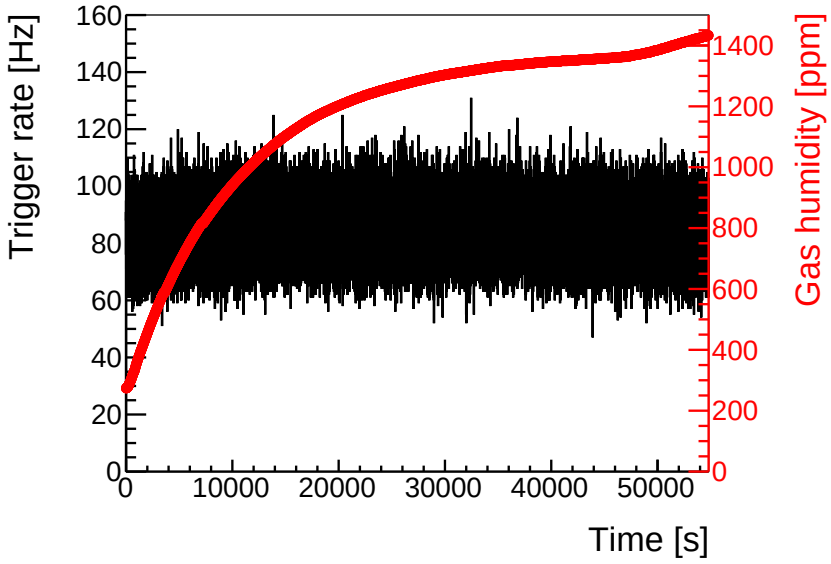

Figure 6.1: When the gas inlet pipe is placed directly in water, the gas humidity in the detector increases from about 250 ppm to 1400 ppm in the course of about 14 h. The plastic pipes allow for a small diffusion of water vapor. The trigger rate remains constant and is therefore independent of the gas humidity in this operation regime.

Moisture (water vapor) from ambient humidity enters the detector through small leaks in the detector housing. In addition, moisture gets into the detector through the gas line [Trost, 2020]. To prevent this contamination of the detector gas, short gas pipe paths are preferred. The moisture in the gas is monitored with a dew point transmitter [VAISALA, 2024]. The trigger rate measured over approximately 14 h is shown in figure 6.1 with respect to the gas humidity, which is increased artificially. In the range up to 1400 ppm, the H_2O content in the gas has no influence on the trigger rate. All measurements in this thesis are performed at about (400 ± 200)ppm.

6.2 Temperature and Relative Humidity

According to equation 2.20, the gas amplification depends on the temperature. This variable is not further investigated here, but to eliminate its influence on the measurement results, the detector is installed in a climate cabinet [Memmert, 2013]. The temperature remains constant at around (25 ± 1)°C and the relative humidity of the air at (25 ± 2)%. Consequently, the measurements are independent of these parameters.

6.3 Pressure

Similar to the temperature, the environmental pressure influences the gas amplification according to equation 2.20. In order to achieve the identical gas amplification for all measurements, the pressure has to be controlled and the measurement results have to be scaled accordingly. The trigger rate as a function of the pressure is shown in figure 6.2.

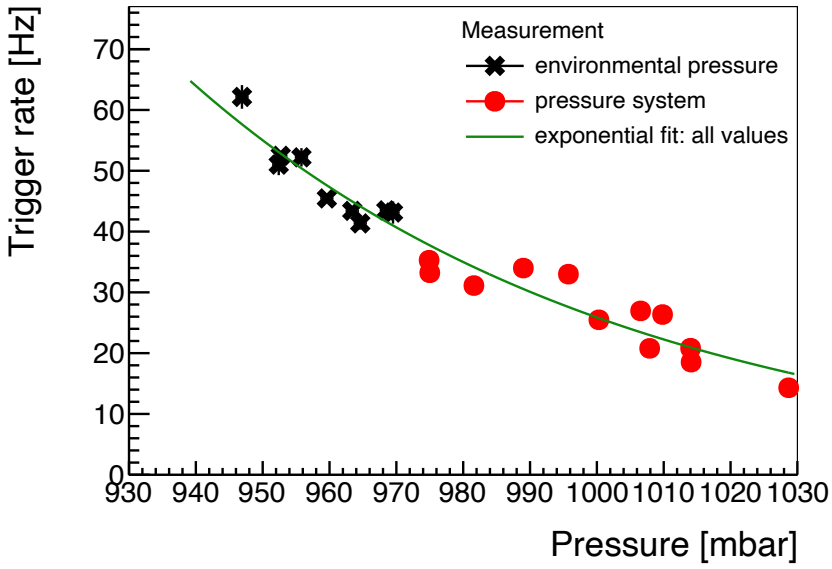

Figure 6.2: The trigger rate is measured for different pressures, whereby ΔU_y = 400 V, ΔU_x = 0 V and ΔU_{GEM} = 280 V are applied. A distinction is made between the environmental pressure and the pressure provided by a pressure system. The measurement points of the environmental pressures have been taken on different days over a period of 2 weeks. The fitted exponential function describes both the environmental pressure and the controlled pressure, proving that the system is providing the correct pressure. Furthermore, the development of a method to control the pressure fluctuations is necessary, as these have a major influence on the trigger rate. It varies by a factor of 4 over the entire pressure range and by a factor of 1.5 for environmental pressure.

A distinction is made between the environmental pressure and the pressure generated by an external pressure system[1]. The pressure system is set up as follows: A vacuum pressure transducer [MKS, 2024a] is installed at the end of the gas line, measuring the pressure in the system. This value is sent to the MKS Type 670 Signal Conditioner [MKS, 1998]. It is connected to the MKS Type 250 Pressure/Volume Flow Controller [MKS, 1997], to which the pressure value is passed on. The MKS Type 250 compares this current pressure value with the value set in the system. To adjust the gas pressure, the controller supplies a DC voltage of 0 V to 15 V to the valve [MKS, 2024b], which is installed in the gas line controlling the gas flow. If, for example, the pressure falls below the set value, the voltage is reduced and the valve closes gradually to reach the set point. This increases the pressure in the detector and the gas pressure in the detector is constant.
The pressure system is still slightly dependent on the environmental pressure and is not always able to reach the set point. But it can precisely determine the current pressure and keep it constant. Therefore, a calibration method has to be implemented additionally.
With higher pressure the measured trigger rate decreases exponentially, which is shown in figure 6.2. All measurements in this section are performed with the same converter layer setup installed in the GEM detector as introduced in chapter 5.4. By fitting an exponential function to the pressure dependent trigger rate curve in figure 6.2, the measured trigger rate f is described by

$$f = \exp((18.3 \pm 1.4) - (0.015 \pm 0.002)p) \tag{6.1}$$

where p is the pressure. To estimate the deviation between data points and fit, the Root Mean Square (RMS) is calculated as:

$$\begin{aligned} \Delta f_{\mathrm{RMS}} &= \sqrt{\frac{\sum_{i=1}^{N}(f_{\mathrm{data}} - f_{\mathrm{fit}})^2}{N}} \\ &= 2.9\,\mathrm{Hz} \end{aligned} \tag{6.2}$$

Depending on the absolute trigger rate, this leads to a deviation between 5–10 %. The trigger rate varies up to a factor of 4 if all applied pressures are considered in figure 6.2 and a factor of 1.5 if only natural environmental fluctuations are included. The reason for this behavior is the strong dependence of gas amplification on pressure, which is further investigated in the following.

As shown in figure 6.3, the cluster charge differs for two different pressures $p_1 = 946.9\,\mathrm{mbar}$ and $p_2 = 1014.0\,\mathrm{mbar}$. The dominant first peak is suppressed for p_2. Due to the higher pressure, the corresponding Townsend coefficient α (see equation 2.20) is smaller, leading to a lower gas amplification. The resulting pulse height is not sufficient to exceed the threshold in the discriminator and no trigger signal is sent. As a result, the clusters with low charge are not measurable at p_2 leading to a decrease in the charge cluster peak. As fewer trigger signals are sent, the trigger rate for p_2 decreases compared to p_1, which can be seen in figure 6.4.

[1] The installation and investigation of this pressure system was part of a supervised bachelor thesis [Meiser, 2024].

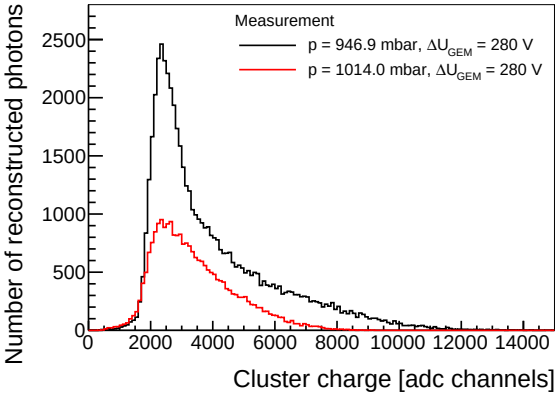

Figure 6.3: With higher pressure, the measured cluster charge decreases. In particular, the small charges are no longer detected and the maximum cluster charge is smaller. Both distributions are normalized to the same measurement time.

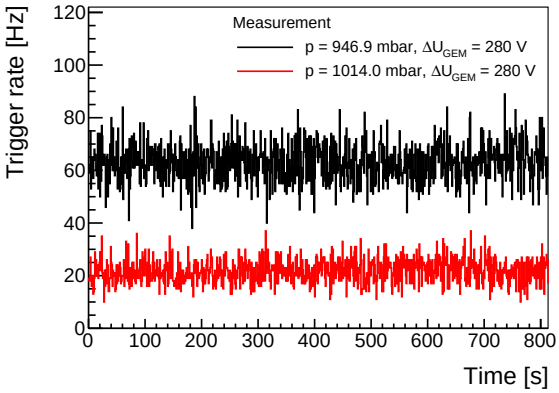

Figure 6.4: At a higher pressure, the trigger rate decreases. The GEM voltage is constant.

One approach is to change the discriminator value, but this leads to a higher noise level, which is unfavorable [Meiser, 2024].
Another method of counteracting this pressure dependence is adapting the gas amplification to various pressures. Therefore, a pressure-voltage calibration is introduced. The voltage ΔU_{GEM} at each GEM foil is changed for different pressure values, as shown in figure 6.5.

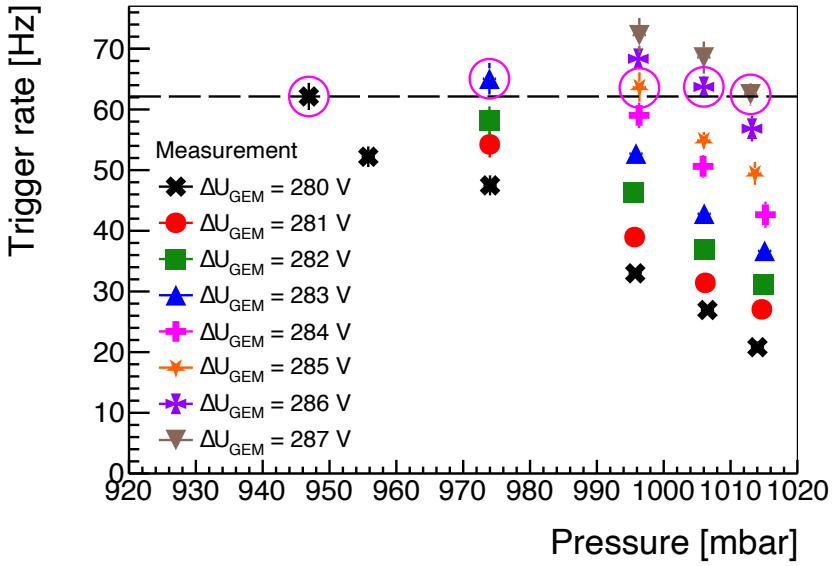

Figure 6.5: For different pressure values, the GEM voltages ΔU_{GEM} of the triple-GEM detector are changed in 1 V steps for each foil and the resulting trigger rate is plotted. Following the current example, a trigger rate of about 62 Hz is achieved for p_1 = 946.9 mbar with $\Delta U_{\mathrm{GEM},1}$ = 280 V, which is marked with the dashed black line. The ΔU_{GEM} value closest to this line has to be applied for the different pressures to obtain the same trigger rate. For p_2 = 1014.0 mbar, a voltage of $\Delta U_{\mathrm{GEM},2}$ = 287 V has to be set to achieve the same trigger rate. For the pressure values in between the voltages scale accordingly (marked by pink circles). Thus, pressure-dependent trigger rate fluctuations are equalized by changing the GEM voltage.

According to the results from this figure, a GEM voltage of $\Delta U_{\mathrm{GEM},2}$ = 287 V has to be applied for p_2 = 1014.0 mbar to achieve the same trigger rate as for p_1 = 946.9 mbar with

$\Delta U_{\mathrm{GEM},1} = 280\,\mathrm{V}$. Using these values, the cluster charge and the trigger rate are shown in figure 6.6 and figure 6.7, respectively. Both exhibit exactly the same behavior, proving that the pressure fluctuations are counteracted by adjusting ΔU_{GEM}.

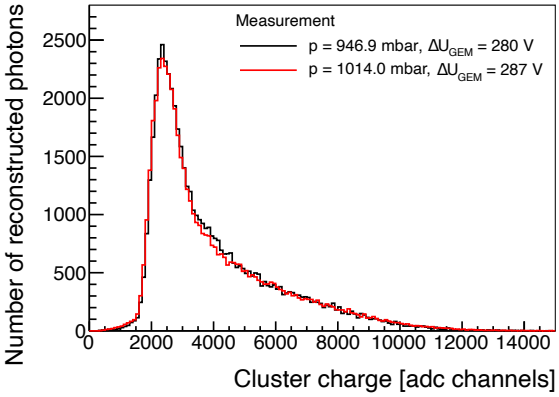

Figure 6.6: Compared to figure 6.3, the same pressure values are shown, but ΔU_{GEM} is adjusted. Therefore, the initial cluster charge distribution is restored by adjusting the GEM voltage for a different pressure value. Both distributions are normalized to the same measurement time.

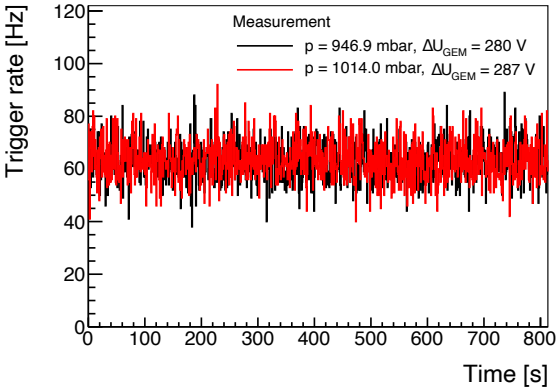

Figure 6.7: As expected from figure 6.5 and figure 6.6, using an adjusted GEM voltage provides the same trigger rate for the different environmental pressures. The discrepancies in figure 6.4 have been resolved.

For a more general approach, a formula for a proper pressure-voltage calibration is derived. The gas amplification, characterized by the Townsend coefficient $\alpha(p,U)$, has to remain constant for two different pressures p_1 and p_2:

$$\alpha(p_1,U_1) = \alpha(p_2,U_2) \tag{6.3}$$

U_1 and U_2 refer to the GEM voltage $\Delta U_{\mathrm{GEM},1}$ and $\Delta U_{\mathrm{GEM},2}$. The aim is to find the appropriate voltage U_2 for the pressure p_2 to calibrate it to another combination of p_1 and U_1. Substituting equation 2.20 into equation 6.3 gives

$$\frac{Ap_1}{T}\exp\left(-\frac{Bp_1d}{U_1T}\right) = \frac{Ap_2}{T}\exp\left(-\frac{Bp_2d}{U_2T}\right) \tag{6.4}$$

The temperature is assumed to be constant due to the climate cabinet with $T = T_1 = T_2$ (see chapter 6.2). The electric field is rewritten as $E = U/d$, where U is the amplification voltage, which corresponds to ΔU_{GEM}, and d is the amplification distance. Rearranging equation 6.4 results in

$$\ln\left(\frac{p_1}{p_2}\right) = -c\left(\frac{p_2}{U_2} - \frac{p_1}{U_1}\right) \tag{6.5}$$

with the constant $c = \frac{Bd}{T}$, which includes the gas parameter B (see chapter 2.3.2). To determine c, the value pairs with different pressure and voltage but the same trigger rate $f_1(p_1,U_1) \approx f_2(p_2,U_2)$ and therefore the same amplifications are extracted from figure 6.5. These value pairs are inserted into equation 6.5 and plotted in figure 6.8. The slope of the resulting line corresponds to c, which is determined by a fit to $c = (0.44 \pm 0.01)\,\mathrm{V\,mbar^{-1}}$. With $T = (25 \pm 1)\,^{\circ}\mathrm{C}$ and $d = 50\,\mu\mathrm{m}$ the gas constant B is calculated as

$$B = \frac{cT}{d} = (2622 \pm 69)\,\mathrm{V\,K\,\mu m^{-1}\,bar^{-1}} \tag{6.6}$$

which is in agreement with the gas constant $B = 2600\,\mathrm{V\,K\,\mu m^{-1}\,bar^{-1}}$ reported by [Herrmann, 2019] for the same gas mixture.

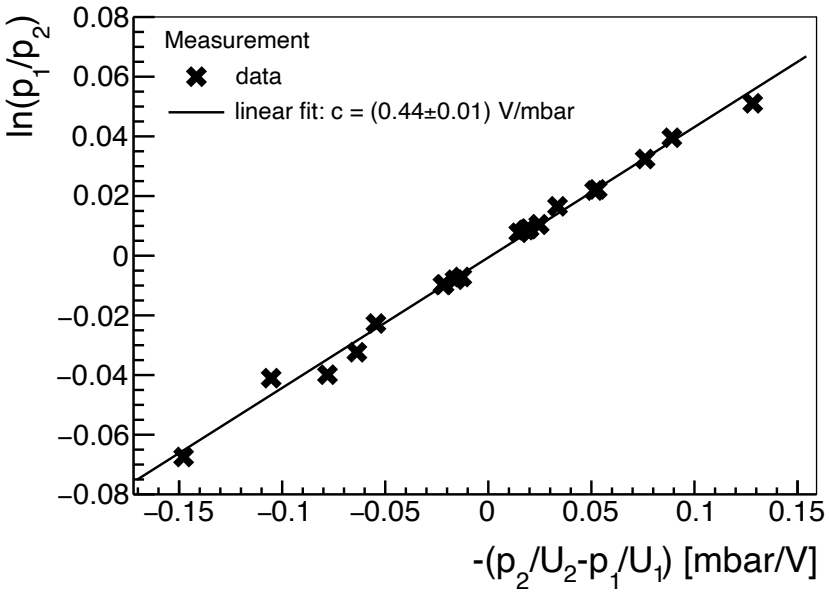

Figure 6.8: To determine the constant c, a value pair from figure 6.5 with the same trigger rate but different pressure and voltage is inserted into equation 6.5 and the results are plotted here. The slope corresponding to c is determined by fitting a first-degree polynomial to the data points.

With this parameter, the voltage that has to be applied for a correct pressure-voltage calibration is defined by:

$$U_2 = p_2\left(-\frac{\ln\left(\frac{p_1}{p_2}\right)}{c} + \frac{p_1}{U_1}\right)^{-1} \tag{6.7}$$

Although the pressure is controlled by the pressure system, it is difficult to set a precise value as the system is inert and slightly dependent on the environmental pressure and temperature. After a pressure value has stabilized and is kept constant by the system, the pressure-voltage calibration is carried out (see Appendix C). This enables pressure-independent measurements that provide reliable and comparable results.

Chapter 7

3D Position Reconstruction

7.1 Working Principle

Enabling a complete 3D position reconstruction of an interacting X-ray in a converter layer is one of the main goals of this thesis, as it is essential for various applications such as imaging (see chapter 1.2.1) and PET (see chapter 1.2.2).
When imaging an object using the introduced setup with converter layers (see figure 5.2), the object is placed between the source and the first layer. To resolve the shape of the object at different heights, the y-position has to be accessible. For PET, the track of the 511 keV photons has to be reconstructed very precisely in order to determine the LoR (Linie of Response), which is the line connecting two coincident detected events. Thus the position of the tumor can be determined (see figure figure 1.4). At the same time, to ensure high detection efficiency of the 511 keV photon for PET, the detector has to be positioned such that the layers face the center of the gantry. Consequently, the reconstruction of the track of the 511 keV photons requires a precise y-position as well.
The setup of the perpendicular converter layers leads to a perpendicular electron drift (see figure 5.28), which does not allow a direct extraction of the y-position. Therefore, a new approach is chosen. Its working principle is shown in figure 7.1. Here, the converter layers are tilted by a rotation angle α.

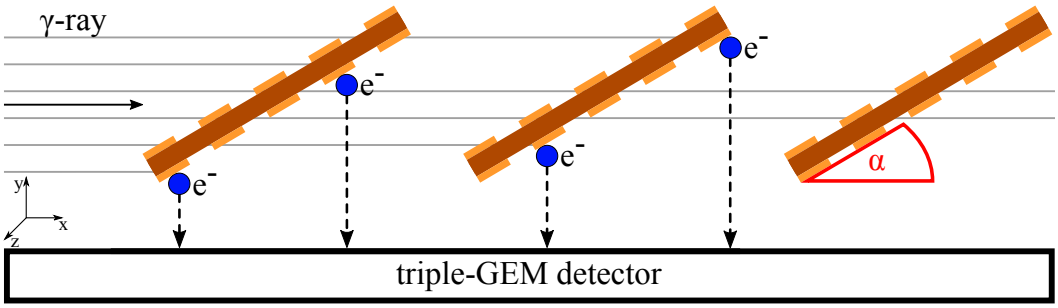

Figure 7.1: The photons interact with the converter layers, which are tilted by an angle α. The electron produced in an interaction process and extracted from the copper strip, is guided downwards by the electric field. If the electron is guided perpendicularly downwards (as indicated here), the y-position depends on the x-position. The basic geometric reconstruction approach is based on $y(x) \sim x \tan\alpha$.

In this chapter, the working principle of this new setup is investigated with the 59.5 keV photons used in the previous chapters, while chapter 9 focuses on the detection of 511 keV

photons.
As introduced in chapter 5, the 59.5 keV photon interacts with the copper strips of the converter layers via the photoelectric effect producing an electron. The photoelectron leaves the copper strip and induces secondary ionization in the gas. The created electron-cluster drifts downwards along the electric field lines towards the triple-GEM detector. Consequently, the y-position is reconstructable by accurately measuring the x-position. Two different reconstruction approaches are tested.
In the first approach, the position is reconstructed using a geometric calculation. It requires a perpendicular electron drift, as shown in figure 7.1. By measuring the x-position and considering the tilting angle α, the y-position is given as

$$y = c + x \tan \alpha \tag{7.1}$$

where the constant c accounts for the known layer position.
The second method for reconstructing the position is simulation-based by modeling the electron trajectory. A good agreement between the measurement results and the simulated results would validate this approach. If additionally a distinct electron drift is achieved, meaning each detected x-position has a unique y-position, the y-position is extractable from the simulation and can be used for the measured position reconstruction.

7.2 Investigation of a Single Converter Layer

Although the use of multiple converter layers leads to higher conversion efficiency and is therefore advantageous, the focus in this section is on understanding the electron drift in the detector, which is investigated in an initial study with one converter layer. Furthermore, a good agreement between simulation and measurement is desired as it allows a better understanding of the occurring physical processes and electron drift in the detector.

7.2.1 Measurement Setup

For a first investigation of the introduced reconstruction methods, one converter layer is placed inside the triple-GEM detector as shown in figure 7.2.
Compared to chapter 5, the converter layer consists of a thinner FR4 material (250 µm instead of 1520 µm), but still has 35 µm thick copper strips on both sides. Although the layer is thinner, it remains very rigid and does not bend. It is positioned at an angle of 60° with respect to the GEM foil (see figure 7.1). All environmental factors (see chapter 6) are controlled and listed in Appendix C for completeness.
The setup is irradiated with 59.5 keV photons emitted from the ^{241}Am point source (see chapter 5.4.2). In the following, the side of the converter layer facing the source is referred to as the back side and the side facing away from the source as the front side. This labeling refers to the emission direction of the detectable electrons[1].

[1] Only the electrons extracted from the front side in the forward direction are detectable, as are the electrons extracted from the back side of the copper strips in the backward direction

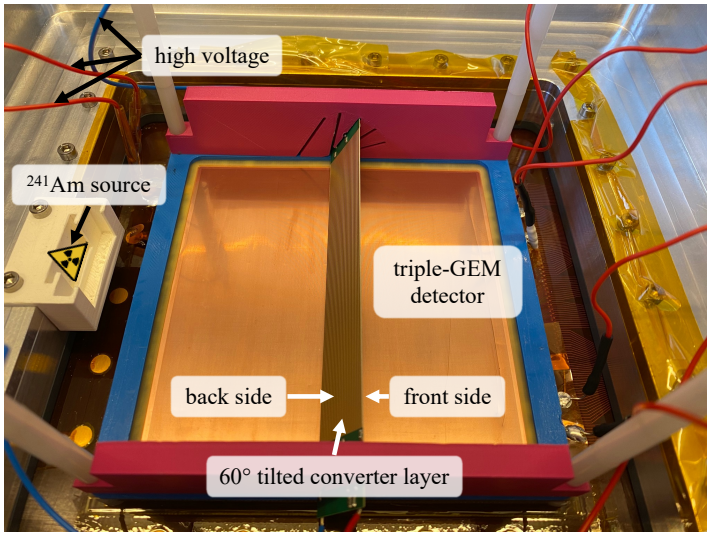

Figure 7.2: For an initial investigation of the electron drift behavior in the triple-GEM detector, a converter layer made of 250 µm FR4 and 35 µm copper strips is installed at an angle of 60° with respect to the GEM foil. The radioactive source (not shown) is placed in the source holder. The side of the converter layer facing the radiation source is referred to as the back side and the opposite side as the front side.

In order to investigate the electron drift behavior, ΔU_y and ΔU_x voltage scans are performed. By changing these voltages, which are applied to the converter layers (see chapter 5.3.2), various electric fields are investigated to optimize the electron guiding. While $\Delta U_{drift} = 100\,V$ remains constant for all measurements, ΔU_y and ΔU_x are varied separately. Their influence on the resulting electric field and electron drift is analyzed in the next sections, including a comparison with the corresponding simulation results.

7.2.2 Measurement Results: Voltage Scan

The reconstructed 2D position on the anode is shown in figure 7.3.

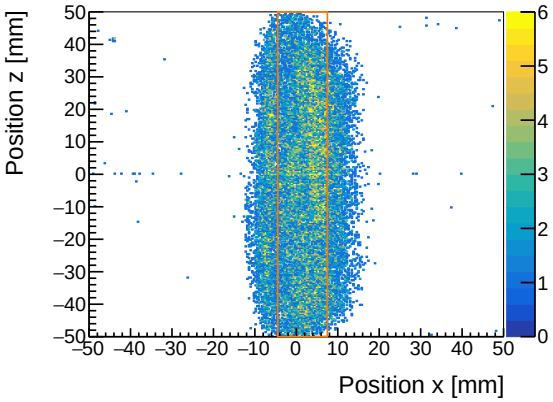

Figure 7.3: The measured 2D hit distribution at the anode plane solely shows hits in the expected area around the converter layer (orange box). Electrons are guided downwards and detected. Here, the voltages $\Delta U_y = 600\,V$ and $\Delta U_x = 0\,V$ are applied.

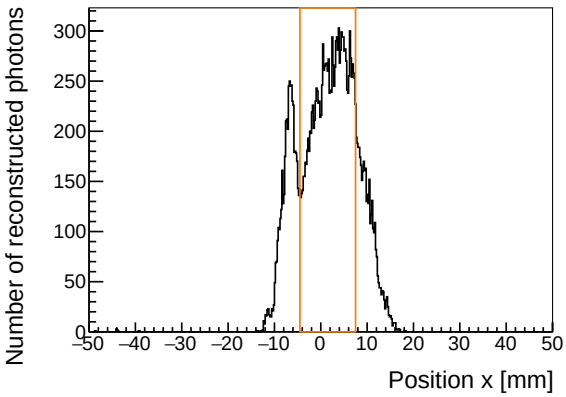

Figure 7.4: In the profile in x-direction of figure 7.3, two peaks are formed with a minimum at the left edge of the layer (orange box). Electrons from both sides of the layer are detected. The second peak is more dominant.

Since the particles are reconstructed around the layer position, this demonstrates a successful electron extraction and guiding. The events are detected homogeneously along the z-axis, while two peaks form in the x-direction. This can be clearly seen in figure 7.4, where the profile in x-direction of figure 7.3 is shown. The orange box in all figures indicates the position of the converter layer, with the left edge of the box marking the bottom edge of the layer and the right edge marking the top edge of the layer (see figure 7.2).
Electrons produced on both sides of the converter layer are directed downwards, creating two distinct peaks. For this voltage combination, both peaks have approximately the same height, with the second one (at $x = 4\,\text{mm}$) being broader, compared to the first peak (at $x = -6\,\text{mm}$). Thus, the second peak has a higher contribution to the total detection efficiency. Based on the position of the peaks with respect to the position of the converter layer, the first peak is formed by electrons emerging from the back of the converter layer and the second peak by those coming from the front side as defined in figure 7.2.
Since the electrons extracted in the forward direction are guided directly downwards to the GEM foil, the electrons coming from the back side have to be guided around the layer for detection. In the latter case, more electrons are absorbed by the layer, resulting in a smaller first peak. The corresponding electric field configuration and electron drift are discussed in chapter 7.2.3.

To investigate the electron drift and its influence on the measured trigger rate (see figure 7.5) and the profile of the hit distribution (see figure 7.6), the voltage ΔU_y is varied while $\Delta U_\text{x} = 0\,\text{V}$ is kept constant. With a higher ΔU_y, the trigger rate and thus the photon detection efficiency increases. Due to the higher voltages, the resulting stronger electric field leads to a better and faster guiding of the electrons. More electrons with a higher y-value are detected, which can be seen in figure 7.6, as the second peak is broader with a higher ΔU_y. In addition, the first peak is more pronounced than for small ΔU_y values. Both effects lead to an overall increase in the trigger rate by a factor of 5 at $\Delta U_\text{y} = 800\,\text{V}$ compared to $\Delta U_\text{y} = 0\,\text{V}$. Compared to the perpendicular converter layer arrangement, the trigger rate does not start to saturate in this ΔU_y range (see figure 5.16). A high ΔU_y is preferred in order to obtain a high photon detection efficiency.

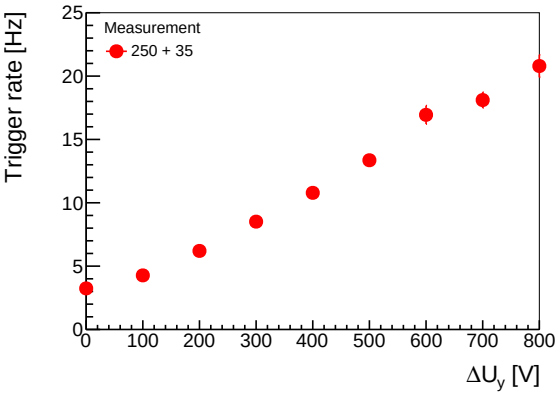

Figure 7.5: A ΔU_y voltage scan is performed ($\Delta U_\text{x} = 0\,\text{V}$ is constant). At higher ΔU_y values, the trigger rate increases because more electrons are guided downwards and are detected due to the stronger electric field. For high detection efficiency, a large ΔU_y is preferred.

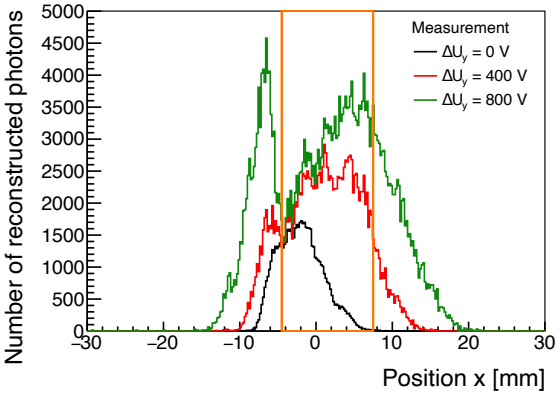

Figure 7.6: The increasing trigger rate from figure 7.5 is directly correlated with the measured peak profile, which is normalized to the same measurement time for the different voltages. With increasing ΔU_y, the second peak becomes broader and the first peak more dominant. More electrons produced at higher y-values are directed downwards and more electrons are detected from the back side of the layer.

The same measurement procedure is performed with constant $\Delta U_y = 600\,V$ [2] while changing ΔU_x. For this measurement, the voltage of the copper strip closest to the GEM foil, which is for the tilting angle of 60° the strip on the front side of the layer, is kept constant and ΔU_x is changed with respect to these strips. The resulting trigger rate and profile are shown in figure 7.7 and figure 7.8, respectively. ΔU_x is changed from $-400\,V$ to $400\,V$. Since for $\Delta U_x = -400\,V$ the first peak disappears completely, the lowest trigger rate is measured for this voltage combination. While the second peak is not strongly influenced by a change in ΔU_x apart from a slight increase, ΔU_x has a strong influence on the first peak. As ΔU_x increases, it becomes broader and higher, which results in a higher trigger rate. This behavior implies that for these voltage combinations with higher ΔU_x, the electric field is influenced such that more electrons are guided downwards. These effects are analyzed in the next section, considering the simulated electric fields and electron drift.

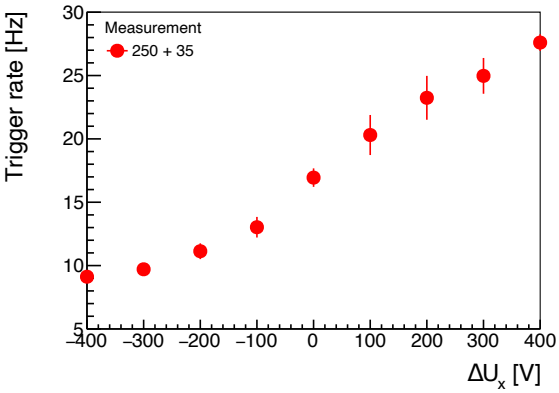

Figure 7.7: ΔU_x is varied, while $\Delta U_y = 600\,V$ is kept constant. Compared to $\Delta U_x = 0\,V$, the trigger rate is doubled by applying $\Delta U_x = 400\,V$.

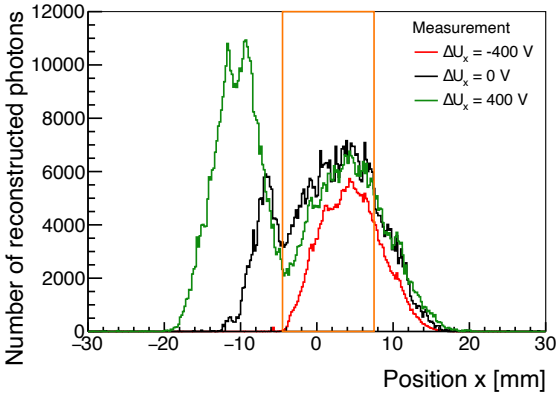

Figure 7.8: With a higher ΔU_x, more electrons are guided downwards from the back side of the layer, increasing the first peak and the overall trigger rate. All measurements are normalized to the same measurement time.

Due to the geometry of the layer regarding height and tilting angle, the second peak is expected to have a width of about 10 mm [3] in the case of a vertical drift. All voltage combinations shown in figure 7.8 are close to this expectation. This means that either all electrons drift vertically downwards or another electron drift behavior causes this distribution (see figure 7.11). This electron drift is discussed in the next section.

In addition, the first peak is more dominant than expected from the theoretical consideration in figure 2.2, which indicates a very low probability of backward emission of photoelectrons at this energy. Either the photon conversion probability in the gas is of a similar order of magnitude as the forward electron extraction from copper or there is another reason that is not covered in the previous consideration of the functioning principle of the converter layers (see chapter 8).

[2] Although $\Delta U_y = 800\,V$ provides a higher trigger rate, a lower ΔU_y voltage is required for the ΔU_x scan. For the voltage scan, it is not possible to use for example $\Delta U_y = 800\,V$ and $\Delta U_x = 400\,V$ because the absolute value is higher than the maximum voltage provided by the HV supply.

[3] The layer is tilted by 60° with respect to the GEM foil. The converter layer has a height of 20.6 mm (see figure 5.3). This results in a width of $20.6\,mm \cdot \cos(60°) = 10.3\,mm$ in x-dimension.

7.2.3 Simulation: Electron Drift in Electric Field

As the simulation and measurement results in chapter chapter 5 exhibit a good agreement, the same simulation procedure presented in chapter 5.6 is used here, including Geant4, ANSYS, Garfield++ and the clustering algorithm. The corresponding programs are adapted to all changes in the setup, including the dimensions of the converter layers, the tilting angle and the applied voltages. The resulting equipotential distribution[4] provided by ANSYS for ΔU_y = 600 V and ΔU_x = 400 V is shown in figure 7.9 with the corresponding y-component of the electric field in figure 7.10.

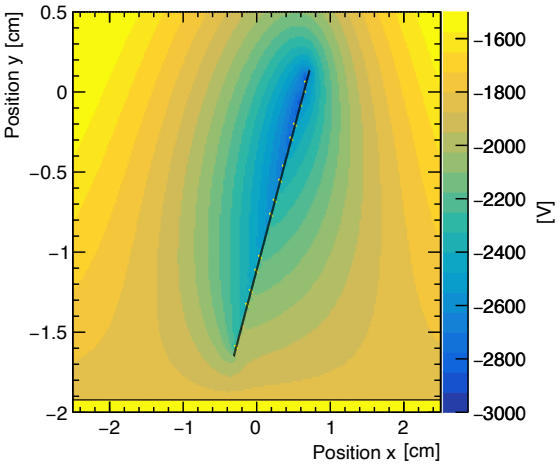

Figure 7.9: Applying ΔU_y = 600 V and ΔU_x = 400 V leads to the presented equipotential distribution for one tilted converter layer in the GEM detector. The electrons move perpendicular to the equipotential lines.

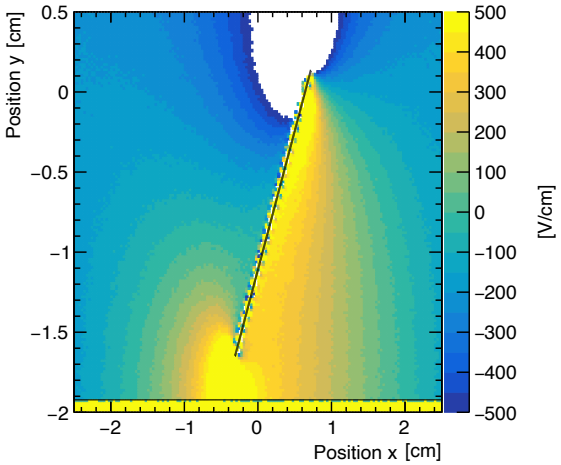

Figure 7.10: The y-component of the electric field resulting from figure 7.9, provides field strengths of up to 500 V cm^{-1} between the bottom of the layer and the GEM foil. Between the front side and the GEM a field strength of 300 V cm^{-1} is achieved. The electric guiding field lines are not necessarily perpendicular to the GEM foil. The white areas lie outside the visualized field strength range.

The electron drift[5] for this voltage combination can be seen in figure 7.11. As expected from the measurement results, the electric field allows the electrons to be guided downwards from both sides of the layer, which leads to the formation of the two peaks. The electrons produced at the upper part of the converter layers are not directed downwards but instead upwards due to the grounded housing and are therefore undetectable.
For ΔU_y = 600 V and ΔU_x = −400 V, the electron drift is shown in figure 7.12. The resulting electric field influences the electrons from the back side such that they either drift upwards or downwards. In the latter case, they are absorbed by the layer. Consequently, no first peak forms. In addition, the electrons on the lower right side of the converter layer partially drift around the lower edge and are absorbed by the layer, which leads to a narrower second peak for this voltage combination (see figure 7.8).

[4] In particular, in these simulations with the tilted converter layers the implementation of the grounded housing (see figure 5.22) has a strong influence on the electric field and thus on the electron drift as well as on the detected hit distribution. If the grounded housing is not taken into account, the simulation and measurement results differ considerably.

[5] For all visualizations of electron drift in this chapter, 5 electrons with an initial energy of 0.1 eV are placed equidistant on each side of the converter layers. No information from Geant4 is implemented and no secondary ionization is simulated. These effects are taken into account in the complete simulation and all shown hit distributions.

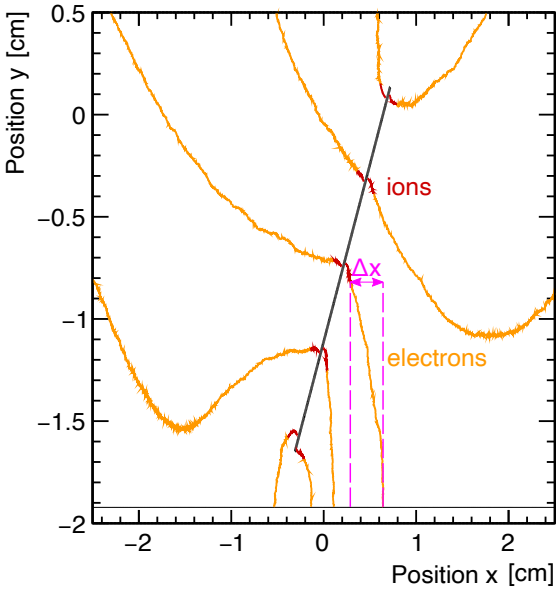

Figure 7.11: To investigate the electron drift in the electric field from figure 7.10 (with ΔU_y = 600 V and ΔU_x = 400 V), 5 electrons are positioned on the front and back side of the converter layers. The electrons start where the orange and red lines diverge. The electrons with a high y-value are guided upwards and those with a low y-value downwards. For the downward drift, the electrons exhibit a deviation Δx in the start and end position.

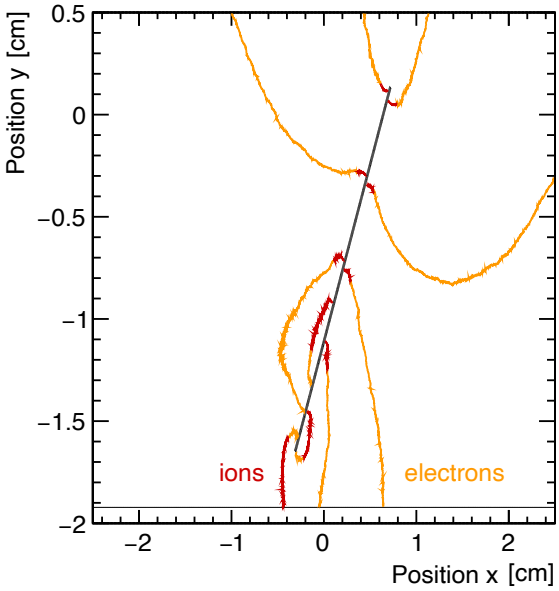

Figure 7.12: The electron drift is simulated for the voltage combination ΔU_y = 600 V and ΔU_x = −400 V. Due to the resulting electric field, some electrons on the back side of the layer are guided upwards and others downwards, where they are absorbed by the layer. No first peak forms. The electron drift on the front side is similar to figure 7.11, leading to an equivalent second peak.

With regard to the discussion of the measurement results in the previous section, neither the electrons created in the entire height of the layer are guided downwards, nor is the drift of the remaining electrons perpendicular. Instead, there is a discrepancy between the x-values of the start and end positions of the electrons, which is defined as follows

$$\Delta x = x_{\text{end}} - x_{\text{start}} \tag{7.2}$$

and is marked in figure 7.11.

The profile of the simulated distribution is shown in figure 7.13, using the same voltage combinations as for the measurements displayed in figure 7.8. Although a more detailed comparison between simulation and measurement is carried out in chapter 7.2.5, it can be seen here that both exhibit similar behavior. For ΔU_x = −400 V, the first peak does not form, as expected from the resulting simulated electron drift in figure 7.12 and in agreement with the measurement. Only the second peak is visible for ΔU_x = −400 V. While this second peak barely changes its shape with increasing ΔU_x, the first peak is formed and increases in height and width. This behavior is identical for simulation and measurement. The first peak is more pronounced in the measurement.

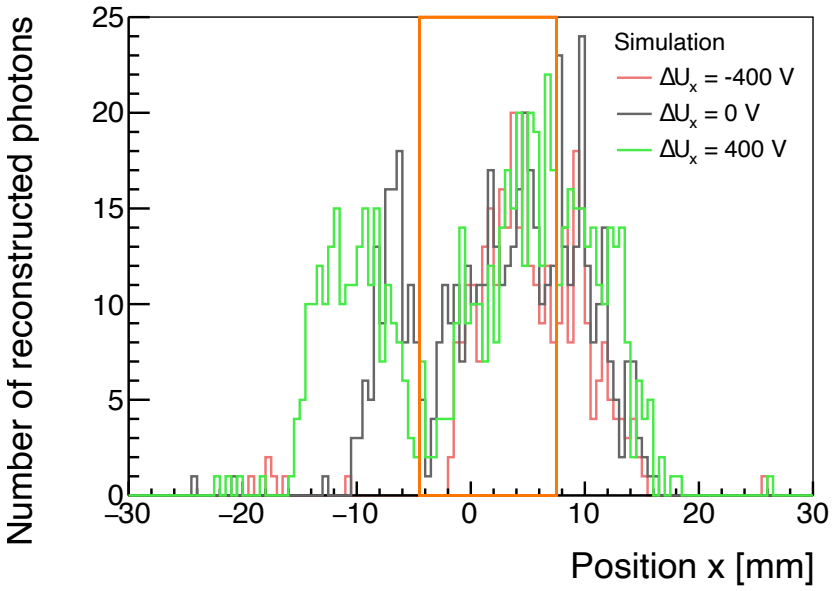

Figure 7.13: The simulated profile of different ΔU_x values and fixed $\Delta U_y = 600\,\mathrm{V}$ exhibits the same behavior as the measurement results in figure 7.8: For all ΔU_x values the shape of the second peak is similar and as ΔU_x increases, the first peak appears.

This comparison between simulation and measurement demonstrates a good agreement between the results, particularly with regard to the hit distribution. If there is a bijective correlation between the measured x-position and y-position of the X-ray interaction, the y-position can be determined for a measured x-value from the simulation prediction.

7.2.4 Simulation: First Study on Perpendicular Drift and Position Reconstruction

The first concept introduced in chapter 7.1 is the geometric y-position reconstruction based on the prerequisite of a perpendicular drift. While the voltage combination $\Delta U_y = 600\,\mathrm{V}$ and $\Delta U_x = 400\,\mathrm{V}$ provides a high photon detection efficiency (see figure 7.7), which is one main goal of this project, the perpendicular drift is not guaranteed for all electrons, as shown in figure 7.11. The marked deviation Δx (see equation 7.2) is further analyzed with regard to its influence on the y-position reconstruction.
In figure 7.14 Δx is displayed for all electrons in all detected electron-clusters. Since a vertical electron drift for electrons detected in the first peak is not possible by geometry, these are neglected. The distribution shows a tail of up to 9 mm, with the majority of the Δx-values being less than 1 mm. This non-perpendicular drift results in a discrepancy Δx with $\Delta x > 0$, indicating $x_{\mathrm{end}} > x_{\mathrm{start}}$ and thus an electron drift to larger x-values. To determine this influence of Δx on the y-position reconstruction, the y-position for all electrons in the second peak is determined using equation 7.1, which is adapted for the setup. The constant c considers the layer position y_{layer}. The reconstructed y-position is given by

$$y_{\mathrm{reco}} = y_{\mathrm{layer}} + (x - x_{\mathrm{layer}}) \tan\alpha \tag{7.3}$$

Here, $y_{\mathrm{layer}} = -16.7\,\mathrm{mm}$ and $x_{\mathrm{layer}} = 3.0\,\mathrm{mm}$ is used. The reconstructed y_{reco}-positions are compared with the initial electron y-position, which is an accessible variable in the simulation. These two values are shown in figure 7.15 for $\Delta U_y = 600\,\mathrm{V}$ and $\Delta U_x = 400\,\mathrm{V}$. A discrepancy between the initial and reconstructed electron y-position is observed.

For the initial electron y-position −10 mm, y-values between −8–15 mm are reconstructed (indicated in figure 7.15 by the orange dashed lines). This deviation of 23 mm is higher than the height of the tilted converter layer ($\sin(\alpha) \cdot 20.6\,\text{mm} = 17.8\,\text{mm}$). With the geometric approach using one tilted converter layer, the initial position cannot be resolved over the entire layer height.

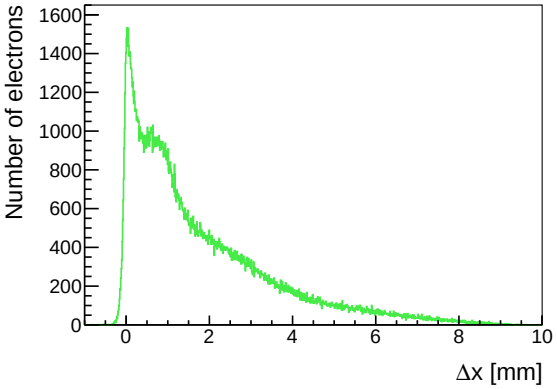

Figure 7.14: For all detected electrons for the voltage combination ΔU_y = 600 V and ΔU_x = 400 V, the Δx value is determined according to equation 7.2. For the majority of electrons, there is a deviation of a few millimeters between the start and end position of the x-value.

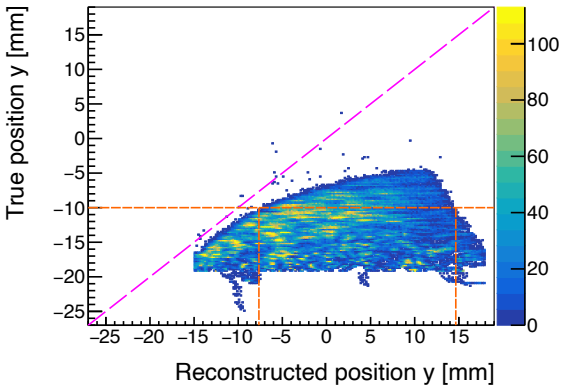

Figure 7.15: The y_{reco}-position reconstructed from the simulation using equation 7.3 is compared with the initial electron y-position. Due to the non-perpendicular drift, the reconstructed position shows a large deviation from the real y-position. For the true y-position −10 mm, the orange dashed lines mark the range of the reconstructed y-positions. The pink dashed line indicates perfect agreement between the two quantities.

An accurate reconstruction of the y-position by a purely geometric approach with one layer is not possible. This can either be resolved by parameterizing the detected and initial positions (second method introduced in chapter 7.1) or by making experimental adjustments. For the first approach a good agreement between simulation and measurement is mandatory. The experimental adjustment is achieved by inserting several converter layers at the same height into the detector and adjusting the voltages for a perpendicular electron drift (see chapter 7.3).

7.2.5 Comparison: Measured and Simulated Hit Distribution

For a direct comparison between the simulated and measured hit profile, both are superimposed for ΔU_x = −400 V (see figure 7.16), ΔU_x = 0 V (see figure 7.17) and ΔU_x = 400 V (see figure 7.18).
These voltage combinations provide a good agreement with regard to the width of the individual peaks and their position. The main difference is the height and thus the integral of the first peak for ΔU_x = 400 V. It is more pronounced in the measurement than in the simulation. This discrepancy typically results from differences in the electric field. Not all components that are placed in the detector and are grounded are implemented in the simulation. Nevertheless, they influence the configuration of the electric field.

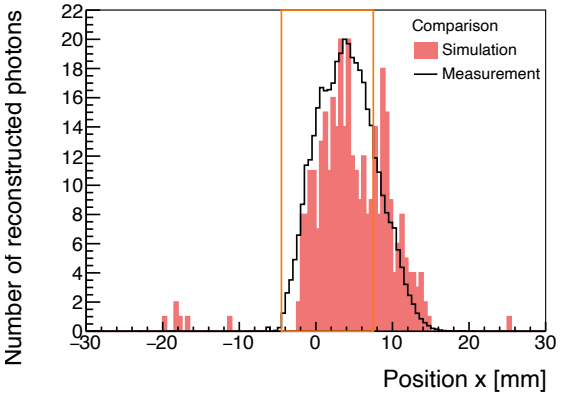

Figure 7.16: The voltage combination ΔU_y = 600 V and ΔU_x = −400 V provides a good agreement for simulation and measurement in terms of position, width and shape. Only the second peak is observed, while the first peak does not occur with this voltage combination. The distributions are scaled to the same maximum value.

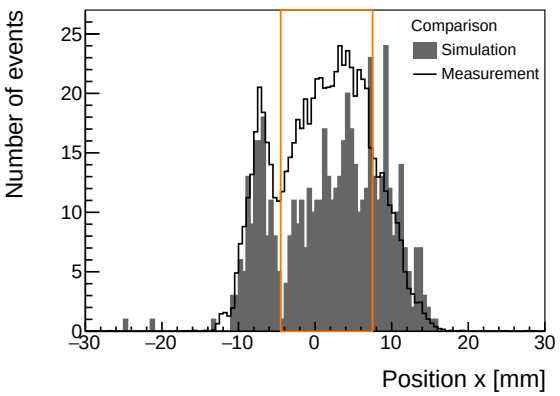

Figure 7.17: When applying ΔU_y = 600 V and ΔU_x = 0 V, both peaks are visible in simulation and measurement. They coincide in their peak positions and width as well as provide a similar peak integral ratio (see figure 7.19). Both distributions are scaled to the same maximum value.

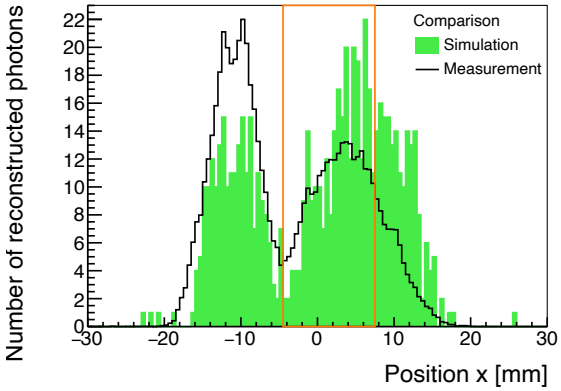

Figure 7.18: In simulation and measurement a double peak structure is formed for the voltage combination ΔU_y = 600 V and ΔU_x = 400 V. The first peak is more dominant in the measurement. But the position and width of both peaks are in good agreement. Both are scaled to the same maximum value.

To enable a more accurate comparison, a Gaussian function is fit to each peak of the distribution, providing the mean peak position. In addition, the edges of the distribution and the integral of the peaks are determined. The ratio of these integrals I of the two peaks (I_1/I_2) is shown in figure 7.19. Since there is no first peak for ΔU_x = −400 V, the ratio is defined as 0. For ΔU_x = 0 V there is good agreement, while for ΔU_x = 400 V the difference increases due to the larger measured first peak described above.
Furthermore, the total width of the distribution in figure 7.20 and the position of the individual peaks in figure 7.21 provide a good agreement.

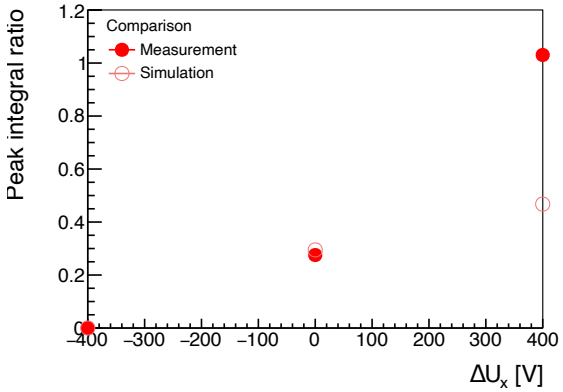

Figure 7.19: Comparison of the integral ratio of both peaks (I_1/I_2) between simulation and measurement. The different behavior of the first peak between simulation and measurement in figure 7.18 is responsible for the deviation in the peak ratio at $\Delta U_x = 400\,\mathrm{V}$. A good agreement between simulation and measurement is achieved for $\Delta U_x = 0\,\mathrm{V}$, while for $\Delta U_x = -400\,\mathrm{V}$ the ratio for simulation and measurement is defined to be 0 because both have no first peak.

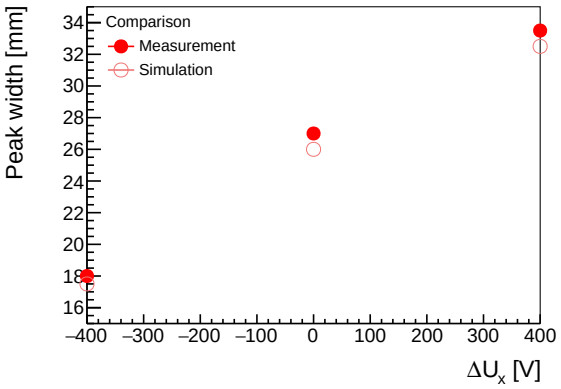

Figure 7.20: The overall width of the distribution exhibits good agreement for all voltage combinations, which represents a good verification of the simulated electron drift and electric field configuration. There is no first peak for $\Delta U_x = -400\,\mathrm{V}$.

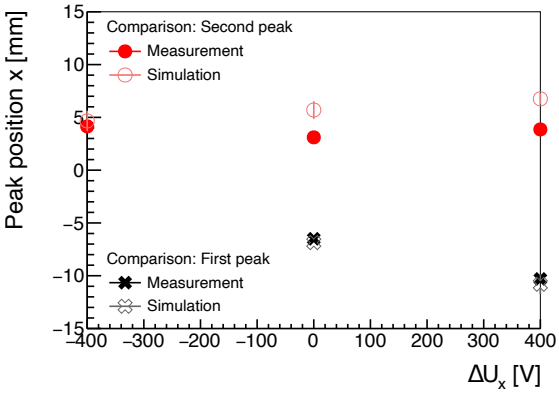

Figure 7.21: The peak position, meaning the mean value of the fit Gaussian function, is in good agreement for the first and second peak for simulation and measurement.

For the single converter layer, there is good agreement between the simulation and measurement results. In particular, the measured peak structure of the hit distribution is accurately understood by simulating the electron drift. Due to this good agreement, the approach of extracting the measured y-position from the simulation is an interesting and justified alternative to the perpendicular electron drift reconstruction method, as the latter method shows large discrepancies when using a single layer (see chapter 7.2.4).

7.3 Investigation of Multiple Converter Layers

The voltage scans with one converter layer reveal the main challenge for the position reconstruction approach: A perpendicular or generally distinct electron drift with a simultaneously high guiding efficiency is difficult to achieve, especially with one converter layer in the GEM detector. For this reason, several converter layers are incorporated into the detector and investigated in this section.
The use of multiple tilted converter layers in the detector overcomes two main challenges. The photon detection efficiency is increased when using several converter layers (see chapter 5). Additionally, by adjusting the voltage, in particular ΔU_x, the equipotential lines are aligned parallel to the GEM foil. This results in a perpendicular electron drift.
Due to the good description of the electron drift by the simulation in chapter 7.2, it is used to demonstrate the basic idea. The aim of this section is to obtain a proof of concept for the functional principle of position reconstruction with multiple tilted converter layers. Measurement results are compared with those of the simulation in order to gain an understanding of the functionality. Afterwards, a first attempt to image an object is carried out.

7.3.1 Simulation: Electric Field and Electron Drift

In order to achieve high efficiency in photon conversion while enabling position reconstruction, several tilted layers are arranged in the detector. Moreover, applying the same voltage to strips with the same y-position at each layer leads to rather horizontal equipotential lines (see figure 7.22), enabling a perpendicular electron drift (see figure 7.23).

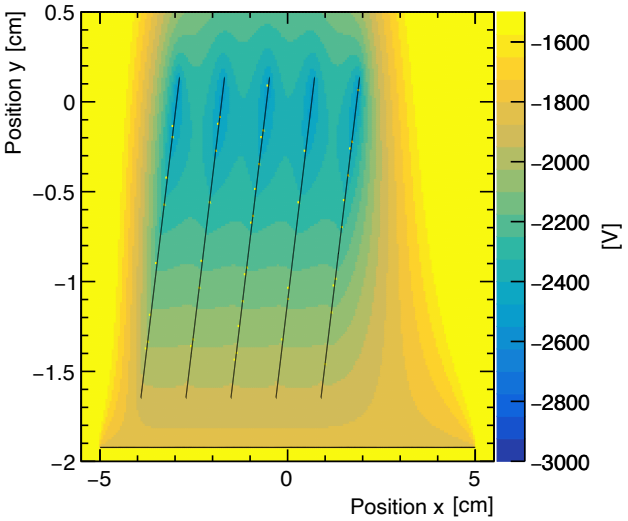

Figure 7.22: If several converter layers are used, the voltage combination $\Delta U_y = 600\,\mathrm{V}$ and $\Delta U_x = 0\,\mathrm{V}$ results in equipotential lines that are almost parallel to the GEM foil. The electrons move perpendicularly to such equipotential lines.

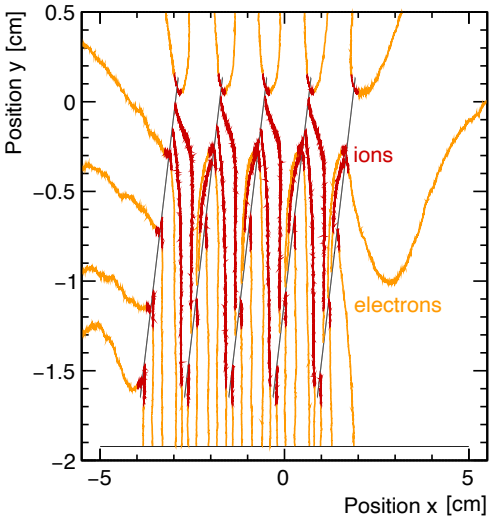

Figure 7.23: To simulate the corresponding electron drift from figure 7.22, on each side of the 5 layers 5 electrons are placed. The electrons on the front side of the layer are guided downwards almost vertically, while nearly all electrons from the back side are absorbed by the layer or end at the housing.

To ensure that all electrons extracted from the copper strips in the forward direction are guided downwards regardless of their y-position, the converter layers are arranged such that they do not overlap in the x-position. Instead, the upper edge of one layer and the lower edge

of the next layer lie next to each other regarding the x-position, as shown in figure 7.22. According to the simulation results presented in figure 7.23, the configuration with $\Delta U_x = 0\,V$ allows a vertical drift for the electrons extracted in the forward direction. Due to the layer arrangement, these electrons are not absorbed by the neighboring layer, but are detected. The majority of the electrons on the back side of the layer is not detected as it is absorbed by the converter layers due to the electric field configuration.

7.3.2 Measurement Setup

The measurement setup corresponding to figure 7.22 can be seen in figure 7.24. Five of the 250 µm FR4 layers with 35 µm Cu strips on both sides are positioned[6] without overlap in the x-direction in the detector and tilted by $\alpha = 60°$ with respect to the GEM foil.
To investigate the working principle for this new setup, a voltage scan is performed and its influence on the trigger rate and hit distribution is examined.

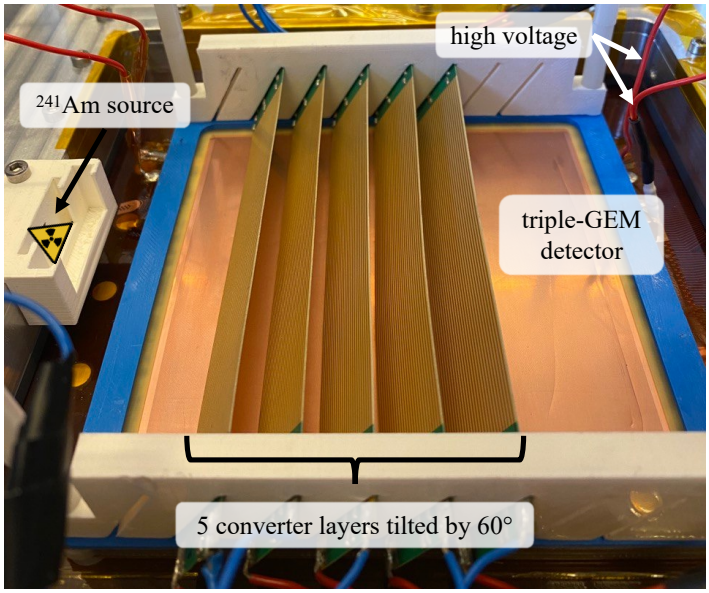

Figure 7.24: The 5 converter layers are positioned in the detector such that they are each inclined by $\alpha = 60°$ with respect to the GEM foil and do not overlap. This setup is identical to the one simulated in figure 7.23 and thus enables the vertical electron drift.

7.3.3 Measurement Results: Voltage Scan

As with the previous measurements, a ΔU_x voltage scan is performed for this new setup with 5 tilted layers to investigate its influence on the detector performance. $\Delta U_y = 600\,V$ is kept constant.
The measured trigger rate (see figure 7.25) for multiple converter layers increases with ΔU_x. Compared to the trigger rate of a single converter layer (see figure 7.7), it is a factor 4 higher for 5 layers. For a better understanding of the trigger rate curve, the respective profile of the hit distribution is shown in figure 7.26.

[6] In figure B.2 the used holding structure is displayed. The single layer position from the measurements in chapter 7.2 corresponds to the position of the fourth layer. The holding structure is designed that neighboring gaps are aligned in the x-direction with $\Delta x_{gaps} = 0\,mm$. Due to the SMD resistors on the converter layers, these gaps have to be larger than the total PCB thickness. Thus, there is a small distance between two adjacent layers $\mathcal{O}(\Delta x_{layers}) = 1\,mm$.

For $\Delta U_x = -400\,\mathrm{V}$, only some electrons created at the front side of the layer at low y-positions are detected. The other electrons from this lower part of the converter layer are guided around the bottom edge of the layer, similar to the single layer setup (see figure 7.12), and are absorbed. Most of the electrons created at higher y-values between the layers are not detected. The voltage configuration leads to drift lines ending on a layer causing the absorption of the electrons, resulting in small peaks and a low trigger rate.
The voltage combination with $\Delta U_x = 0\,\mathrm{V}$ causes the peaks of the profile to become wider with an increase at the right edge of the layers. Electrons extracted in the forward direction of the layer are directed vertically downwards, as shown in figure 7.23, resulting in the observed broad distribution. A few electrons from the back side of the next layer are detected, leading to the additional increase at the right edge of the layer.
If ΔU_x is increased further, the trigger rate increases since more electrons are detected from the back side of the layer and therefore a peak forms at the left edge of each layer. Nevertheless, a vertical drift of the electrons is not guaranteed at a high trigger rate.

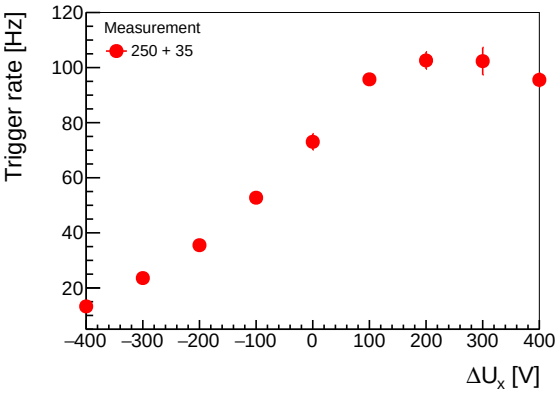

Figure 7.25: The overall trigger rate is higher with 5 layers than with 1 layer. It increases up to 105 Hz between $\Delta U_x = 200\,\mathrm{V}$ and $\Delta U_x = 300\,\mathrm{V}$ and decreases slightly for higher ΔU_x voltage differences. Since the trigger rate is influenced by the electric field and the resulting electron drift, it is likely that at higher ΔU_x the electric field configuration results in more electrons being absorbed (see figure 7.29). $\Delta U_y = 600\,\mathrm{V}$ remains constant.

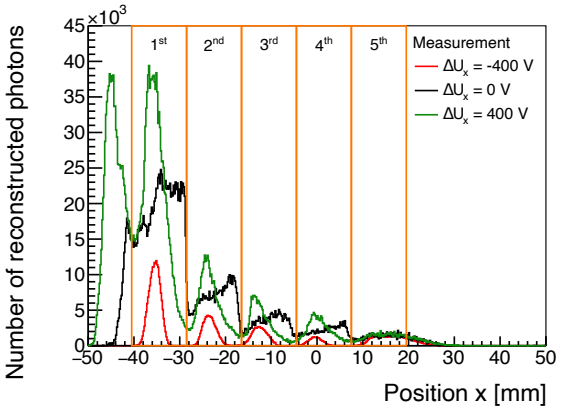

Figure 7.26: The shape of the peaks in the hit distribution is strongly influenced by ΔU_x. At $\Delta U_x = -400\,\mathrm{V}$ the peaks are centered beneath the layers and symmetrical. At $\Delta U_x = 0\,\mathrm{V}$ the peaks are shifted to the right edge of the layer and at $\Delta U_x = 400\,\mathrm{V}$ to the left. The orange boxes with labels indicate the layer positions.

The measurement and simulation results demonstrate that when using multiple converter layers, the photon detection efficiency increases as intended and when applying $\Delta U_x = 0\,\mathrm{V}$ the electrons drift downwards perpendicularly.

7.3.4 Comparison: Simulation and Measurement Results

The simulation and measurement results are compared for $\Delta U_x = 0\,\mathrm{V}$ in figure 7.27 and $\Delta U_x = 400\,\mathrm{V}$ in figure 7.28. While a strong decrease in peak height with increasing x-position can be observed for both voltages in the measurement, this decrease is smaller in the simulation.

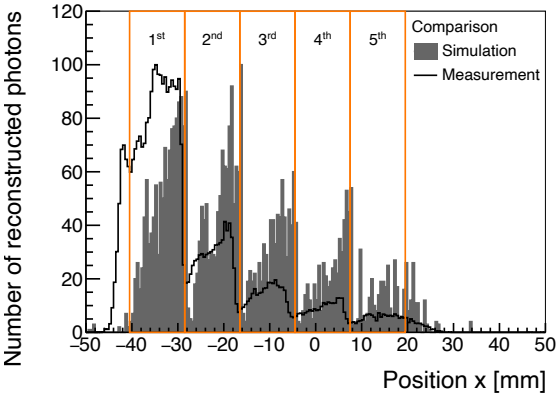

Figure 7.27: Although the measured decrease in peak height is stronger with increasing x-position, the measured and simulated peak shapes agree reasonably well for $\Delta U_x = 0\,\mathrm{V}$. For both, there is an increase in intensity in the direction of the right edge of the converter layer. The corresponding simulated electron drift is shown in figure 7.23.

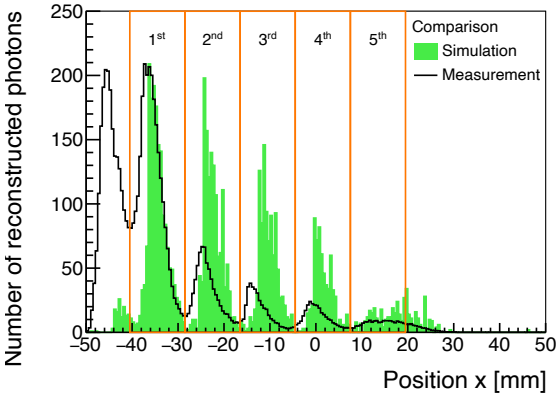

Figure 7.28: As with the previous voltage combination, the decrease in peak height for $\Delta U_x = 400\,\mathrm{V}$ differs between simulation and measurement, but the shape of the peaks is similar with a drop in intensity in the direction of the right edge of the converter layer. The electron drift is shown in figure 7.29.

There are various effects that are not considered in the simulation (see chapter 5.6.4), such as the recombination effect or the electron-electron interaction. As shown in figure 7.23, the ions produced at the bottom back of the layer move upwards. Recombination occurs due to interactions with electrons drifting downwards. This is not explicitly shown in figure 7.23. It leads to a lower number of detected electrons per cluster in the measurement and, if the charge threshold value is not reached, to fewer detected events. This effect is not considered in the simulation and more electron-clusters are detected.

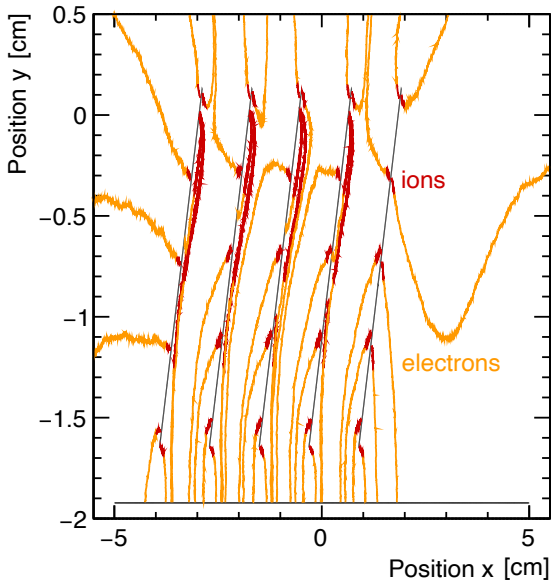

Figure 7.29: For $\Delta U_y = 600\,\mathrm{V}$ and $\Delta U_x = 400\,\mathrm{V}$, electrons are guided downwards and detected from the front and back sides of the layers. The electrons on the front side drift very close along the layer. This drift is leads to the observed drop in intensity towards in direction of the right edge of the layer in figure 7.28. Since the electron drift for all X-ray interaction positions y ends at about the same x-position, the reconstruction of the y-position is not possible.

In addition, differences between the actual and simulated electric field lead to discrepancies in the hit distribution. In the simulated electron drift in figure 7.29 for $\Delta U_x = 400\,V$, the electrons drift rather closely along the front side of the layers. Due to the ideal drift conditions in the simulation, the majority of the electrons are guided downwards and detected. Since the configuration of the electric field in combination with the electron drift between the layers is very sensitive to changes in the setup, even small variations in the electric field can lead to the absorption of electrons. This is another reason for the differences between simulation and measurement in figure 7.28.
Considering the limitations of the simulation and measurement, a reasonable agreement is obtained in terms of peak width and shapes. Therefore, these simulation results are used for further investigations in the next section.

7.4 Imaging of an Object

7.4.1 Measurement: Influence on the Hit Distribution

For a first imaging approach, a 5 mm thick, 5 mm wide and 18 mm high copper block is placed between the source and the first layer, as shown in figure 7.30. The edge of the block is located at $z = 0\,mm$ (see figure 7.31), which is identical to the position of the point source. Therefore, the photons emitted in this direction are almost completely absorbed by the object. The copper block is positioned at a distance of 15 mm with respect to the first converter layer. It is additionally grounded by connecting the block to the housing via a cable. The rest of the setup is identical to the one presented in chapter 7.3.2. A voltage combination of $\Delta U_y = 600\,V$ and $\Delta U_x = 0\,V$ is taken to provide an appropriate trigger rate and vertical electron drift.

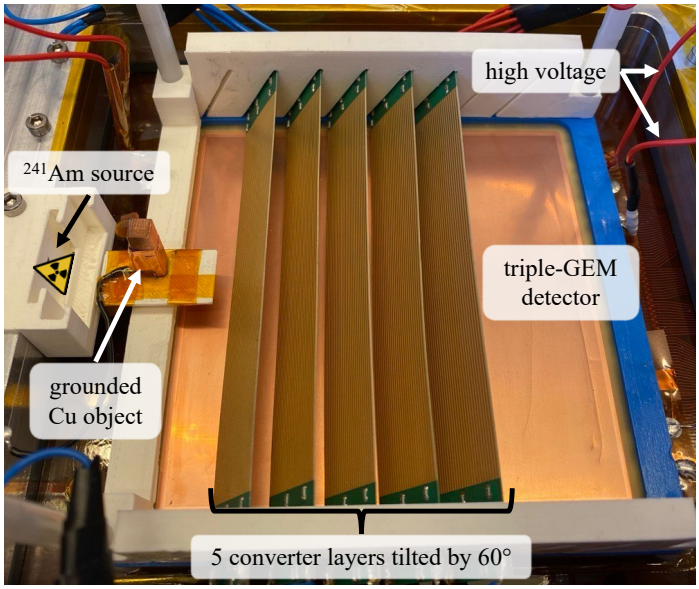

Figure 7.30: There are 5 converter layers tilted by 60° in the GEM detector. In addition, a grounded copper block with the size of $18 \times 5 \times 5 mm^3$ is positioned on a holder between the source and the first layer. The aim is to image this object.

The influence of the object on the hit distribution is investigated, which can be seen in figure 7.31 and in more detail for the second to fourth layer in figure 7.32. In the x-direction (see figure 7.33) the intensity decreases similarly to the setup without the object, while in the z-direction (see figure 7.34) fewer photons are detected in the region where the object is

located. For better comparison, the profile in the x-direction is shown in figure 7.33. Despite the first peak, the distribution looks similar.

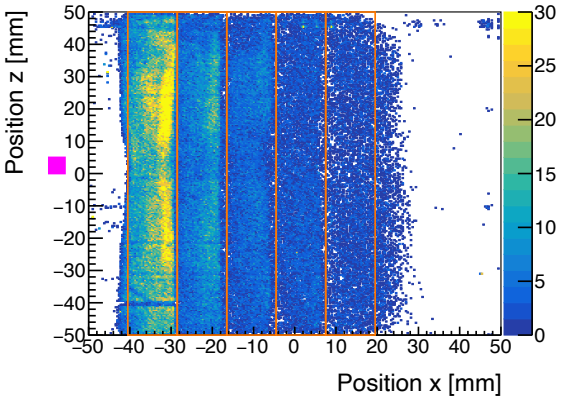

Figure 7.31: For $\Delta U_y = 600\,\mathrm{V}$ and $\Delta U_x = 0\,\mathrm{V}$, the measured hit distribution with the copper object, whose position is indicated by the pink box. As without the object, the intensity in the x-direction decreases with greater distance from the source. The position of the block is clearly visible in x- and z-dimension, since less entries are detected in this area.

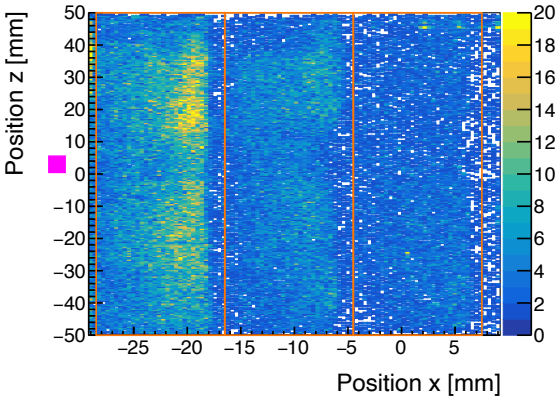

Figure 7.32: Focus on the second to fourth layer of figure 7.31 with an adapted maximum value on the color axis for better visualization. The position of the copper block is indicated by the pink box. Although the layers are at a greater distance from the object, the object is clearly visible in the hit distribution. The drop in the z-dimension is broader than for the first layer.

The grounded copper object close to the first converter layer influences the electric field, resulting in a narrower peak. This result shows how the grounded surroundings influence the electric field and thus the electron drift. As discussed in chapter 7.2.5, this can lead to deviations in the hit distribution between simulation and measurement, as not all components of the detector are included in the simulation. The effects are most pronounced closest to these non-simulated materials. Therefore, especially the first converter layer is influenced.

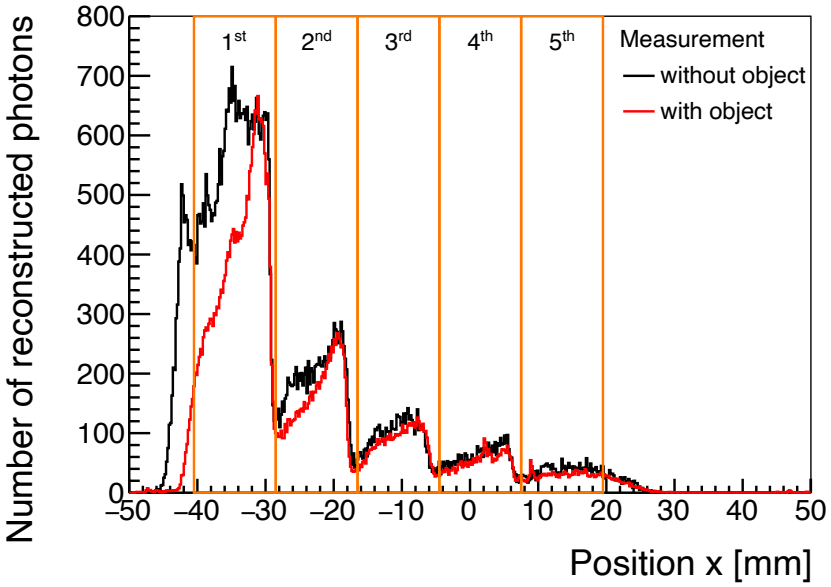

Figure 7.33: Profile of the x-dimension of the hit distribution from figure 7.31 (with object) is compared to one without object: The grounded copper object influences the shape of the first peak, which becomes narrower. The shape of the other peaks does not change.

The z-profile is shown in figure 7.34. Compared to the profile without the object the object leads to a dip. This dip is wider than the object itself and does not lead to a sharp 5 mm wide decrease. The photons are emitted in 4π and thus the object is showing a broadening in z-direction with increasing x-position. In addition the intensity decreases with x-position, resulting in the contrast decreasing simultaneously (see figure 7.31). For this reason, there is an overall decrease between approximately $-30\,\text{mm} < z < 25\,\text{mm}$, but with a minimum in the area of the object. When performing a position reconstruction, these effects have to be considered.
In addition, a more distinct edge is expected at $z = 0\,\text{mm}$. A slight misalignment of the source and block object can cause this behavior, when the point source is placed completely behind the block. Although the absorption of 59.5 keV photons in 5 mm copper is more than 99 % [Berger et al., 2010], events are detected in this region. After the extraction of the electrons from the copper strips, they have to be guided downwards. This drift causes a deviation of the z-position and therefore electrons are detected in the region of the object. But the deviation in the drift is typically smaller and therefore it does not solely explain the effect (see chapter 8.8.2).
While for $z > 25\,\text{mm}$ in figure 7.34 both measurements show good agreement, for $z - 30\,\text{mm}$ they differ. This deviation can occur due to variations in the source position. To place and remove the source from the mount, the gap is slightly larger than the source causing a shifts in the position ($\mathcal{O}(\Delta z_{\text{source}}) = 2\,\text{mm}$). Moreover, there is an additional mount installed in the detector for placing the object (see figure 7.30). As discussed above, those additional objects can influence the measurement results. These effects lead to the observed discrepancies.

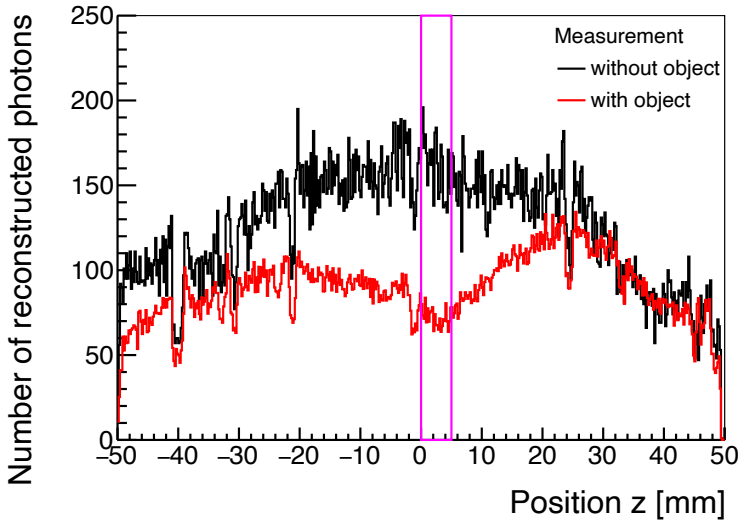

Figure 7.34: Profile of the z-dimension of the hit distribution from figure 7.31 (with object) is compared to one without object: In the area where the object is located (pink box), fewer photons are reconstructed. This dip is wider than the object itself and particles are still detected in this region although the absorption of 59.5 keV photons is more than 99 % in 5 mm copper. Both are measured at the same voltages and are normalized to the same measurement time.

The block object leaves a signature in the hit distribution, which can be used for a position reconstruction attempt.

7.4.2 Simulation: Accuracy of Position Reconstruction Method

Due to the previous good agreement of the simulation and measurement, the simulation is used for the imaging measurement to obtain information about the y-position. The first step in this process is to determine the achievable accuracy of the reconstruction method, regarding this y-position.
Therefore, all detected events with x-positions that agree within 200 µm are grouped together in the simulation. For all events in such a group, the maximum deviation from the corresponding initial electron y-positions is shown in figure 7.35. It extends up to 20 mm, which corresponds to the complete layer height and is therefore too large for a unique reconstruction process. Similar detected x-positions are associated with very different initial y-positions, as shown in figure 7.36.

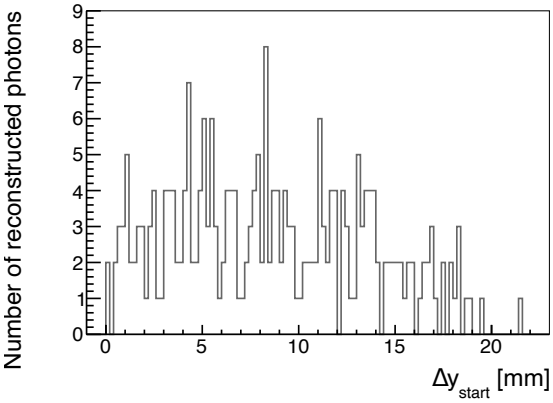

Figure 7.35: In the simulation, the deviation in the initial y-position is determined for all events whose x-positions coincide within 200 µm. It reaches up to 20 mm, which causes an inaccurate position reconstruction.

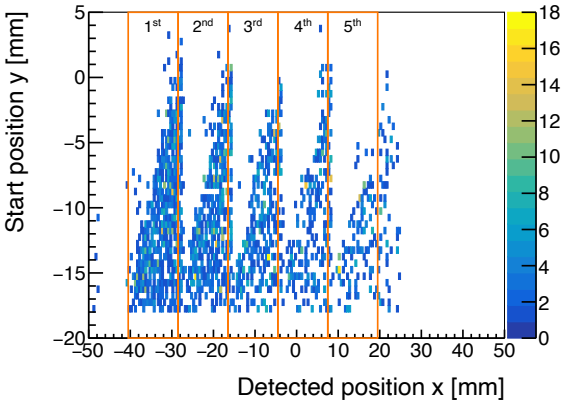

Figure 7.36: Despite the vertical electron drift achieved for $\Delta U_x = 0$ V, different initial y-positions (range: 20 000 µm) belong to similar detected x-values (range: 200 µm). Independent of the starting y-value, the identical x-position is detected. This is most pronounced for $x = -30$ mm, where the y-starting positions are in the range of −17 mm to 3 mm.

Thus, despite a perpendicular drift, which occurs according to figure 7.23 for the investigated voltage combination of $\Delta U_y = 600$ V and $\Delta U_x = 0$ V, an exact y-position reconstruction is not possible with the methods introduced so far. According to the simulation results, many electrons are created directly in the gas and not emerging from the copper strips. This behavior is in contrast to the previous assumption of the occurring interaction processes in the converter layers. Thus, either a large number of photons interact in the gas or there is another effect responsible for the observed behavior.

The introduction of an object into the detector leads to an expected change in the hit distribution, which is the first step for position reconstruction. However, before proceeding with the position reconstruction procedure, the underlying physical effects leading to the high photon conversion in the gas and the resulting large fluctuation of the initial y-position have to be understood. This is a main part of the next chapter, where the final results and their influence on the position reconstruction are discussed in chapter 8.8.

7.5 Summary on the 3D Position Reconstruction

Various applications of the converter layers require a complete 3D position reconstruction of the interaction point of the X-rays. While the x- and z-position are provided by the readout anode, the y-position is determined by adapting the converter layer setup. The layers are tilted by 60° with respect to the GEM foil. Two reconstruction approaches are investigated. The first one is a geometrical approach requiring a perpendicular electron drift. For the second method a good agreement between simulation and measurement as well as a distinct electron drift is mandatory. This would allow using the simulation to extract the y-position for each detected x-position.
As a proof of concept for the working principle of the tilted converter layers, the behavior of a single layer is investigated. It provides a good agreement between simulation and measurement regarding the hit distribution for various ΔU_x and ΔU_y combinations, including peak position and width. The electron drift for different electric field configurations is simulated, indicating two main challenges: Due to the electric field many electrons are guided upwards or are absorbed by the converter layer, resulting in a low trigger rate. But for voltage combinations with higher trigger rate, no perpendicular electron drift is achieved, resulting in deviations of the reconstructed y-position.
To achieve a higher trigger rate and perpendicular drift, multiple tilted converter layers are incorporated in the detector. For $\Delta U_\mathrm{x} = 0\,\mathrm{V}$ and $\Delta U_\mathrm{y} = 600\,\mathrm{V}$ the electrons are guided downwards perpendicularly according to the simulation and the trigger rate is 4 times higher than for a single layer setup. For higher ΔU_x the trigger rate increases further, but no vertical or unique electron drift is given, thus $\Delta U_\mathrm{x} = 0\,\mathrm{V}$ is used for subsequent studies. With this setup an imaging measurement is performed, where a copper block is placed between the source and the converter layers. The projection of this object is measured, providing a promising results in 2D. There is also a good agreement between simulation and measurement for multiple converter layers. Thus, for accessing information about the y-position the simulation is used. It shows, that for similar detected x-positions the initial electron y-positions vary by 20 mm. This deviation prevents an accurate position reconstruction and has to be understood.
There are remaining unsolved deviations: The number of electrons extracted from copper in backward direction is higher than expected by theory and the large range of y-values for the same x-position is limiting the 3D position reconstruction. Since simulation and measurement show good agreement, the physical processes leading to these effects can be investigated.

Chapter 8

Material Optimization for High Photon Detection Efficiency

After introducing the main purpose of converter layers, demonstrating their working principle and introducing a simulation procedure to verify the measurement results in chapter 5, further improvement of photon detection efficiency is required, which is the aim of this chapter. The photon conversion probability is strongly dependent on the material and its thickness. Therefore, both parameters are examined in more detail here. For this purpose, different types of converter layers and their effects on the detector performance are investigated, including a detailed analysis of the results through simulation.

8.1 Simulation: Motivation

The basic idea of this material optimization process is to find a converter layer composition that maximizes the number of electrons produced and extracted and thus the photon conversion probability. These two parameters are influenced by the material and its thickness.

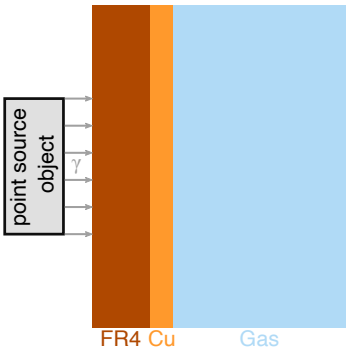

Figure 8.1: To motivate the process of material optimization, a Geant4 simulation is performed. A PCB consisting of a layer of 1550 µm FR4 and a single layer of 35 µm copper, without strip structure, is irradiated with 59.5 keV photons. Next to the copper layer is a gaseous volume.

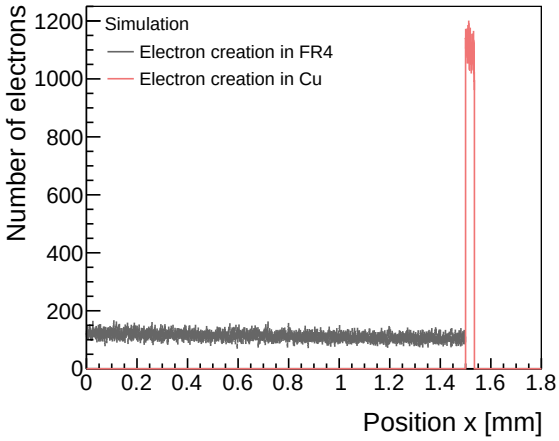

Figure 8.2: The number of electrons created in FR4 and Cu is simulated. In both materials, electrons are produced homogeneously over the entire material thickness. Since Cu has a higher-Z compared to FR4, the number of electrons created per path length is higher. 20 % of all electrons are produced in Cu and 80 % in FR4.

In order to motivate and understand these influences of material and thickness on the conversion probability in more detail, a Geant4 simulation is carried out.
The simulation setup is shown in figure 8.1, where a FR4 layer is completely covered with copper on one side. A gas volume is located next to the copper layer. Thus, the simulation setup approximates the converter layer in a gaseous detector. It is irradiated with 59.5 keV photons. Figure 8.2 shows the x-position of these electrons in the different materials. The electrons are produced homogeneously in the material. Since copper is a high-Z material compared to FR4[1], the electron production density is much higher (see equation 2.7).
Although many electrons are generated in both materials, these electrons have a limited range in the material and therefore not all of them are extracted, reducing the conversion efficiency. This average range of charged particles in a certain medium is described by the Continuous Slowing Down Approximation (CSDA) [Carron, 2006]. For a first estimation, the CSDA range of an electron in copper is calculated: After the interaction of the 59.5 keV photons with copper, the resulting electron has an energy of 50.5 keV due to the dominant interaction of the photons with the electrons in the K-shell [Berger et al., 2010] of the atom, which have a binding energy of 9.0 keV [Bearden, 1967]. According to [Berger et al., 2017], 50.5 keV electrons have a CSDA range of $6.95 \times 10^{-3}\,\mathrm{g\,cm^{-2}}$. With the density of copper $\rho_{\mathrm{Cu}} = 8.96\,\mathrm{g\,cm^{-3}}$, the final range of the electron x_{CSDA} in copper is calculated as:

$$\begin{aligned} x_{\mathrm{CSDA}} &= \frac{6.95 \times 10^{-3}\,\mathrm{g\,cm^{-2}}}{8.96\,\mathrm{g\,cm^{-3}}} \\ &= 0.78 \times 10^{-3}\,\mathrm{cm} \\ &= 7.8\,\mu\mathrm{m} \end{aligned} \tag{8.1}$$

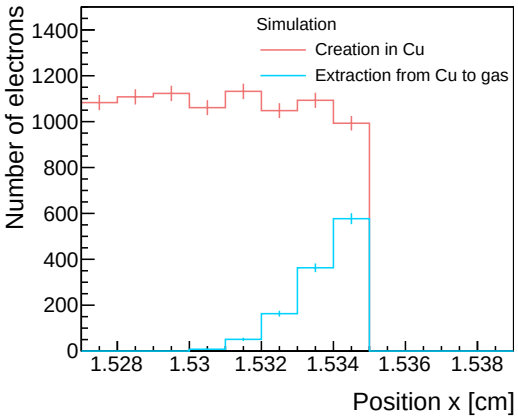

Figure 8.3: Due to the limited range of electrons in the material, only those produced close to the gas-copper interface are extracted. In the simulation electrons created within the last 5 µm up to the copper-gas interface have the possibility of extraction and thus detection. None of the electrons produced in FR4 reach the gas.

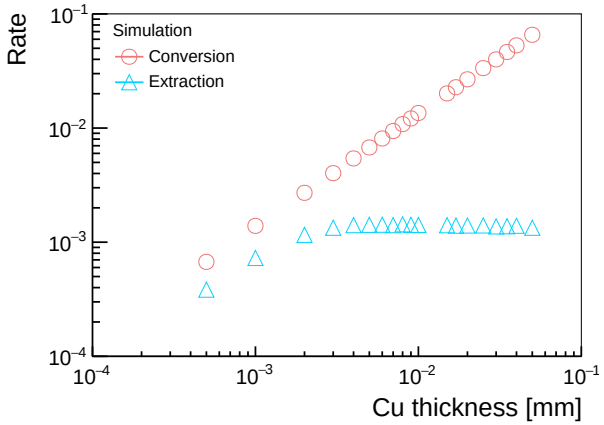

Figure 8.4: In the simulation, the thickness of the copper layer is varied. While the rate of created electrons increases with a higher thickness, the extraction rate begins to saturate at a thickness of 5–6 µm. If the copper layer exceeds the thickness of 6 µm, electrons that are not created near the edge are not detectable. To avoid this, the thickness of the materials has to be optimized.

The corresponding simulation result is shown in figure 8.3, verifying the calculation. The electrons generated in FR4 are either absorbed directly or enter the copper and are absorbed

[1] FR4 consists mainly of C, H, Si and O, but also contains a small amount of Br. More information is provided in chapter 8.2.4.

there due to their limited range. None of these electrons reach the gas. In the copper layer 38.5×10^3 electrons are created, while only about 1250 are extracted. This corresponds to 3 %, which agrees with the calculated value in chapter 5.8. Only electrons that are created within the last 5 µm in copper have the possibility to reach the gas. This result is consistent with figure 8.4, showing a saturation of the copper extraction rate at a thickness of 5 µm. Compared to equation 8.1, there is a deviation of 2.8 µm between simulation and calculation. While in the simulation the transition between copper and gas is taken into account where additional energy is needed[2], it is not considered in the calculation.
Although a higher photon interaction is achieved with increasing copper thickness (see figure 8.4), the majority of the electrons is not detectable as they do not reach the gas. Thus, these simulation results demonstrate the importance of adjusting the layer thickness as part of material optimization in order to maximize the number of extracted electrons and minimize the number of absorbed and thus undetectable photons.

8.2 Material Compositions and Dimensions of the Converter Layer Types

8.2.1 Overview

For a further increase of the photon detection efficiency compared to chapter 5, various converter layer types are investigated. These converter layers are PCBs with the same design as shown in figure 5.3, with varying material thicknesses. Two types of insulating materials are tested. Layers with an insulator thickness of 1520 µm and 250 µm are rigid PCBs made of FR4. Thinner converter layers are flexible PCBs consisting of PI as carrier material.
In total, 6 different layer types are studied, which are industrially available. An overview of all these layers including their composition and dimensions is given in Table 8.1. The labeling of the layers used in the following refers to the thickness of the insulating material and the thickness of the strip. For example refers the label 1520 + 41 to a converter layer with a carrier material thickness of 1520 µm and 41 µm thick strips on each side.

Naming	d_{total}	d_{in}	Insulating material	d_{strip}	d_{Cu}	d_{Ni}	d_{Au}	ϵ_{r}
1520 + 41	1600	1520	FR4	41	35	6	0.05	4.6
250 + 33	320	250	FR4	33	30	3	0.05	4.6
100 + 38	170	100	PI	38	35	3	0.05	3.4
100 + 18	140	100	PI	18	15	3	0.05	3.4
50 + 38	120	50	PI	38	35	3	0.05	3.4
50 + 18	90	50	PI	18	15	3	0.05	3.4

Table 8.1: Overview of the dimensions of the various components of the converter layer types investigated in this chapter. All thicknesses d_{x}, where x represents the different components, are given in µm.
The converter layers consist of an insulating material (d_{in}) made of FR4 or PI. Each side of the insulating material is covered with strips (d_{strip}), consisting of copper (d_{Cu}) and are covered with a protection layer of nickel (d_{Ni}) and gold (d_{Au}). These values refer to the strips on one side. The permittivity value ϵ_{r} is extracted from [Multi Circuit Boards, 2021] and the total thickness d_{total} is measured with a digital caliper. These quantities are implemented in the simulation of the converter layer.

The knowledge of the exact dimensions and material compositions is essential to simulate the

[2] To extract an electron from a metal a minimum energy is required, which is defined as work function [Yoshitake, 2020]. For copper the work function is 4.7 eV [Kumar et al., 2014].

photon interaction in the converter layers using Geant4.

8.2.2 Strip Composition

The strips are made of copper coated with Electroless Nickel Immersion Gold (ENIG). This is a protective layer that prevents the oxidation of copper. According to [Multi Circuit Boards, 2024b], ENIG consists of at least 3–6 µm nickel with an additional layer of at least 0.05 µm gold, as shown in figure 8.5. In addition, ENIG provides a very planar PCB surface and is well suited for SMD components.

Figure 8.5: Sketch (not to scale) of a strip on the insulator made of either FR4 or PI. The strip consists of copper coated with nickel and a layer of gold. In the simulation, the ENIG coverage is approximated by neglecting the side areas and only covering the top surface area. Design information extracted from [Multi Circuit Boards, 2024a].

As the thickness of the protection layer is only specified within a certain range, this can lead to uncertainties. It is assumed that all layers of the same type have the same nickel thickness on both sides. For example, if the nickel thickness is 6 µm instead of 3 µm per strip, for 5 layers this leads to a variation of $3\,\mu\text{m} \cdot 2 \cdot 5 = 30\,\mu\text{m}$ nickel. For $E_\gamma = 59.5\,\text{keV}$, in these 30 µm 4–5 % of all incident photons are absorbed. To minimize these uncertainties, the strip thickness of 4 different layer types is measured. The results are shown in figure 8.6 for one strip[3] per layer. Although PCBs have been ordered with either 18 µm or 35 µm thick copper strips covered with ENIG, meaning at least additional 3 µm nickel, the measurements provide a different result for certain layer types. The layer 1520 + 41 FR4 has a total strip thickness of 41 µm, indicating it consists of 35 µm copper and 6 µm nickel.
Instead, the layer 250 + 33 FR4 has a total strip thickness of 33 µm, which is smaller than the ordered 35 µm copper with additional ENIG. The thickness of copper probably varies due to the production process in the company. Since nickel has an atomic number of $Z = 28$, similar to copper ($Z = 29$), both materials provide very similar photon absorption properties. Therefore, it is assumed, that the strip consists of 3 µm nickel and the remaining strip thickness is made of copper.
This approximation is performed for the remaining layers and all considered strip values are listed in Table 8.1. In addition, a gold thickness of 0.05 µm is taken for all converter layers types. For the layers made of 50 µm insulating material, the same strip values are used as for the 100 µm layers.

[3] A total of 5 strips have been measured on each side for each layer type presented in figure 8.6. The same result is obtained for the single strip shown here.

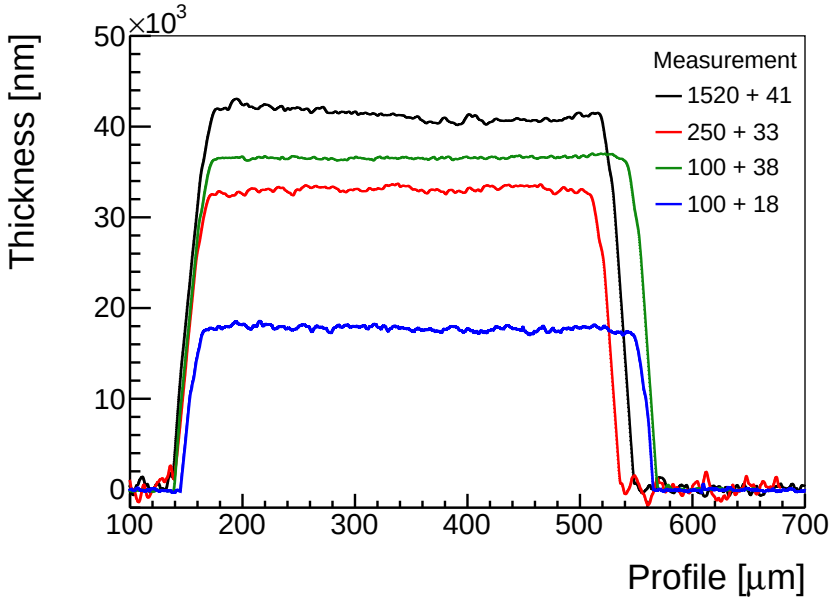

Figure 8.6: The strip profile of 4 different converter layer types is measured. All strips have an expected width of about 400 µm, but small deviations of 8 % are observed. The thicker strips (> 30 µm) should all have the same copper thickness of 35 µm and differences should only result from the ENIG coating. But these layers show variations of almost 8 µm, reaching from 33–41 µm. The strip thicknesses measured here are listed in Table 8.1 and implemented in the simulation. The measurements have been performed by Julius Kühne (internal communication) with a Dektak 150 Surface Profiler from Veeco.

8.2.3 Insulating Material: PI

The insulating material consists of either FR4 or PI. Those made from PI are flexible PCBs and, as the name implies, not as rigid as PCBs made of FR4. PI offers excellent performance regarding dielectric and mechanical properties [Qiu et al., 2020]. It is flexible, but also provides good mechanical durability as well as a low dielectric constant (see Table 8.1) and high insulation. Furthermore, PI is a homogeneous material with the chemical formula $C_{22}H_{10}O_5N_2$ and a density of $\rho = 1.42\,\mathrm{g\,cm^{-3}}$ [NIST, 2024]. As presented in Table 8.1, 4 converter layer types are made of PI[4] with a thickness of either 100 µm or 50 µm.

8.2.4 Insulating Material: FR4

FR4 is a more complex material having a varying substructure, as shown in figure 8.7. It is made of several layers of woven glass fibers embedded in epoxy resin [Goosey and Poole, 2004]. Typically, the epoxy resin contains bromine[5] to improve the flame retardancy of FR4. Similar to PI it offers good mechanical properties in terms of durability, mechanical support and very good insulation properties.

According to [Multi Circuit Boards, 2024c], the standard FR4 layer ordered is called Duraver DE104 and manufactured by the company ISOLA (see [ISOLA, 2024]). The 250 µm

[4] The same thickness of insulating material made of FR4 instead of PI is not industrially available at the company.

[5] Bromine is a halogen. Since halogens have a negative impact on the environment and health, halogen-free FR4 is part of current research [Choate, n.d.]. Halogen-free PCBs are already industrially available. The layers used here are not halogen-free.

FR4 layer is made of 2 glass fiber layers (glass type 1652), while the 1520 µm FR4 layer consists of 8 layers (glass type 7628), as shown in figure 8.7.
There are different types of glass fabrics (see [ISOLA, 2023]), which differ, for example, in their thickness, warp and weft count and their general glass yarn dimensions such as width and pitch. For the glass type 1652 (in layer 250 + 33 FR4), the latter dimensions are shown in figure 8.8. One layer of this glass fiber fabric has a thickness of 114 µm.
In addition, the chemical composition[6] of the glass yarn is provided by [ISOLA, 2022]: 54 % SiO_2, 22 % CaO, 14 % Al_2O_3, 7 % B_2O_3, 2 % MgO and 1 % Na_2O.

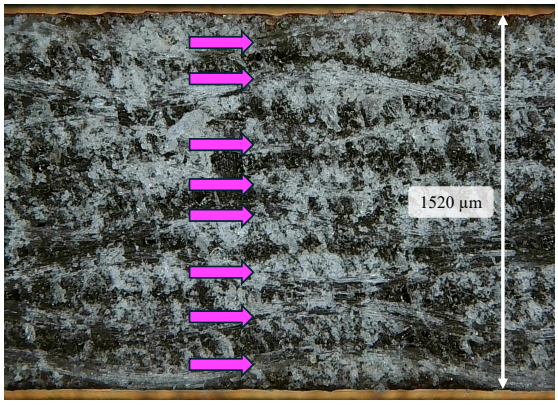

Figure 8.7: 1520 + 41 FR4 layer: Picture of the side view of one layer, consisting of 8 woven glass fiber cloth layers, indicated by the pink arrows. This number corresponds to the information provided by [ISOLA, 2024].

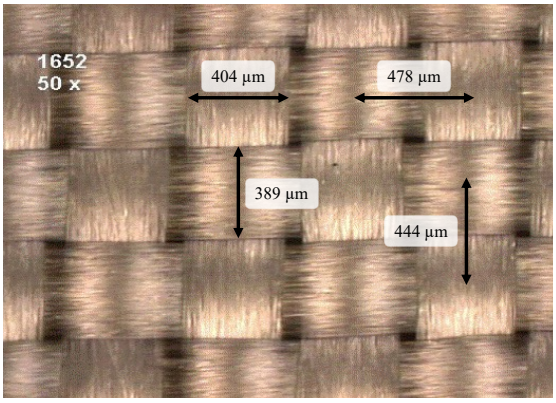

Figure 8.8: 250 + 33 FR4 layer: Top view of one woven glass fiber cloth layer in the glass style 1652. The different tensions of the fibers in both directions result in varying values for width and pitch. Figure and values taken from [ISOLA, 2023] (edited).

To implement this woven glass fabric in Geant4, it is modeled using a Computer Aided Design (CAD) software [Autodesk, Inc., 2021]. One unit cell of the fabric is shown in figure 8.9.

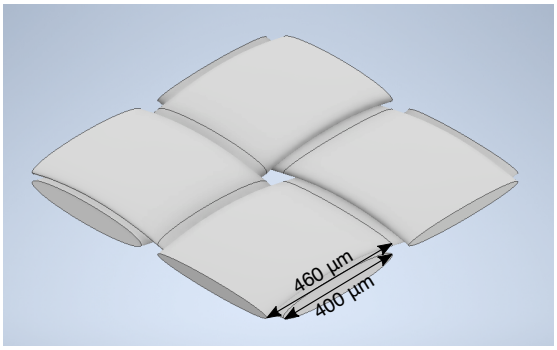

Figure 8.9: 250 + 33 FR4 layer: A unit cell is created for the woven fiberglass cloth of type 1652 using a CAD software. This cell is implemented in Geant4 and periodically extended to achieve an entire glass cloth layer. Although in reality the glass yarns have different values in both dimensions (see figure 8.8), both are approximated with the same width of 400 µm and pitch of 460 µm. It has a total thickness of 114 µm.

In the FR4 layer these glass fibers are embedded in brominated epoxy resin. Both, the 1520+41 FR4 layer and the 250+33 FR4 layer, have a resin content of 42 %. According to [Choate, n.d.]

[6] The composition is given within a certain range. These presented values lie within this range and are taken for the simulations performed in this chapter.

(information from ISOLA), brominated epoxy resin is a mixture of Tetrabromobisphenol-A (TBBA), which has the chemical composition $C_{15}H_{12}Br_4O_2$, and Bisphenol A Diglycidyl Ether (BADGE) with the chemical formula $C_{21}H_{24}O_4$. During polymerization, both components do not typically react in the ratio 1 : 1 [Mumby, 1989]. In [Mackenzie and Kopinke, 1996], a weight fraction of 7.4 % for bromide in the FR4 layer Duraver DE104 is reported and confirmed by ISOLA. Therefore, the ratio of TBBA and BADGE is adjusted such that it approximates this weight fraction as closely as possible. This results in a ratio of 1 : 4 with a Br weight fraction of 7.1 %. Brominated epoxy resin has a density of $1.2\,\mathrm{g\,cm^{-3}}$. $C_{99}H_{108}O_{18}Br_4$ is taken as the final composition of the brominated epoxy resin:

$$C_{15}H_{12}Br_4O_2 + 4\,C_{21}H_{24}O_4 \longrightarrow C_{99}H_{108}O_{18}Br_4$$

When using the layer type 250 + 33 FR4, the insulator consists of 250 µm brominated epoxy resin in which two glass fabrics layers are embedded, as introduced in figure 8.9. As shown in Appendix D, the simulation provides the same results for this converter layer design and the simpler approach of a 250 µm layer of 58 % glass fabric and 42 % brominated epoxy resin without any substructure. Consequently, the latter approach is applied to the 1520 + 41 FR4 converter layers, which have the same ratio of glass fabrics and brominated epoxy resin.
With the knowledge of all these variables, the composition of the converter layer is included in the simulation and verified by performing a photon absorption measurement, introduced in the next section.

8.3 Photon Absorption Measurement Using a High-Purity Germanium Detector

In order to verify the thicknesses and material composition of the various converter layer types from chapter 8.2, a photon absorption measurement with a High Purity Germanium (HPGe) detector is carried out and compared with simulation.

8.3.1 Measurement and Simulation Setup

The setup for the photon absorption measurement is shown in figure 8.10. The ^{241}Am source is placed at a distance of 65 mm to a germanium detector (see Appendix E). This detector is capable of detecting photons with high efficiency and very good energy resolution. The absorption behavior is investigated by inserting layers between source and detector.
The detector provides the energy spectrum shown in figure 8.11 for the photon peak of 59.5 keV. By inserting the 1520 + 41 FR4 layers, the intensity of this peak decreases. The ratio of the integral of the peaks is a measure of the absorption.

To simulate this measurement setup and underlying physical processes, a Geant4 simulation is performed. The simulated point source emits photons with an energy of 59.5 keV in 4π and the germanium is approximated by a counting volume that provides the number of all transmitted photons. For the simulation of the converter layers the quantities introduced in Table 8.1 are taken with the corresponding PI and FR4 compositions from chapter 8.2.3 and chapter 8.2.4, respectively. In addition, the same dimensions and distances are taken as for the measurement.

By determining the absorption properties of different converter layer types in simulation and measurement, the material thickness and composition approximations are verified.

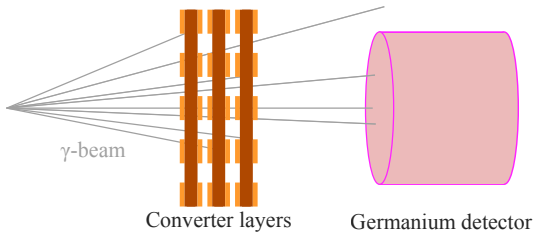

Figure 8.10: Sketch of the measurement setup (not to scale): The ^{241}Am source emits photons with an energy of 59.5 keV, which are detected by a germanium detector. By inserting the converter layers between the source and detector, their absorption properties are analysed. The distance between the source and the layers is about 5 mm and between the layers and the detector about 60 mm.

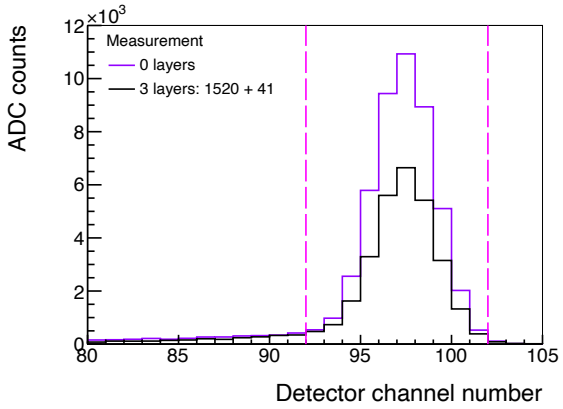

Figure 8.11: Each detector channel number is associated with a specific particle energy. Here, the measured peak corresponds to the photon energy of 59.5 keV. By inserting the 3 layers, the intensity decreases due to the absorption inside the layers. The pink-colored lines indicate the interval used to define the peak integral and the corresponding absorption.

8.3.2 Photon Absorption in Copper

The two 100 µm PI layer types are arranged between the source and the HPGe detector, as shown in figure 8.10. The number of layers is varied. Both layer types differ only in the assumed copper thickness of 15 µm and 35 µm. The measurement and simulation results are summarized in figure 8.12. As expected from equation 2.2, the intensity decreases exponentially with a higher number of converter layers.
Simulation and measurement show good agreement. Both layer types exhibit a deviation of 8 % in absorption when 3 layers are inserted. To understand this difference between the layer types, the measured and simulated values are compared with calculation: Since both layers are made of the same insulating material and the same thicknesses are assumed for nickel and gold, the different absorption properties result from the different copper thickness, which is 20 µm per strip (see Table 8.1). A total of 3 layers (·3) are inserted. Each layer is double-sided (·2), but only half of it is covered with strips ($\cdot\frac{1}{2}$). This corresponds to an additional $20\,\mu\text{m} \cdot 3 \cdot 2 \cdot \frac{1}{2} = 60\,\mu\text{m}$ copper for 3 layers of the type 100 + 38 PI. In this 60 µm copper, the photon absorption is 8 %[7], which is consistent with simulations and measurements and demonstrates that the difference between the two converter layer types arises from the different copper thicknesses.
According to the calculation principle introduced above, the total absorption in the strips is calculated for 3 layers of the type 100 + 38 PI. It is assumed that nickel has the same absorption properties as copper. This results in a total strip thickness of $38\,\mu\text{m} \cdot 3 \cdot 2 \cdot \frac{1}{2} = 114\,\mu\text{m}$ and an absorption of 15 %. If this calculated value is compared with the results in figure 8.12, it corresponds to the total absorption. This implies, that in the converter layer types consisting of PI as insulating material the entire photon absorption occurs in the strips and is negligible in PI.

Calculation, simulation and measurement show a good coincidence, which proves the appropriate material compositions and thicknesses of these converter layer types.

[7] For the calculation data from [Berger et al., 2010] is used.

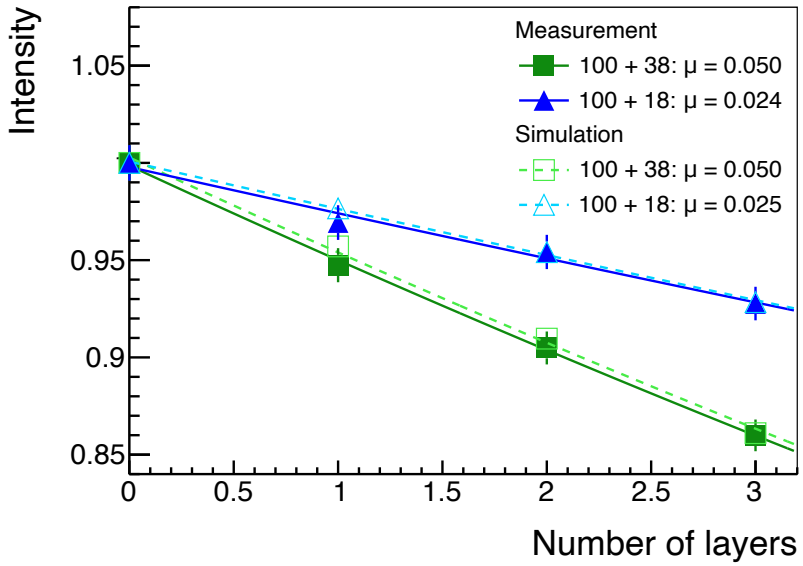

Figure 8.12: The absorption in the two 100 µm thick PI layers for different strip thicknesses is investigated using simulation and measurement. Following equation 2.2, an exponential function[8]is fit to the measured and simulated data points. The slope value μ is extracted. It characterizes the absorption behavior per converter layer. The fit provides an error of $\Delta\mu_{\text{meas}} = 0.004$ for the measurement and $\Delta\mu_{\text{sim}} = 0.001$ for the simulation. Simulation and measurement show good agreement.

8.3.3 Photon Absorption in FR4 and Polyimid

The absorption properties of both converter layer types made of FR4 can be seen in figure 8.13.

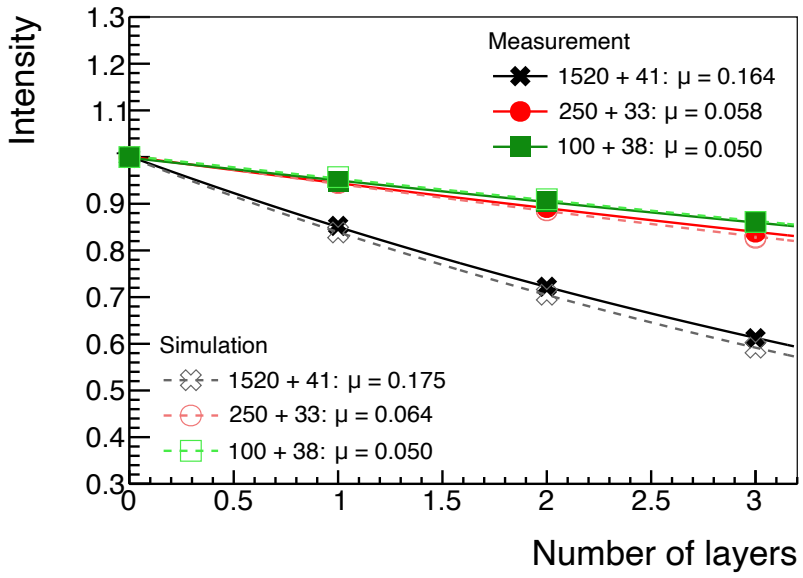

Figure 8.13: In order to characterize the absorption behavior of the different insulating materials, the two FR4 layer types and a PI layer type are compared. As introduced in figure 8.12, an exponential function is fit to the data, providing the slope μ for the various converter layers. In addition, the fitting errors of $\Delta\mu_{\text{meas}} = 0.004$ for the measurement and $\Delta\mu_{\text{sim}} = 0.001$ for the simulation are given. The FR4 layers show a slight deviation between simulation and measurement, within the error interval. Simulation and measurement show good agreement.

[8] The exponential decrease is described by the formula $\exp(-\mu x)$, where x is the number of layers and μ is the attenuation coefficient per converter layer (see chapter 2.2).

The dimensions from Table 8.1 and material composition for FR4 from chapter 8.2.4 are used. For comparison, the previous results of the 100 + 38 PI layer are added.
The deviations for FR4 are slightly larger than for PI, mainly due to the more complex structure and the resulting discrepancies in the assumed material. Nevertheless, simulation and measurement show good agreement. When comparing 3 layers of the different types, the 100 + 38 PI absorb about 14 % and 250 + 33 FR4 about 17 %. Therefore, these two types show a similar photon absorption behavior. The absorption in the 1520 + 41 FR4 layers is higher with around 40 %. These layers have approximately the same strip thickness as the 100 + 38 PI layers, so according to the calculation in chapter 8.3.2, 15 % is absorbed by the strips and the other 25 % by the 1520 µm thick FR4 layer. Since half of the insulating layer is covered with copper strips, at least half of the electrons produced in FR4 are absorbed by the copper strips (see chapter 8.1) and are therefore not detectable, resulting in a low detection efficiency. The influence of the material on the detection probability is analyzed later in this chapter.
A correct and verified description of the converter layers in terms of material composition and thickness has been found and implemented in Geant4 for further application in the simulations.

8.3.4 Simulated Photon Absorption and Interaction Processes in Different Converter Layer Components

Figure 8.14 shows the simulated contributions of the different materials to photon absorption for 3 layers. A distinction is made between the 4 components of the layer: FR4 or PI, copper, nickel and gold. The absorption in gold is 0.1 % and is therefore negligible. The two layers made of 100 µm PI differ in the strip thickness (38 µm and 18 µm). This deviation in the copper thickness causes the different absorption properties of the two layer types, as can be expected from chapter 8.3.2. Copper is responsible for the main absorption, while only 0.7 % is absorbed in PI. The contribution of PI is therefore negligible.

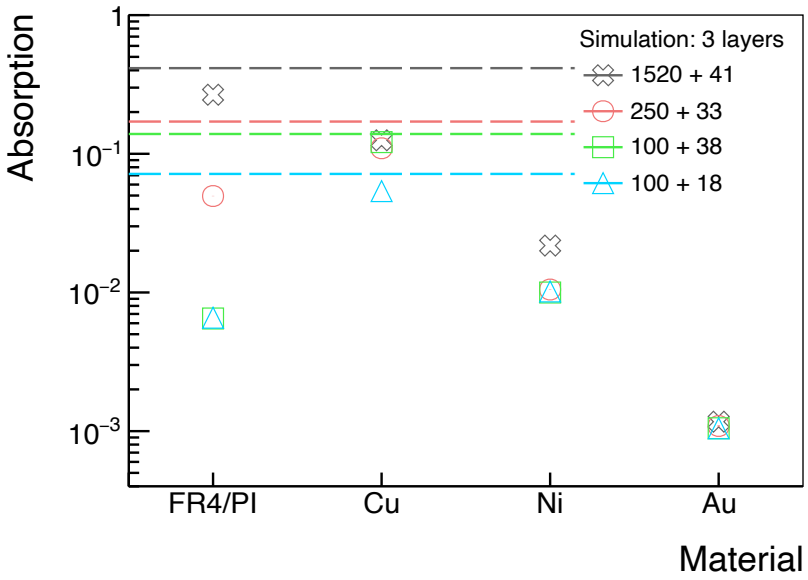

Figure 8.14: The simulation provides information about the absorption contribution of the various materials. The absorption in 3 consecutively placed layers is considered. Their total absorption is indicated by the dashed horizontal lines. For the 100 µm thick PI layers, the main absorption occurs in copper. The difference in absorption is more pronounced in the insulating material, due to the stronger variation in thickness. While for the 250 + 33 FR4 layers the main contribution of absorption arises from copper, for 1520 + 41 FR4 the insulating layer contributes with about 25 %. The absorption in gold is negligible.

The comparison of the two layer types made of FR4 with the 100 + 38 PI layer shows that FR4 absorbs a factor of 7 more for 250 + 33 FR4 and about 40 times more for 1520 + 41 FR4. This significantly stronger absorption behavior in 1520 µm FR4 is the main reason for the observed difference compared to the 100 + 38 PI layer in figure 8.13. Only considering the insulating layer, 250 µm FR4 absorbs more than 100 µm PI. This difference between both types is not as pronounced in the complete absorption, as it is compensated by the thicker strips of the 100 + 38 PI layer.

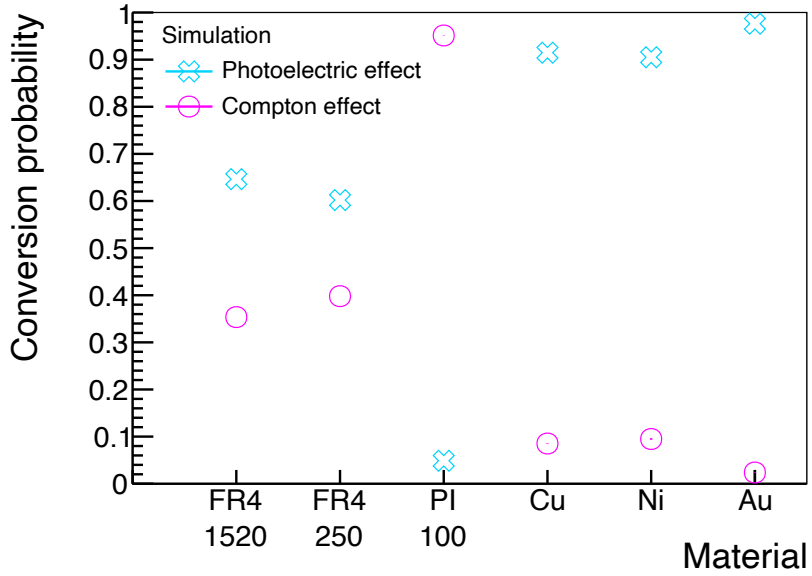

Figure 8.15: Depending on the material, the photoelectric effect or Compton scattering occur to varying degrees. While the photoelectric effect dominates for copper, nickel and gold, the Compton effect mainly occurs for PI. In FR4, the photoelectric effect is about 20–30 % more likely than the Compton effect. In each material the sum of the occurring processes add up to 1.

In addition, the simulation provides information about the probability of the contributing processes (see figure 8.15). As expected from figure 2.1, for the photon energy of 59.5 keV the photoelectric effect dominates in copper, nickel and gold. For the insulating material, the Compton effect is more pronounced. In FR4, about 35–40 % of the photons interact via Compton scattering, while in PI it is over 95 %.
With the measurements and simulations, the material compositions and thicknesses of the different components of the converter layers are verified. In addition, the simulation provides a first estimate about the photon interaction processes and the absorption behavior of the various converter layer types.

8.4 Measurement: Influence of Various Converter Layer Types on GEM Detector Performance

8.4.1 Measurement Setup and Procedure

The influence of the different converter layer types (see Table 8.1) on the performance of the GEM detector is investigated. For each type, 5 layers are incorporated vertically in the detector as shown in figure 5.6. While the thick layers made of FR4 are simple to place due to their rigidity, the PI layers are more flexible and need to be stretched in order to be straight[9].

[9] The appropriate supports for this purpose have been developed in [Schneider, 2023].

To avoid the influence of environmental fluctuations on the measurement results, the detector is placed in a climate cabinet (see chapter 6.2) and is connected to a pressure stabilization system (see chapter 6.3). The charging-up effect of the GEM foil [Hauer et al., 2020] is another external parameter influencing the detector performance. This latter effect is resolved by waiting until the detector provides a stable trigger rate. Since these parameters strongly influence the measurements, it is important to control them in order to achieve independent and reproducible measurement results[10].

The 1520 + 41 FR4 layers from chapter 5 are remeasured with the pressure control system at a pressure of $p_2 = 1017\,\text{mbar}$. In order to obtain a comparable result to the measurement from chapter 5 ($p_1 = 962.5\,\text{mbar}$ and $\Delta U_{\text{GEM},1} = 280\,\text{V}$), the pressure-voltage calibration[11] according to equation 6.7 results in a GEM voltage of $\Delta U_{\text{GEM},2} = 286\,\text{V}$. This pressure-voltage calibration ensures that the same charge is deposited as in chapter 5. This is necessary because the operating point of the GEM (see chapter 5.5.3) and the settings of the readout electronics, in particular the threshold value (see chapter 4.2), have been adjusted in chapter 5 to this deposited charge. Since the pressure system does not always provide exactly the same pressure, a pressure-voltage calibration is carried out for each measurement. A summary of all values is given in Appendix C.

8.4.2 Hit Distribution

The profile of the hit distribution of all 6 layer types is shown in figure 8.16. As expected from chapter 5.5.1, peaks form between the vertical layers and the peak height decreases with $1/r^2$. This behavior is identical for all converter layer types. In addition, the peaks have the same width of 11 mm, which corresponds to the distance of two adjacent layers.

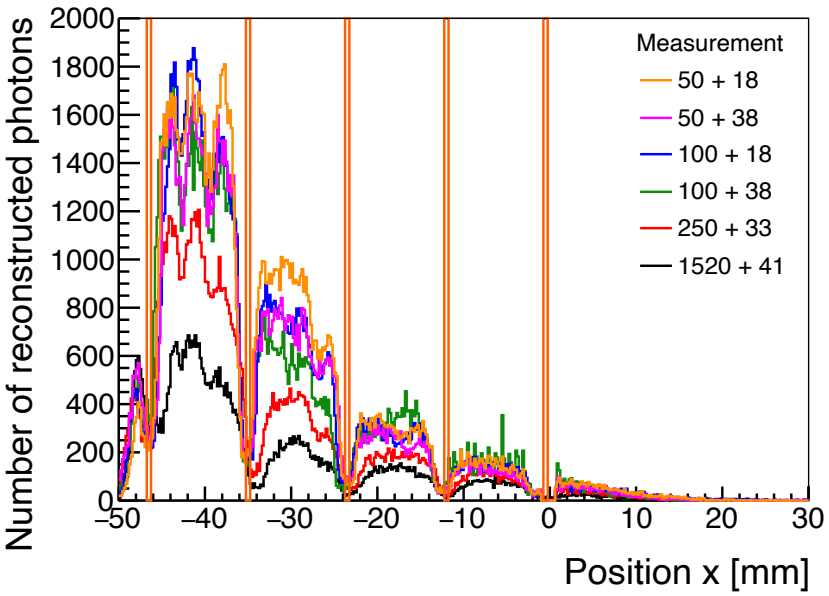

Figure 8.16: Between the layers (orange boxes) peaks are generated for all layer types that correspond in position and width. The first peak shows a substructure with 3 peaks, while for the second peak the first two sub-peaks merge. For the other peaks no substructure is observed. A voltage difference of $\Delta U_y = 600\,\text{V}$ is applied and all profiles are normalized to the same measurement time. The main difference between the layers is the peak integral, which is directly correlated to the detection efficiency. It is increased in the thinner PI layers compared to the FR4 layers.

[10] It should be noted here that the measurement results differ from those in [Schneider, 2023], which is most likely due to pressure fluctuations, since it has not been controlled there.

[11] The GEM voltages are adjusted in 0.5 V steps.

According to figure 5.26, most electron-clusters have an extension of 5 mm. As motivated in chapter 8.1, is is assumed that the primary electrons emerge from the copper strips. With the perpendicular electron drift for $\Delta U_x = 0\,V$ (see figure 5.28), asymmetric peaks with many entries close to the front side of each layer are expected. The first two peaks show a sub-structure with individual peaks. For some layers the third sub-peak close to the back side of the converter layer show a slight asymmetry in figure 8.16 with more hits close to the front side. Nevertheless, many electrons are detected close to the back side of the next layer. This behavior is similar to that observed in chapter 7.2.2, where more electrons are detected from the back side of the layer than expected.
In figure 8.16, the main difference between the converter layer types lies in the peak integral. Since all distributions for the layer types are normalized to the same measurement time, this parameter offers an indication of the photon detection efficiency. The 1520 + 41 FR4 layer exhibits the smallest peaks, followed by the layer types 250 + 33 FR4 and 100 + 38 PI. The remaining converter layers provide equal results within small deviations, showing the highest peaks and thus the highest detection efficiency.
Assuming photoelectric effect in copper, the detected electrons emerge from the last 5 µm (see figure 8.4) of the strips. Since for all layer types the strip thickness is larger, the main difference between the layer types should arise from their different absorption behavior. As expected from figure 8.13, the 1520 + 41 FR4 layers have a stronger absorption behavior than 250 + 33 FR4 or 100 + 38 PI and therefore the peak integrals in figure 8.16 are smaller. While the absorption for 1520 + 41 FR4 and 100 + 38 PI differs by about 10 % for one layer, the first peak in figure 8.16 differs by a factor of 2.3, which is higher than expected. Furthermore, the 250 + 33 FR4 and 100 + 38 PI layer types are not supposed to differ strongly in performance due to a similar strip thickness and a negligible absorption in the insulating material (see figure 8.13 and figure 8.14). But in figure 8.16 the first peak of these two layers varies by a factor of 1.4.
Based on the assumed working principle of the converter layers and the results from the photon absorption measurements (see chapter 8.3), a different behavior of the converter layers is observed when placing them in the GEM detector than expected. A stronger asymmetry of peaks between the layers in the hit distribution and a different behavior of the peak integrals of the various converter layer types is anticipated. These discrepancies are investigated and resolved in this chapter.
This measurement already demonstrates that the desired result is achieved with material optimization. By replacing the 1520 + 41 FR4 converter layers with thinner layers of PI instead of FR4 the photon detection efficiency increases.

8.4.3 Trigger Rate

For a better comparison of the photon detection efficiency for the converter layer types, the measured trigger rate is shown in figure 8.17 for different ΔU_y voltages. All data points are normalized to the converter layer 1520 + 41 FR4 at $\Delta U_y = 0\,V$. A similar curve shape is observed for all layers, beginning to saturate at ΔU_y = 600–700 V. As expected from the measured hit distribution (see figure 8.16), 1520 + 41 FR4 exhibits the lowest relative trigger rate. For $\Delta U_y = 0\,V$ the trigger rate is higher for 250+33 FR4 by a factor of 1.3, for 100+38 PI by a factor of 1.8 and for the other converter layers by a factor of 2, each with respect to the 1520 + 41 FR4 layers[12]. Although $\Delta U_y = 0\,V$ is applied, the electrons are guided downwards due to $\Delta U_{drift} = 100\,V$. The maximum trigger rate is obtained for the 50 + 18 PI converter

[12] It should be noted here that with a thinner insulating material and thinner strips, the converter layers lose their stiffness and a straight alignment in the detector becomes more challenging. The thinner the strips, or in general the converter layers, the higher the expected measurement uncertainties, which cannot be determined more precisely. This can lead to discrepancies for the thin layers.

layers. It is a factor of 2.8 higher compared to the 1520 + 41 FR4 layers at $\Delta U_y = 600\,\mathrm{V}$.

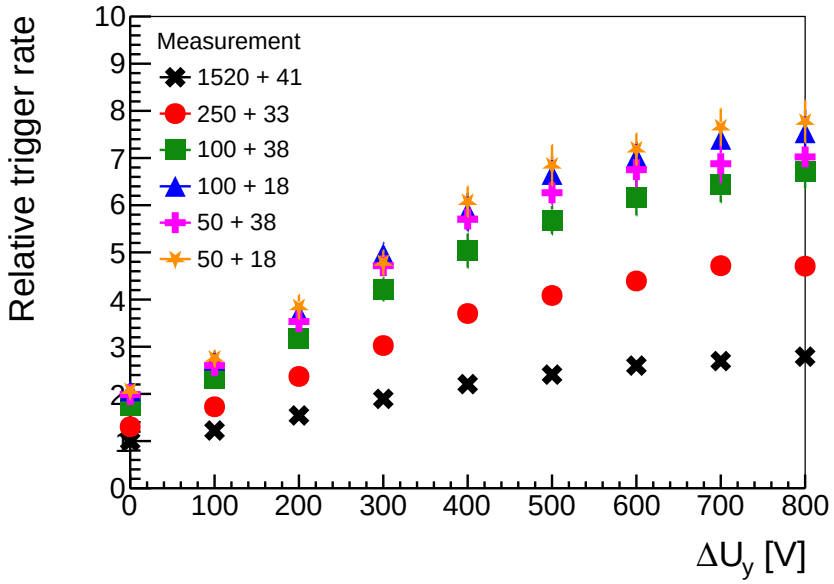

Figure 8.17: In the GEM detector, 5 converter layers of each type are inserted and a ΔU_y scan is performed. All values are normalized to the 1520 + 41 FR4 layer at $\Delta U_y = 0\,\mathrm{V}$. While the 1520 + 41 FR4 layers provide the lowest trigger rate, followed by the 250 + 33 FR4 layers, all layers made of PI show higher trigger rates. At $\Delta U_y = 600\,\mathrm{V}$, it is up to a factor of 2.8 higher than for the 1520 + 41 FR4 layers. Optimization of the converter layer types shows an increased trigger rate and thus a higher photon detection efficiency.

Based on figure 8.17, the relative trigger rate in figure 8.18 is normalized for each data point to the $\Delta U_y = 0\,\mathrm{V}$ value of the corresponding layer. This normalization of the relative trigger rate minimizes the influences of the different photon conversion probabilities in the various layer types. Thus, a better comparison of the efficiency of electron guiding between the layers is given. While the relative trigger rate for the 1520 + 41 FR4 layers increases by a factor of 2.6, all other layers exhibit an increase by a factor of 3.4. The 1520 + 41 FR4 layers exhibits a different guiding behavior, probably due to the greater thickness of the insulating material.

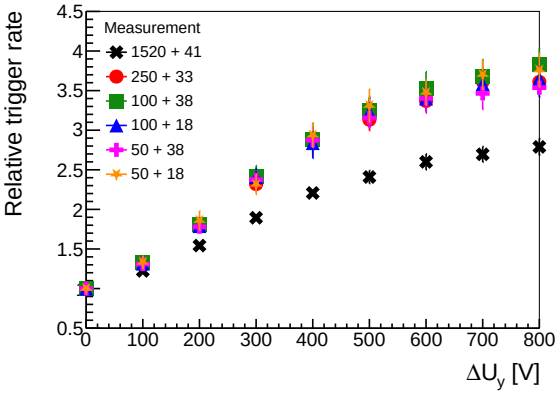

Figure 8.18: The measured relative trigger rate is normalized for each layer to their value at $\Delta U_y = 0\,\mathrm{V}$. Thus, the electron guidance by the electric field is comparable between the layer types. The increase in the relative trigger rate is lower for the 1520 + 41 FR4 layers than for the others.

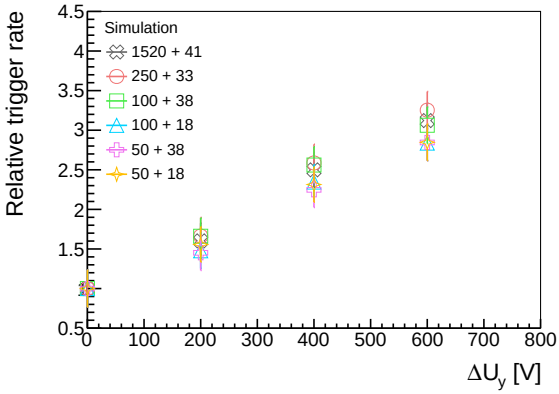

Figure 8.19: In the simulation the guiding efficiency for all layers is the same within the error interval. This behavior differs from the measurement in figure 8.18, where 1520 + 41 FR4 provides a smaller relative trigger compared to the other layers. In the simulation the relative trigger rate is about 0.7 lower for the thin layers.

The corresponding simulation results can be seen in figure 8.19. Here all values agree within their error interval, meaning all converter layer types have the same electron guiding efficiency in the simulation. Therefore, all electric fields simulated by ANSYS are identical and thus independent of the material thicknesses and properties of the different converter layers types. In addition, the simulated relative trigger rate is smaller than the measured one. These deviations in guiding efficiency between simulation and measurement have to be taken into account when comparing simulation and measurement results in course of this chapter.

8.4.4 Cluster Charge

The measured cluster charge is compared for the different converter layer types (see figure 8.20). The distribution forms a double-peak structure for all layers, which is pronounced to varying degrees. While for the 100 + 18 PI layer both peaks are clearly distinguishable, for the 100 + 38 PI layer the first peak is not that strongly pronounced. The rising and falling edge as well as the positions of the peaks agree within 10–15 % for all layers. Small pressure fluctuations or discrepancies in the applied voltage can cause the observed differences in the cluster charge[13].

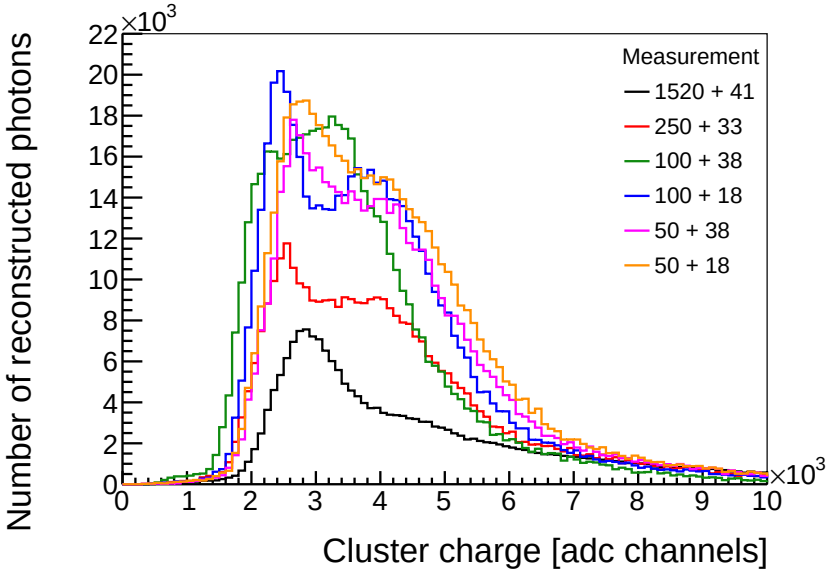

Figure 8.20: For all converter layer types the cluster charge distribution exhibits a double-peak structure. Within 10–15 %, the peak positions of the different layers agree[14]. Thus, the photons deposit the same amount of energy per interaction for all layer types, indicating that the same interactions occur in the same materials. Since all measurements are normalized to the same measurement time, the layer types influence the number of entries in the distribution and thus the conversion probability, while the double-peak shape is the same within the uncertainties. All measurements are performed with a voltage difference of $\Delta U_y = 600\,\mathrm{V}$.

[13] The maximum discrepancy between the first peak in figure 8.20 of the different converter layer types is about 400 adc channels. By using the results of chapter 5.5.2 and equation 3.2 this discrepancy is estimated. A discrepancy of 400 adc channels can occur, for example, if $\Delta U_{\mathrm{GEM}} = 285.6\,\mathrm{V}$ is used instead of $\Delta U_{\mathrm{GEM}} = 286.0\,\mathrm{V}$ or a pressure of $p = 1013.0\,\mathrm{mbar}$ instead of $p = 1017.0\,\mathrm{mbar}$. The fluctuations of the pressure system are around $\pm 1.5\,\mathrm{mbar}$. Due to the pressure-voltage calibration (see chapter 6), different GEM voltages (see Appendix C) have been applied, which are adjusted in 0.5 V steps. The combination of these experimental adjustments and fluctuations can lead to systematic uncertainties in the measured order of magnitude.

[14] Differences in the peak position of the 1520 + 41 FR4 layer compared to figure 5.11 results from different amplification voltages.

This double-peak indicates that at least two different energies are deposited in the detector. Here it is assumed that the same physical processes occur in the same components of the different converter layers. For the thinner insulating layers more of these interactions are detected providing a higher photon conversion efficiency.
For a first estimation of the observed peak behavior, a double Gaussian function is fit to the 100 + 18 PI cluster charge distribution, as presented in figure 8.21. Both peaks overlap and the second is wider than the first. Comparing the peak positions leads to a ratio $\mu_2/\mu_1 \approx 1.6$. In order to investigate the shape and origin of the cluster charge peaks in more detail, a simulation is performed, and the results are shown in chapter 8.5.2.

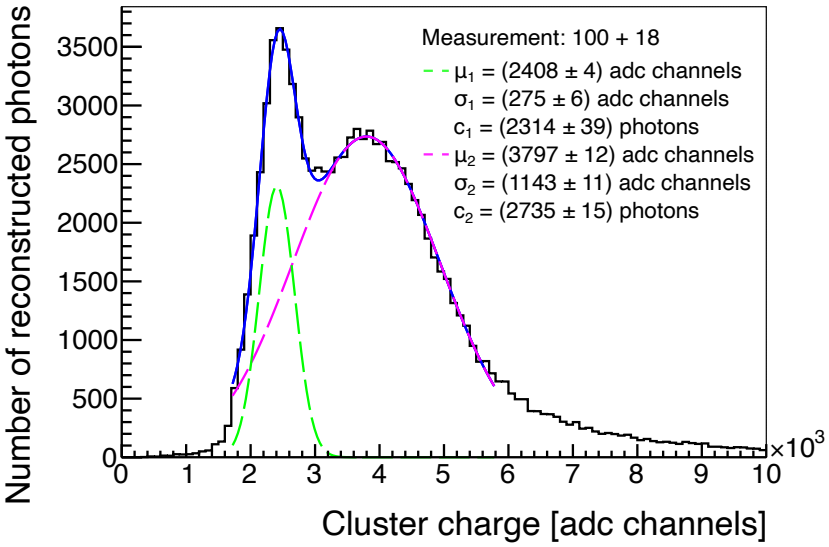

Figure 8.21: A double Gaussian function (blue) is fit to the cluster charge distribution of the 100+18 PI layers. For each peak the individual Gaussian function is visualized by the dashed line. The peaks have a position ratio of $\mu_2/\mu_1 \approx 1.6$.

8.5 Simulation of Photon Interactions in Converter Layers

In this section the origin of the peaks in the cluster charge distribution is studied including the interaction processes and materials. In addition, the reason for the different performance of the converter layer types regarding the trigger rate (see figure 8.17) is examined. This is done by precisely analyzing the simulation results, in particular from Geant4.

8.5.1 Energy Spectrum Analysis

A double-peak structure is observed in the cluster charge distribution for all layer types (see figure 8.20). Within the measurement uncertainties due to the pressure-voltage calibration (see chapter 8.4.4), the peak positions μ_1 and μ_2 are similar for the different layer types and have a position ratio of about 1.6. Furthermore, the converter layer types influence the measured trigger rate (see figure 8.17). This indicates that more photons with the same energy are detected for the PI layers than for the FR4 layers.
With the results of the Geant4 simulation, the origin of the peaks is investigated using the 100 + 18 PI converter layers with the dimensions from Table 8.1 including the ENIG protection layer. The simulated energy distribution of all primary electrons entering or created in

the active gas volume is shown in figure 8.22, with and without converter layers[15]. Without converter layers, no photoelectron peak appears between 4–8 keV, indicating that these peaks originate from a photon interaction with the converter layers. The most pronounced peak in this energy range is at 4.8 keV. In chapter 5.6.3, this simulated peak is associated with the first peak of the measured cluster charge distribution and is therefore analyzed in more detail in this chapter. The influence of all photopeaks on the measured cluster charge is also discussed within this section.
The same spectrum with the 100 + 18 PI converter layers is shown in figure 8.23, but here the distinction is made between the materials in which the photon interaction occurs. Only interactions where the generated electron subsequently enters the active gas volume are considered. While almost no electrons are extracted from PI or copper, some originate from ENIG.

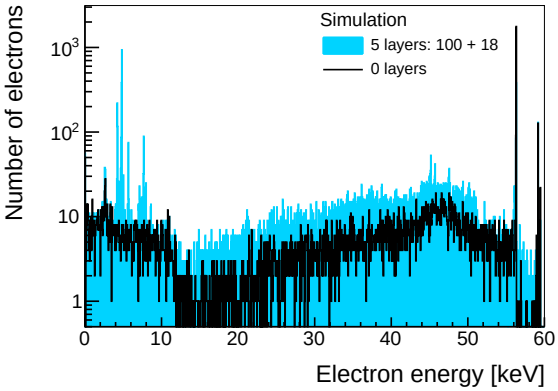

Figure 8.22: The simulated energy spectrum of the primary electrons entering the active gas volume with and without converter layers is compared. It indicates that the photopeaks below 10 keV are caused by the interaction of photons with the layers. The photopeaks above 50 keV overlap for both setups.

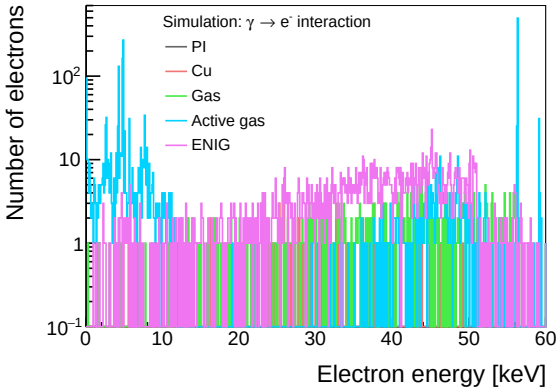

Figure 8.23: The energy distribution for all primary electrons entering the active gas volume is influenced by photon interactions with the various components of the detector. In particular, photon interactions in the active gas volume produce the dominant photopeaks. For the primary photoelectrons with an energy below 10 keV, the photon has to have an energy of about (10 ± 3) keV due to the argon binding energy of 3.2 keV. The simulation is performed with the 100 + 18 PI converter layer type.

Combining these two results, the simulation indicates that the 59.5 keV photons emitted by the source are influenced by the converter layers and lead to the photopeaks below 10 keV (see figure 8.22). However, these peaks originate from a photon interaction with the Ar:CO_2 93:7 vol. % gas mixture in the active gas volume (see figure 8.23). Due to the argon binding energy of 3.2 keV [Thompson et al., 2001], the photon creating the < 10 keV photopeaks should have an energy of (10 ± 3) keV.
These results arise from the following interaction processes occurring in the converter layers: When considering the 59.5 keV photon interaction in copper, the dominant process is the photoelectric effect (see figure 2.1). Thereby, the photons mainly interact with the electrons of the K-shell in copper [Berger et al., 2010]. This leads to an electron vacancy in the K-shell, which is filled by an electron from the L-shell. Due to the energy difference between these two shells, the additional energy in this K_α transition is emitted by a photon with an energy of 8.0 keV [Deslattes et al., 2005]. This 8.0 keV enters the active gas volume where it interacts with the K-shell electron in argon [Berger et al., 2010] via the photoelectric effect. Since this

[15] Slight deviations in the peak distributions compared to chapter 5 may occur due to variations in the layer composition and the additional ENIG protection layer.

electron has a binding energy of 3.2 keV, the resulting primary photoelectron has an energy of 4.8 keV.
The effects described here appear in ENIG as well, but the K_α transition photon has an energy of 7.4 keV and the primary electron in gas an energy of 4.2 keV.

Therefore, the interaction processes in the converter layers differ significantly from the initially assumed working principle. Instead of detecting the extracted photoelectron directly, due to the photoelectric effect a K-shell transition photon is emitted. In figure 8.24 the simulated photon energy of these transition photons is shown. The dominant peaks at 7.4 keV and 8.0 keV belong to the K_α transition in ENIG and copper, respectively. At 8.0 keV there are two peaks visible, one at 8.0057 keV and the other one at 7.9847 keV. Both values arise from the K_α transition, but differ, depending on the L-orbital from which the electron transitions[16]. If the transition photons leave the converter layer, they can interact with the detector gas and produce electrons. The energy distribution of these electrons is shown in figure 8.25. If the transition photons leave the converter layer, they can interact with the detector gas and produce electrons. The energy distribution of these primary electrons[17] is displayed in figure 8.25. The expected dominant peaks at a photon energy of 7.4 keV and 8.0 keV are observed.

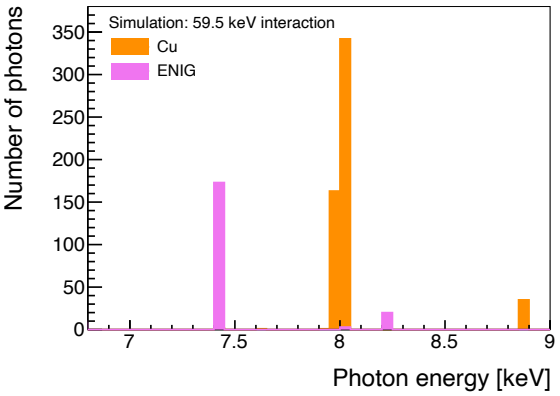

Figure 8.24: The 59.5 keV photon interacts in Cu via the photoelectric effect. The resulting vacancy in the K-shell is filled by an electron from a higher shell, causing the emission of a 8.0 keV K_α photon. In ENIG a 7.4 keV K_α photon is emitted. The corresponding peaks at higher energies result from the K_β transition in each material.

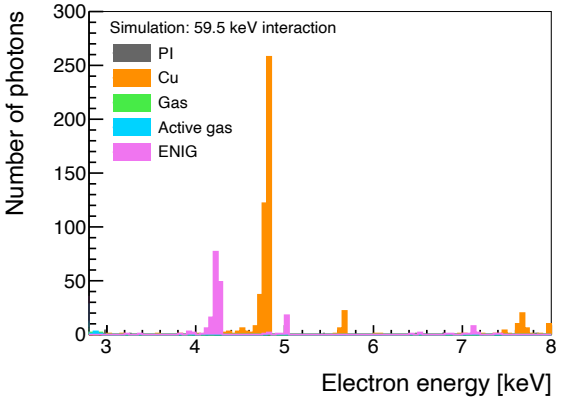

Figure 8.25: The 59.5 keV photon from the source interacts with the converter layer, leading to the emission of a transition photon. It interacts with the active gas volume, producing a primary photoelectron. Depending on the energy of the transition photon (see figure 8.24) and the electron binding energy (see [Thompson et al., 2001]), the resulting primary electron differs. The dominant peak at 4.8 keV results from the 8.0 keV K_α transition photon in Cu, which interacts with argon via the photoelectric effect. Due to the K-shell binding energy of 3.2 keV, the resulting photoelectron has an energy of 4.8 keV. Similar processes occur in ENIG, leading to a photopeak at 4.2 keV.

[16] These values are provided by the internal Geant4 database and slightly differ from [Deslattes et al., 2005].
[17] In contrast to figure 8.23, here it is distinguished between the materials with which the 59.5 keV photon interacts.

In addition to the peak < 10 keV in figure 8.23, there are two photopeaks at energies > 50 keV, which are caused by the direct interaction of the 59.5 keV photons with argon. All primary electrons lead to secondary ionization in the gas. The simulated number of secondary electrons per detected electron-cluster can be seen in figure 8.26. It is distinguished between all primary electrons and those with energies > 10 keV. The latter lead to a background in the distribution, the primary electrons with < 10 keV cause peaks, including a dominant one at about 190 electrons (see figure 8.27).

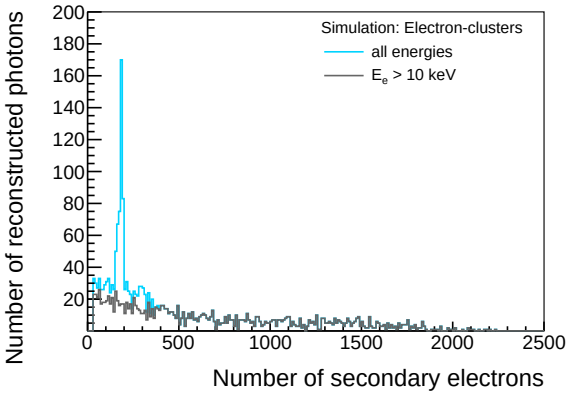

Figure 8.26: The primary electrons from figure 8.23 cause secondary ionization in the gas. The resulting distribution of the number of secondary electrons in an electron-cluster per reconstructed photon exhibits a dominant peak (see figure 8.27) with a tail of up to 2000 electrons. While the background of the distribution (in gray) arises from primary electrons with energies > 10 keV, the peaks (in blue) at about 200 secondary electrons are produced by primary electrons with energies < 10 keV. The background contribution decreases linearly up to 800 electrons, where it remains constant. For the simulation the 100 + 18 PI layers are used.

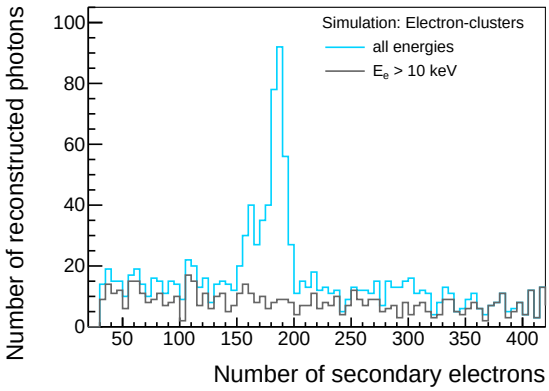

Figure 8.27: The peak is particularly dominant at around 190 electrons. It is produced by the 4.8 keV primary electrons (see figure 8.29). The small peak at about 160 electrons arises from the 4.2 keV primary electrons. Both peaks are not clearly separated from each other, which is mainly due to binning of the histogram. The gas amplification is not considered here. Compared to the background, there are a few slight rises in the distribution, for example at 300 electrons.

The simulated distribution in figure 8.26 is equivalent to the measured cluster charge, but without the gas amplification in the GEM foils. As with the measurement (see figure 8.20), it has a peak structure with a tail, whereby the exact peak structure is further analyzed in chapter 8.5.2. The peak around 190 electrons originates from primary electrons with an energy of less than 10 keV. Furthermore, in chapter 5.6.3 this simulated peak is associated with the first measured peak in the cluster charge distribution. Since the integral of these cluster charge peaks changes for different converter layer types in the measurement, the corresponding peaks should change in the simulation as well. Hence, the focus of the simulation is on primary electron energies of less than 10 keV.

For a first estimate regarding the interaction of 8.0 keV photons in the used materials, the total linear attenuation coefficients μ_{total} and their contribution from the photoelectric effect and Compton scattering as well as the mean free path λ are summarized in Table 8.2. Due to the lower photon energy compared to Table 2.1, the photoelectric effect is more dominant and the photon attenuation is stronger. The mean free path in copper is 22 µm, which is smaller than the strip thickness. Therefore, many 8.0 keV photons are absorbed directly and do not leave the strip.
In addition, the transition photon is emitted in 4π and interacts somewhere in the gas, as

the mean free path length in argon is $\lambda = 48\,\text{mm}$. Therefore it has no information about the initial photon, regarding momentum direction or interaction position.
Taking this knowledge into account, previous results are understood. Due to the emission in all directions, photons also emerge from the copper strips on the back side of the layers. Specifically, the conversion efficiency on the front and back sides of the layer is similar, explaining the previously unexplained high detection efficiency near the back side of a converter layer, as shown in figure 7.6 and figure 8.16. A more detailed discussion of the effects on the 3D position reconstruction is given in chapter 8.8.

Material	μ_{photo}		μ_{C}		μ_{total}	λ
	value [cm^{-1}]	fraction	value [cm^{-1}]	fraction	value [cm^{-1}]	value [mm]
Cu	453.5	99.9 %	0.6	0.1 %	454.1	0.022
PI	8.23	97.9 %	0.18	2.1 %	8.41	1.19
Ar	0.2087	99.9 %	0.0002	0.1 %	0.2089	47.9
CO_2	0.0184	98.9 %	0.0002	1.1 %	0.0186	537.5

Table 8.2: The total linear attenuation coefficient μ_{total} and its contributions from the Photoelectric effect and Compton Scattering are compared for four different materials for 8.0 keV photons. Pair creation does not contribute at this energy and the contribution from Rayleigh scattering is neglected. In all materials, the photoelectric effect dominates strongly. Compared to 59.5 keV photons (see Table 2.1), the absorption is stronger in all materials and thus the mean free path λ smaller. Data extracted from [Berger et al., 2010], but none is provided for FR4.

8.5.2 Cluster Charge Comparison between Simulation and Measurement

When comparing the measured cluster charge (see figure 8.21) with the simulated one (see figure 8.26), several aspects have to be taken into account:

- GEM amplification and energy resolution: Since the gas amplification in the triple-GEM detector is a stochastic process, it causes a broadening of the peaks.

  A GEM detector typically has an energy resolution of about 20 % [Heereman, 2010]. To separate for example the 2 peaks at 4.2 keV and 4.8 keV (see figure 8.25) with 1σ, an energy resolution of at least 15.6 % is required[18]. Thus, these peaks are probably indistinguishable and overlap to form a single peak in the measurement.
  In contrast to the measurement, the gas amplification process is not taken into account in the simulation, leading to sharper and more distinguishable peaks in the simulated distributions.

- Background: As shown in the simulation, the charge distribution contains a continuous background and peaks (see figure 8.26). Both can be easily separated in the simulation. However, they have to be taken into account in the measurement as well.

- Peaks: A double peak structure with a peak position ratio of 1.6 is observed in the measurement. Due to the GEM amplification and the limited resolution it can occur that a measured peak contains several overlapping peaks.
  In the simulation, there is a main peak at 190 secondary electrons (see figure 8.27), which originates from 4.8 keV primary electrons. This peak is associated with the first peaks in the cluster charge distribution.

[18] The energy resolution R is defined as $R = \Delta E/E$, where ΔE is the full width at half maximum (FWHM) of the peak with $\Delta E = \text{FWHM} = 2.355 \cdot \sigma$. To separate the peaks with 1σ, the distance between the peaks ΔP has to fulfill: $\Delta P \geq \sigma_1 + \sigma_2$. This results in $\Delta P \geq R(E_1 + E_2)/2.335$. For the 4.2 keV and 4.8 keV peak $\Delta P = 0.6\,\text{keV}$. Therefore, the required resolution is $R \leq (2.335 \cdot 0.6)/(4.2 + 4.8) = 15.6\,\%$.

Simulation and measurement initially exhibit some differences, which are examined in more detail. In order to investigate the simulated peaks, the primary electron energy distribution is compared in figure 8.28 for 4 different converter layer types. The peak positions are the same for all layers, but they differ in their integral, which is compared in chapter 8.5.3. At least 2 peaks with a peak position ratio of 1.6 are expected from the measurement. The second largest peak with respect to the integral is at 4.2 keV and does not fulfill this peak ratio. Furthermore, due to the energy resolution, it is anticipated that the 4.2 keV and 4.8 keV peaks are not resolvable.
With respect to the dominant 4.8 keV, the theoretical peak positions with a ratio of 1.6 are indicated in figure 8.28. For electron energies < 4.8 keV there is no peak fulfilling this requirement, but there is a peak at 7.65 keV that has the desired ratio. For the further analysis, a total of 4 peaks are considered: The peaks at 4.2 keV and 4.8 keV, as both have a large integral and thus a large contribution to the total charge, and the peaks at 5.65 keV and 7.65 keV, as they lie within the energy range.

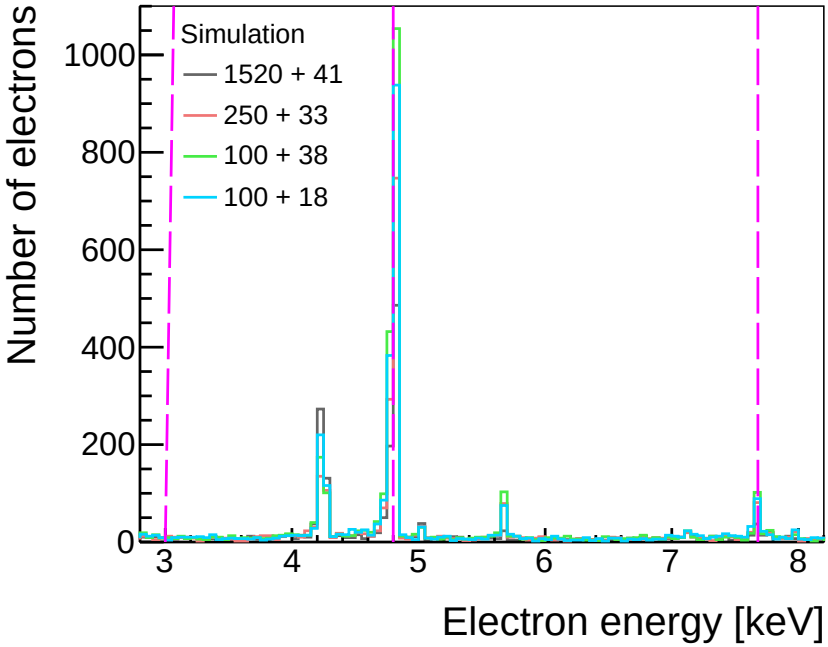

Figure 8.28: The positions of the primary electron energy peaks for 4 different converter layer types coincide. A peak ratio of 1.6 is expected from the measured cluster charge distribution (see figure 8.21). Since the peaks originate from primary electrons with energies < 10 keV, there should be 2 peaks with approximately this ratio in the simulation in this energy range. Assuming that the 4.8 keV peak can be assigned to one of the measured cluster charge peaks, either a peak around 4.8 keV/1.6 = 3.0 keV or 4.8 keV · 1.6 = 7.7 keV is anticipated. These values are indicated by pink dashed lines. There is no peak in the region of 3.0 keV. Instead, the 7.65 keV peak fulfills the ratio and is considered. In total, 4 peaks are in this energy range and are included in the following cluster charge analysis: 4.2 keV, 4.8 keV, 5.65 keV and 7.65 keV.

All these electrons cause secondary ionization. The correlation between the primary electron energy and the number of electrons per reconstructed electron-cluster is shown in figure 8.29. Each primary electron peak is thus associated with a number of secondary electrons. Thus, each primary electron peak is associated with a number of secondary electrons. The projection of the y-axis is shown in figure 8.30, where the background contribution of primary electrons > 10 keV is neglected.

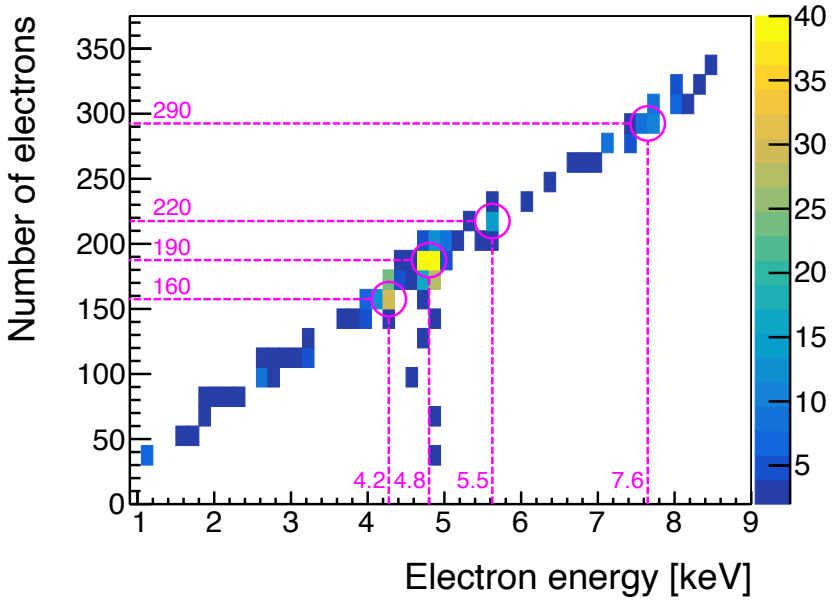

Figure 8.29: There is a correlation between the primary electron energy and the number of secondary electrons in the detected electron-cluster. Thus, the electrons from each peak in figure 8.28 produce a specific number of secondary electrons, resulting in peaks in the electron-cluster charge distribution. The correlation for these peaks is indicated by the pink dashed lines. Due to the binning, there is a slight deviation between the actual axis values and the labeling.

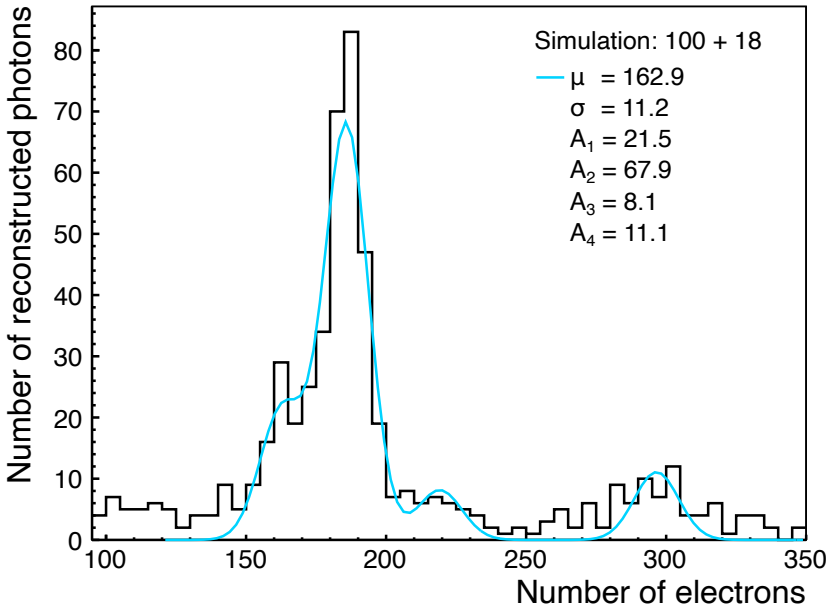

Figure 8.30: In the simulated electron-cluster charge distribution, 4 peaks are observed at the positions specified in figure 8.29. The contributions of the background (see figure 8.27) are neglected. A fourfold Gaussian function (see equation 8.2) is fit to the distribution, where the mean values μ_i are fixed relative to each other and the width σ is kept constant for all peaks. Although the first 3 peaks overlap, they are distinguishable in the simulation. The GEM amplification is not included. All values are summarized in Table 8.3.

A fourfold Gaussian function

$$f(x) = \sum_{i=1}^{4} A_\mathrm{i} \exp\left(-\left(\frac{x - c_\mathrm{i}\mu}{\sigma}\right)^2\right) \tag{8.2}$$

is fit to the distribution, with an amplitude A_i and a constant width σ for all four peaks. The mean value $\mu_\mathrm{i} = c_\mathrm{i}\mu$ for each Gaussian is defined by the energy ratio c_i with respect to the position of the first peak $\mu_1 = \mu$. For the second peak, for example, this results in $c_2 = 4.8\,\mathrm{keV}/4.2\,\mathrm{keV} = 1.14$ and thus $\mu_2 = c_2\mu = 1.14\mu$. All parameters are summarized in Table 8.3.

Peak	Energy [keV]	ratio c_i	$\mu_\mathrm{i} = c_\mathrm{i}\mu$	A_i
Peak 1	4.20	1	163	21.5
Peak 2	4.80	1.14	186	67.9
Peak 3	5.65	1.35	220	8.1
Peak 4	7.65	1.82	297	11.1

Table 8.3: Each peak belongs to a primary electron energy. Therefore, the expected distance between the mean values μ_i of the individual Gaussian functions is known and is kept constant. It is defined by the primary electron energy ratio $c_\mathrm{i} = E_\mathrm{i}/E_1$ with $E_1 = 4.2\,\mathrm{keV}$. The quadruple Gaussian function (see equation 8.2) is fit to the distribution and provides the mean value $\mu = \mu_1$ as well as the amplitudes of the peaks A_i. The width of each Gaussian function is kept constant, which leads to $\sigma = 11.2$.

The simulated electron-cluster charge can be approximated by a fourfold Gaussian function. Some of the peaks lie close together. Since the peaks are broadened by the electron amplification in the GEM foil during the measurement, it is expected that these individual peaks are not visible in the measured distribution. In addition, for the third and fourth peaks at 220 and 297 electrons a large background contribution is expected (see figure 8.27).
A background estimate is not possible for the measurement results shown in figure 8.21, because the distribution starts with the first peak and thus a linear background fit cannot be performed. It is resolved by considering a measurement with a lower threshold value allowing more events with smaller charge to be detected[19]. As shown in figure 8.31, a shoulder appears before the first peak. By fitting a first-degree polynomial to this shoulder and the tail, the measured background can be estimated. If this background is neglected, the second peak has a much smaller integral compared to figure 8.21 and the first peak is dominant, which is in better agreement with the simulation result in figure 8.30.
In combination with the linear background estimation ($f_\mathrm{back} = 950 - 0.12x$, where x is the cluster charge in adc channels), a quadruple Gaussian function is fit to the distribution in figure 8.31, which is given by :

$$f(x) = 950 - 0.12x + \sum_{i=1}^{4} A_\mathrm{i} \exp\left(-\left(\frac{x - c_\mathrm{i}\mu}{\sigma}\right)^2\right) \tag{8.3}$$

In the simulation, the peak position ratios between the peaks are defined (according to Table 8.3) and all peaks have the same width σ. These boundary conditions are also applied to the fit for the measurement with the corresponding peak ratios. As shown in figure 8.31, the first measured peak is most likely an overlap of the first two peaks with an additional

[19] This measurement was performed with a different GEM detector and different settings, therefore the cluster charge distribution differs compared to figure 8.21. Differences are also attributed to the pressure-voltage calibration. The 100 + 18 PI converter layers are incorporated and the same voltages applied.

contribution from the third peak. The second measured peak at about 4000 adc channels can be associated with the fourth peak. However, there are slight discrepancies regarding the mean value and the width. The peak is not fully described by the fourfold Gaussian fit, which does not account for the larger charges above 4000 adc channels. Due to the used approximations and the various aspects described at the beginning of this section, such deviations are expected. These differences might be eliminated by an optimized Gaussian fit, for example by using different σ values for the peaks. In the simulation, the distribution of the fourth peak is also broader than the fit. A more accurate description of the background could be obtained by measuring with lower thresholds. However, an exact characterization has no influence on further investigations in this chapter.
This estimate provides a reasonable understanding of the origin of the peaks in the measured cluster charge distribution, showing that the two measured peaks are an overlap of several individual peaks and that the first peak is associated with the 4.8 keV primary electron energy.

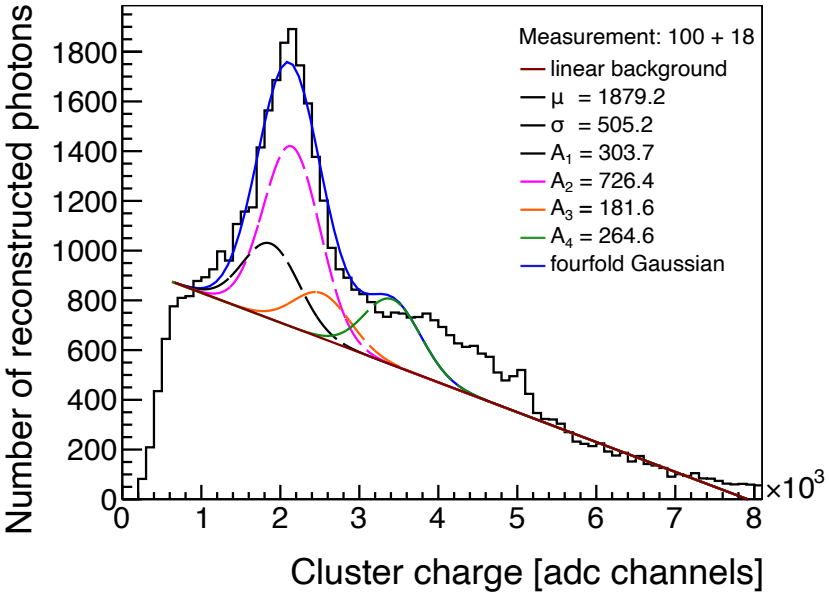

Figure 8.31: By including the background ($f_{\text{back}} = 950 - 0.12x$), the contribution of the second peak is reduced and the first dominates. The peaks are thus more similar to the simulation result from figure 8.30. Based on the simulation, a fourfold Gaussian function is fit (see equation 8.3) with fixed relative peak positions $\mu_i = c_i\mu$ according to Table 8.3. The resulting fourfold Gaussian function is shown in blue, providing the mean value μ for the first peak and the same width σ for all peaks. The 4 individual peaks are indicated. In particular, a good approximation is achieved for the first measured peak, while the fit to the second peak shows slight discrepancies. The measured cluster charge comprises several overlapping peaks with the first peak having the main contribution from the 4.8 keV electrons.

8.5.3 Cluster Charge Simulation of Various Converter Layer Types

After understanding the origin of the peaks in the simulation and in the measurement, the influence of the different converter layer types is examined. Since the main contribution comes from the first measured peak (see figure 8.31), the corresponding simulated peaks at 4.2 keV and 4.8 keV are analyzed in more detail. The peaks at higher energies arise from the same material, thus the relative changes are the same. These simulated peak values are compared for 4 different layer types in figure 8.32. The results are extracted directly from Geant4. Similar to the measurement (see figure 8.20), the peak integral at 4.8 keV increases with thinner insulating material.

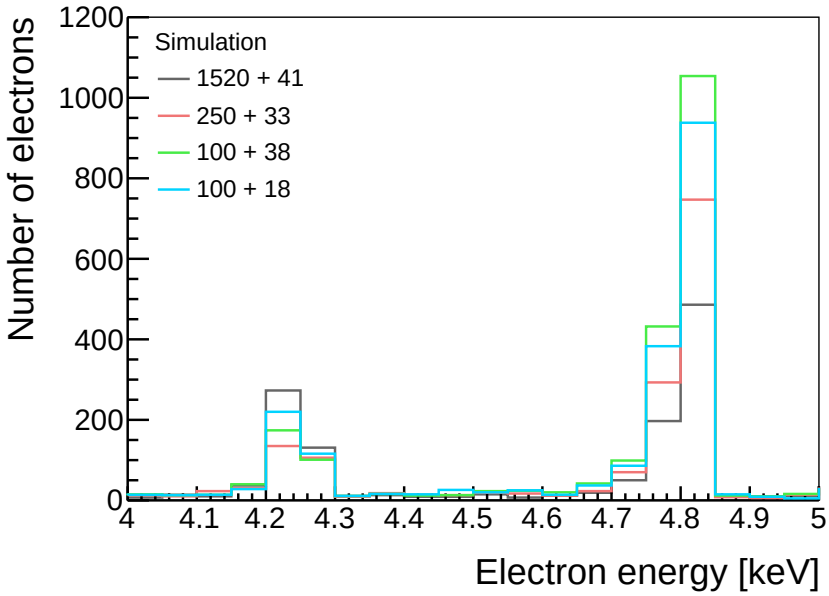

Figure 8.32: The Cu peak at 4.8 keV increases as the insulation layers become thinner. This behavior corresponds to the expectations of the measurement from figure 8.20. The 100 + 18 PI peak is smaller than the 100 + 38 PI peak. For the ENIG peak at 4.2 keV, the 1520 + 41 FR4 layer yields the highest peak. All simulations have been carried out with the same number of initial photons.

The copper peak at 4.8 keV increases for thinner converter layers, which is consistent with the measurement. Compared to the 1520 + 41 FR4 layers, the 250 + 33 FR4 peak is about 1.4 times higher and the 100 + 38 PI peak is about twice as high. In addition, the measured difference of 1.5 between the 250 + 33 FR4 and 100 + 38 PI layers is resolvable here. The peak of the 100 + 18 PI layers is slightly smaller than that of the 100 + 38 PI layers, contradicting the measurement results. Especially for the thin layers, deviations can occur in the measurement, as they may not be completely stretched when installed in the detector.
In figure 8.32 there is another peak at about 4.2 keV, which is caused by the ENIG protection layer of the strips. As this layer is thinner than the copper layer, the photon emission and thus the total integral of the peak is lower. For the 1520 + 41 FR4, the thickest nickel layer is assumed to be 6 µm, while for the other layers it is 3 µm. Consequently, the 1520 + 41 FR4 has the highest 4.2 keV peak.
In the measurement results, both peaks overlap, forming a single peak and merging their distinct behaviors. A complete comparison between the different converter layer types, including all peaks, is provided in chapter 8.6.
These values, which could not be resolved by considering the 59.5 keV photon absorption, are reproducible with this simulation. The main reason for the deviation between the converter layer types is discussed in the next section.

8.5.4 Photon Tracking and Energy Distribution in the Converter Layers

A performance difference in the trigger rate is observed between the converter layer types (see figure 8.17), which is studied here. The focus lies on the comparison between 1520 + 41 FR4 with the 100 + 38 PI converter layers. According to figure 8.17, the trigger rate between these two layer types differs by a factor of 1.8 for $\Delta U_y = 0\,\mathrm{V}$ and a factor of 2.5 for $\Delta U_y = 600\,\mathrm{V}$. In order to understand the different trigger rates for the same ΔU_y between these two converter layer types, the occurring physical processes are analyzed.
This difference between the layer types is apparent in the measured cluster charge intensity (see figure 8.20) as well as in the simulated energy distribution (see figure 8.32). Since the

measurement and simulation results are associated (see figure 8.32), the physical reason for the result is accessible by analyzing the simulation results. For simplicity[20], only the photon interaction in copper is considered here. As shown in chapter 8.5.1, this process is associated with the creation of an 8.0 keV photon in copper, which produces a primary electron with the energy of 4.8 keV in argon.

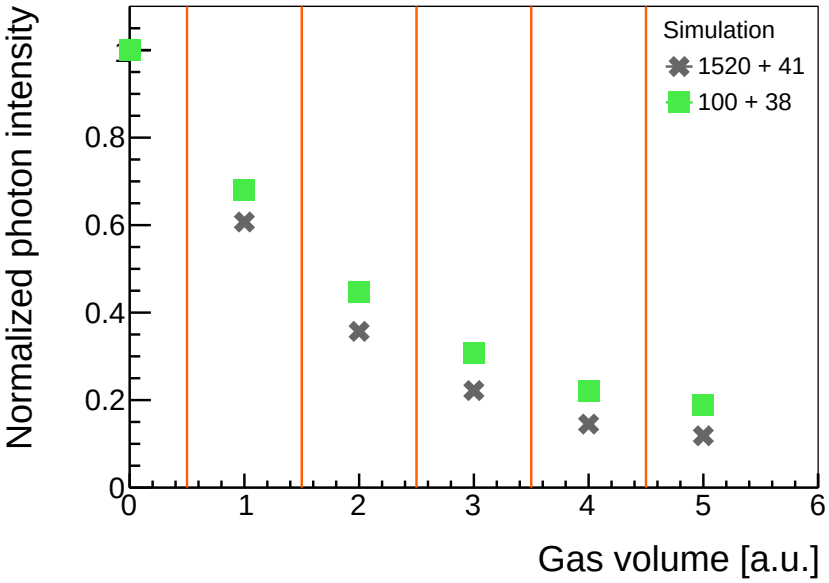

Figure 8.33: Both layers show a different absorption behavior for the 59.5 keV photos, as known from figure 8.13. Due to the stronger absorption of the 1520 + 41 FR4 layers, the photon intensity decreases more strongly, resulting in fewer photon interactions. The orange lines indicate the positions of the layers, and each dot represents the remaining photon intensity in each gas volume between two layers. The absorption of the layers differs by 10–15 %.

The different 59.5 keV photon absorption properties of both converter layer types in the GEM detector are investigated by simulation. Figure 8.33 shows the resulting attenuation of the photon beam, whereby the photons that reach the active gas volume between two layers are considered. Due to the different absorption properties of FR4 and PI in combination with their respective thicknesses, there is a difference of about 10–15 % between the layers. Since the 59.5 keV photons are emitted in 4π, some exit the active gas volume without an interaction. Thus, the values in figure 8.33 account for the complete setup of the converter layer in the GEM detector, not just the absorption in the layers. This leads to differences compared to the absorption measurement in figure 8.13, but the trend is similar.
The number of produced 8.0 keV photons should be proportional to the number of 59.5 keV photon interactions in copper. Since the factor of 1.8 observed in the simulation and measurement is not observed in figure 8.33, additional effects have to be present. These are determined by tracking the photon interactions in the various components of the converter layer.

[20] Since all components of the converter layer contribute to the overall performance to varying degrees, only the dominant or relevant processes that are required to understand the differences in performance are considered in this section. All effects are taken into account in chapter 8.6.

Instead of considering all occurring processes for photon tracking, the following simplifications are applied[21]:

- The main contribution in the cluster charge arises from the 4.8 keV primary electron, which is created by the interaction of the 8.0 keV K_α transition photon produced in copper. The majority of the 8.0 keV photons generated in copper are directly reabsorbed and do not leave the material (see Table 8.2). This accounts for around 80 % of all photons produced, while the remaining 20 % leave the copper. Therefore, the emphasis is on tracking these 8.0 keV photons exiting copper.
  The K_α photons created in ENIG are neglected here.
- The K_α transition photons created in copper are emitted in 4π. Here only the photons exiting the copper in forward direction are tracked.
- For all 5 layers in the GEM detector the processes are summarized.
- Effects with small contributions are neglected

A complete schematic overview of the considered photon tracking is shown in figure 8.34, whereby the different parts are considered separately later for a better understanding. It is distinguished between the 8.0 keV photons that are emitted from copper strips before the FR4/PI layer and those afterwards.

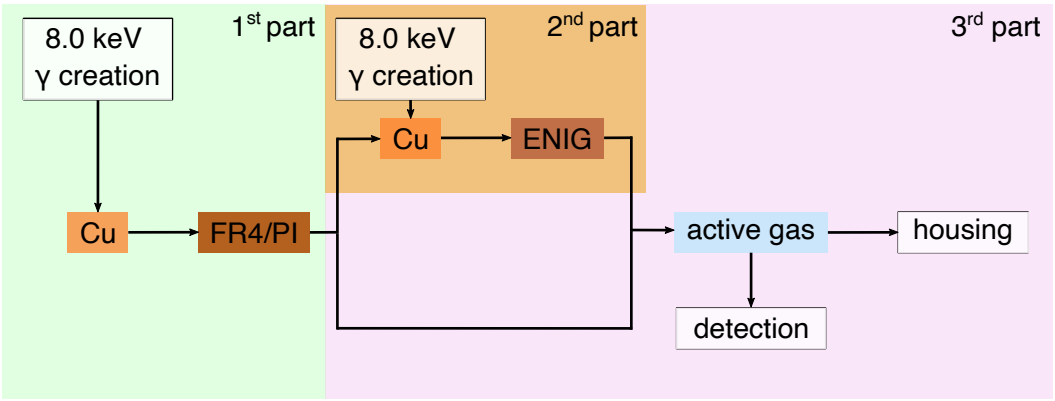

Figure 8.34: For simplification of the photon tracking in the layers, only photons produced in Cu and emitted in the forward direction are considered. From Cu, the photons reach the insulating layer, which consists of FR4 or PI (first part). Since half of the insulator surface is covered with Cu strips, the photon either reaches Cu (second part) or enters the gas directly (third part). In the latter case, the photons penetrating Cu and ENIG reach the gas. Either the photon interacts in the gas producing detectable electrons or it exits. Thus, this photon tracking chain is divided into 3 parts, as indicated by the different colored background.

Following figure 8.34 from left to right, the 8.0 keV photons are produced and those emitted in forward direction from the first copper strip are tracked. They reach the insulating material. Some of them are absorbed, whereas the rest emerges from this material (first part). As half of the insulating material of the converter layer is covered with strips, the photons either reach the next strip of the second copper layer (second part) or enter directly the active gas (third part). When the photons enter the next copper strip, some are absorbed, while simultaneously new 8.0 keV photons are created by the 59.5 keV photons. If the photons are not absorbed

[21] These simplifications are chosen such that the other processes are influenced in the same way and only have a minimal impact on the final result.

by the ENIG protection layer, they reach the active gas. Some of these photons entering the gas from FR4 or ENIG interact with the gas producing the 4.8 keV primary electrons that are detectable afterwards. The other photons leave the active gas without further interaction and are absorbed by the housing or exit the detector.

The detailed results for the 3 parts are shown from figure 8.35 to figure 8.40. For comparison, all values are normalized to the total number of photons generated in both copper strips in all 5 1520 + 41 FR4 layers and exit copper, independently of the direction and energy. For the tracking only the photons in the energy range around 8.0 keV are considered. This includes the K_α transitions at 8.0 keV and K_β transitions at about 8.9 keV.
The first part is shown in figure 8.35. Due to the lower absorption and thus higher photon intensity for 100 + 38 PI (see figure 8.33), about 1.2 times more photons exit the copper, when taking all 5 layers into account. About 17 % of all created photons are emitted in the forward direction and have an energy of around 8.0 keV. They reach the insulating material which consists of either 1520 µm FR4 or 100 µm PI. While in PI the total photon ratio is reduced by about 3 % due to absorption, in FR4 all 8.0 keV photons are absorbed. Due to this different absorption behavior of both these layer types, more photons reach the next material for 100 + 38 PI than for 1520 + 41 FR4. This large discrepancy between both layer types is the main reason for their different measured trigger rate and therefore detection efficiency. The stronger photon absorption in the 1520 µm FR4 layer is known from the photon absorption measurement (see chapter 8.3). All results from measurements and simulation investigate the absorption of 59.5 keV photons. However, the absorption behavior of the 8.0 keV photons is essential here, which differs significantly between the two converter layer types. This can be seen in figure 8.36, where the energy distribution before the photons pass through the insulating material (Cu → FR4/PI interface) and afterwards (FR4/PI → Cu or gas interface) is shown. In agreement with figure 8.35, in FR4 all 8.0 keV photons are absorbed and do not reach the next interface. In contrast, about 80 % of the photons penetrate the PI layer. This demonstrates a clear difference in the performance of the converter layers in the critical energy range.
For the second part, figure 8.37 shows the fraction of photons reaching the second layer of copper from FR4 or PI, with the corresponding energy distribution shown in figure 8.38. Since for the 1520 + 41 FR4 layers no photons reach the FR4 → Cu interface, the remaining photon ratio is 0. For the 100 + 38 PI layers, about 80 % of the photons are absorbed in copper, while the remaining photons reach ENIG. Additional photons are produced in this second copper layer, due to the 59.5 keV interactions. Due to the stronger absorption of the 59.5 keV photons in the insulating FR4 layer, less photons reach the second copper layer compared to the first one. Therefore, more transition photons originate from the first copper layer (see figure 8.35) than from the second copper layer (see figure 8.37). Since the 59.5 keV absorption in PI is lower, this effect is less pronounced for the 100 + 38 PI layers. All 8.0 keV photons emitted by this second copper layer in forward direction and the non-absorbed photons coming from the insulating material reach ENIG. In ENIG the total photon ratio is reduced by 5 % for both layer types due to absorption. The 3 µm thicker nickel layer of the 1520 + 41 FR4 layers has only a minimal influence compared to the 100 + 38PI layers. Twice as many photons reach the gas interface for the 100 + 38 PI layer compared to the 1520 + 41 FR4 layers. This difference is evident in the energy spectrum in figure 8.38. Therefore, the deviation between both layer types is also influenced by the different absorption behavior of the 59.5 keV photons in the insulating material.
In the third part, all photons that reach the interface to the gas are considered. They originate either from the FR4-gas interface (first part) or from the ENIG-gas interface (second part). Due to the various aspects influencing photon absorption, in total 2.5 times more photons reach the gas interface for the 100 + 38 PI layers compared to the 1520 + 41 FR4 layers, as

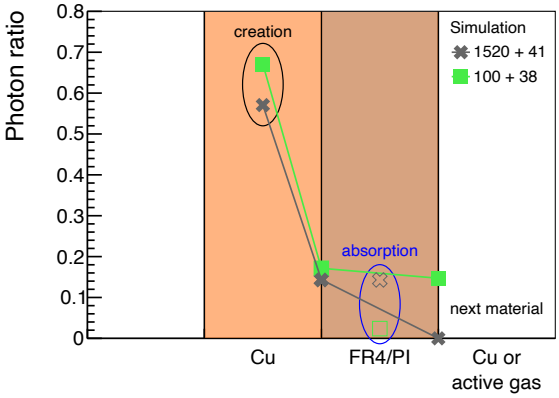

Figure 8.35: First part: The 8 keV photons exiting Cu have a different absorption behavior in FR4 (1520 µm) and PI (100 µm). In FR4 all photons are absorbed while in PI the majority reaches the next material, which is Cu or gas.

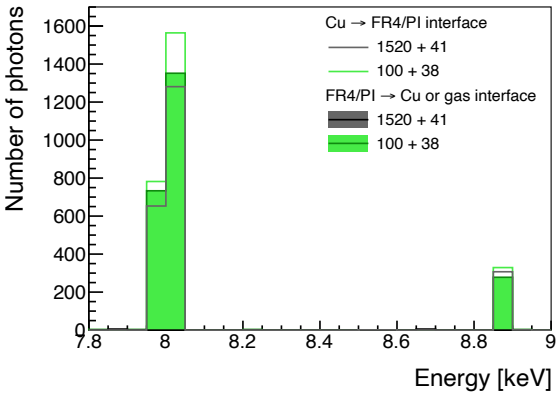

Figure 8.36: First part: None of the 8 keV photons entering FR4 exit it, resulting in no gray peak. In PI about 80 % of the photons reach the next material. This difference leads to the varying detection efficiencies for both layers.

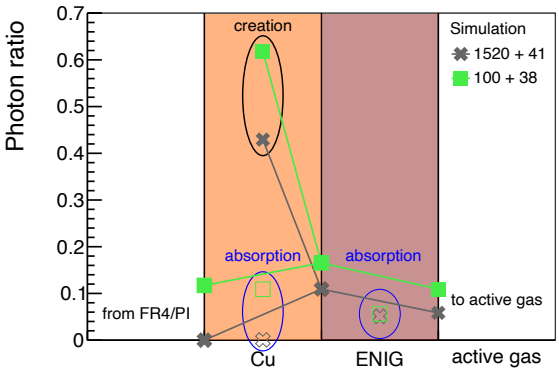

Figure 8.37: Second part: 80 % of the photons after PI are absorbed in Cu. New 8 keV photons are created by rearrangement in the second copper layer. If they are not absorbed by ENIG, they reach the gas interface.

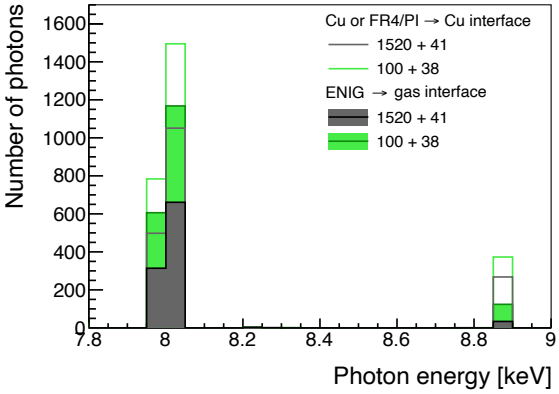

Figure 8.38: Second part: The photons penetrate the FR4/PI or are newly produced in this Cu layer. Twice as many 8.0 keV photons reach the Cu or gas interface for the 100 + 38 layer.

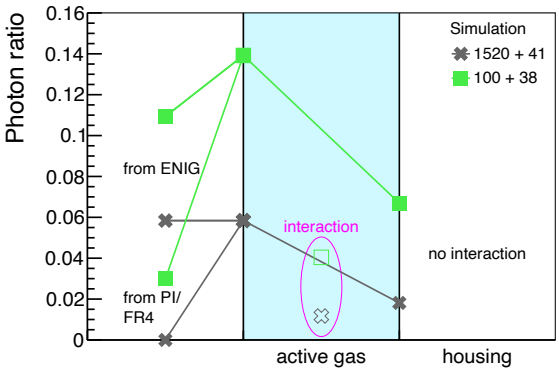

Figure 8.39: Third part: Photons from FR4 or PI (first part) or ENIG (second part) reach the gas, where they either interact and produce detectable electrons or leave the gas.

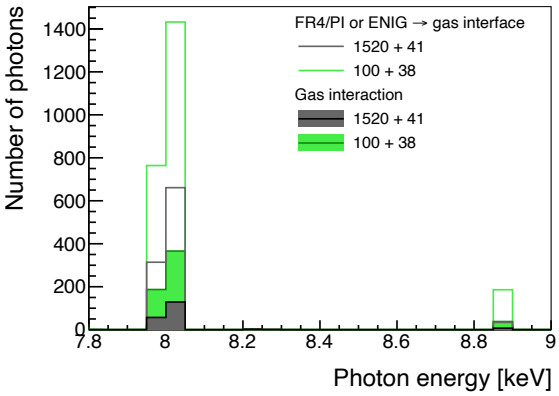

Figure 8.40: Third part: With the 100 + 38 layers, 2.5 times more 8.0 keV photons enter the gas compared to the 1520 + 41 layers and 25 % of the 8.0 keV photons interact with gas.

shown in figure 8.39. This difference between the converter layers is also visible in the energy spectrum in figure 8.40. 25 % of the 8 keV photons interact with the detector gas producing an electron, while the other part leaves the active gas volume. In the end, the conversion efficiency of the 100 + 38 converter layers is 2.5 times higher than for the 1520 + 41 FR4 layers, which is in agreement with the difference in the measured trigger rate at ΔU_y = 600 V (see figure 8.17). A complete comparison between simulated and measured trigger rate including all processes is carried out in the next section.

To summarize, the main reason for the different performance of the converter layers is their distinct absorption behavior of the 8 keV photons. While the majority of these photons is able to penetrate the 100 µm PI layer, they are completely absorbed in the 1520 µm FR4 layer due to its greater thickness. In addition, the stronger absorption of 59.5 keV photons in FR4, leads to less photon interactions in the second copper strip layer compared to the PI layers.

In order to compare the different absorption behavior of 8.0 keV photons in both insulating materials, a simulation is performed with the same thicknesses of all components and FR4 and PI as insulating materials. Therefore, the dimensions of the 250 + 33 layer type are used and the result is shown in figure 8.41. It corresponds to the energy distribution in figure 8.36, so the ratio of 8.0 keV photons before and after the insulating material is compared. Compared to figure 8.36, the 8.0 keV photon transmission in 250 µm is higher than in 1520 µm FR4. For the same insulator thickness the photon absorption is about 15 times higher for FR4 compared to PI, due to the different material composition, in particular the bromide content in FR4. Thus, not only the thickness but also the material composition of the insulator influences the detection efficiency. This effect explains the differences between 250 + 33 FR4 and 100 + 38 PI layers. While the 59.5 keV photon absorption in both layer types is similar, in 250 µm FR4 more 8.0 keV photons are absorbed than in 100 µm, resulting in a difference of about 1.5 in the measured trigger rate.

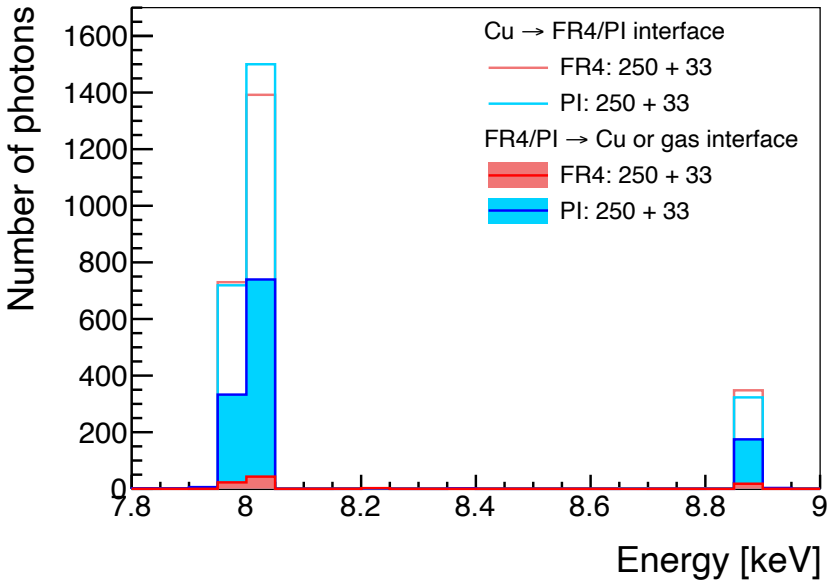

Figure 8.41: For a direct comparison of the absorption behavior of 8.0 keV photons between FR4 and PI, layers with the same thicknesses (250 + 33) are investigated. Only the insulating material differs. The energy distributions before and after the insulating layers, as in figure 8.36, are compared. The 8.0 keV photon absorption in FR4 is about 15 times higher than in PI.

The two types of 100 µm PI layers, one with 35 µm copper, the other with 15 µm copper, behave similarly. Although in 35 µm copper more 8.0 keV photons are produced than in 15 µm

copper, more of these photons are reabsorbed due to the greater thickness. In return, these effects compensate, resulting in a similar performance.

Additionally, with the simulation results the contribution of the 8.0 keV transition photons on the complete conversion efficiency can be estimated, using the 100 + 38 PI converter layers. In total, 5 double-sided converter layers are used, where half of the carrier material is covered by 35 µm thick copper strips. This leads to $35\,\mu m \cdot 5 \cdot 2 \cdot 0.5 = 175\,\mu m$ copper, where 22 % of the 59.5 keV photons are absorbed [Berger et al., 2010]. As mentioned above, only 20 % of all 8.0 keV K_α transition photons leave the material, which corresponds to $0.2 \cdot 22\,\% = 4.4\,\%$ of all initial photons. About 4 % of the forward emitted K_α photons interact with the detector gas (see figure 8.39). Since for the backward emitted photons the occurring processes are similar, a total interaction probability of 8 % is given. With respect to all 59.5 keV photons, this leads to a conversion probability of $0.08 \cdot 4.4\,\% = 0.35\,\%$ only considering the 8.0 keV K_α photons. In section chapter 8.7, this efficiency is compared to the overall detection efficiency.
The measured and simulated increase in detection efficiency towards thinner converter layers is understood by tracking the photons in the material and investigating the 8.0 keV photon absorption behavior using simulation.

8.6 Comparison of Simulated and Measured Trigger Rate

In order to fully compare the measured trigger rate (see figure 8.17) with simulation, the complete simulation procedure is performed for all converter layer types. This includes Geant4, ANSYS, Garfield++ and the clustering algorithm (introduced in chapter 5.6).
The normalized trigger rate[22] for simulation and measurement for 4 different converter layer types is displayed in figure 8.42. At $\Delta U_y = 0\,V$, simulation and measurement show good agreement. Both provide an improvement by a factor of 1.3 if the 1520 + 41 FR4 layers[23] are replaced by the 250 + 33 FR4 layers, and a further increase by a factor of 1.5 if the layers are replaced by the 100 + 38 PI layer type. While the 100 + 18 PI layer performs about 20 % better than the 100 + 38 PI layer in the measurement, both layer types give the same result in the simulation. This difference can be caused by the difficulty of installing the thin layers straight into the detector, as previously mentioned.
When increasing ΔU_y, the deviation between simulation and measurement increases by up to 20 % at 600 V. This observed deviation at higher ΔU_y values is mainly caused by the electric fields of ANSYS. As the comparison of measurement (see figure 8.18) and simulation (see figure 8.19) shows, the simulated fields behave identical for all layers, while the 1520 + 41 FR4 layer shows a lower guiding efficiency in the measurement. Since the results for simulation and measurement are each normalized to the 1520 + 41 FR4 layer, the increase in the relative trigger rate is lower in the simulation than in the measurement.
In the simulation, there is a statistical uncertainty of about 20 % due to the limited statistical data. Within this error interval, the results of simulation and measurement for the 4 investigated converter layers types agree.

For a more detailed comparison of these results including the two 50 µm PI layer types, the simulated and measured relative trigger rate values for the same voltage difference ΔU_y are investigated. Figure 8.43 shows the final comparison result of the relative trigger rate for

[22] The main peaks in the detected cluster charge above the background originate from the 59.5 keV photon interaction processes with the converter layers (see chapter 8.5.1). To better compare the effects of the converter layers in the simulation, a cut is performed in the simulation on the primary electron energy between 2.0 keV and 8.0 keV.

[23] Due to minor changes compared to chapter 5, such as the implementation of the ENIG layer, there are slight deviations in the relative trigger rate compared to figure 5.36.

all converter layer types and all voltage differences ΔU_y.

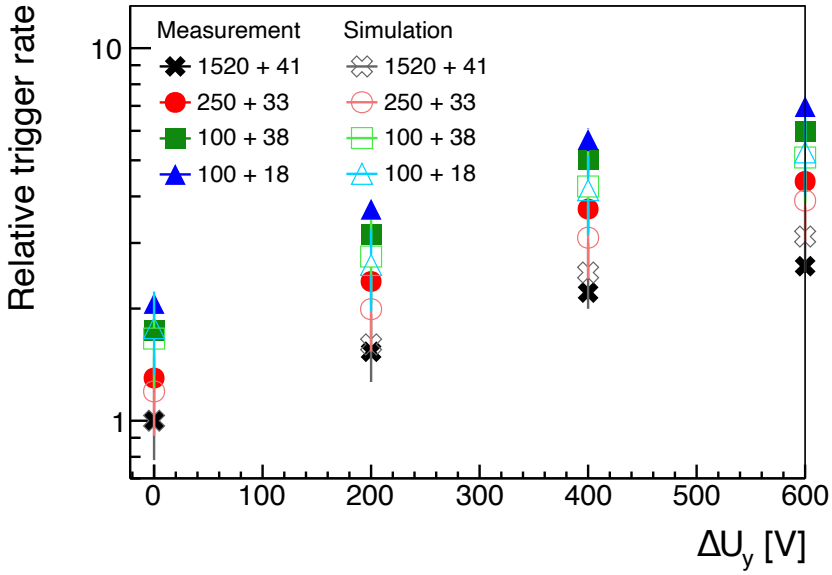

Figure 8.42: The relative trigger rate is determined for different ΔU_y values and 4 converter layer types. The simulation and measurement results are each normalized to the 1520 + 41 FR4 layer at $\Delta U_y = 0\,V$. At $\Delta U_y = 0\,V$ the simulated and measured relative trigger rate for the 100 + 38 PI layers is a factor of 1.8 higher than for the 1520 + 41 FR4 layers. The trigger rate increases with ΔU_y. The other layers types behave accordingly, providing an overall good agreement between simulation and measurement within the error interval.

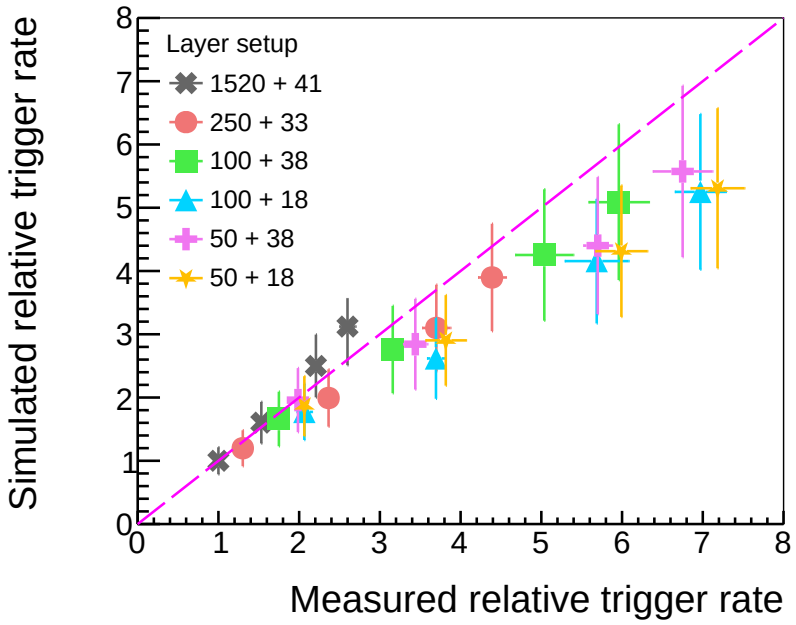

Figure 8.43: For each ΔU_y of the same converter layer type, the ratio of the measured and simulated value of the trigger rate is extracted from figure 8.42 and presented in this correlation plot. The pink dashed diagonal line indicates perfect agreement between simulation and measurement. For small relative trigger rates, meaning small ΔU_y, the results lie very close to this line, indicating good agreement. For higher values, the simulated trigger rate is smaller than the measured one, but still in good agreement regarding the error intervals.

Especially for low relative trigger rate values, all converter layer types show good agreement

between simulation and measurement. As expected from the above discussion, the discrepancies increase with higher ΔU_y values.
The converter layer types made of a thin PI insulating material (50 µm or 100 µm of PI) provide the highest trigger rate and therefore photon detection efficiency. This behavior is in agreement with the expectations from section chapter 8.5.4. Thus, the good agreement between simulation and measurement also confirms the results extracted by simulation about the processes occurring in the converter layers. A precise understanding of the occurring physical processes and their influence on the working principle of the converter layers and the photon detection probability is obtained.

8.7 Improved Photon Detection Efficiency

Since the detection efficiency correlates directly with the trigger rate, the converter layers consisting of a thin PI layer as carrier material have a higher detection efficiency than 1520+41 FR4 layer types.
In chapter 5.8 the detection efficiency for the 1520 + 41 FR4 converter layers is determined to be 0.46 % at ΔU_y = 600 V (see equation 5.11). The 0.46 % corresponds to the simulated relative trigger rate of 3.1, which has an error of 0.5 according to figure 8.43. Thus, the error in the detection efficiency is estimated to be $(0.46 \pm 0.07)\%$.
According to figure 8.17, the measured trigger rate increases by a factor of 3 for the 50 + 18 PI layer at ΔU_y = 800 V, resulting in a photon detection efficiency of[24]:

$$\begin{aligned} \varepsilon_{\text{detection (50 + 18)}} &= 3 \cdot \varepsilon_{\text{detection (1520 + 41)}} \\ &= 3 \cdot (0.46 \pm 0.07)\% \\ &= (1.38 \pm 0.21)\% \end{aligned} \tag{8.4}$$

This is twice as large as the pure conversion probability of $\varepsilon_{\text{conversion}}$ = 0.69 % for 59.5 keV photons in gas, ignoring losses due to the electron guiding. When comparing the simulation and measurement with respect to the initial simulated trigger value of (3.1 ± 0.5) for the 1520+41 FR4 layer type, the measured value is (2.6 ± 0.1) (see figure 8.43), which corresponds to the lower range of the simulated value including the error interval and thus a detection probability of 1.17 %. These deviations between simulation and measurement arise mainly due to the limited statistics in the simulation and the electric field configuration provided by ANSYS (see chapter 8.4.3). Since the simulation and measurement agree within this error interval, the estimated detection efficiency of the 50 + 18 PI layers is within $(1.38 \pm 0.21)\%$.
To disentangle the various contributions to the detection efficiency of 1.38 %, the simulation results obtained in this chapter are used, focusing in particular on the 4.8 keV electron peak. While 70 % of the detected electrons form the background in the cluster charge distribution, 30 % arise from peak values originating from the converter layers (see chapter 8.5.1). Thus, the peaks account for 1.38 % · 0.3 = 0.41 % of the overall detection efficiency.
Here, the main contribution comes from the 4.8 keV electrons (see figure 8.32), which are created by the 8.0 keV K_α transition photons in copper. For these photons a conversion efficiency of 0.35 % is estimated in chapter 8.5.4 for the 5 layers of the type 100 + 38 PI. Including the guiding efficiency of 67 % (see figure 5.37 and figure 8.19) this results in a detection efficiency of 0.23 %. Since this value refers to the 100 + 38 PI layers, the value for the 50 + 18 PI layers is supposed to increase by 20 %, to about 0.28 %, when comparing the trigger rate between both layer types (see figure 8.17). This value for the 4.8 keV electron peak is smaller than

[24] While the trigger rate for the 1520 + 41 FR4 layers starts saturating at 600 V, it continues to increase for the 50 + 18 PI layers up to a voltage difference of 800 V.

the 0.41 % for all peaks. Since the 0.41 % accounts for all peaks and the 0.28 % only for the 4.8 keV peak as well as considering all assumed estimations, these two values demonstrate a reasonable agreement and thus provide consistency between both approaches.

Overall, the material optimization process increases the photon detection efficiency of the converter layers as intended.

8.8 Effects on 3D Position Reconstruction and Improvement of Detection Efficiency

The working principle of the converter layers differs from the initially assumed one, which has been applied as a basis for the position reconstruction method (see chapter 7.1). Instead of the photoelectron, the K_α transition photon exits the converter layer strips, where both are created by the 59.5 keV photon interaction via the photoelectric effect. The K_α transition photon has an energy of 8.0 keV, is emitted in 4π and can interact anywhere in the gas, creating a detectable electron. Thus, it does not contain any information about the initial 59.5 keV photon like momentum or interaction position. This different working principle of the converter layers strongly affects the position reconstruction method, as mentioned in chapter 8.5.1, but also explains some unresolved results from chapter 7.
The effects on position reconstruction and approaches for improving the photon detection efficiency are discussed here.

8.8.1 Measurement: Tilting Angle

The measured hit distribution with a single converter layer exhibits two peaks for $\Delta U_\mathrm{x} = 400\,\mathrm{V}$ (see figure 7.8). While the first peak originates from electrons from the back side of the layer, the second peak comes from electrons from the front side. According to figure 2.2, about 16 % of the photoelectrons are emitted in the backward direction ($\theta > 90°$) and 84 % in forward direction ($\theta < 90°$), so when considering the initial working principle, a smaller first peak in the hit distribution has been expected than actually measured.
The 59.5 keV photon interacts with the strips of the converter layer. Since the converter layer is a double-sided PCB, the interactions occur in the strips on the front and back side of the layer. Since the 8.0 keV photons exit the strips in a random direction in 4π, half of these photons leave the strip in backward direction (negative component in x-momentum direction) and the other half in forward direction (negative component in x-momentum direction). Depending on the position of the strips on the front or back side of the converter layer, the photons either enter the gas directly or traverse the carrier material (see chapter 8.5.4). The crucial aspect is that about the same amount of photons emerge from the front and back of the strips.

For a proof of concept a single tilted converter layer is placed in the GEM detector, as introduced in chapter 7.2.1. Instead of tilting it by 60° with respect to the GEM foil, it is tilted by 120°, meaning in the mirrored configuration as presented in figure 7.2. The configuration of the electric field is adjusted such that the electrons produced at the back side of the 120° setup experience the same force as the electrons produced at the front side of the 60° setup. In figure 8.44 the measured trigger rate for both setups is compared. Both measurements provide the same trigger rate within the uncertainties. In particular, for $\Delta U_\mathrm{x} = 0\,\mathrm{V}$ the same trigger rate is measured. For this voltage difference the peak integral ratio between the first and second peaks is $I_1/I_2 = 0.3$ for the 60° setup (see chapter 7.2.5), so the contribution of second peak is higher due to the electric field configuration. For the 120° setup, the main

contribution arises from the first peak on the back side. Due to the mirrored configuration and the equal exit probability of the 8.0 keV photons in all directions, a similar trigger rate is measured[25].
Therefore, the origin of the large first peak for $\Delta U_x = 400\,\mathrm{V}$ in the hit distribution in figure 7.8 is understood.

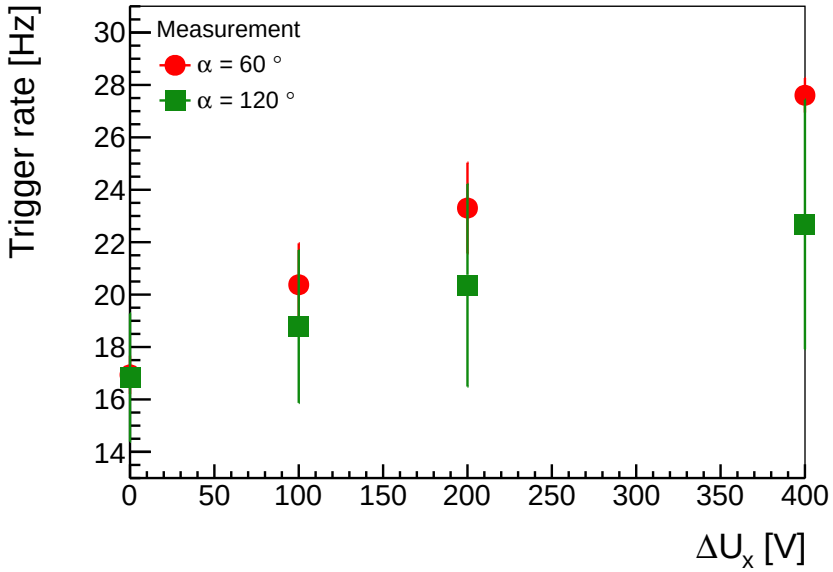

Figure 8.44: For a single tilted converter layer, as shown in figure 7.2, a ΔU_x voltage scan is performed. Two tilting angles are compared: 60° and 120°, meaning the mirrored configurations. Both setups provide the same trigger rate within the given uncertainties. Therefore, in a mirrored configuration, the trigger rate is independent of the tilting angle and the same amount of transition photons emerge in the forward and backward directions. This is another proof of concept for the detection of K_α transition photons. $\Delta U_y = 600\,\mathrm{V}$ is constant.

8.8.2 Simulation: Photon Conversion and Interaction

This working principle of the converter layers has a significant effect on the accuracy of the position reconstruction method.
The 8.0 keV photon has an interaction probability of about 25 % in 11 mm argon [Berger et al., 2010]. This interaction probability can be seen in figure 8.40, when considering the number of photons entering gas and interacting there. Thus, the interaction occurs in 25 % somewhere between two layers, which have a distance of 11 mm. But the majority of photons is either absorbed by the next layer or leaves the gas volume without interaction. Moreover, the transition photon leaves the strip in a random direction. Consequently, the interaction of the 8.0 keV photon occurs anywhere in the gas and the created and detected electron contains no information about the initial 59.5 keV photon and its interaction.

[25] For $\Delta U_x = 0\,\mathrm{V}$ simulation and measurement show a good agreement regarding the peak profile properties like width or integral ratio. The latter is $I_1/I_2 = 0.3$, whereby the integral I is influenced by the number of created electrons on the corresponding side of the converter layer e and the guiding efficiency g, resulting in $I_1/I_2 = (e_1 \cdot g_1)/(e_2 \cdot g_2) = 0.3$. The total number of electrons is thus given by $I_1 + I_2 = 1.3 \cdot I_2 = 1.3 \cdot e_2 \cdot g_2$. Assuming the initial working principle of detecting the photoelectron exiting the copper strips, about 5.3 times more photoelectrons are emitted forward direction ($\theta < 90°$ in figure 2.2), leading to $e_1 = 0.19 \cdot e_2$. The electron drift is defined by the drift lines starting at the converter layer (see figure 7.11 for $\Delta U_x = 400\,\mathrm{V}$). Thus, for the voltage combination used here $g_1 < 0.5 \cdot g_2$ can be estimated. When using a mirrored configuration, the total integral is $\tilde{I}_1 + \tilde{I}_2 = e_1 \cdot g_2 + e_2 \cdot g_1 < 0.19 \cdot e_2 \cdot g_2 + 0.5 \cdot e_2 \cdot g_2 \approx 0.7 \cdot e_2 \cdot g_2 \approx 0.5(I_1 + I_2)$. This shows, with the initially assumed working principle, tilting the converter layers would lead to half of the trigger rate at $\Delta U_x = 0\,\mathrm{V}$.

Assuming the 59.5 keV photon interacts in copper at the position $pos_{\text{int 59.5 keV}}$, where the 8.0 keV K_α transition photon is created. It exits the strip and interacts with the detector gas at the position $pos_{\text{int 8.0 keV}}$, creating a detectable electron. The distance between these two interaction points is defined as:

$$\Delta pos_{\text{int}} = pos_{\text{int 59.5 keV}} - pos_{\text{int 8.0 keV}} \tag{8.5}$$

It is presented in figure 8.45 for the x-, y- and z-dimension. In all dimension Δpos_{int} mainly ranges from −10 mm to 10 mm, with a peak around 0 mm. Therefore, for the x-position the 8.0 keV interaction occurs anywhere between the point of creation in the copper strip of one layer and the next neighboring converter layers in forward or backward direction, which have a distance of ±11 mm. The y-position shows fluctuations that are similar to the layer height of 20 mm.
This effect explains the result in figure 7.36, for the position reconstruction approach in chapter 7.4.2, where large discrepancies of the reconstructed y-position for similar detected x-positions is observed. Due to the high Δpos_{int} values in all dimensions, the electron is produced anywhere in the gas, resulting in different y- values for the same x-value. This effect and the absence of almost any correlation between the detected position and the interaction position make it impossible to reconstruct the 59.5 keV interaction position using this method.

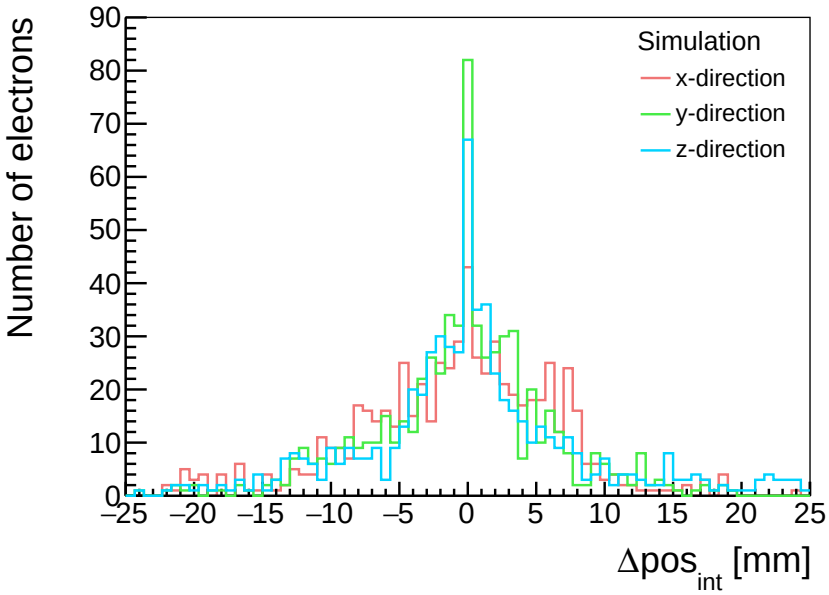

Figure 8.45: The distance between the 59.5 keV and 8.0 keV photon interaction position for the x -, y- and z-coordinate is calculated using equation 8.5. Although for all dimensions there is a sharp peak around 0 mm, meaning both interaction points lie close to each other, the distances extend up to ±10 mm. The latter behavior strongly limits the position reconstruction method. Only the interactions in the gas volume where the converter layers are placed (between −42.5 mm < x < −0.4 mm) are considered.

The variation in the z-dimension also ranges between ±10 mm, according to figure 8.45. Due to this variation in the z-position, the copper block to be imaged is not clearly visible in figure figure 7.34. The 8.0 keV photons exiting the copper strip can interact behind the copper block, leading to the detected events behind the block and reducing the contrast in this region where the copper block is expected.

8.8.3 Outlook: Future Challenges for Improved Position Reconstruction and Detection Efficiency

Understanding the functional principle of the converter layers and their effects on 3D position reconstruction forms the basis for future developments and improvements of the converter layers. The investigations in this chapter have demonstrated that the physical processes occurring deviate from the initial assumptions. This influences further optimization processes to improve detection efficiency, as additional aspects have to be taken into account. Consequently, this leads to more complex correlations, which are discussed here.

To realize a 3D position reconstruction with the converter layers, the distance between the 59.5 keV photon interaction position and the electron creation position (see figure 8.45) has to be minimized.
One option is finding a material where the extraction of the photoelectron is the dominant process. When considering this operation principle, the influences of the electric field and ion movement also have to be studied. Due to the secondary ionization in the gas, ions are created, which move towards the converter layers (see figure 5.28). When the photoelectron exits the strip, there are many ions in the vicinity of the strip, increasing recombination and reducing the detection probability of this photoelectron. This effect complicates the implementation of this approach.
Another approach is a more efficient detection of the transition photon, produced by the photoelectric effect of the 59.5 keV photon. This is a major challenge if a high photon detection efficiency is required at the same time. The photoelectric cross-section σ_{photo} scales with Z^5, according to equation 2.7, so the photon interaction probability increases with high-Z materials. As shown in this chapter, the detected electron is created by the K_α transition photon. The photon energy of the K_α transition can be estimated by Moseley's law [Moseley, 1914]:

$$E_{\text{K}\alpha} = 10.2 \cdot (Z-1)^2 \text{eV} \tag{8.6}$$

This correlation indicates the main challenge, when searching for an alternative conversion material: While a higher-Z material increases the photon conversion efficiency, the energy of the transition photon rises simultaneously with Z^2. Consequently, the transition photon has a higher energy in a material with a higher Z, which reduces the interaction probability in the detector gas due to $\sigma_{\text{photo}} \sim E_\gamma^{-3.5}$ (see equation 2.7). In addition, the low interaction probability increases the range of the transition photon in the detector, leading to a high deviation between its creation and interaction point and renders the reconstruction of the position impossible.
Therefore, a high-Z material does not automatically increase the overall detection efficiency. The choice of the appropriate material is more complex, as all these contributing aspects have to be included in a thorough investigation. An option could be the usage of multilayer converter strips, consisting of at least 2 different materials with different atomic numbers Z. First a material with high Z for an efficient 59.5 keV photon conversion, followed by a material with lower Z in which the transition photons interact, leading to a further energy reduction according to equation 8.6. This process can be repeated as often as required with different, coordinated materials. Each material thickness has to be optimized with regard to the number of transition photons produced and directly absorbed. In addition, materials that are too thick ($\mathcal{O}(d)$ = mm) reduce the position reconstruction accuracy. In the end, a photon with a high interaction probability in detector gas is needed. As an alternative, the last material could be chosen such that the photoelectron emerges, whereby the aspects discussed above have to be taken into account. Thus, the distance between initial interaction and detection point is reduced. To what extent this is feasible has to be investigated in more

detail in future research.

8.9 Summary on Material Optimization

In this chapter the working principle of the converter layers is understood. Despite the initial assumption of detecting the photoelectron exiting the copper strip, the photon of a K_α transition is detected. The 59.5 keV photon interacts with the strip of the converter layer via the photoelectric effect. In K-shell the vacancy is filled by an electron from a higher shell, leading to the emission of a K_α transition photon. For copper this photon has an energy of 8.0 keV. It exits the strip in a random direction and interacts with the gas anywhere in the detector, creating a 4.8 keV primary electron. This electron causes secondary ionization in the gas and is detected. The same processes occur in ENIG. While the K_α transition is the dominant effect, also the transitions from other shells arise.
Due to this working principle, there is no correlation between the interaction position of the initial 59.5 keV photon and the detection position of the electron, created by the K_α transition photon. Therefore, the results from chapter 7 are understood, but the introduced position reconstruction methods with the converter layers used here are not feasible.

This chapter aims to increase the detection efficiency of the detector compared to chapter 5 by material optimization. In total 6 different converter layer types are investigated, differing in the insulator thickness, the insulating material and the strip thickness. For the various components the thicknesses and compositions are found and verified with a photon absorption measurement using a HPGe detector. In addition, the absorption properties of the layers are investigated. While in 3 layers 1520 µm FR4 about 30 % 59.5 keV photons are absorbed, the absorption in 100 µm PI is negligible.
The trigger rate and thus the detection efficiency increases when using thinner converter layers consisting of PI instead of FR4 as insulating material. For 5 converter layers in a GEM detector, the highest trigger rate is achieved with the converter layers made of 50 µm PI and 18 µm thick strips. It is about 3 times higher compared to 1520 µm FR4 layers with 41 µm thick strips at a voltage difference of ΔU_y = 800 V, resulting in an increased detection efficiency of $(1.38 \pm 0.21)\%$
The main reason for the different detection efficiency of the converter layers is their photon absorption behavior, especially for the transition photons. In 1520 µm all 8.0 keV photons are absorbed, whereas in 100 µm PI it is about 20 %. This deviation is the main reason for the different detection efficiency of both layers. With a detailed analysis of the Geant4 simulation results the exact contributions of the various interaction processes of the 8.0 keV photons and their influence on the detection efficiency is understood. The measured and simulated relative trigger rate for all converter layer types show a good agreement.

Therefore, this chapter provides a detailed understanding of the operating principle of the different converter layer types, which can be used for future improvements. In addition, the photon detection efficiency is improved by adapting the material and its thickness.

Chapter 9

Detection Efficiency of a GEM Detector with Converter Layers for 511 keV Photons

9.1 Motivation

PET (Positron Emission Tomography) is an imaging technique used in medical diagnostics, for example, for detecting cancer (see chapter 1.2.2). This imaging procedure includes a radioactive tracer, which emits a positron as a result of β^+ decay. When this positron annihilates, two 511 keV photons are emitted in opposite directions, which have to be detected with a good spatial resolution and high efficiency.
Therefore, the application of the GEM detector with converter layers for PET requires a complete 3D position reconstruction (see chapter 7.1) and a high detection efficiency for 511 keV photons. The latter requirement is investigated in this chapter, aiming at an experimental determination of the detection efficiency for 511 keV photons. This measurement is done using a newly designed coincidence setup with scintillation detectors. The working principle of this setup and a verification of its functionality are also presented.

9.2 Measurement Setup

9.2.1 Working Principle of Scintillation Detector

A scintillation detector [Curran and Craggs, 1949] consists of two optically coupled main components: a scintillator and a Photomultiplier Tube (PMT). Its main advantages are a high sensitivity, a good energy resolution, and a fast response time.
Its working principle [García-León, 2022; Leo, 1995] is illustrated in figure 9.1. When a photon enters the scintillator it interacts with the material via the photoelectric effect, the Compton effect or by pair production. In these processes, electrons are created. These can further ionize the material. In addition, the electrons cause excitation when transferring their energy to the atoms or molecules in the scintillation material. The de-excitation to the ground state leads to the emission of low-energy photons whose wavelengths are typically in the visible or ultraviolet range and are collectively known as scintillation light. The amount of photons produced is proportional to the energy deposited and thus to the energy of the initial photon. The scintillation light is directed to the PMT, where it interacts with the photocathode via the photoelectric effect, producing photoelectrons. Focusing electrodes accelerate the

photoelectrons to the first dynode, resulting in the creation of secondary electrons on impact. As a result of the voltage differences between the dynodes, the electrons are accelerated to the next dynode, where more electrons are emitted. This process is repeated for all the dynodes, amplifying the number of electrons. At the anode, the electrons are collected, producing a current signal which is converted into a voltage pulse. The amplitude of this voltage pulse is proportional to the energy deposited by the initial particle and is further processed by the readout electronics.

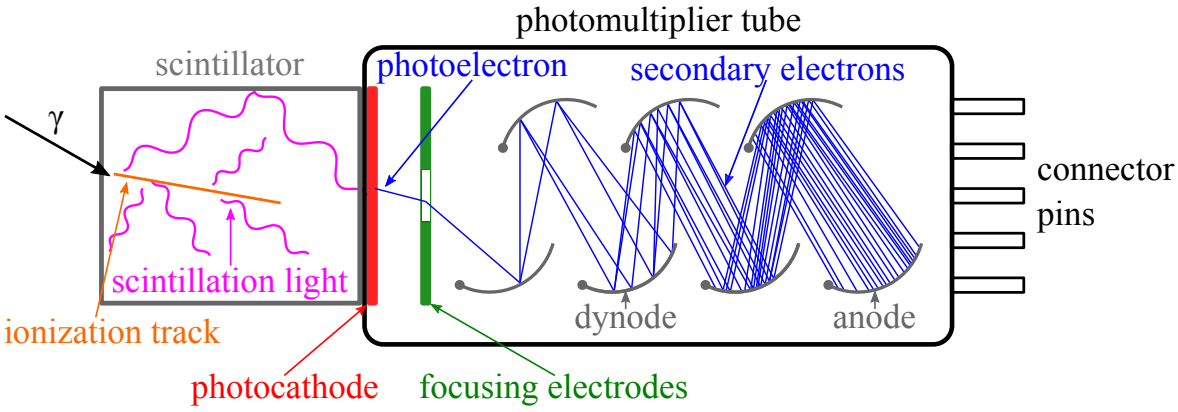

Figure 9.1: Schematic of a scintillation detector: An incoming photon interacts with the scintillation material, creating an electron that excites the atoms in the material to a higher energy state. Scintillation light is emitted in the de-excitation process. This light is guided to the PMT. It interacts with the photocathode, producing a photoelectron, which is directed to the dynode by focusing electrodes. Due to the impact of the electron, new electrons are released. As a result, the electrons are amplified by the dynode structure in the PMT. The anode provides the output signal.

In this thesis, detectors with two different scintillation materials are used: lanthanum bromide ($LaBr_3$) or sodium iodide (NaI). Although $LaBr_3$ offers a better energy resolution and a faster response time compared to NaI, NaI detectors are widely used due their low cost and adequate performance [Milbrath et al., 2007].

9.2.2 Sodium-22 Particle Source

The measurements are performed with a Sodium-22 (^{22}Na) particle source, as 511 keV photons are produced in its decay. Figure 9.2 shows the decay scheme.
The dominant decay mode of ^{22}Na is the β^+ decay via the excited state of Neon-22 (^{22}Ne*), resulting in the emission of a positron (e^+) and electron neutrino ν_e:

$$\begin{aligned} {}^{22}_{11}\mathrm{Na} &\rightarrow {}^{22}_{10}\mathrm{Ne}^* + \mathrm{e}^+ + \nu_e \\ {}^{22}_{10}\mathrm{Ne}^* &\rightarrow {}^{22}_{10}\mathrm{Ne} + \gamma\,(1275\,\mathrm{keV}) \end{aligned} \tag{9.1}$$

In the de-excitation process of ^{22}Ne*, a 1275 keV photon is emitted. The emitted positron annihilates with a surrounding electron, creating two 511 keV photons, which are emitted back-to-back:

$$\mathrm{e}^+ + \mathrm{e}^- \longrightarrow \gamma(511\ \mathrm{keV}) + \gamma(511\ \mathrm{keV}) \tag{9.2}$$

The rare decay of ^{22}Na directly into the ground state of ^{22}Ne is neglected.
There is also the possibility of Electron Capture (EC), where an orbital electron is captured, leading to the the excited ^{22}Ne* state:

$$^{22}_{11}\mathrm{Na} + \mathrm{e}^- \longrightarrow {}^{22}_{10}\mathrm{Ne}^* + \nu_e \tag{9.3}$$

In that case, the same de-excitation process as described previously occurs, leading to the emission of a 1275 keV photon. However, no 511 keV photons are produced.

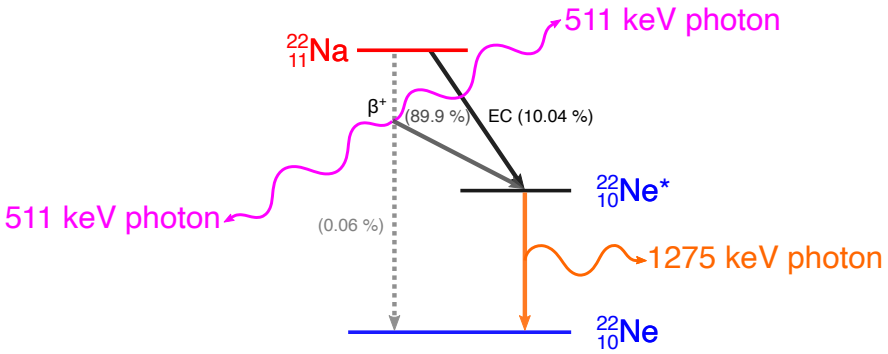

Figure 9.2: ^{22}Na decay scheme following [Basunia, 2015]: The two main decay processes for ^{22}Na are β^+ decay, with a rate of 90 %, and electron capture, with a rate of about 10 %. Both result in the excited state of ^{22}Ne*. In the de-excitation process a 1275 keV photon is emitted. The positron from the β^+ decay annihilates with an electron, creating two 511 keV photons, which are emitted back-to-back. The direct β^+ decay is negligibly small.

^{22}Na has a half-life of 2.6 years and an activity of 3.2 MBq. Altogether, one 1275 keV photon is emitted in every decay and two 511 keV photons are emitted in 90 % of the decays, resulting in intensities of 100 % and 180 %, respectively.

9.2.3 Sodium-22 Spectrum Measured with $LaBr_3$ Scintillation Detector

The energy spectrum of the ^{22}Na particle source is measured[1] with a $LaBr_3$ scintillation detector[2] and shown in figure 9.3.
The 511 keV and 1275 keV photopeaks as well as the corresponding Compton edges (see figure 2.3) are clearly visible. A peak position ratio of μ_2/mu_1 = 1143.6/467.7 = 2.45 is measured, which is in good agreement with the expected 1275 keV/511 keV = 2.50. The relative energy resolution of a detector at the energy E is defined as [Leo, 1995]:

$$\text{resolution} = \frac{\Delta E}{E} \tag{9.4}$$

where ΔE is the FWHM of the energy peak. The FWHM is given as FWHM = $2\sqrt{2\ln 2}\cdot\sigma \approx 2.355\cdot\sigma$. With the values from figure 9.3, this results in an energy resolution of 4.7 % at 511 keV and 3.9 % at 1275 keV.
Since the 511 keV photons have a 1.8 times higher intensity and an approximately 2.3 times higher photopeak efficiency [Aldawood et al., 2015] compared to the 1275 keV photons, it is expected that 4.2 times more photons are detected in the 511 keV photopeak than in the

[1] The voltage pulse from the scintillation detector is shaped and amplified and fed to a Digital Multichannel Analyzer [Amptek, 2024], which measures the amplitude and creates a pulse height spectrum.
[2] It is a Saint Gobain 38S38 LaBr3 Detector [Saint-Gobain Crystals, Scintillation Products, 2009] with a Hamamatsu R6231 photomultiplier [Hamamatsu, 2024]. The scintillating crystal has a size of diameter of 3.81 cm (1.5″) and the same thickness. In addition, the scintillator contains about 5 % Ce [Saint-Gobain Crystals, Scintillation Products, 2009].

1275 keV peak. Comparing the integral of both peaks leads to a difference of $I_2/I_2 = 4.4$, which is close to the expected value.

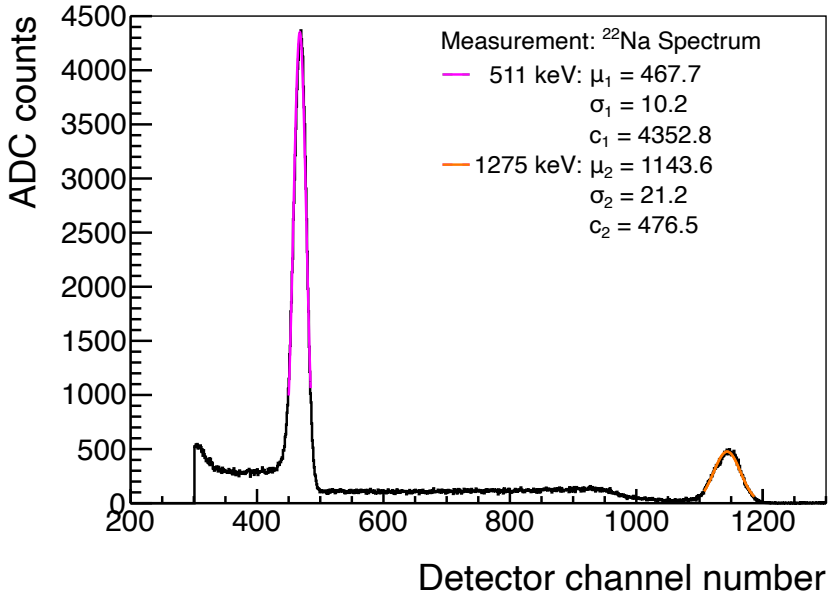

Figure 9.3: Energy spectrum of the ^{22}Na source measured with the $LaBr_3$ scintillation detector. The Compton distribution with its edge and the two photopeaks are visible, with the left peak originating from the 511 keV photons and the right from 1275 keV the photons. A Gaussian function is fit to each peak, providing the mean value μ, the width σ and the amplitude c of the peak. The detector has an energy resolution of 4.7 % at 511 keV and of 3.9 % at 1275 keV.

9.2.4 Coincidence Measurement Setup with Scintillation Detectors

A newly designed coincidence setup with scintillation detectors and the ^{22}Na source is used to determine the 511 keV photon detection efficiency. This setup is shown in figure 9.4.
Due to the high activity of the source, it is placed in a brass cylinder, which provides shielding. The photons emerge through three openings[3] As mentioned previously, in the dominant ^{22}Na decay process one 1275 keV and two 511 keV photons are released. Two scintillation detectors are placed at the top and right opening, one made of $LaBr_3$ and the other of NaI as scintillation material. The readout electronics, which is described in more detail in chapter 9.3.2, is adjusted to ensure that the $LaBr_3$ detector only detects 1275 keV photons. The coincidence measurement is performed by requiring that both scintillation detectors record the photons within the same time frame. A coincidence signal indicates that a 511 keV photon is emitted in the direction of the testing detector. The comparison of the number of these coincident signals with the number of photons actually detected provides the detection efficiency of the testing detector.

[3] The brass shielding cylinder has been designed for this purpose [Dörfler, 2024]. It has a diameter of 20 cm and an length of 16 cm (see figure F.1 in appendix). The opening angle of the 511 keV photons is chosen such that all converter layers in the GEM detector experience the same photon intensity, if GEM detector is used as testing detector. For the 1275 keV photons, it is a round aperture with a diameter of about 1 cm.

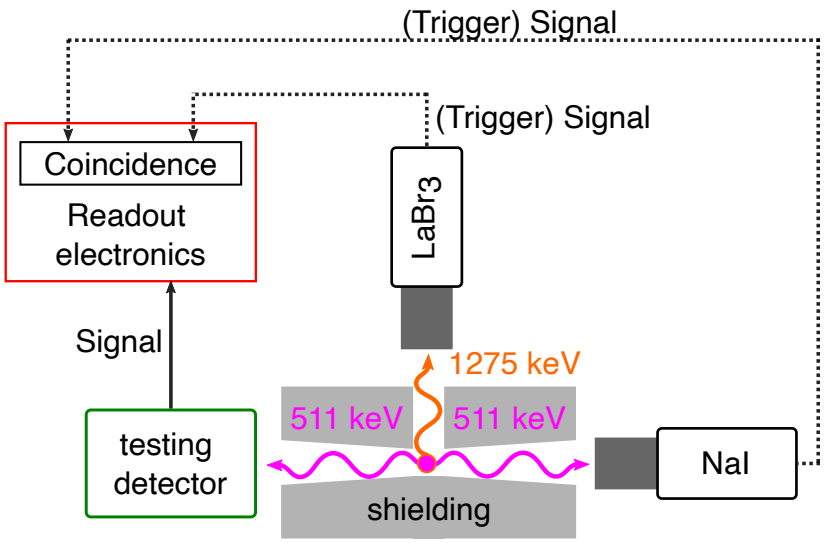

Figure 9.4: Sketch of the coincidence measurement setup. The ^{22}Na is placed in a brass cylinder with three openings through which the photons emerge. In front of these openings, the two scintillation detectors and the testing detector are positioned. If the 511 keV photon and the 1275 keV photon are detected by the NaI and $LaBr_3$ detector simultaneously, a 511 keV photon has to be emitted in the direction of the testing detector. If this 511 keV photon is detected, a signal is sent to the readout electronics. The detection efficiency is measured by comparing the number of coincident trigger signals from the scintillation detectors with the number of signals provided by the test detector.

Scintillation detectors are particularly suitable for the coincidence setup, as they offer an excellent energy resolution, which enables explicitly triggering on the 1275 keV photons. In addition, they provide a high detection efficiency, which allows for a relative high trigger rate compared to other detector types.

The expected coincidence trigger rate is between 2–5 Hz. As demonstrated in Appendix F, this can be calculated knowing the geometry of the setup. A trigger rate in this order of magnitude is necessary, especially for a reliable measurement using the GEM detector as a testing detector[4]
With this setup, the efficiency of two different detectors is determined: a scintillation detector and the GEM detector with converter layers.

[4] In a first study, a coincidence setup between both 511 keV photons, meaning the NaI detector and the testing detector, has been investigated [Dörfler, 2024]. The scintillation detectors have a detection efficiency of about 80 %, resulting in a trigger rate of approximately 10×10^4 Hz for such a setup. Since the efficiency of the GEM detector is much lower ($\lesssim 1$ %, as shown in chapter 8.7) the probability of random coincidence is higher. Therefore, an additional triggering on the 1275 keV photons is used.

9.3 511 keV Photon Detection Efficiency of NaI Scintillation Detector

9.3.1 Coincidence Measurement Setup

A NaI scintillation detector[5] is used as a testing detector in order to verify that the coincidence setup operates as expected. The NaI testing detector has an efficiency of about 80 % for 511 keV photons [The Harshaw Chemical Company, n.d.]. A picture of the measurement setup is shown in figure 9.5.

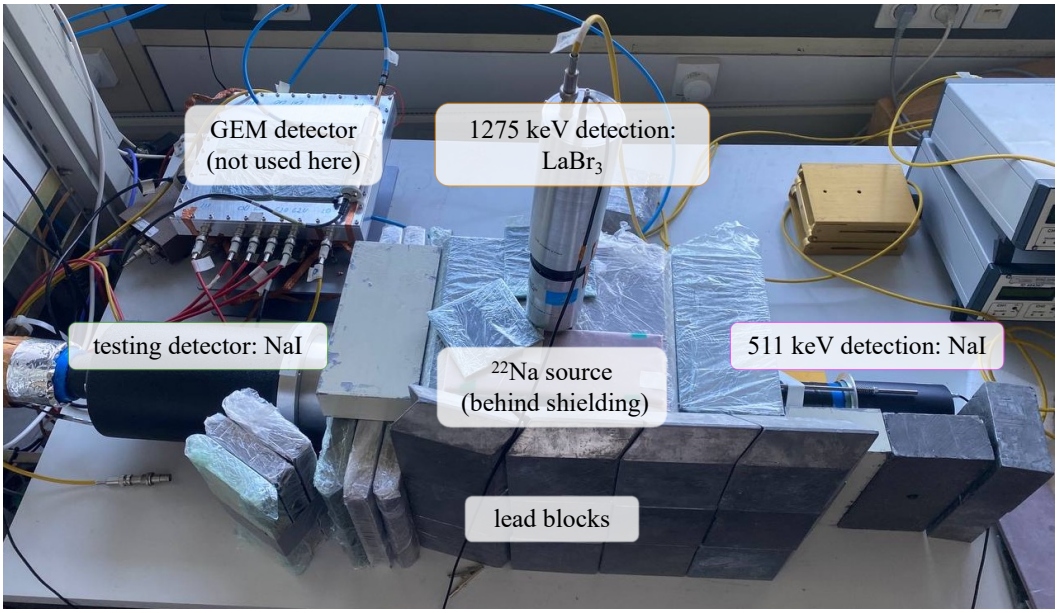

Figure 9.5: Picture of the coincidence measurement setup using a NaI scintillation detector for testing. For additional shielding, the brass cylinder with the ^{22}Na source is covered with lead blocks and is therefore not visible. The $LaBr_3$ scintillation detector is used to measure the 1275 keV photons. It is located on top of the shielding, while the NaI detector, which is utilized to detect the coincident 511 keV photons, is placed on the right-hand side. The NaI testing detector is located on the left. The GEM detector at the back of the image is not used in this specific measurement.

9.3.2 Readout Electronics

All output voltage signals from the scintillation detectors are processed by a trigger and DAQ system to provide digital data for further analysis. As introduced in chapter 9.2.4, the settings of the readout electronics have to ensure that the $LaBr_3$ detector only detects 1275 keV photons. In addition, a coincidence between the NaI and the $LaBr_3$ detector has to be established. The readout electronics logic for the coincidence measurement using a NaI scintillation detector for testing is sketched in figure 9.6.

The voltage signal of each detector is either fed directly into a delay unit, as with the $LaBr_3$ detector, or via a Timing-Filter-Amplifier [Ortec, 1969], as with both NaI detectors. In the latter case, the signal is additionally shaped and amplified. In the delay unit [CAEN, 2024b], the transmission of the signal can be delayed. Setting this delay time ensures that the signal

[5] It is a NaI(TI) scintillation crystal from the company Harshsw/Filtrol of the type 20MB24/51-LXN with a diameter of 12.7 cm (5″) and the same thickness.

timing is aligned between all detectors. This is mainly necessary to compensate for time differences that occur in the readout electronics, for example, due to cables of different lengths or additional modules.
To generate a coincident trigger signal with the NaI and $LaBr_3$ detector, the signal of these two detector is split and sent to the discriminator [CAEN, 1996] and the Charge-to-Digital-Converter (QDC) [CAEN, 2024c]. For both detectors, the threshold in the discriminator has to be adjusted. While with the NaI detector it has to be ensured that no noise is measured, with the $LaBr_3$ detector only the 1275 keV photons should fall below the threshold. Each signal is forwarded from the discriminator to a coincidence unit [CAEN, 2024a]. If both signals arrive within the same time window, meaning that their discriminator signal durations overlap, a NIM signal is fed into the Dual Timer [CAEN, 2023b]. It indicates the measurement of a coincident event. This trigger signal is used as a gate for the QDC. It defines the time window in which the QDC integrates the charge of the input signal and converts it into a digital value. The output signal from all three scintillation detectors is sent to the QDC, thus the deposited charge in these detectors is measured for a coincidence signal and forwarded to the DAQ Computer for further analysis.

The ^{22}Na energy spectrum of the LaBr3 detector measured with the QDC is shown in figure 9.7. It includes the full spectrum and a spectrum with a set threshold value in which only the 1275 keV photons are detected, which is required for the coincidence setup.

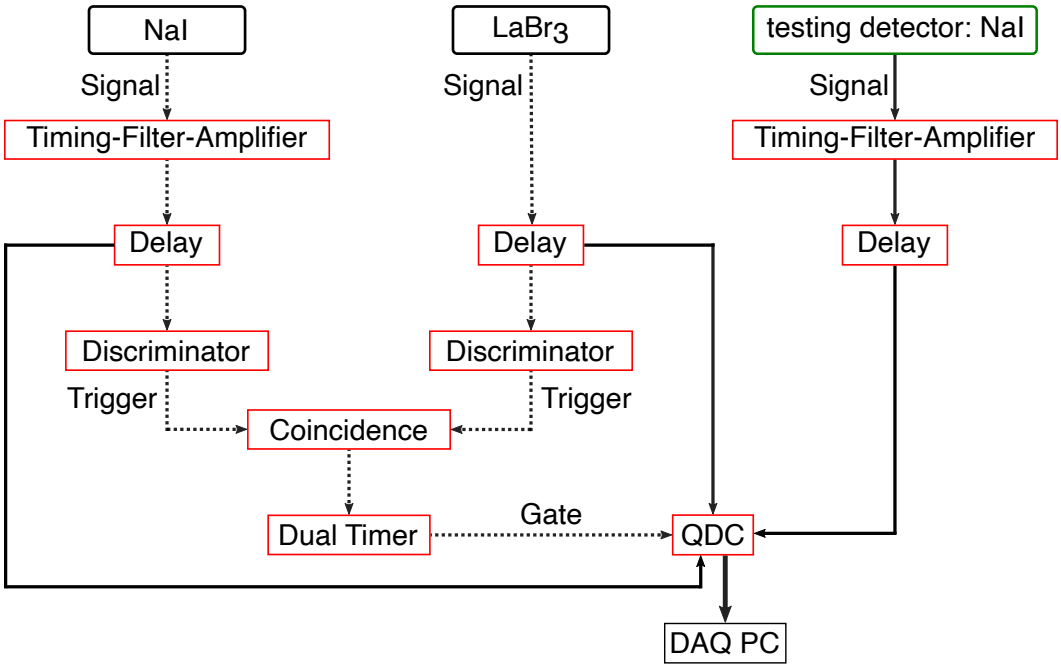

Figure 9.6: Sketch of the trigger and DAQ system for the coincidence measurement with a NaI scintillation detector as testing detector. The signals from all three detectors are processed by different components of the readout electronics and fed to a QDC. The signals of the NaI and $LaBr_3$ detectors are each sent to a discriminator for triggering. For the $LaBr_3$ detector, the threshold value is adjusted to enable the detection of 1275 keV photons. If both trigger signals indicate the simultaneous measurement of a 1275 keV and a 511 keV photon, the QDC is read out and thus the deposited charge is measured in all three detectors.

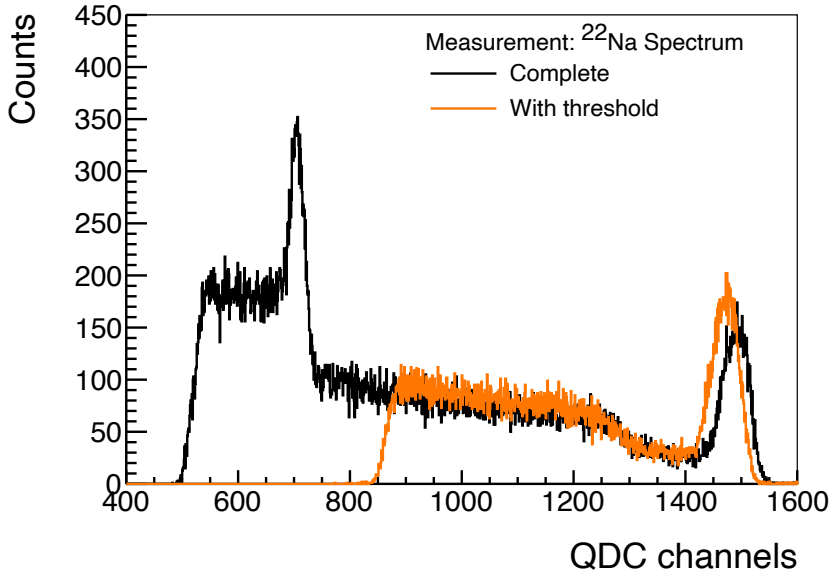

Figure 9.7: The ^{22}Na energy spectrum is measured with the $LaBr_3$ scintillation detector using the QDC. The full spectrum (black) is measured without the coincident trigger signal, thus the 511 keV and 1275 keV photopeak is observed[6]. By adapting the threshold value of the discriminator, only the 1275 keV photon is detected (orange), including the corresponding Compton distribution and the photopeak.

9.3.3 Determination of Detection Efficiency

If a coincident trigger signal is measured, a 511 keV is emitted in the direction of the NaI testing detector. By comparing the number of coincident signals and the number of detected events with this testing detector, its detection efficiency $\varepsilon_{\text{detection}}$ is obtained.
The correlation between the charge deposited in the $LaBr_3$ and in the NaI detector, which is measured at a coincident event, is shown in figure 9.8. For the $LaBr_3$ detector the 1275 keV photopeak is measured at about 1480 QDC channels, as expected from the spectrum in figure 9.7. The 511 keV photopeak from the NaI detector is at approximately 1900 QDC channels[7]. In both detectors, the lower measured energies are caused by Compton scattering of the respective initial photons.
This correlation diagram shows that a total of $I_{\text{Trigger}} = 44993$ signals are measured where a 511 keV photon and a 1275 keV photon are detected simultaneously. A total of 50 000 coincident trigger signals are measured, which leads to about 10 % of a random coincidence being detected. In the data acquisition process a precise measurement time is provided, resulting in an overall coincidence trigger rate of 1.08 Hz and, if the random coincidences are neglected, a true trigger rate of 0.97 Hz. It is smaller than the expected 2–5 Hz.
The deposited energy measured with the NaI testing detector is presented in figure 9.9, where the photopeak is observed at about 1400 QDC channels. In total, $I_{\text{Signal}} = 24508$ events with an initial photon energy of 511 keV are detected.

[6] This ^{22}Na spectrum shows slight differences compared to the previously measured spectrum in figure 9.7. Both spectra are measured with the same $LaBr_3$ detector and the discrepancies arise from the different measurement techniques of the digital multichannel analyzer and the QDC used for data acquisition.
[7] The measured QDC channels differ for various scintillation detectors. These differences arise for example from the detector material or geometry, the applied voltage or gain settings and are resolved by an energy calibration. It enables a correct correlation between the measured QDC channel and the deposited charge.

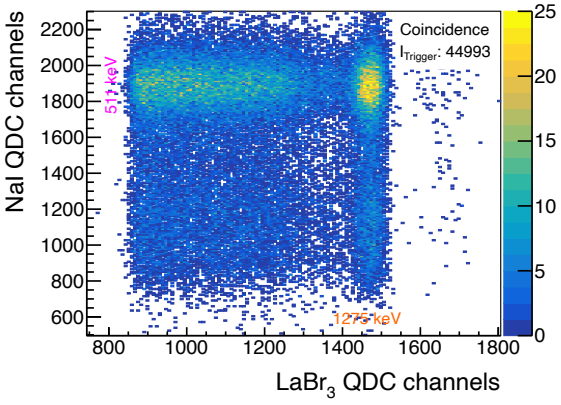

Figure 9.8: Correlation between the deposited charge in the NaI and $LaBr_3$ detectors for the coincident signals. The photopeaks and Compton distributions are measured in each detector. As intended in the measurement setup, a 1275 keV photon and a 511 keV photon are detected simultaneously for a trigger signal. In total, $I_{\text{Trigger}} = 44993$ real coincident signals are measured.

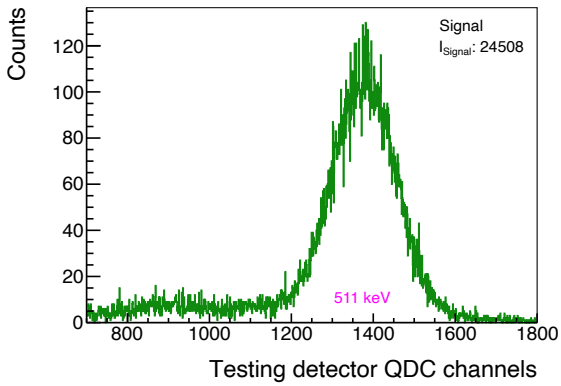

Figure 9.9: With the NaI testing detector $I_{\text{Signal}} = 24508$ 511 keV photons are measured with the coincident trigger setup. Thus, of about 45×10^3 511 keV photons emitted in the direction of the testing detector, around half of them are detected.

This results in a detection efficiency of

$$\begin{aligned} \varepsilon_{\text{detection(NaI)}} &= \frac{I_{\text{Signal}}}{I_{\text{Trigger}}} \\ &= \frac{24508}{44993} = 54.47\,\% \\ \Delta\varepsilon_{\text{detection(NaI)}} &= \sqrt{\varepsilon_{\text{detection(NaI)}} \cdot \frac{1-\varepsilon_{\text{detection(NaI)}}}{44993}} \\ &= \sqrt{0.54 \cdot \frac{1-0.54}{44993}} = 0.23\,\% \end{aligned} \tag{9.5}$$

which is smaller than the expected 80 %. This can arise from degradation in the efficiency due to the age and long usage of the detector [Zhu, 1998].
In conclusion, a reasonable detection efficiency for the NaI detector is determined with the coincidence measurement setup.

9.4 511 keV Photon Detection Efficiency of GEM Detector with Converter Layers

9.4.1 GEM Detector Setup with Converter Layers

To determine the 511 keV photon detection efficiency of a GEM detector with converter layers, the NaI testing detector used in the measurement setup in figure 9.5 is replaced by the GEM detector. In this GEM detector, 9 perpendicular arranged converter layers of the type 1520 + 41 FR4 are placed (introduced in chapter 8.2). It is shown in figure 9.10. All measurements are performed with a voltage difference of $\Delta U_y = 600\,\text{V}$ and $\Delta U_x = 0\,\text{V}$.

To verify the functionality of the GEM detector and the converter layers, a test measurement is performed without implementing the coincidence setup. The measured hit distribution is shown in figure 9.11. Photons are detected between all layers, which demonstrates that the detector and converter layers, including the electron guiding, are functioning.

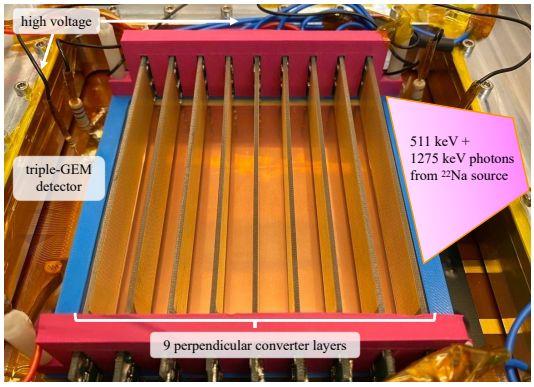

Figure 9.10: In the GEM detector, 9 converter layers of type 1520 + 41 FR4 are mounted perpendicular to the GEM foil. The 511 keV and 1275 keV photons emitted by ^{22}Na particle source emerge from the right through the detector housing.

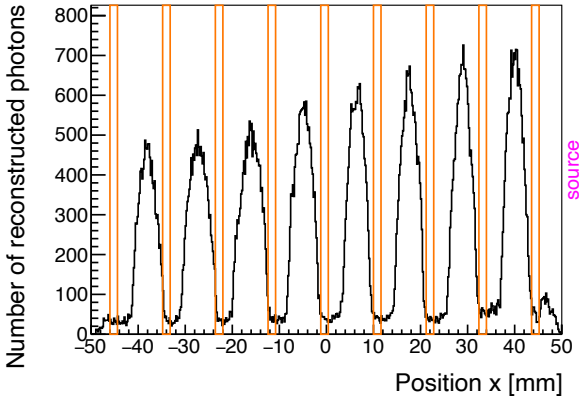

Figure 9.11: Hit distribution measured with 9 converter layers (orange boxes) in the GEM detector and the ^{22}Na particle source emitting 511 keV and 1275 keV photons.

9.4.2 Readout Electronics

For the coincidence setup with the GEM detector, the readout electronics has to be adapted, since the GEM detector provides an additional trigger signal. The coincidence readout setup for the $LaBr_3$ and NaI detector introduced in figure 9.6 is combined with the GEM detector readout from figure 4.1 and further extended[8]. The final readout scheme is shown in figure 9.12, whereby only the new components are displayed for a better overview.
For the GEM detector the trigger signal is provided by the bottom side of the lowest GEM foil, while the data signal is sent from the APV25 hybrid boards to the ADC. If the FEC receives a trigger signal, the detector is read out and the data is sent to the DAQ PC. This trigger signal is produced by measuring a coincidence between all three detectors.
Therefore, the trigger signal from the $LaBr_3$ and NaI detector is fed to the Coincidence unit, which sends a NIM signal to a Discriminator [LeCroy, 1996] in case of a simultaneous detection. Using this discriminator, the width of the signal is prolonged to about 800 ns. This is required, because the response time of the scintillation detectors is much faster than of the GEM detector with converter layers. The electron needs around 700 ns to drift from the top of the converter layer to the amplification stage of the GEM detector (see equation 5.7). This signal is transmitted via a dual timer to a coincidence unit, which also receives the trigger signal from the GEM detector. If both scintillation detectors measure a coincident signal and the GEM detector also measures a signal in the time window of 800 ns, a NIM signal is sent to the FEC and the GEM detector is read out and a coincident signal between all three detectors is measured.

[8] The various components of the readout electronics logic and their functionality are introduced in the corresponding sections.

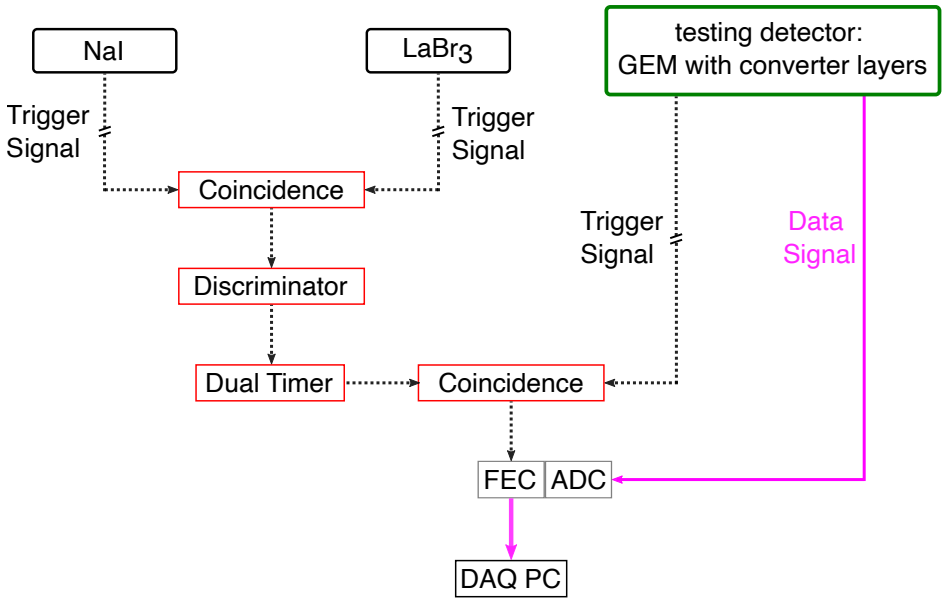

Figure 9.12: Simplified schematic of the readout electronics logic using the GEM detector as testing detector. The horizontal lines interrupting a connecting line indicate that additional readout modules are installed. The coincident signal from both scintillation detectors is fed to a discriminator for extending the pulse width to about 800 ns to account for drift time of the electron in the GEM detector. If this trigger signal and a trigger signal from the GEM detector are measured within this time window, it indicates a coincidence between all three detectors and the GEM detector is read out.

9.4.3 Determination of Detection Efficiency

For a first approximation of the expected increase when using converter layers instead to pure gas, the same Geant4 simulation introduced in chapter 5.6.1 is carried out, but with 9 converter layers of the type 1520 + 41 FR4 and the particle source emits 511 keV photons. According to this simulation, the 511 keV photon detection efficiency should increase by a factor of 2.1 when using these converter layers instead of pure gas.
The conversion efficiency in 100 mm argon is 0.14 % [Berger et al., 2010]. Thus, with converter layers in the GEM detector a conversion efficiency of

$$\begin{aligned} \varepsilon_{\text{expected conversion}} &= 2.1 \cdot 0.14\,\% \\ &= 0.29\,\% \end{aligned} \tag{9.6}$$

is expected.

In chapter 9.3.3 a true coincidence rate of 0.97 Hz between the NaI and $LaBr_3$ is given. If the true coincidence trigger rate between all three detectors would be the same, the GEM detector would have a detection efficiency of 100 %. But instead, a true coincidence of 1.5×10^{-3} Hz is measured between all detectors[9]. Thus, on average a signal is measured every 666 s. For the GEM detector with converter layers this results in a (preliminary) detection efficiency of:

$$\begin{aligned} \varepsilon_{\text{detection (prelim)}} &= \frac{1.5 \times 10^{-3}\,\text{Hz}}{0.97\,\text{Hz}} \cdot 100\,\% \\ &= 0.15\,\% \end{aligned} \tag{9.7}$$

[9] The true trigger rate for the GEM detector is provided after data analysis as in the previous chapters.

The GEM detector has to be placed at that distance of 14 cm from the brass cylinder opening due to the additional shielding with lead blocks. Consequently, not all layers see the complete radiation. As shown in Appendix F, in total 30 % of the 511 keV photons are emitted outside the active conversion area where the converter layers are positioned and are therefore not detectable. Thus, $\varepsilon_{\text{detection (prelim)}}$ has to be corrected by this effect, to obtain the real detection efficiency of the GEM detector with converter layers:

$$\begin{aligned} \varepsilon_{\text{detection}} &= \varepsilon_{\text{detection (prelim)}} \cdot \frac{1}{1-0.3} \\ &= 0.15\,\% \cdot \frac{1}{1-0.3} = 0.21\,\% \end{aligned} \tag{9.8}$$

Using the guiding efficiency for these converter layers of 67 %, which has been determined in chapter 5.7.3, the conversion efficiency is calculated:

$$\begin{aligned} \varepsilon_{\text{conversion}} &= \frac{\varepsilon_{\text{detection}}}{\varepsilon_{\text{guiding}}} \\ &= \frac{0.0021}{0.67} \qquad = 0.0031 = 0.31\,\% \end{aligned} \tag{9.9}$$

which is in good agreement with the estimated 0.29 % from the simulation. This demonstrates that the coincidence measurement setup works reliably and provides a good determination of the 511 keV detection efficiency of a detector. In addition, by using the converter layers instead of pure gas, the conversion efficiency is increased by a factor of about 2.

The detection efficiency of the GEM detector with converter layers can be increased by preventing the electrons created in the upper part of the converter layers from drifting upwards (see figure 5.28), for example by installing an additional cathode on top of the layers parallel to the GEM foil and applying a higher negative voltage. In future studies the different measurable quantities like cluster extension or cluster charge, the occurring interaction processes as well as the influence of the various converter layer types on the 511 keV photon detection efficiency can be investigated using this coincidence setup.

Chapter 10

ASD2 Chips Testing for ATLAS

10.1 Motivation

MDT (Monitored Drift Tube) chambers [Arai et al., 2008] are used in the ATLAS muon spectrometer [The ATLAS Collaboration, 2008] (see figure 1.1) for precision momentum determination of muons. Due to the High-Luminosity LHC (HL-LHC) upgrade, the luminosity increases by about an order of magnitude, leading to higher particle and background fluxes. Therefore, several upgrades of the different experiments take place, such as the Phase-II upgrade for the ATLAS MDT chambers [Kortner, 2019].
MDT chambers are made of two Drift Tube (DT) multi-layers, as shown in figure 10.1. The cross-section of one DT is visible in figure 10.2. It consists of an aluminum tube with an anode wire in the center. The design values of the DT are precisely specified with an outer diameter of $30.000 \pm^{0.000}_{0.030}$ mm and a wall thickness of 400 ± 20µm [ATLAS Muon Collaboration, 1997]. While the tube is grounded, a voltage of about 3080 V is applied to the wire, creating the electric field for the electron movement. The DT is filled with a gas mixture of Ar:CO_2 (93:7 vol. %) at an absolute pressure of 3 bar [The ATLAS Collaboration, 2008].

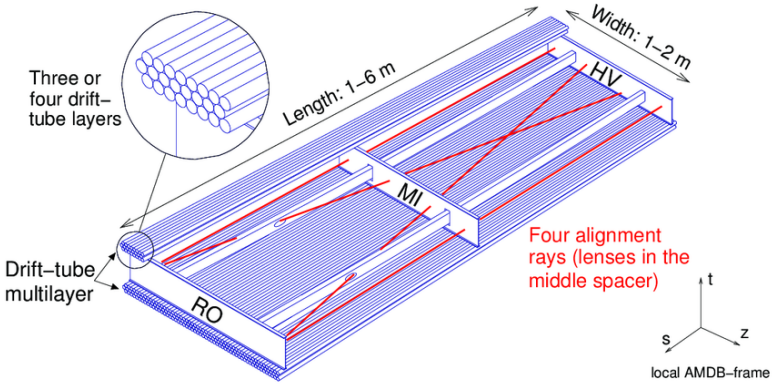

Figure 10.1: An MDT chamber consists of two multi-layers of three or four DT layers, which are mounted on an aluminum spacer frame. There are four optical alignment rays (indicated by the red lines), monitoring the internal geometry of the layer. HV indicates the position of the high voltage supply and RO the position of the readout electronics. Figure taken from [The ATLAS Collaboration, 2008].

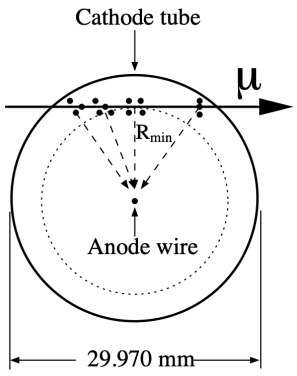

Figure 10.2: A muon ionizes the DT gas, creating electrons which are amplified towards the anode wire, due to a high electric field. The DT has a precise outer diameter of 29.970 mm. Figure taken from [The ATLAS Collaboration, 2008].

When a muon passes trough the DT, the gas is ionized (see chapter 2.1), creating electron-ion pairs. This process is also visualized in figure 10.2. Due to the electric field, the electrons drift towards the anode wire. Close to the anode wire the electrons gain enough kinetic energy for secondary ionization, producing an electron avalanche (see chapter 2.3.2) and thus a detectable signal on the anode wire.
The crucial parameter provided by the DT is the measured drift time. It is the time that an electron needs from its point of creation to the anode wire. Thereby, the start time is provided by an external trigger signal (see chapter 10.2). With this drift time and the drift velocity of an electron, which is given for the gas mixture and the applied electric field (see figure 2.4), the distance of the muon trajectory with respect to the anode wire is determined. By applying this method and using multiple DTs, the entire muon trajectory is determined precisely, which is achieved with the MDT chambers (see figure 10.1) in ATLAS [Gadow, 2016]. A single-hit spatial resolution of about 82 µm is obtained [The ATLAS Collaboration, 2019].
In order to guarantee the flawless performance of these MDT chambers during HL-LHC, the trigger and DAQ system needs an essential upgrade because the current front-end electronics does no longer meet the requirements [Sundararajan and Ntekas, 2023]. The signal is processed by the readout electronics, from which the Amplifier-Shaper-Discriminator (ASD) chip forms the first stage. It is crucial for the MDT performance regarding time resolution, noise and efficiency [Fras et al., 2018]. For the HL-LHC Phase-II upgrade, a new 8-channel ASD2 chip has been developed. About 80 000 of these new ASD2 chips have been produced, 50 000 are needed for installation.
The functionality and performance of the ASD2 chip is investigated in this chapter. In addition, a procedure has been developed to identify the 50 000 best-performing ASD2 chips out of a 80 000 chips for the ATLAS experiment. It is used for the production test of the ASD2 chips in a specialized company.

The results presented in this chapter have been published in previous work [Penski, 2024] and more detailed information can be found in [Penski et al., 2023].

10.2 MDT Trigger and Readout Chain

The ASD2 chip will be part of the ATLAS MDT trigger and readout electronics (see figure 10.3), forming the first stage of signal processing. This readout chain is briefly described here, following [Liang et al., 2019] and [Zhu, 2019].
The signals from the MDTs are read out by the ASD2 chips. Three of these chips are mounted on a mezzanine board. Since the ASD2 has 8 channels, each connected to one MDT, one mezzanine board reads out 24 DTs. After the signal is processed by the ASD2 (see chapter 10.3), it is digitized by the 24-channel Time-to-Digital-Converter (TDC) chip [Guo, 2021], which can be operated in triggerless mode as required for the Phase-II upgrade. Through the Chamber Service Module (CSM) these time measurements are sent to an MDT Data Processor Board. In order to extract the hits from the raw data stream, timing information from fast trigger chambers is required. In the barrel region of the ATLAS detector, these are provided by the Resistive Plate Chambers (RPC)s, while in the endcap region they come from the Thin Gap Chamber (TGC)s (detailed information can be found in [Amelung, 2019]). They define the time t_0 at which the triggering muon has passed the chamber. Therefore, the time difference between t_0 and the arrival time of the signal at the tube wire corresponds to the drift time, from which the distance of the track to the wire is determined. The resulting precision coordinates are further processed, as shown in figure 10.3. If the hit coincides with the first trigger level (L1), the data is saved for forwarding to the Front End LInk eXchange (FELIX)

readout [Anderson et al., 2015; Paramonov, 2021]. It is an interface between the detector and the trigger electronics. In addition, the momentum of the muon is identified using the segment finder and the track fitter algorithm. All this extracted muon information is sent to the ATLAS Muon-to-Central Trigger Processor interface (MuCTPi) [Spiwoks et al., 2017].

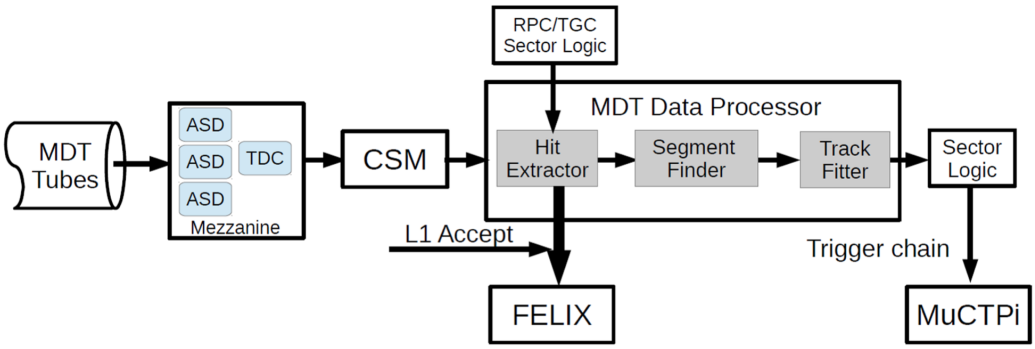

Figure 10.3: MDT trigger and readout electronics in the ATLAS experiment for HL-LHC: The ASD and the TDC, both located on the mezzanine board, form the on-chamber electronics together with the CSM, which processes the muon hits from the MDT. From there, they are forwarded to the off-chamber electronics. Using the time information from the RPC and TGC trigger chambers, relevant hits are identified and, in the case of an L1 acceptance trigger, forwarded to the detector readout system FELIX. A segment finder and track fitter algorithm determines the momentum of the muon, which is transmitted to the central trigger processor MuCTPi. Figure taken from [Liang et al., 2019].

10.3 The ASD2 Chip

For the ASD2 chip the IBM 130 nm CMOS (Complementary Metal–Oxide–Semiconductor) 8RF-DM technology [The ATLAS Collaboration, 2017; Fras et al., 2018] is used. Since it is an 8-channel chip, it can serve 8 MDTs. The functionality of one ASD2 chip channel is visualized in figure 10.4 [Matteis et al., 2016; Posch et al., 2007]. An overview of the various stages is provided here, while the detailed operation and influence of the programmable parameters is explained in the corresponding chapters.

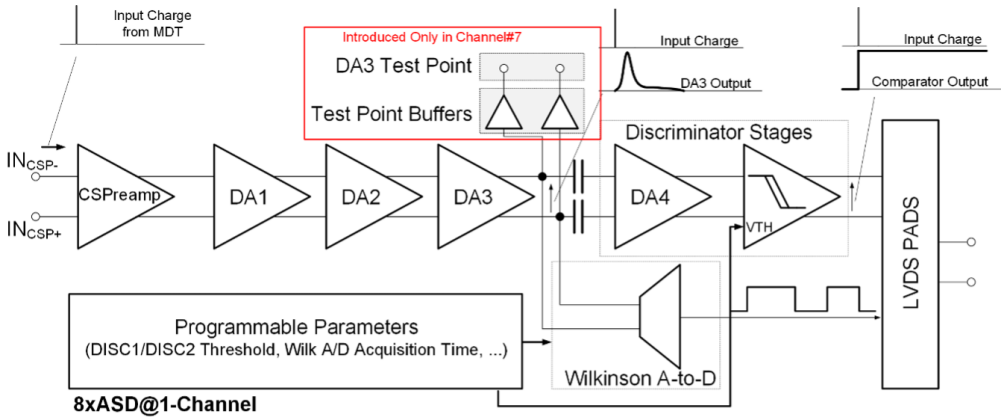

Figure 10.4: Block chain of one ASD chip channel (from left to right): The input charge from an MDT is detected by a charge-sensitive preamplifier (CSPreamp) whereupon a proportional voltage signal is generated. It is amplified and shaped by three Differential Amplifiers (DAi, i=1,2,3). Then it reaches the discriminator stage, where the threshold and hysteresis values are set. In the Wilkinson ADC the rundown current and integration gate are defined. The output signal reaches the LVDS Pads. Information taken from [Posch et al., 2007].

The charge collected at the anode wire from one MDT (see chapter 10.1) is received by a preamplifier, which generates a proportional voltage signal. It is amplified and shaped by three Differential Amplifiers (DAi, i=1,2,3), creating a bipolar signal. In the discriminator stage, the threshold and hysteresis value are set. The influence of these two programmable parameters on the chip's performance is discussed in chapter 10.5.2. In the next step, the signal is sent to a Wilkinson ADC, where a voltage to time conversion is performed. This allows for improved time resolution when applying the time-slewing correction [Bagnaia et al., 2008]. For the ASD2 chip there are several programmable parameters, such as dead time (see chapter 10.5.3) or integration gate and rundown current (see chapter 10.5.4), which are investigated. At the end, the signal is sent to the Low Voltage Differential Signaling (LVDS) PADS cell, where it is converted to an external low-level signal and digitized by a subsequent TDC (see figure 10.3).

10.4 Testing Procedure

For the chip testing a (prototype) test board has been designed (see figure 10.5), which supplies the chip with a voltage of 3 V and a bias current of 10 µA. An USB port ensures the communication with the computer, where the testing script is running.

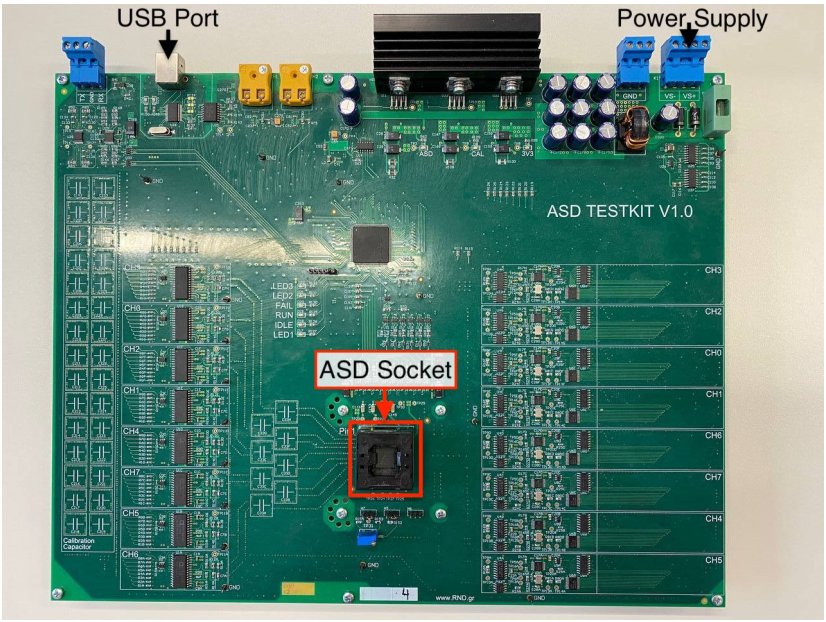

Figure 10.5: Picture of the prototype tester board: The ASD chip is placed into the socket for testing. The USB port provides communication between the board and the computer, through which the programmable parameters are set and the resulting performance values are returned.

100 pre-production ASD2 chips have been tested to investigate the influence of the programmable parameters (see chapter 10.5). In chapter 10.6 the pre-production chips are compared to the first batch of production ASD chips. Both are expected to behave identical. For the production testing at the company a new tester board has been developed. In chapter 10.7 it is compared to the prototype tester. In the last section of this chapter the final parameters and cut values are set and verified to be used for the production testing of the 80 000 ASD2 chips in a specialized company. Therefore, 1175 production chips are tested. The challenge is to reject all non-functioning chips as well as to achieve high uniformity between the channels of all chips while aiming for sufficient yield. A final categorization principle is implemented.

10.5 Functionality and Performance of 100 Pre-Production ASD2 Chips

100 pre-production ASD2 chips are characterized using the prototype tester board (see figure 10.5) in order to study the chip's behavior regarding the various programmable parameters. If the chips are finally used in the ATLAS experiment, the same programmable parameters are applied for all 50 000 chips. In order to ensure that all these chips provide the same results, a uniform performance regarding all parameters is mandatory. For this reason, cuts are introduced excluding outlier chips beyond the borders of the various investigated distributions.

10.5.1 Basic Health Measurement

For all chips a homogeneous power supply for all channels is mandatory. Therefore, the power supply pads are placed at the top and bottom of the chip. The measured current for two of these power domains (VDD3 and VDDA) is presented in figure 10.6. If the current drawn by the domain lies outside the acceptance intervals $39\,\text{mA} < I_{\text{VDD3}} < 43\,\text{mA}$ and $12\,\text{mA} < I_{\text{VDDA}} < 16\,\text{mA}$, the chip is rejected.

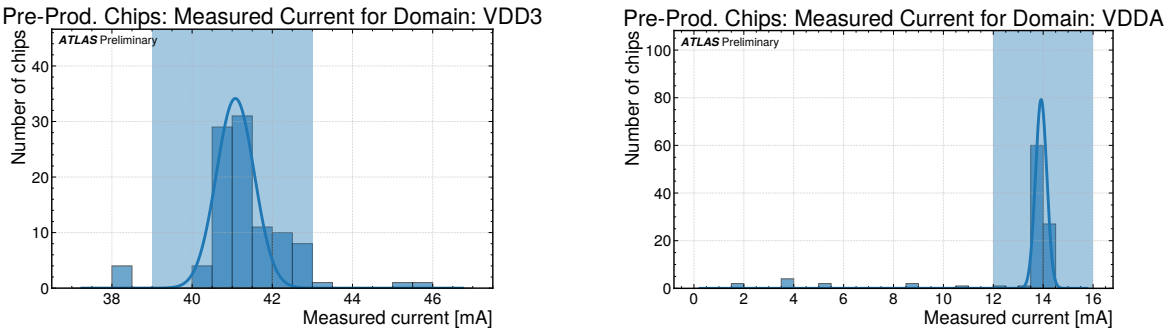

Figure 10.6: Measured current drawn by two of the power domains, VDD3 (left) and VDDA (right). The blue area marks the acceptance interval. If a chip draws an abnormal current outside this acceptance interval it is rejected.

10.5.2 Threshold Measurement

An event is processed, if the collected charge exceeds the threshold value, which is one programmable parameter in the discriminator stage.
The threshold value ranges between 0 and 128 (see figure 10.7). It is defined in such that a threshold value of 128 corresponds to signals with amplitudes close to 0. A threshold value of 10 corresponds to an input charge of about −20 fC (see figure 10.11). A precise association between threshold value and detectable charge is provided in this section.
Noise can lead to multiple threshold crossing, which is prevented by a hysteresis value. Both values form the effective threshold value. The influence of the hysteresis is shown in figure 10.8. 100 pulses with a predefined input charge $Q_{\text{in}} = -10\,\text{fC}$ are injected in each channel for this measurement. If Q_{in} exceeds the threshold value, the pulses are detected, causing the efficiency to rise from 0 to 1. A sigmoid function is fit to the data points, where L is the curve's maximum value, k is the steepness of the curve, x_0 the x value of the sigmoid midpoint and b an offset in y direction. It is defined as

$$f(x) = \frac{L}{1 + \exp(-k \cdot (x - x_0))} + b \tag{10.1}$$

In figure 10.8, $b = 0$ and $L = 1$. The inflection point of the fit is the threshold value. In case of a dead channel, the efficiency stays constant and the corresponding chip is rejected.

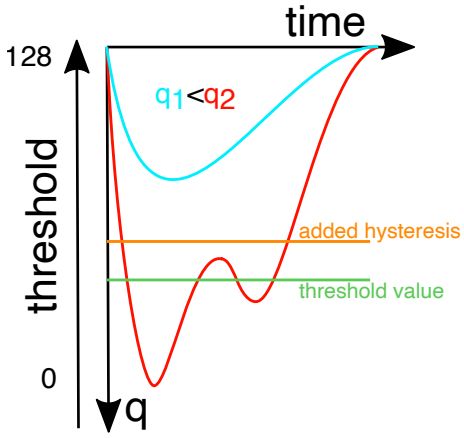

Figure 10.7: If the input charge q is large enough to exceed the threshold value, the signal is processed. While q_1 is not high enough to fall below the threshold (green line), q_2 is sufficient to fulfill the condition and be processed further. To avoid multiple threshold crossings, e.g. due to noise, a hysteresis value is set (orange line).

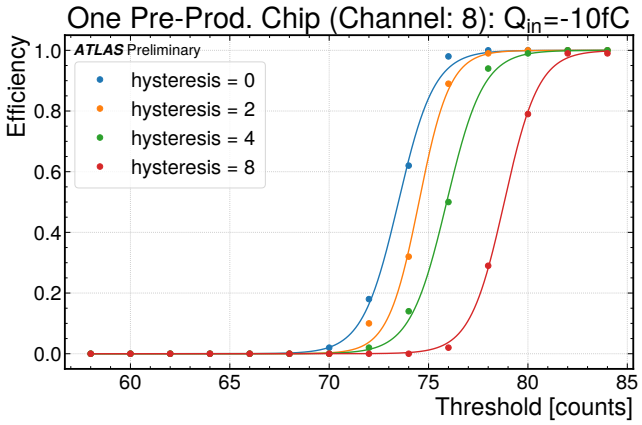

Figure 10.8: The ratio of detected to generated pulses (efficiency) is measured as a function of the threshold value for various hysteresis values and a constant input charge $Q_{\text{in}} = -10\,\text{fC}$. Higher hysteresis values increase the effective threshold value.

Additionally, a high uniformity between all channels is necessary. Thus, the RMS of the 8 channels of one chip is calculated using

$$RMS = \sqrt{\frac{\sum_{i=1}^{N}(x_{\text{i}} - \bar{x})^2}{N}} \tag{10.2}$$

in order to measure the deviation between the mean threshold value $\bar{x}$ and the individual threshold values x_{i}. This is done for all chips and the result is shown in figure 10.9.

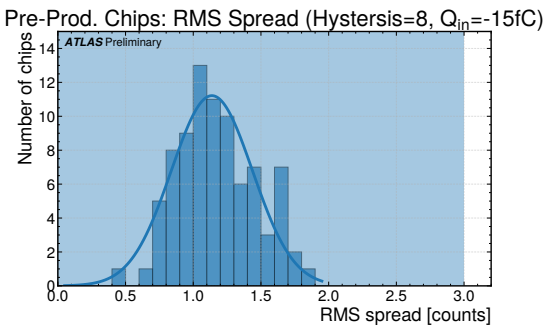

Figure 10.9: For each chip the RMS spread of the threhold vlaue for the 8 channels is calculated and plotted for all chips. Normally, it is smaller than 2 counts. Only chips with a RMS spread of less than 3 counts are accepted (blue area). An input charge of $Q_{\text{in}} = -10\,\text{fC}$ and hysteresis value of 8 are used.

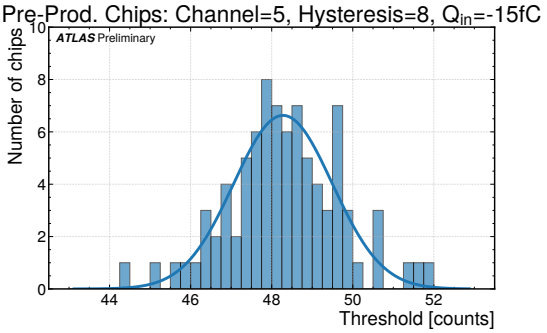

Figure 10.10: Distribution of the threshold values for channel 5 of all chips. A Gaussian function is fit, to provide the mean value and the standard deviation. An input charge of $Q_{\text{in}} = -10\,\text{fC}$ and hysteresis value of 8 are used.

To guarantee high homogeneity, all chips with a RMS of more than 3 counts are rejected. The final distribution is presented in figure 10.10, giving a mean threshold value for a certain Q_{in} and hysteresis value. This measurement and analysis is performed for various input charges and hysteresis values and the relation can be seen in figure 10.11.

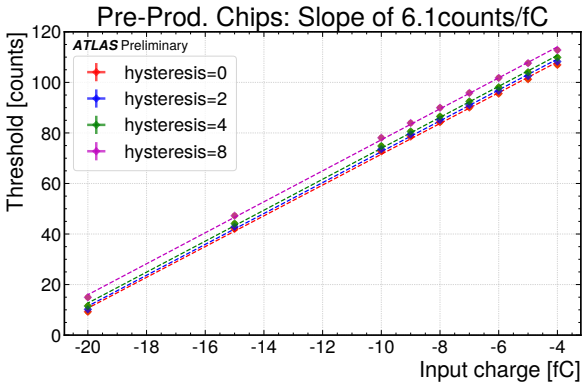

Figure 10.11: The threshold value is plot as a function of the input charge. There is a linear dependence between these two parameters. As expected from figure 10.8, the different hysteresis values lead to an offset.

In order to be sensitive to charges around −4 fC, the corresponding threshold value of about 115 counts is chosen. A hysteresis value of 8 avoids noise effects.

10.5.3 Dead Time Measurement

Since a single muon track can cause multiple threshold crossing, a dead time for the total MDT drift time (see chapter 10.1) of about 700 ns has to be introduced [Posch et al., 2007]. In the ASD2 chip the dead time is another programmable parameter called dead time code. Each dead time code corresponds to a certain dead time. By measuring the number of hits for different delays between two pulses for a specific dead time code (see figure 10.12), the dead time value is determined.

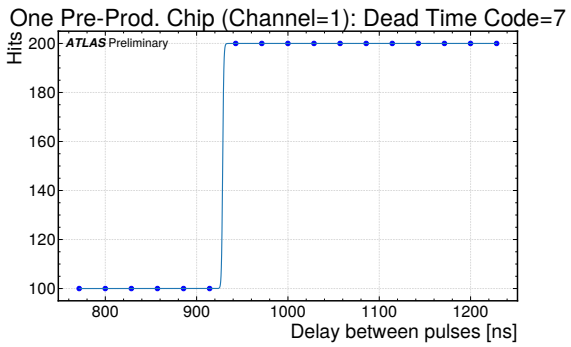

Figure 10.12: Two pulses with different delays are injected, while measuring the number of hits as a function of this delay. To the resulting data points a sigmoid function is fit, taking the inflection point as dead time for the corresponding dead time code 7.

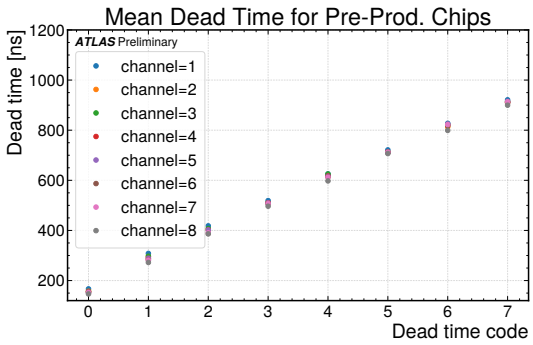

Figure 10.13: The corresponding dead time is assigned to each programmable dead time code. Both values have a linear dependency. A dead time of 700 ns corresponds to a dead time code of 5. The 700 ns drift time applies to standard conditions but can vary due to different temperatures and magnetic field strengths in the ATLAS muon spectrometer. Thus, typically a dead time code of 6 or 7 is used.

The analysis procedure is the same as for the threshold values introduced in chapter 10.5.2. The sigmoid function (see equation 10.1, with the offset value $b = 100$ and curve's maximum value $L = 100$) is fit to the data points and the inflection point is taken as dead time value. A distribution plot is created for all chips, to which a Gaussian function is fit, and the mean and standard deviation are extracted and summarized in figure 10.13. The required MDT dead time of at least 700 ns is usually realized by the dead time code 6 or 7.

10.5.4 Pulse Width Measurement

In the measurement procedure, a predefined charge is injected, but in the experiment, the ASD chip has to provide information about the deposited charge in the MDT. Thus, the measured signal charge is encoded into a pulse width by the dual-slope Wilkinson technique. The basic principle of this technique involves integrating the signal charge on a capacitor during the gate time with subsequent discharge of a capacitor with a constant current [Posch et al., 2001]. The corresponding programmable parameters are the integration gate and the rundown current (rdc), respectively. By measuring the charge and discharge timing of the capacitor, a pulse width is provided. In this way a conversion from voltage to time is executed.

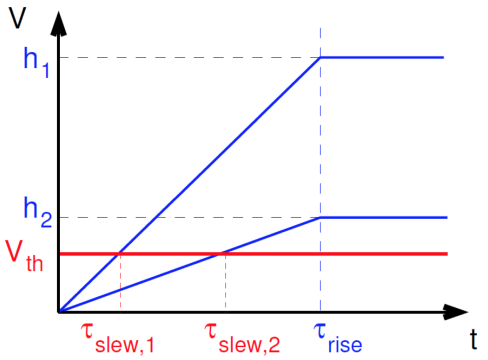

Figure 10.14: Time-slew correction: Two different input charges differ in their pulse height h. Due to the shaping, the rise time τ_{rise} of these pulses is constant. By introducing the threshold V_{th}, the pulse height h is inversely proportional to the slew-time τ_{slew} ($\tau_{\text{slew},1} \sim 1/h_1$ and $\tau_{\text{slew},2} \sim 1/h_2$). Thus, smaller signals cross the threshold later than larger signals. Figure taken from [Yang, 2019].

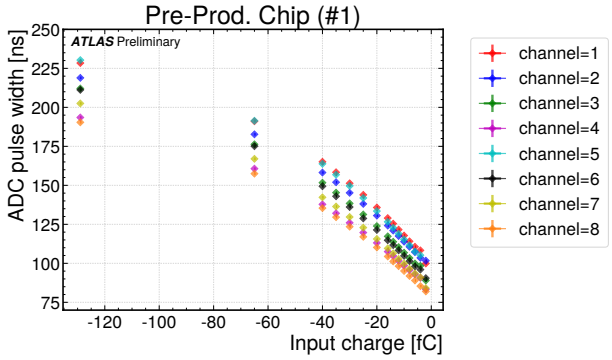

Figure 10.15: Measured pulse width for all 8 channels of a pre-production chip. Compared to other chips, the behavior of the channels is different, meaning that it is an effect of the ASD chip and not the test board. A small ADC pulse width corresponds to a small charge as the charge and discharge timing of a capacitor is measured.

Two signals with different input charge and thus various amplitudes (here h_1 and h_2) have the same rise time τ_{rise} (see figure 10.14). But depending on the pulse height, the signal exceeds the threshold value V_{th} at different times, which is referred to as slew-time τ_{slew}. Smaller signals arrive later than larger ones, which leads to inaccuracies in the event timing and has to be corrected. For a given experimental threshold V_{th} the slew-time τ_{slew} depends on the pulse height h (see figure 10.14), which is given by

$$\tau_{\text{slew}} = \frac{\tau_{\text{rise}}}{h} \cdot V_{\text{th}} \tag{10.3}$$

Using the pulse height measured by the Wilkinson ADC, the slew-time can be corrected. This correction guarantees a high time resolution.

The measured pulse width of all channels of one chip is presented in figure 10.15. For larger input charges the ADC pulse width increases. There is a variation of up to 40 ns between the channels. As for the previous measurements, also the pulse width measurement is carried out for several chips, the results are analyzed using Gaussian distributions fit to histograms. Figure 10.16 summarizes the mean values and figure 10.17 the RMS spread.

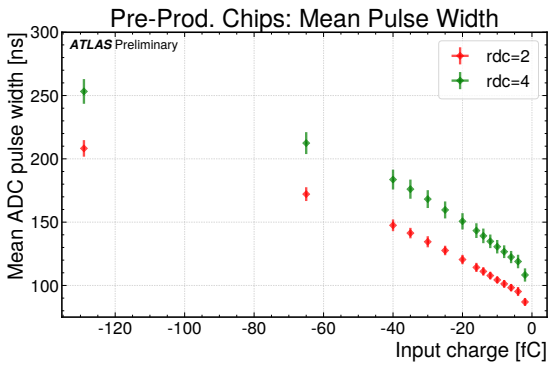

Figure 10.16: There is a rather linear relation between charge and pulse width. It starts saturating for charges larger than −40 fC.

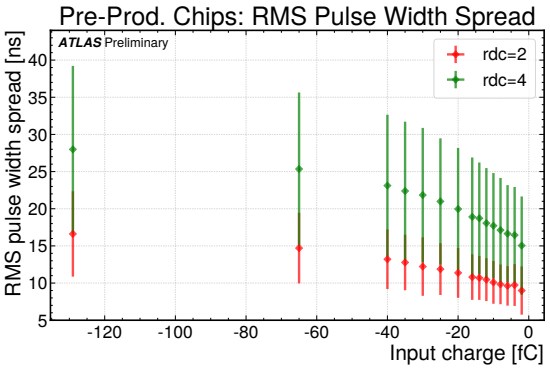

Figure 10.17: The RMS pulse width spread is about twice as large for rundown current rdc=4 as for rdc=2.

Due to the linear relation between input charge and pulse width for rundown current rdc=2 and rdc=4, for both the charge can be decoded by the pulse width. But the RMS for rdc=2 is much smaller than for rdc=4, which reduces uncertainties when encoding. For this reason rdc=2 is favorable.

10.6 Performance of the Production ASD2 Chips

In order to characterize the functionality of the production ASD2 chips, they are compared to the previously tested pre-production ASD2 chips using the prototype tester board. The results are presented in figure 10.18, for all four testing procedures.

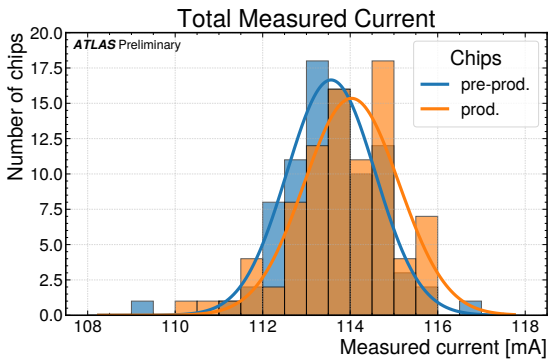

a) Basic Health Measurement

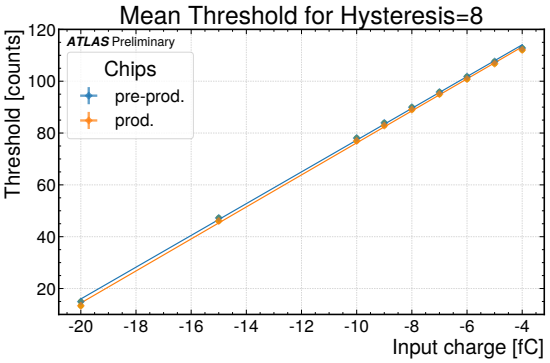

b) Threshold Measurement

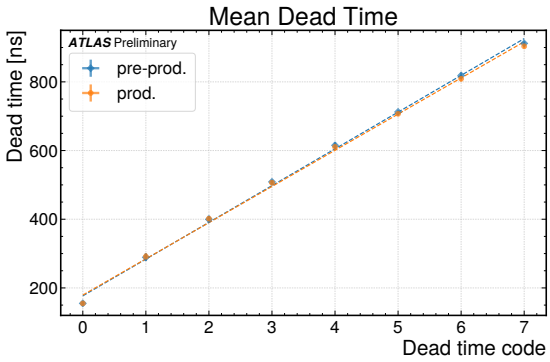

c) Dead Time Measurement

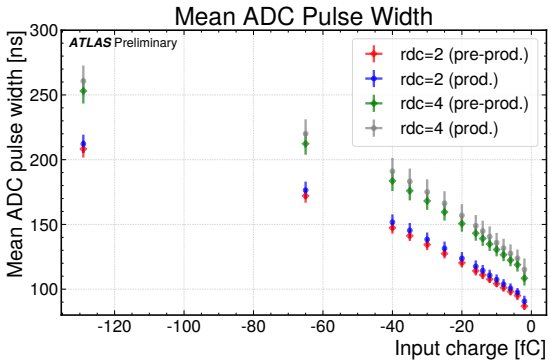

d) Pulse Width Measurement

Figure 10.18: Comparison of pre-production with the production ASD2 chips: For all measurements introduced in chapter 10.5 no difference in performance is observed.

For the basic health measurement the total current (sum of the four power domains VDD1, VDD2, VDD3 and VDDA) is shown in figure 10.18a, where the Gaussian fit provides a mean value of (113.6 ± 1.1) mA for the pre-production ASD2 chips and (114.1 ± 1.1) mA for the production ones. Within the standard deviation, both chip types draw the same current. In addition, there is a difference of less than 1 count for the threshold measurement (see figure 10.18b), about 10 ns for the dead time measurement (see figure 10.18c) and less than 5 ns for the ADC pulse width measurement (see figure 10.18d) between the pre-production and production ASD2 chips. Considering the standard deviation intervals as well as statistical fluctuations, both chips do not show any difference.

10.7 The Production Testing QAQC Tester Board

For the testing of the 80 000 ASD2 chips in a specialized company a newly designed Quality Assurance and Quality Control (QAQC) tester board will be used, which meets the following requirements:

- It has a more rigid design than the previous one because it has to withstand the pressure of the robotic arm which will perform the production testing.
- The socket is improved since the old one suffered from fatigue.

In this section the performance of the new QAQC tester board will be verified by testing the same 100 production chips from chapter 10.6 with this board and compare the results to the ones from the prototype board. There is one known difference between both testers, namely the injection capacitor and the resistor, both leading to different bias currents in the tester. The clock used to measure the dead time is independent of the bias current, thus there is no difference in the dead time measurement for either tester, as shown in figure 10.19c. Despite that, the other measurements (see figure 10.19a, figure 10.19b, figure 10.19d) show an offset in the measured data because of the different bias current. Despite this calibratable offset, however, there is no practical difference between the two tester boards.

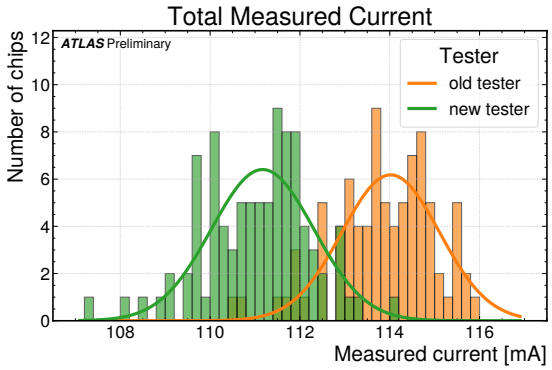

a) Basic Health Measurement

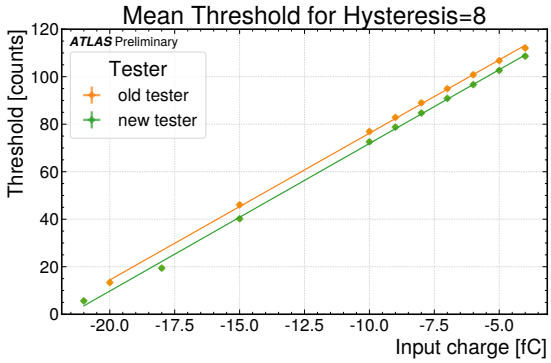

b) Threshold Measurement

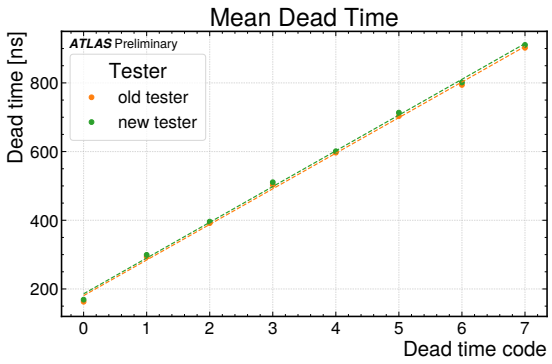

c) Dead Time Measurement

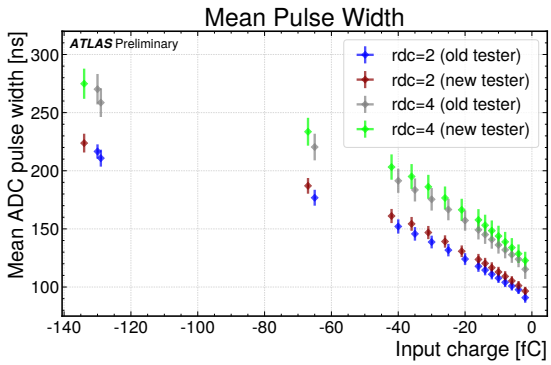

d) Pulse Width Measurement

Figure 10.19: Comparison of the prototype tester board with the new QAQC tester board using the production ASD2 chips: Due to the different bias currents there is a slight offset for the basic health test, the threshold measurement and the pulse width measurement. Only for the dead time measurement no difference is observed.

10.8 Categorization and Final Testing Procedure

For better verification of the testing parameter and cut intervals, 1175 production ASD2 chips are tested using the new QAQC tester board. Moreover, the chips are sorted into three categories:

- Category C: non-working chips, e.g., abnormal currents, dead channel
- Category B: working chips, outside acceptance interval
- Category A: working chips, within acceptance interval

It should be noted here that although the chips in category B function, they are at the edge of the distributions and are therefore excluded, as motivated at the beginning of chapter 10.5. For the Phase-II upgrade, approximately 50 000 functioning ASD2 chips are required. As it is expected that some chips are defect, a total of 70 000 chips is produced. After excluding the non-functioning chips (category C) from the 70 000 chips, the aim is to provide the best 50 000 functioning ASD2 chips from the production batch to ATLAS. This is equivalent to a yield of 70 % of all ASD2 chips in category A, which is achieved by optimizing the cuts.

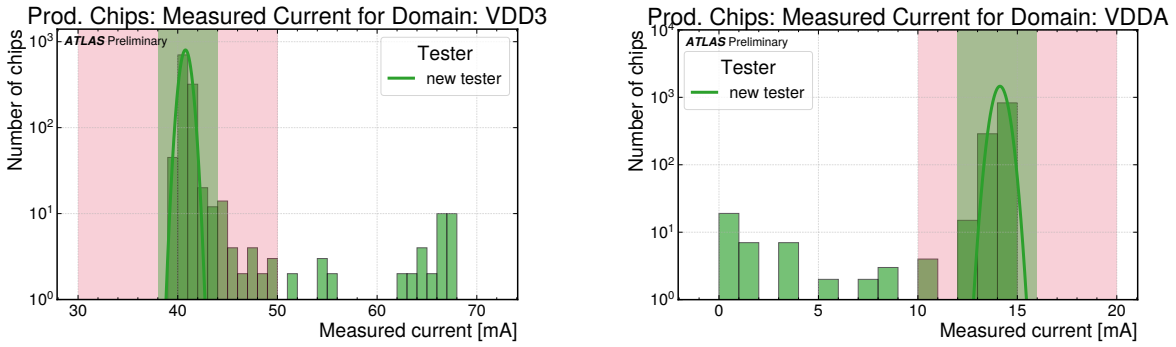

Figure 10.20: Measured current drawn by two of the power domains, VDD3 (left) and VDDA (right) in logarithmic scale. The green area marks the category A acceptance interval, otherwise a chip falls into category B (rose). If it even lies outside the rose acceptance interval, it belongs to category C because of the abnormally high drawn current.

Again, the same testing and analysis procedure is applied as in chapter 10.4. For the basic health test the drawn current is plot in figure 10.20 for two of the four power domains. For the categorization process two cuts for each domain are performed. Compared to chapter 10.4, they are adapted to the new QAQC tester due to the shift (see chapter 10.7). If the measured current is within the acceptance intervals $30\,\text{mA} < I_{\text{VDD3}} < 50\,\text{mA}$ and $10\,\text{mA} < I_{\text{VDDA}} < 20\,\text{mA}$, the chip belongs to category B. If it lies within the interval $38\,\text{mA} < I_{\text{VDD3}} < 44\,\text{mA}$ and $12\,\text{mA} < I_{\text{VDDA}} < 16\,\text{mA}$, it is a category A chip. If these two requirements are not met, the current drawn deviates too much from the mean value and the chip is in category C.

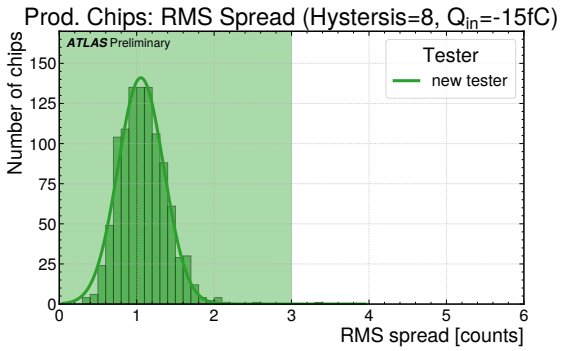

Figure 10.21: Chips with a RMS threshold spread of less than 3 counts (green area) are category A chips, otherwise they belong to category B.

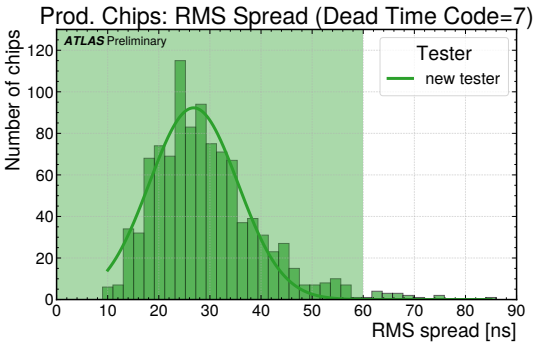

Figure 10.22: If the dead time RMS spread of one chip is less than 60 ns (green area) it belongs to category A. If it is larger, it goes into category B.

For both the threshold measurement and the dead time measurement, a chip automatically falls into category C if it has at least one dead channel. The cuts for category A and B are shown in figure 10.21 and figure 10.22 for the threshold measurement and the dead time measurement, respectively. After the cuts for the basic health, threshold and dead time measurements, there are 14 % of the chips in category C, 3 % in B and 83 % in A. Especially, all non-working chips (category C) are now identified. Measuring now the pulse width, the cuts performed aim to achieve high uniformity between the chips to obtain the 70 % best in category A. Therefore, the tails in the distribution plots (see figure 10.23) are reduced for both rdcs. Since the distribution becomes wider for a larger rdc (see figure 10.24), the cuts for the two rdcs complement each other.

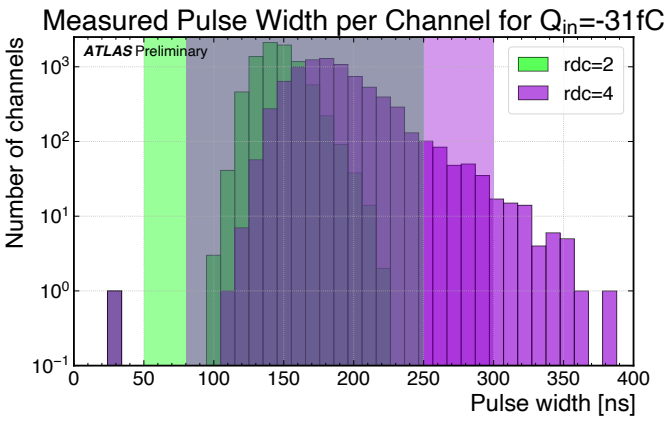

Figure 10.23: For the pulse width measurement, distribution cuts are performed for rdc=2 (green): [50, 250] ns and rdc=4 (purple): [80, 300] ns. Chips within the intervals belong to category A, otherwise to category B.

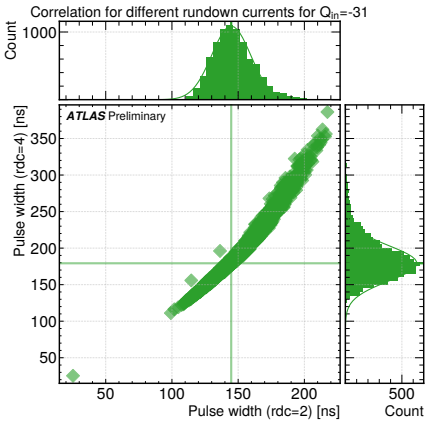

Figure 10.24: Pulse width correlation for rdc=2 and rdc=4: For rdc=4 the distribution gets broader. By cutting off the tail for one of the rundown currents, the same chips fall into category B for both rundown currents.

The final yields after each cut performed are presented in Table 10.1. The target of 70 % in category A is reached by choosing the best performing chips.

Criteria	Category C	Category B	Category A
Basic Health	4 %	3 %	93 %
Threshold	12 %	0 %	88 %
Dead Time	14 %	3 %	83 %
Pulse Width	14 %	15 %	71 %

Table 10.1: Cut values are set for all four criteria, resulting in different yields in each category. The categories are updated after each criteria, which means, for example, that the 3 % of the chips in category B after the basic health measurement move to category C after the threshold test, which then leads to 0 % in category B. Finally, there are 14 % non-working chips. The 71 % in category A are the best working 50 000 chips.

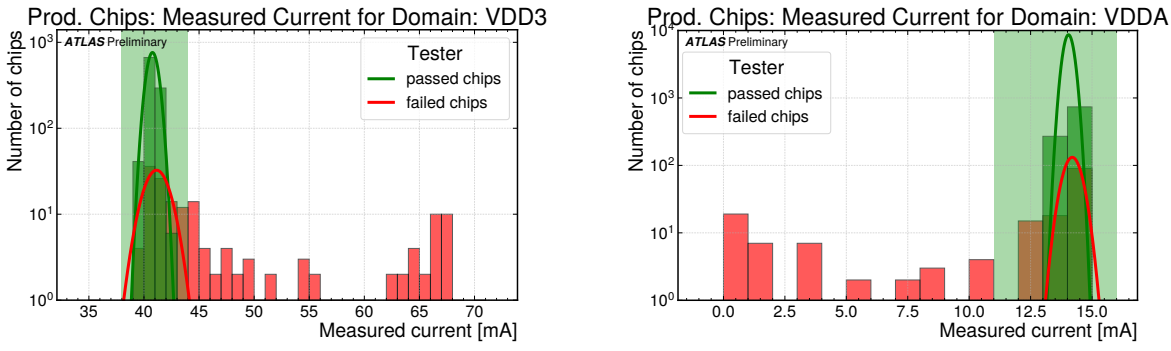

Figure 10.25: In order to justify the basic health cuts, chips that fail any criteria other than basic health are marked in red, while those that pass all criteria are green. For both, VDD3 (left) and VDDA (right), only chips that fail a later testing stage, are rejected by the health cuts. The green marked areas are the acceptance intervals of the basic health test for category A.

In a last step the cut intervals in the basic health measurement should be verified to ensure, that the introduced cuts do not reject working chips. Therefore, it is distinguished between

the chips that fail at a stage other than the basic health test and those that pass, as shown in figure 10.25. Using the previously used cut intervals from figure 10.20, figure 10.25 shows that only chips that would fail at a later stage are rejected by the basic health cut values, justifying the cuts in the basic health test as they only select non-working chips.

Furthermore, a time budget of 15 s per chip is available for testing in the company. The measurement time achieved for the presented key parameters is around 7 s.

10.9 Conclusion

A new ASD2 chip has been developed for the necessary MDT readout electronics upgrade due to HL-LHC. Before integration, these chips have to be tested in order to guarantee full functionality. Therefore, in a first step, the influence of the different programmable parameters on the chip's behavior has been successfully investigated. To detect small charges in the range of about −4 fC, a threshold value of about 115 counts is mandatory. The elimination of noise is realized by adding a high hysteresis value, in this case 8. A dead time of at least 700 ns, which corresponds to the maximum drift time in a 30 mm ATLAS DT, is typically provided by a dead time code of 6 or 7. For an accurate charge encoding, a rundown current of 2 is preferable. A second step categorization procedure with additional cut values ensures that only the best performing 50 000 ASD2 chips are provided to ATLAS. The cuts are optimized to reject all non-working chips and to achieve highest uniformity of the performance of all channels of all chips, while maintaining a yield of 70 % for the best chips. These cuts are used for the ASD2 chip production testing in a specialized company.

Chapter 11

Summary and Outlook

In this thesis, the application of multiple stacked converter layers to enhance photon detection while providing complete position information in GEM detectors is investigated.

GEM detectors are thin gaseous detectors and exhibit, due to the low atomic number Z and low density of the active gas volume, a poor photon detection efficiency. For photons the detection via the photoelectric effect can be increased by a solid converter cathode with higher-Z materials, as the photoelectric cross-sections σ_{photo} scales with Z^5. In the novel technique, multiple converter layers are arranged in a stacked configuration perpendicular to the readout anode in the drift region of a GEM detector. Each converter layer increases the probability of photon interaction.
The converter layers are PCBs with an active area of 100 mm × 20.6 mm and various thicknesses. They consist of an insulating carrier material with 25 strips on each side. These strips are made of copper that is either 35 µm or 15 µm thick and is covered with a 3–6 µm thick ENIG protection layer. On each layer side, the 25 strips are connected via SMD resistors. Applying a voltage difference ΔU_{y} between the lower and upper strips and a voltage difference ΔU_{x} between the two sides generates an electric guiding field.

All measurements are performed with a point source emitting 59.5 keV X-rays. Following the anticipated working principle, the 59.5 keV photon interacts with the copper strip of the converter layer via the photoelectric effect, creating a photoelectron. When this photoelectron exits the strip into the surrounding gas volume, it causes secondary ionization in the gas. The created electrons are guided down by the electric guiding field to the active area of the triple-GEM detector, where the electrons are amplified. A signal is created on the 2D readout strip structure on the anode. This x- and z-position of the charge-cluster is determined using the centroid method.

For an initial study, 5 converter layers made of 1520 µm FR4 as insulating material and 35 µm thick copper strips are placed perpendicularly to the GEM foil with a distance of about 11 mm from each other. The electrons are guided down by the electric field between the layers. The goal is to understand the working principle of the layers, including the interaction processes in the various components of the layer, the electron drift for different electric field configurations and the cluster charge properties as well as their effects on the photon detection efficiency. Therefore, a detailed simulation procedure is set up. It comprises Geant4 for the simulation of the photon-matter interaction, ANSYS for the electric field configuration, and Garfield++ for the electron drift and gas ionization. Comparing the simulation results with measurable quantities, like the hit distribution, number of reconstructed clusters, deposited charge, cluster extension as well as the influence of the applied voltage differences

ΔU_y and ΔU_x, provides good agreement. For the perpendicular setup with these converter layers, the highest trigger rate is achieved with a voltage combination of ΔU_y = 600 V and ΔU_x = 0 V resulting in a guiding efficiency of 67 %. Due to a high absorption in FR4, the 1520 µm FR4 layers exhibit a detection efficiency of 0.46 %, which is similar to the conversion efficiency in a setup without layers, thus further improvement regarding insulating material and material thickness was required.

In order to increase the photon detection efficiency of the converter layers, 6 different types are compared using the perpendicular configuration with 5 layers. For a reliable and reproducible comparison between the converter layers types in the GEM detector, the measurement results have to be independent of environmental fluctuations, and therefore, a pressure-voltage calibration was established.
The converter layer types differ in their material thickness and insulating material. Using FR4 as the insulating material, the layers have a thickness of either 1520 µm or 250 µm, with about 35 µm thick copper strips. The other 4 layer types consist of PI as an insulating material with a thickness of 100 µm or 50 µm, each with 2 different copper thicknesses (15 µm or 35 µm).
In a first study, the absorption behavior of the 59.5 keV photons by the various components is examined using a HPGe detector. It shows that in 3 layers made of 1520 µm FR4, about 30 % of the photons are absorbed, while in 100 µm PI, it is less than 1 %. Since photons absorbed by the insulating material are not detectable, thin insulating layers made of PI are favorable. In addition, in 35 µm thick copper strips of 3 converter layers, about 15 % of the 59.5 keV photons are absorbed. Of all interactions occurring in the converter layers, only particles resulting from photon conversion in the copper strips are detected.
The influence of the different converter layer types on the trigger rate and thus detection efficiency of the GEM detector are investigated, by placing 5 layers in the detector and performing a ΔU_y voltage scan. Since the measurement results did not align with expectations based on the anticipated working principle and photon absorption measurements, the interaction processes in the converter layers and the gas volume of the GEM detector were analyzed and understood using simulations. The dominant effect is the 59.5 keV photon interaction with the copper strip via the photoelectric effect. In this process, the photons interact with the electrons in the K-shell in copper, creating a 50.5 keV photoelectron and a vacancy in the K-shell. Due to electron rearrangement, this vacancy is filled by an electron from the L-shell, leading to the emission of a K_α transition photon with an energy of 8.0 keV. While the majority of the 50.5 keV photoelectrons are directly absorbed in copper and do not exit the strip, the dominant detection process is the interaction of the 8.0 keV transition photon with the gas, creating a 4.8 keV electron, which is detected. So instead of directly detecting the photoelectron created by the 59.5 keV photon interaction in copper, the photoelectrons produced in gas by the 8.0 keV transition photons are measured.
In addition, simulations show that the 8.0 keV photons are completely absorbed by the 1520 µm FR4 layer, while in the 100 µm PI layer only 20 % absorption occurs. These effects influence the measured trigger rate of the GEM detector when using various converter layer types. Overall, compared to the 1520 µm FR4 layers, the photon detection efficiency in the GEM detector is about 1.3 times higher for the 250 µm FR4 and 1.8 times higher for the 100 µm PI, all with 35 µm thick copper strips at ΔU_y = 0 V. For even thinner layers, a factor of 2 is achieved at ΔU_y = 0 V. These values agree for simulation and measurement, also with respect to other voltage combinations.
Since the thinner layers provide better guiding efficiency for higher ΔU_y compared to the 1520 µm FR4 layers, the highest detection efficiency is achieved with the converter layer made of 50 µm PI and 15 µm Cu at ΔU_y = 800 V. It is 3 times higher compared to the maximum of the 1520 µm FR4 layer, resulting in a detection efficiency of (1.38 ± 0.21)%.

For various applications, like imaging or PET, a complete 3D position is essential. If the measured 2D position allows for the interaction position on the converter layer to be unambiguously reproduced with high accuracy, the direction of a point source can be reconstructed. Two approaches are investigated, both using a setup where the converter layers are tilted by 60° with respect to the GEM foil. For a geometrical reconstruction the y-position can then be determined by the measured x-position, but it requires a perpendicular electron drift. The second approach needs a good agreement between simulation and measurement, since this would allow for a measured x-position to extract the corresponding y-position from simulation.
Measurements with both a single tilted layer as well as multiple tilted layers were performed, both providing a good agreement with the simulation regarding the measured hit positions. A high detection efficiency is achieved with 5 converter layers and the voltage combination $\Delta U_\mathrm{y} = 600\,\mathrm{V}$ and $\Delta U_\mathrm{x} = 400\,\mathrm{V}$, but the simulated electron drift shows that no distinct electron drift is observed. Instead, applying $\Delta U_\mathrm{y} = 600\,\mathrm{V}$ and $\Delta U_\mathrm{x} = 0\,\mathrm{V}$ results in a perpendicular drift but with a lower detection efficiency. Despite the vertical drift at this voltage combination, the corresponding y-values vary by 20 mm for similar measured x-positions, preventing position reconstruction. This effect results from the occurring interaction processes in the converter layer. Since the 8.0 keV transition photon is emitted isotropically and has a mean free path of about 48 mm in argon, the detected electron has no information about the initial interaction position or direction of the point source. Consequently, it leads to variation in the reconstructed y-position and limits the feasibility of position reconstruction or imaging an object using this layer setup.

For the 59.5 keV photons the detection efficiency is increased by optimizing the material of the converter layers. In addition, detailed knowledge is provided about the working principle of the converters, with their effects on the methods for position reconstruction and the material optimization process. For future work, the detection efficiency can be further increased by improving the guiding efficiency, using more layers and reducing their spacing. The conversion materials have to be adjusted to the energy of the corresponding transition photons, in order to ensure a distinct conversion position.

The detection efficiency for photons with an energy of 511 keV of the GEM detector with converter layers is determined experimentally using a coincidence measurement setup using scintillation detectors and a ^{22}Na source. It emits two 511 keV photons back-to-back and a 1275 keV photon. The setup is designed such that when both scintillation detectors simultaneously detect the 511 keV and 1275 keV photons, a 511 keV photon is emitted in the direction of the detector under test. By comparing the number of expected and measured coincident signals, the detection efficiency is determined. For the GEM detector with 9 converter layers, a detection efficiency of 0.31 % is obtained, which is about twice as high as compared to a setup without layers and close to the expected 0.29 %. This allows for the precise estimation of the detection efficiency.

For HL-LHC, the MDT readout electronics will be upgraded, which includes the implementation of a new ASD2 chip. The influence of various programmable parameters on the performance of the ASD2 chip is investigated, such as threshold, dead time or rundown current. Furthermore, a testing procedure is developed to identify the 50 000 best-performing ASD2 chips out of a 80 000 chips for the ATLAS experiment for integration.

List of Abbreviations

ADC Analog to Digital Converter

ANSYS ANalysis SYStem

APDL ANSYS Parametric Design Language

ASD Amplifier-Shaper-Discriminator

ASIC Application-Specific Integrated Circuit

ATLAS A Toroidal LHC ApparatuS

BADGE Bisphenol A Diglycidyl Ether

CAD Computer Aided Design

CERN Conseil Européen pour la Recherche Nucléaire

CFD Constant Fraction Discriminator

CMOS Complementary Metal–Oxide–Semiconductor

CMS Compact Muon Solenoid

CSDA Continuous Slowing Down Approximation

CSM Chamber Service Module

CT Computed Tomography

DAQ Data AcQuisition

DT Drift Tube

EC Electron Capture

ENIG Electroless Nickel Immersion Gold

FDG 18F-Fluorodeoxyglucose

FEA Finite Element Analysis

FEC Front End Concentrator

FELIX Front End LInk eXchange

FPD Flat-Panel Detector

FR Flame Retardant

FWHM full width at half maximum

Geant GEometry ANd Tracking

GEM Gaseous Electron Multiplier

HEED High Energy ElectroDynamics

HEP High Energy Physics

HL-LHC High-Luminosity LHC

HPGe High Purity Germanium

HV High-Voltage

LHC Large Hadron Collider

LoR Linie of Response

LVDS Low Voltage Differential Signaling

MDT Monitored Drift Tube

MRI Magnetic Resonance Imaging

Micromegas MICRO MEsh GAseous Structure

MPGDs Micro-Pattern Gaseous Detectors

MuCTPi Muon-to-Central Trigger Processor interface

MWPC Multi-Wire Proportional Chamber

NIM Nuclear Instrumentation Standard

NSW New Small Wheel

PCB Printed Circuit Board

PET Positron Emission Tomography

PI Polyimide

PMT Photomultiplier Tube

QAQC Quality Assurance and Quality Control

QDC Charge-to-Digital-Converter

rdc rundown current

RMS Root Mean Square

RPC Resistive Plate Chambers

RWELL Resistive WELL

SEM Scanning Electron Microscopy

SGR Segmented GEM Readout

SMD Surface Mount Device

SRS Scalable Readout System

TBBA Tetrabromobisphenol-A

TDC Time-to-Digital-Converter

TGC Thin Gap Chamber

Bibliography

[Agostinelli et al.(2003)] S. Agostinelli, J. Allison, K. Amako, et al. GEANT4 — a simulation toolkit. *Nuclear Instruments and Methods in Physics Research Section A: Accelerators, Spectrometers, Detectors and Associated Equipment*, 506(3):250–303, 2003. ISSN 0168-9002. doi:https://doi.org/10.1016/S0168-9002(03)01368-8. URL `https://www.sciencedirect.com/science/article/pii/S0168900203013688`.

[Agrawal et al.(2021)] K. Agrawal, A. Skillen, A. Esmail, and S. Usmani. *PET/CT Imaging - Basics and Practice*. Clinicians' Guides to Radionuclide Hybrid Imaging. Springer Cham, 1. edition, 2021. ISBN 978-3-030-75476-1. doi:https://doi.org/10.1007/978-3-030-75476-1.

[Aldawood et al.(2015)] S. Aldawood, I. Castelhano, R. Gernhäuser, et al. Comparative Characterization Study of a LaBr3(Ce) Scintillation Crystal in Two Surface Wrapping Scenarios: Absorptive and Reflective. *Frontiers in Oncology*, 5:270, 2015. doi:10.3389/fonc.2015.00270.

[Alexopoulos et al.(2011)] T. Alexopoulos, J. Burnens, R. de Oliveira, et al. A spark-resistant bulk-micromegas chamber for high-rate applications. *Nuclear Instruments and Methods in Physics Research Section A: Accelerators, Spectrometers, Detectors and Associated Equipment*, 640(1):110–118, 2011. ISSN 0168-9002. doi:https://doi.org/10.1016/j.nima.2011.03.025. URL `https://www.sciencedirect.com/science/article/pii/S0168900211005869`.

[Alsamak et al.(2023)] I. Alsamak, K. Baraka, S. Caiazza, et al. Garfield++, 2023. URL `https://garfieldpp.web.cern.ch/garfieldpp/`. [online, accessed: November 2023].

[Amelung(2019)] C. Amelung. Upgrade of the ATLAS muon system for the HL-LHC. *Nuclear Instruments and Methods in Physics Research Section A: Accelerators, Spectrometers, Detectors and Associated Equipment*, 936:420–423, 2019. ISSN 0168-9002. doi:https://doi.org/10.1016/j.nima.2018.09.005. URL `https://www.sciencedirect.com/science/article/pii/S0168900218310878`. Frontier Detectors for Frontier Physics: 14th Pisa Meeting on Advanced Detectors.

[Amptek(2024)] Amptek. MCA-8000D Digital Multichannel Analyzer, 2024. URL `https://www.amptek.com/products/multichannel-analyzers/mca-8000d-digital-multichannel-analyzer`.

[Anderson et al.(2015)] J. Anderson, A. Borga, H. Boterenbrood, et al. FELIX: a High-Throughput Network Approach for Interfacing to Front End Electronics for ATLAS Upgrades. *Journal of Physics: Conference Series*, 664(8):082050, dec 2015. doi:10.1088/1742-6596/664/8/082050. URL `https://dx.doi.org/10.1088/1742-6596/664/8/082050`.

[ANSYS, Inc.(2022)] ANSYS, Inc. ANSYS MAPDL 2022 R2, 2022. URL `https://www.ansys.com/`.

[Arai et al.(2008)] Y. Arai, B. Ball, M. Beretta, et al. ATLAS Muon Drift Tube Electronics. *Journal of Instrumentation*, 3(09):P09001, sep 2008. doi:10.1088/1748-0221/3/09/P09001. URL https://dx.doi.org/10.1088/1748-0221/3/09/P09001.

[ATLAS Muon Collaboration(1997)] ATLAS Muon Collaboration. *ATLAS muon spectrometer: Technical Design Report*. Technical design report. ATLAS. CERN, Geneva, 1997. URL https://cds.cern.ch/record/331068.

[Autodesk, Inc.(2021)] Autodesk, Inc. *Autodesk Inventor Professional 2021*. Autodesk, Inc., 2021. URL https://www.autodesk.com/products/autocad/overview. Version 2021.

[Azevedo et al.(2016)] C.D.R. Azevedo, P.M.M. Correia, L.F.N.D. Carramate, et al. THGEM gain calculations using Garfield++: solving discrepancies between simulation and experimental data. *JINST*, 11(08):P08018, 2016. doi:10.1088/1748-0221/11/08/P08018. URL https://cds.cern.ch/record/2161485.

[Bachmann et al.(2002)] S. Bachmann, A. Bressan, M. Capéans-Garrido, et al. Discharge studies and prevention in the gas electron multiplier (GEM). *Nucl. Instrum. Methods Phys. Res., A*, 479(2-3):294–308, 2002. doi:10.1016/S0168-9002(01)00931-7. URL https://cds.cern.ch/record/483487.

[Bagnaia et al.(2008)] P. Bagnaia, T. Baroncelli, O. Biebel, et al. Calibration model for the MDT chambers of the ATLAS Muon Spectrometer. Technical report, CERN, Geneva, 2008. URL https://cds.cern.ch/record/1089868. backup paper for Atlas Detector paper.

[Basunia(2015)] M.S. Basunia. Nucl. Data Sheets. *Nuclear Data Sheets*, 127, 69, 2015.

[Bearden(1967)] J.A. Bearden. X-Ray Wavelengths. *Rev. Mod. Phys.*, 39:78–124, Jan 1967. doi:10.1103/RevModPhys.39.78. URL https://link.aps.org/doi/10.1103/RevModPhys.39.78.

[Beer(1852)] A. Beer. Bestimmung der Absorption des rothen Lichts in farbigen Flüssigkeiten. *Annalen der Physik und Chemie*, 162(5):78–88, 1852. doi:10.1002/andp.18521620505. Determination of the absorption of red light in colored liquids.

[Bencivenni et al.(2015)] G. Bencivenni, R. De Oliveira, G. Morello, and M. Poli Lener. The micro-Resistive WELL detector: a compact spark-protected single amplification-stage MPGD. *Journal of Instrumentation*, 10(02):P02008, feb 2015. doi:10.1088/1748-0221/10/02/P02008. URL https://dx.doi.org/10.1088/1748-0221/10/02/P02008.

[Berger et al.(2010)] M.J. Berger, J.H. Hubbell, S.M. Seltzer, et al. XCOM: Photon Cross Sections Database. NIST Standard Reference Database 8 (XGAM), 2010. URL https://dx.doi.org/10.18434/T48G6X. The National Institute of Standards and Technology (NIST) [online, accessed: October 2023].

[Berger et al.(2017)] M.J. Berger, J.S. Coursey, M.A. Zucker, and J. Chang. Stopping-Power & Range Tables for Electrons, Protons, and Helium Ions. NIST Standard Reference Database 124, 2017. URL https://dx.doi.org/10.18434/T4NC7P. The National Institute of Standards and Technology (NIST) [online, accessed: June 2024].

[Bethe(1930)] H.A. Bethe. Zur Theorie des Durchgangs schneller Korpuskularstrahlen durch Materie. *Annalen der Physik*, 5:325, 1930. doi:10.1002/andp.19303770204.

[Bhopatkar et al.(2017)] V. Bhopatkar, M. Hohlmann, and A. Zhang. Measurement of the Charge Induced on the Readout Strips of a GE1/1 Detector Prototype for the CMS Muon Endcap GEM Upgrade, 2017. URL https://research.fit.edu/media/site-specific/

researchfitedu/hep/heplaba/documents/research/Strip_charge_analysis_VB_SUBMITTED_Internal_CMS_note_full_note_number_April2017.pdf.

[Biagi(1995)] S. Biagi. MAGBOLTZ - transport of electrons in gas mixtures, 1995. URL https://magboltz.web.cern.ch/magboltz/.

[Bianco et al.(2021)] M. Bianco, F. Fallavollita, D. Fiorina, et al. Rate Capability of Large-Area Triple-GEM Detectors and New Foil Design for the Innermost Station, ME0, of the CMS Endcap Muon System. In *2021 IEEE Nuclear Science Symposium and Medical Imaging Conference (NSS/MIC)*, pages 1–5, 2021. doi:10.1109/NSS/MIC44867.2021.9875626.

[Blackett and Occhialini(1933)] P.M.S. Blackett and G.P.S. Occhialini. Some Photographs of the Tracks of Penetrating Radiation. *Proceedings of the Royal Society of London. Series A, Mathematical and Physical Sciences*, 139(839):699–726, 1933. doi:10.1098/rspa.1933.0159.

[Bloch(1933)] F. Bloch. Zur Bremsung Rasch Bewegter Teilchen beim Durchgang durch Materie. *Annalen der Physik*, 408:285–320, 1933. doi:10.1002/andp.19334080303.

[Bortfeld(2006)] T. Bortfeld. IMRT: a review and preview. *Physics in Medicine and Biology*, 51 (13):R363–R379, 2006. doi:10.1088/0031-9155/51/13/R21.

[Bortfeldt(2014)] J. Bortfeldt. *Development of floating strip micromegas detectors*. PhD thesis, Ludwig-Maximilians Universität München, München, 2014. URL https://edoc.ub.uni-muenchen.de/16972/.

[Bushberg et al.(2011)] J.T. Bushberg, J.A. Seibert, E.M. Leidholdt, and J.M. Boone. *The Essential Physics of Medical Imaging*. Lippincott Williams & Wilkins, third edition, 2011. ISBN 978-0781780575.

[Byszewski(2012)] M. Byszewski. MMDAQ Q and A - ATLAS micromegas DAQ, 2012. URL https://indico.cern.ch/event/218341/contributions/1519619/attachments/352429/491014/mmdaq_QA.pdf. [online, accessed: November 2023].

[CAEN(1996)] CAEN. CAEN - Tools for Discovery - N417 8 Channel Low Threshold Discriminator - User's Manual, 1996. URL https://virgilio.mib.infn.it/brofferio/didattica/datasheet/caen_N417-8chDiscriminator.pdf. [online, accessed: August 2024].

[CAEN(2023a)] CAEN. CAEN - Tools for Discovery - N842 8 Channel Constant Fraction Discriminator, 2023a. URL https://www.caen.it/products/n842/.

[CAEN(2023b)] CAEN. CAEN - Tools for Discovery - N93B Dual Timer, 2023b. URL https://www.caen.it/products/n93b/.

[CAEN(2023c)] CAEN. CAEN - Tools for Discovery - GECO2020 GEneral COntrol Software for CAEN HV Power Supplies, 2023c. URL https://www.caen.it/products/geco2020/.

[CAEN(2023d)] CAEN. CAEN - Tools for Discovery - A1015G 14/16 Stacked Channel Multipin Radiall to SHV connector Adapter for A1515TG/A1515QG, 2023d. URL https://www.caen.it/products/a1015g/.

[CAEN(2023e)] CAEN. CAEN - Tools for Discovery - SY5527 Universal Multichannel Power Supply System, 2023e. URL https://www.caen.it/products/sy5527/.

[CAEN(2024a)] CAEN. CAEN - Tools for Discovery - N405 Triple 4-Fold Logic Unit/Majority with VETO, 2024a. URL https://www.caen.it/products/n405/.

[CAEN(2024b)] CAEN. CAEN - Tools for Discovery - N108A Dual Delay, 2024b. URL https://www.caen.it/products/n108A/.

[CAEN(2024c)] CAEN. CAEN - Tools for Discovery - V792N 16 Channel Multievent QDC, 2024c. URL https://www.caen.it/products/v792n/.

[Carron(2006)] N.J. Carron. *An Introduction to the Passage of Energetic Particles Through Matter*. Taylor & Francis, 2006. ISBN 978-0-7503-0935-6. doi:10.1201/9781420012378.

[Charpak(1969)] G. Charpak. Development of multiwire proportional chambers. *CERN Courier*, 9 (6):174–176, 1969. URL https://cds.cern.ch/record/1729016.

[Choate(n.d.)] M. Choate. High Tg Bromine-free Laminates for PWB Applications. Presented at IPC Printed Circuits EXPO, n.d. URL http://isola-group.com/wp-content/uploads/High-Tg-Bromine-free-Laminates-for-PWB-Applications.pdf. [online, accessed: May 2024].

[Clapeyron(1834)] B.E. Clapeyron. Memoir sur la puissance motrice de la chaleur. *Journal de l'École royale polytechnique*, pages 153–190, 1834.

[Colaleo et al.(2015)] A. Colaleo, A. Safonov, A. Sharma, and M. Tytgat. CMS Technical Design Report for the Muon Endcap GEM Upgrade. Technical report, 2015. URL https://cds.cern.ch/record/2021453.

[Curran and Craggs(1949)] S.C. Curran and J.D. Craggs. *Counting tubes: theory and applications*. Academic Press, 1949.

[Davisson and Evans(1952)] C.M. Davisson and R.D. Evans. Gamma-Ray Absorption Coefficients. *Rev. Mod. Phys.*, 24:79–107, Apr 1952. doi:10.1103/RevModPhys.24.79. URL https://link.aps.org/doi/10.1103/RevModPhys.24.79.

[Denecke(1987)] B. Denecke. Measurement of the 59.5-keV gamma-ray emission probability in the decay of 241Am with a 4π-CsI(T1) - sandwich spectrometer. *International Journal of Radiation Applications and Instrumentation. Part A. Applied Radiation and Isotopes*, 38 (10):823–830, 1987. ISSN 0883-2889. doi:https://doi.org/10.1016/0883-2889(87)90179-1. URL https://www.sciencedirect.com/science/article/pii/0883288987901791.

[Deslattes et al.(2005)] R.D. Deslattes, E.G. Kessler Jr., P. Indelicato, et al. X-Ray Transition Energies Database. NIST Standard Reference Database 128, 2005. URL https://dx.doi.org/10.18434/T4859Z. The National Institute of Standards and Technology (NIST) [online, accessed: June 2024].

[Dupont(2024)] Dupont. Kapton® polyimide films, 2024. URL https://www.dupont.com/electronics-industrial/kapton-polyimide-film.html. [online, accessed: January 2024].

[Dörfler(2024)] M. Dörfler. Koinzidenzmessung von 511 keV Photonen mit einem mikrostrukturierten Gasdetektor und einem Szintillationsdetektor. Bachelor's thesis, Ludwig-Maximilians-Universität München, 2024. Unpublished.

[Einstein(1905)] A. Einstein. Über einen die Erzeugung und Verwandlung des Lichtes betreffenden heuristischen Gesichtspunkt. *Annalen der Physik*, 322(6):132–148, 1905. doi:https://doi.org/10.1002/andp.19053220607. URL https://onlinelibrary.wiley.com/doi/abs/10.1002/andp.19053220607.

[Fallavollita et al.(2020)] F. Fallavollita, D. Fiorina, and J.A. Merlin. Advanced Aging study on Triple-GEM Detectors. *Journal of Physics: Conference Series*, 1498(1):012038, apr 2020. doi:10.1088/1742-6596/1498/1/012038. URL https://dx.doi.org/10.1088/1742-6596/1498/1/012038.

[Fermi(1940)] E. Fermi. The Ionization Loss of Energy in Gases and in Condensed Materials. *Phys. Rev.*, 57:485–493, Mar 1940. doi:10.1103/PhysRev.57.485. URL https://link.aps.org/doi/10.1103/PhysRev.57.485.

[Flierl(2014)] B. Flierl. Particle Tracking with Micro-Pattern Gaseous Detectors. Master's thesis, Ludwig-Maximilians Universität München, München, 2014. URL https://www.etp.physik.uni-muenchen.de/publications/theses/download/master_bflierl.pdf.

[Flierl(2018)] B. Flierl. *Particle Tracking with Micro-Pattern Gaseous Detectors.* PhD thesis, Ludwig-Maximilians Universität München, München, 2018. URL https://edoc.ub.uni-muenchen.de/22198/.

[Francke and Peskov(2014)] T. Francke and V. Peskov. *Innovative Applications and Developments of Micro-Pattern Gaseous Detectors.* IGI Global, 2014. doi:10.4018/978-1-4666-6014-4.

[Fras et al.(2018)] M. Fras, S. Abovyan, V. Danielyan, et al. An 8-Channel ASD in 130 nm CMOS for ATLAS Muon Drift Tube Readout at the HL-LHC. *PoS*, TWEPP-17:004, 2018. doi:10.22323/1.313.0004. URL https://cds.cern.ch/record/2673783.

[French et al.(2001)] M.J. French, L.L. Jones, Q.R. Morrissey, et al. Design and results from the APV25, a deep sub-micron CMOS front-end chip for the CMS tracker. *Nucl. Instrum. Methods Phys. Res., A*, 466(2):359–65, 2001. doi:10.1016/S0168-9002(01)00589-7. URL https://cds.cern.ch/record/516812.

[Fukuda et al.(2011)] K. Fukuda, N. Kawaguchi, S. Ishizu, et al. Crystal growth and scintillation characteristics of the Nd3+ doped LiLuF4 single crystals. *Optical Materials*, 33(6):924–927, 2011. ISSN 0925-3467. doi:https://doi.org/10.1016/j.optmat.2010.10.053. URL https://www.sciencedirect.com/science/article/pii/S092534671100019X.

[Gadow(2016)] P.P. Gadow. Development of a Concept for the Muon Trigger of the ATLAS Detector at the HL-LHC, 2016. URL https://cds.cern.ch/record/2162398. Presented 20 Jun 2016.

[García-León(2022)] Manuel García-León. *Detecting Environmental Radioactivity.* Graduate Texts in Physics. Springer, 2022. ISBN 978-3-031-09969-4. doi:10.1007/978-3-031-09970-0. URL https://doi.org/10.1007/978-3-031-09970-0.

[Giomataris et al.(1996)] Y. Giomataris, Ph. Rebourgeard, J.P. Robert, and G. Charpak. MICROMEGAS: a high-granularity position-sensitive gaseous detector for high particle-flux environments. *Nuclear Instruments and Methods in Physics Research Section A: Accelerators, Spectrometers, Detectors and Associated Equipment*, 376(1):29–35, 1996. ISSN 0168-9002. doi:https://doi.org/10.1016/0168-9002(96)00175-1. URL https://www.sciencedirect.com/science/article/pii/0168900296001751.

[Gnanvo et al.(2012)] K. Gnanvo, N. Liyanage, C. Gu, and K. Saenboonruang. Calibration of the Gain and Measurement of the Noise for the APV25 Electronics, 2012. URL http://hallaweb.jlab.org/12GeV/SuperBigBite/SBS-minutes/2012/apvGain20121107.pdf. [online, accessed: September 2024].

[Goosey and Poole(2004)] M. Goosey and M. Poole. An introduction to high performance laminates and the importance of using optimised chemical processes in PCB fabrication. *Circuit World*, 30(4):34–39, 2004. doi:10.1108/03056120410539894.

[Guo(2021)] X. Guo. Upgrade of the ATLAS Monitored Drift Tube Frontend Electronics for the HL-LHC. 2021. URL https://cds.cern.ch/record/2770861.

[Hamamatsu(2024)] Hamamatsu. Photomultiplier tube - R6231, 2024. URL https://www.hamamatsu.com/eu/en/product/optical-sensors/pmt/pmt_tube-alone/head-on-type/R6231.html.

[Hauer et al.(2020)] P. Hauer, K. Flöthner, D. Schaab, et al. Measurements of the charging-up effect in Gas Electron Multipliers. *Nuclear Instruments and Methods in Physics Research Section A: Accelerators, Spectrometers, Detectors and Associated Equipment*, 976:164205, 2020. ISSN 0168-9002. doi:https://doi.org/10.1016/j.nima.2020.164205. URL https://www.sciencedirect.com/science/article/pii/S016890022030601X.

[Heereman(2010)] D. Heereman. Development of Micro-Pattern Gaseous Detectors – GEM. Master's thesis, Ludwig-Maximilians Universität München, München, 2010. URL https://www.etp.physik.uni-muenchen.de/publications/theses/download/dipl_dheereman.pdf.

[Heitler(1984)] W. Heitler. *The Quantum Theory of Radiation*. Dover Publications, 3. edition, 1984. ISBN 978-0-486-64558-2.

[Herrmann(2019)] M.G. Herrmann. *Series calibration of segmented and multi-layered micromegas modules for ATLAS*. PhD thesis, Ludwig-Maximilians Universität München, München, 2019. URL https://edoc.ub.uni-muenchen.de/25055/.

[ISOLA(2022)] ISOLA. Glass Fabric, 2022. URL https://www.isola-group.com/wp-content/uploads/Isola-Glass-Fabric-04_2022.pdf. [online, accessed: May 2024].

[ISOLA(2023)] ISOLA. Understanding Glass Fabric, 2023. URL https://www.isola-group.com/wp-content/uploads/Understanding-Glass-Fabric.pdf. [online, accessed: October 2023].

[ISOLA(2024)] ISOLA. DE104 - Low Tg Laminate and Prepreg, 2024. URL https://www.isola-group.com/pcb-laminates-prepreg/de104-laminate-and-prepreg/l. [online, accessed: May 2024].

[Isola et al.(2021)] G.A. Isola, M.K. Akinloye, Y.K. Sanusi, et al. Optimizing X-Ray Imaging Using Plant Mediated Gold Nanoparticles as Contrast Agent: A Review. 08:169–175, 09 2021. URL https://EconPapers.repec.org/RePEc:bjc:journl:v:8:y:2022:i:8:p:169-175.

[Ivanchenko et al.(2011)] V. Ivanchenko, J. Apostolakis, A. Bagulya, et al. Recent Improvements in Geant4 Electromagnetic Physics Models and Interfaces. *Progress in NUCLEAR SCIENCE and TECHNOLOGY*, 2:898–903, 10 2011. doi:10.15669/pnst.2.898.

[Jagfeld(2023)] C. Jagfeld. *Research and development of a segmented GEM readout detector*. PhD thesis, Ludwig-Maximilians Universität München, München, 2023. URL https://edoc.ub.uni-muenchen.de/31894/.

[Janssens(2019)] D. Janssens. CERN summer student program rapport: A better understanding of gas gain simulations in GEM detectors. 2019. URL https://cds.cern.ch/record/2702892.

[Kawamoto et al.(2013)] T. Kawamoto, S. Vlachos, L. Pontecorvo, et al. New Small Wheel Technical Design Report. Technical report, 2013. URL https://cds.cern.ch/record/1552862. ATLAS New Small Wheel Technical Design Report.

[Klein and Nishina(1929)] O. Klein and Y. Nishina. Über die Streuung von Strahlung durch freie Elektronen nach der neuen relativistischen Quantendynamik von Dirac. *Zeitschrift für Physik*, 52:853–868, 1929. ISSN 0044-3328. doi:https://doi.org/10.1007/BF01366453.

[Kleinknecht(2005)] K. Kleinknecht. *Detektoren für Teilchenstrahlung*. Teubner Studienbücher Physik, 4. edition, 2005. ISBN 3-8351-0058-0.

[Klitzner(2019)] F. Klitzner. *Development of novel two-dimensional floating strip micromegas detectors with an in-depth insight into the strip signal formation*. PhD thesis, Ludwig-Maximilians Universität München, München, 2019. URL `https://edoc.ub.uni-muenchen.de/24286/`.

[Korff and Present(1944)] S.A. Korff and R.D. Present. On the Role of Polyatomic Gases in Fast Counters. *Phys. Rev.*, 65:274–282, May 1944. doi:10.1103/PhysRev.65.274. URL `https://link.aps.org/doi/10.1103/PhysRev.65.274`.

[Kortner(2019)] Oliver Kortner. Upgrade of the ATLAS monitored drift tube front-end electronics for the HL-LHC. Technical report, CERN, Geneva, 2019. URL `https://cds.cern.ch/record/2651188`.

[Kumar et al.(2014)] B. Kumar, B.K. Kaushik, and Y. Negi. Perspectives and challenges for organic thin film transistors: Materials, devices, processes and applications. *Journal of Materials Science: Materials in Electronics*, 25, 01 2014. doi:10.1007/s10854-013-1550-2.

[Lambert(1760)] J.H. Lambert. *Photometria, sive de mensura et gradibus luminis, colorum et umbrae*. W. Engelmann, Leipzig, 1760. Published 1892.

[LeCroy(1996)] LeCroy. NIM Model 821 QUAD Discriminator, 1996. URL `https://wwwusers.ts.infn.it/~rui/univ/Acquisizione_Dati/Manuals/LRS%20821.pdf`. [online, accessed: August 2024].

[Leo(1995)] W.R. Leo. *Techniques for Nuclear and Particle Physics Experiments: A How-to Approach*. Springer, 2. edition, 1995.

[Li et al.(2018)] R. Li, G.C. Ravizzini, M.A. Gorin, et al. [the use of pet/ct in prostate cancer. page 4–21, 2018.

[Liang et al.(2019)] Y. Liang, J. Wang, X. Xiao, et al. Design and performance of a TDC ASIC for the upgrade of the ATLAS Monitored Drift Tube detector. *Nuclear Instruments and Methods in Physics Research Section A: Accelerators, Spectrometers, Detectors and Associated Equipment*, 939:10–15, 2019. ISSN 0168-9002. doi:https://doi.org/10.1016/j.nima.2019.05.050. URL `https://www.sciencedirect.com/science/article/pii/S0168900219307065`.

[Lutz(2007)] G. Lutz. *Semiconductor Radiation Detectors: Device Physics*. Springer-Verlag Berlin Heidelberg, 2007. ISBN 978-3-540-71678-5. doi:10.1007/978-3-540-71679-2.

[Mackenzie and Kopinke(1996)] K. Mackenzie and F.D. Kopinke. Debromination of Duroplastic Flame-Retarded Polymers. *Chemosphere*, 33(12):2423–2430, 1996. doi:10.1016/S0045-6535(96)00335-9.

[Maerschalk(2016)] T. Maerschalk. Study of Triple-GEM detector for the upgrade of the CMS muon spectrometer at LHC, 2016. URL `https://cds.cern.ch/record/2291028`.

[Marcus et al.(2014)] C. Marcus, E. Mena, and R.M. Subramaniam. Brain PET in the diagnosis of Alzheimer's disease. *Clin Nucl Med.*, 39(10):e413–e426, 2014. doi:10.1097/RLU.0000000000000547.

[Marić et al.(2005)] D. Marić, M. Radmilović-Radenović, and Z. Petrović. On parametrization and mixture laws for electron ionization coefficients. *The European Physical Journal D - Atomic, Molecular, Optical and Plasma Physics*, 35:313–321, 2005. doi:10.1140/epjd/e2005-00172-y. URL `https://doi.org/10.1140/epjd/e2005-00172-y`.

[Martoiu et al.(2013)] S. Martoiu, H. Muller, A. Tarazona, and J. Toledo. Development of the scalable readout system for micro-pattern gas detectors and other applications. *Journal of Instrumentation*, 8(03):C03015, mar 2013. doi:10.1088/1748-0221/8/03/C03015. URL https://dx.doi.org/10.1088/1748-0221/8/03/C03015.

[Matteis et al.(2016)] M. De Matteis, F. Resta, R. Richter, et al. Performance of the new Amplifier-Shaper-Discriminator chip for the ATLAS MDT chambers at the HL-LHC. *Journal of Instrumentation*, 11(02):C02087, feb 2016. doi:10.1088/1748-0221/11/02/C02087. URL https://dx.doi.org/10.1088/1748-0221/11/02/C02087.

[Meiser(2024)] P. Meiser. Untersuchung des Druckeinflusses auf die Leistung eines Triple-GEM Detektors. Bachelor's thesis, Ludwig-Maximilians-Universität München, 2024. Unpublished.

[Melissinos(1966)] A.C. Melissinos. *Experiments in Modern Physics*. Academic Press, 1966.

[Memmert(2013)] Memmert. *Betriebsanleitung ICH 256*. Memmert GmbH + Co. KG, 2013. URL https://www.memmert.com/index.php?eID=dumpFile&t=f&f=2718&token=fa13b251040b5facb0721a81ae481fb5a254edba. [online, accessed: March 2024].

[Meteorologisches Institut der Ludwig-Maximilians-Universität München(2024)] Meteorologisches Institut der Ludwig-Maximilians-Universität München. Klimawerte Garching, 2024. URL https://www.meteo.physik.uni-muenchen.de/DokuWiki/doku.php?id=wetter:garching:neu:klimagarching. [online, accessed: July 2024].

[Miele et al.(2008)] E. Miele, G.P. Spinelli, F. Tomao, et al. Positron Emission Tomography (PET) radiotracers in oncology – utility of 18F-Fluoro-deoxy-glucose (FDG)-PET in the management of patients with non-small-cell lung cancer (NSCLC). *J Exp Clin Cancer Res*, 27:52, 2008. URL https://doi.org/10.1186/1756-9966-27-52.

[Milbrath et al.(2007)] B.D. Milbrath, B.J. Choate, J.E. Fast, et al. Comparison of LaBr3:Ce and NAI(Tl) scintillators for radio-isotope identification devices. *Nuclear Instruments and Methods in Physics Research Section A: Accelerators, Spectrometers, Detectors and Associated Equipment*, 572:774–784, 03 2007. doi:10.1016/j.nima.2006.12.003.

[MKS(1997)] MKS. *MKS Type 250E Pressure/Flow Controller*. MKS Instruments, Inc, 1997. URL https://nuchem.iucf.indiana.edu/Instrumentation/Elec_Manual/Electronic_pdfs/MKS_250_Manual.pdf. [online, accessed: March 2024].

[MKS(1998)] MKS. *MKS Type 670B High Accuracy Signal Conditioner*. MKS Instruments, Inc, 1998. URL https://www.mks.com/mam/celum/celum_assets/resources/670Bman.pdf. [online, accessed: March 2024].

[MKS(2024a)] MKS. 690A01TRB Baratron - Vacuum Pressure Transducer, 2024a. URL https://www.mks.com/p/690A01TRB. [online, accessed: May 2024].

[MKS(2024b)] MKS. 0248D-00100SV - Upstream Flow Control Valve, 2024b. URL https://www.mks.com/p/0248D-00100SV. [online, accessed: May 2024].

[Moseley(1914)] H.G.J. Moseley. The High-Frequency Spectra of the Elements. Part II. *Philosophical Magazine*, 27:703–713, 1914.

[Multi Circuit Boards(2021)] Multi Circuit Boards. Materialien Standardwerte – FR4, 2021. URL https://www.multi-circuit-boards.eu/fileadmin/user_upload/downloads/leiterplatten_design-hilfe/multi_cb_material-standarwerte.pdf. [online, accessed: April 2024].

[Multi Circuit Boards(2024a)] Multi Circuit Boards. Leiterplatten-Oberflächen, 2024a. URL https://www.multi-circuit-boards.eu/leiterplatten-design-hilfe/oberflaeche/oberflaechen.html. [online, accessed: May 2024].

[Multi Circuit Boards(2024b)] Multi Circuit Boards. ENIG, 2024b. URL https://www.multi-circuit-boards.eu/glossar/enig.html. [online, accessed: May 2024].

[Multi Circuit Boards(2024c)] Multi Circuit Boards. Leiterplattenmaterial / PCB Material Übersicht, 2024c. URL https://www.multi-circuit-boards.eu/leiterplatten-design-hilfe/lagenaufbau/leiterplatten-materialien.html. [online, accessed: May 2024].

[Mumby(1989)] S.J. Mumby. An overview of laminate materials with enhanced dielectric properties. *Journal of Electronic Materials*, 18(3):241–250, 1989. doi:10.1007/BF02657415.

[Nemallapudi(2012)] M. Nemallapudi. Gain of a Single Gas Electron Multiplier. Master's thesis, University of Arkansas, 2012. URL https://scholarworks.uark.edu/etd/533.

[Newton(1846)] I. Newton. *Newton's Principia : the Mathematical Principles of Natural Philosophy.* Daniel Adee, New-York, 1846.

[NIST(2024)] NIST. Composition of KAPTON POLYIMIDE FILM, 2024. URL https://physics.nist.gov/cgi-bin/Star/compos.pl?matno=179. The National Institute of Standards and Technology (NIST) [online, accessed: June 2024].

[Oliveira(2023)] R. De Oliveira. The use of Micro-Pattern Technologies in Micro-Pattern Gaseous Detectors. The use of Micro-Pattern Technologies in Micro-Pattern Gaseous Detectors. 2023. URL https://cds.cern.ch/record/2847292.

[Ortec(1969)] Ortec. Ortec Model 454 Timing Filter Amplifier, 1969. URL https://groups.nscl.msu.edu/nscl_library/manuals/eggortec/454.pdf. [online, accessed: October 2023].

[Ortec(2002)] Ortec. Ortec Model 142PC Preamplifier, 2002. URL https://www.ortec-online.com/products/electronics/preamplifiers/142pc.

[Paramonov(2021)] A. Paramonov. FELIX: the Detector Interface for the ATLAS Experiment at CERN. *EPJ Web Conf.*, 251:04006, 2021. doi:10.1051/epjconf/202125104006. URL https://cds.cern.ch/record/2814356.

[Particle Data Group et al.(2022)] Particle Data Group et al. Review of Particle Physics. *Progress of Theoretical and Experimental Physics*, 2022(8):083C01, 8 2022. ISSN 2050-3911. doi:10.1093/ptep/ptac097. URL https://doi.org/10.1093/ptep/ptac097.

[Penning(1927)] F. M. Penning. Über Ionisation durch metastabile Atome. *Naturwissenschaften*, 15:818–818, October 1927. doi:10.1007/BF01505431.

[Penski(2020)] K. Penski. Neutral Particle Detection by a Structured Cathode of a Micro-Pattern Gaseous Detector. Master's thesis, Ludwig-Maximilians Universität München, München, 2020. URL https://www.etp.physik.uni-muenchen.de/publications/theses/download/master_kpenski.pdf.

[Penski(2024)] K. Penski. Test result of the new ASD2 chips for Phase-II upgrade of the ATLAS MDT chambers at HL-LHC. *Journal of Instrumentation*, 19(05):C05008, may 2024. doi:10.1088/1748-0221/19/05/C05008. URL https://dx.doi.org/10.1088/1748-0221/19/05/C05008.

[Penski et al.(2023)] K.E. Penski, O. Biebel, and C. Valderanis. Test Results of the New ASD Chips for Phase-II Upgrade of the ATLAS MDT Chambers at HL-LHC. Technical report, CERN, Geneva, 2023. URL https://cds.cern.ch/record/2852416.

[Pfeiffer et al.(2019)] D. Pfeiffer, L. De Keukeleere, C. Azevedo, et al. Interfacing Geant4, Garfield++ and Degrad for the simulation of gaseous detectors. *Nuclear Instruments and Methods in Physics Research Section A: Accelerators, Spectrometers, Detectors and Associated Equipment*, 935:121–134, 2019. ISSN 0168-9002. doi:https://doi.org/10.1016/j.nima.2019.04.110. URL https://www.sciencedirect.com/science/article/pii/S0168900219306072.

[Pinto(2010)] S.D. Pinto. Micropattern gas detector technologies and applications the work of the RD51 collaboration. pages 802–807, 2010. doi:10.1109/NSSMIC.2010.5873870.

[Posch et al.(2001)] C. Posch, S.P. Ahlen, E.S. Hazen, and J. Oliver. CMOS front-end for the MDT sub-detector in the ATLAS Muon Spectrometer, development and performance. 2001. doi:10.5170/CERN-2001-005.199. URL https://cds.cern.ch/record/529410.

[Posch et al.(2007)] C. Posch, E. Hazen, and J. Oliver. MDT-ASD, CMOS front-end for ATLAS MDT; rev. version 2.1. Technical report, CERN, Geneva, 2007. URL https://cds.cern.ch/record/684217. revised version number 2.1 was submitted on 2007-09-18 19:14:00.

[Qiu et al.(2020)] G. Qiu, W. Ma, and L. Wu. Low dielectric constant polyimide mixtures fabricated by polyimide matrix and polyimide microsphere fillers. *Polymer International*, 69 (5):485–491, 2020. doi:https://doi.org/10.1002/pi.5979. URL https://onlinelibrary.wiley.com/doi/abs/10.1002/pi.5979.

[Raether(1964)] H. Raether. *Electron Avalanches and Breakdown in Gases*. Butterworths, 1964. ISBN 0598450211, 9780598450210.

[Raymond et al.(2000)] M. Raymond, M. French, J.R. Fulcher, et al. The APV25 025 mum CMOS readout chip for the CMS tracker. 2000. URL https://cds.cern.ch/record/478270/files/raymond.pdf.

[Rinnagel(2023)] M. Rinnagel. *Development of an inverted ring imaging Cherenkov Micromegas*. PhD thesis, Ludwig-Maximilians Universität München, München, 2023. URL https://edoc.ub.uni-muenchen.de/32286/.

[Rose and Korff(1941)] M.E. Rose and S.A. Korff. An Investigation of the Properties of Proportional Counters. I. *Phys. Rev.*, 59:850–859, Jun 1941. doi:10.1103/PhysRev.59.850. URL https://link.aps.org/doi/10.1103/PhysRev.59.850.

[Röntgen(1895)] W.C. Röntgen. Über eine neue Art von Strahlen. *Sitzungsberichte der Physikalisch-Medizinischen Gesellschaft zu Würzburg*, December 1895. Published December 28, 1895.

[Saint-Gobain Crystals, Scintillation Products(2009)] Saint-Gobain Crystals, Scintillation Products. *Scintillation Products - Technical Note - BrilLanCe Scintillators Performance Summary*. Saint-Gobain Crystals, Scintillation Products, 2009. URL https://gammadata.se/wp-content/uploads/2024/01/SGC-BrilLanCe-Scintillators-Performance-Summary2-v2.pdf.

[Sauli(1997)] F. Sauli. GEM: A new concept for electron amplification in gas detectors. *Nuclear Instruments and Methods in Physics Research Section A: Accelerators, Spectrometers, Detectors and Associated Equipment*, 386(2):531–534, 1997. ISSN 0168-9002. doi:https://doi.org/10.1016/S0168-9002(96)01172-2. URL https://www.sciencedirect.com/science/article/pii/S0168900296011722.

[Schindler(2023)] H. Schindler. Garfield++ User Guide. 2023. URL https://garfieldpp.web.cern.ch/documentation/UserGuide.pdf. [online, accessed: November 2023].

[Schlegel et al.(2018)] W. Schlegel, C.P. Karger, and O. Jäkel, editors. *Medizinische Physik: Grundlagen – Bildgebung – Therapie – Technik*. Springer Spektrum, Berlin, Germany, 1 edition, 2018. ISBN 978-3-662-54800-4. doi:10.1007/978-3-662-54801-1.

[Schneider(2023)] N. Schneider. Efficiency Increase of Photon Detection of Micro-Structured Gas Detectors via Material Optimisation of Converter Layers. Master's thesis, Ludwig-Maximilians Universität München, München, 2023. URL https://www.etp.physik.uni-muenchen.de/publications/theses/download/master_nschneider.pdf.

[Seeram(2023)] E. Seeram. *X-Ray Imaging Systems for Biomedical Engineering Technology: An Essential Guide*. Springer Spektrum, 2023. ISBN 978-3-031-46265-8. doi:10.1007/978-3-031-46266-5.

[Smirnov(2005)] I. Smirnov. HEED, 2005. URL https://ismirnov.web.cern.ch/ismirnov/heed. [online, accessed: November 2023].

[Spiwoks et al.(2017)] R. Spiwoks, A.J. Armbruster, G.D. Carrillo-Montoya, et al. The ATLAS Muon-to-Central Trigger Processor Interface (MUCTPI) Upgrade. 2017. URL https://cds.cern.ch/record/2266932.

[Sundararajan and Ntekas(2023)] P. Sundararajan and K. Ntekas. New developments in the MDT Trigger Processor for the ATLAS Level-0 Muon Trigger at High Luminosity LHC. Technical Report 02, CERN, Geneva, 2023. URL https://cds.cern.ch/record/2837164.

[Terada et al.(2016)] K. Terada, S. Nakamura, T. Nakao, et al. Measurements of gamma-ray emission probabilities of 241, 243Am and 239Np. *Journal of Nuclear Science and Technology*, 53(11):1881–1888, 2016. doi:10.1080/00223131.2016.1174167. URL https://doi.org/10.1080/00223131.2016.1174167.

[The ATLAS Collaboration(2008)] The ATLAS Collaboration. The ATLAS Experiment at the CERN Large Hadron Collider. *Journal of Instrumentation*, 3(08):S08003, aug 2008. doi:10.1088/1748-0221/3/08/S08003. URL https://dx.doi.org/10.1088/1748-0221/3/08/S08003.

[The ATLAS Collaboration(2017)] The ATLAS Collaboration. Technical Design Report for the Phase-II Upgrade of the ATLAS Muon Spectrometer. Technical report, CERN, Geneva, 2017. URL https://cds.cern.ch/record/2285580.

[The ATLAS Collaboration(2019)] The ATLAS Collaboration. Resolution of the ATLAS muon spectrometer monitored drift tubes in LHC Run 2. 14(09):P09011, sep 2019. doi:10.1088/1748-0221/14/09/P09011. URL https://dx.doi.org/10.1088/1748-0221/14/09/P09011.

[The ATLAS Collaboration(2023)] The ATLAS Collaboration. The ATLAS Experiment at the CERN Large Hadron Collider: A Description of the Detector Configuration for Run 3. Technical report, CERN, Geneva, 2023. URL https://cds.cern.ch/record/2859916. 233 pages in total, author list starting page 214, 116 figures, 15 tables, submitted to JINST. All figures including auxiliary figures are available at http://atlas.web.cern.ch/Atlas/GROUPS/PHYSICS/PAPERS/GENR-2019-02/.

[The CMS Collaboration(2008)] The CMS Collaboration. The CMS experiment at the CERN LHC. *Journal of Instrumentation*, 3(08):S08004, aug 2008. doi:10.1088/1748-0221/3/08/S08004. URL https://dx.doi.org/10.1088/1748-0221/3/08/S08004.

[The Harshaw Chemical Company(n.d.)] The Harshaw Chemical Company. *Harshaw Scintillation Phosphor Catalog*, n.d. 6801 Cochran Road, Solon, Ohio 44149 USA.

[Thompson et al.(2001)] A.C. Thompson, D. Vaughan, et al. *X-ray data booklet*, volume 8. Lawrence Berkeley National Laboratory, University of California Berkeley, CA, 2001.

[Thompson and Thompson(2017)] M.K. Thompson and J.M. Thompson. *ANSYS Mechanical APDL for Finite Element Analysis*. Elsevier Science, 2017. ISBN 9780128131107. URL https://books.google.de/books?id=qbT5DQAAQBAJ.

[Thorpe and Vahsen(2023)] T.N. Thorpe and S.E. Vahsen. Avalanche gain and its effect on energy resolution in GEM-based detectors. *Nuclear Instruments and Methods in Physics Research Section A: Accelerators, Spectrometers, Detectors and Associated Equipment*, 1045:167438, 2023. ISSN 0168-9002. doi:https://doi.org/10.1016/j.nima.2022.167438. URL https://www.sciencedirect.com/science/article/pii/S0168900222007306.

[Townsend(1910)] J.S. Townsend. *The Theory of Ionisation of Gases by Collision*. London: Constable & Company Ltd, 1910.

[Trost(2020)] S. Trost. Studies on the Influence of PPM-Water-Pollutions in the Working Gas of Square Meter Micromegas Detectors for the ATLAS New Small Wheel Upgrade and Identification of Muons in High Background Environments. Master's thesis, Ludwig-Maximilians Universität München, München, 2020. URL https://www.etp.physik.uni-muenchen.de/publications/theses/download/master_strost.pdf.

[VAISALA(2024)] VAISALA. Miniature Dew Point Transmitters DMT143 & DMT143L (Long), 2024. URL https://www.vaisala.com/en/products/instruments-sensors-and-other-measurement-devices/instruments-industrial-measurements/dmt143.

[Valk et al.(2006)] P.E. Valk, D. Delbeke, D.L. Bailey, et al. *Positron Emission Tomography: Clinical Practice*. Springer-Verlag, 2006. ISBN 1852339713.

[Vogel(2024)] Fabian Vogel. Long-term irradiation studies of large-area Micromegas detectors for the ATLAS NSW upgrade, Februar 2024. URL http://nbn-resolving.de/urn:nbn:de:bvb:19-332969.

[Weishaupt et al.(2006)] D. Weishaupt, V.D. Köchli, B. Marincek, et al. *How does MRI work?: an introduction to the physics and function of magnetic resonance imaging*, volume 2. Springer, 2006.

[Wright and Incerti(n.d.)] D. Wright and S. Incerti. A short guide to choosing physics lists, n.d. URL http://geant4.in2p3.fr/IMG/pdf_PhysicsLists.pdf. [online, accessed: May 2024].

[Yang(2019)] Z. Yang. Cosmic Ray Test with sMDT Prototype Chamber using modified miniDAQ system. Phase-2 MDT electronics, 2019. URL https://indico.cern.ch/event/821237/contributions/3433359/attachments/1852150/3040996/sMDT-talk-Zhe-0528.pdf. [online, accessed: November 2023].

[Yoshitake(2020)] M. Yoshitake. *Work Function and Band Alignment of Electrode Materials: The Art of Interface Potential for Electronic Devices, Solar Cells, and Batteries*. NIMS Monographs. Springer Tokyo, Tokyo, 1st ed. edition, 2020. ISBN 978-4-431-56896-4. doi:10.1007/978-4-431-56898-8. URL https://doi.org/10.1007/978-4-431-56898-8.

[Zhu(2019)] J. Zhu. The Phase-II Upgrade of the ATLAS Muon Spectrometer. Technical report, CERN, Geneva, 2019. URL https://cds.cern.ch/record/2689144.

[Zhu(1998)] R.Y. Zhu. Radiation Damage In Scintillating Crystals. *Nuclear Instruments and Methods in Physics Research Section A: Accelerators, Spectrometers, Detectors and Associated Equipment*, 413:297–311, 08 1998. doi:10.1016/S0168-9002(98)00498-7.

[Ziegler(2010)] Eckert & Ziegler. Recommended Nuclear Decay Data - Am241, 2010. URL `https://www.ezag.com/fileadmin/ezag/user-uploads/isotopes/isotopes/Isotrak/isotrak-pdf/Decay_Schema_Data/Am-241.pdf`. [online, accessed: November 2023].

[Şahin et al.(2014)] Ö. Şahin, T.Z. Kowalski, and R. Veenhof. High-precision gas gain and energy transfer measurements in Ar–CO2 mixtures. *Nuclear Instruments and Methods in Physics Research Section A: Accelerators, Spectrometers, Detectors and Associated Equipment*, 768: 104–111, 2014. ISSN 0168-9002. doi:https://doi.org/10.1016/j.nima.2014.09.061. URL `https://www.sciencedirect.com/science/article/pii/S0168900214010924`.

Appendix A

Simulation: GEM Amplification Process

The GEM foil is responsible for the electron multiplication in the detector in order to provide a detectable signal. This mechanism is introduced in chapter 3.2. The amplification factor depends on the voltage difference ΔU_{GEM}. For a valid estimation of the gas gain in a GEM foil, a corresponding simulation is carried out. First, a the performance of a single-GEM detector is investigated, followed by the study of a triple-GEM detector. For these simulations the software ANSYS (see chapter 4.1.2) and Garfield++ (see chapter 4.1.4) is utilized.

Specifications

A SEM picture of the GEM foil is shown in figure 3.2, including the relevant dimensions. In the simulation the geometry of this foil is created using ANSYS, which can be seen in figure A.1. The detailed measures of the simulated GEM foil are summarized in Table A.1. The foil is embedded in a gas volume, creating a drift region of 3 mm and an induction region of 2 mm. In Garfield++, the GEM cell from figure A.1 is periodically expanded in x- and z-dimension and forms a large-area foil.

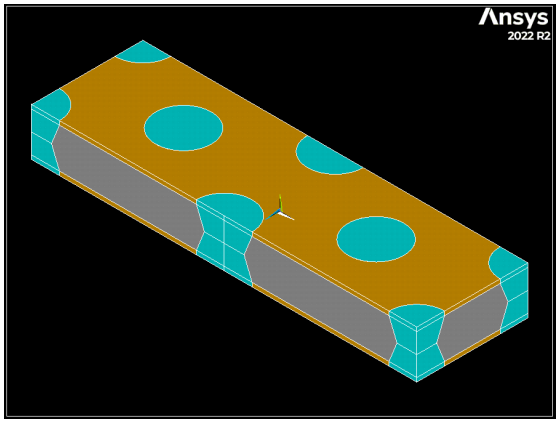

Figure A.1: In ANSYS, the GEM foil geometry is constructed with the parameters from Table A.1. It is a copper-plated Kapton foil, which is visualized in grey and orange, respectively. There are holes in the foil that are arranged periodically at a certain pitch. This foil is located within a gas volume, consequently the holes are filled with the detector gas, depicted in cyan. The gas volumes on the top and bottom of the foil are not shown here, but are included in the simulation.

Parameter	Value
Kapton thickness	50 µm
Copper thickness	5 µm
Outer diameter	70 µm
Inner diameter	50 µm
Pitch	140 µm

Table A.1: In this table the dimensions of the simulated GEM foil are listed, including the material thicknesses, hole diameters and the pitch. The GEM foil in figure 3.2 has these proportions as well as the ANSYS model in figure A.1.

In addition, ANSYS provides the electric fields, as shown in figure 3.3 for a single-GEM foil using $E_{\text{drift}} = 2\,\text{kV}\,\text{cm}^{-1}$ and $E_{\text{ind}} = 3\,\text{kV}\,\text{cm}^{-1}$, while the GEM voltage ΔU_{GEM} is varied. The electric field information are imported to Garfield++ where the amplification process is simulated by the inclusion of MAGBOLTZ (see chapter 4.1.3).

Single-GEM Simulation

All single-GEM simulations carried out with 10000 initial electrons starting at $y = 0.02\,\text{cm}$ (see figure 3.4) with an initial energy of 0.1 eV. If an electron exceeds the limit $y = -0.02\,\text{cm}$, it is considered detected. The temperature is set to 293.5 K and the pressure to 750 Torr. First, the simulation is verified by comparing it with reference papers in order to subsequently adjust the relevant parameters and ensure reliable simulation results.

Verification

For simulation verification of a single-GEM detector the results are compared to [Janssens, 2019]. The GEM's geometry, the electric fields and the physical properties like the gas mixture properties including the Penning effect are identical.

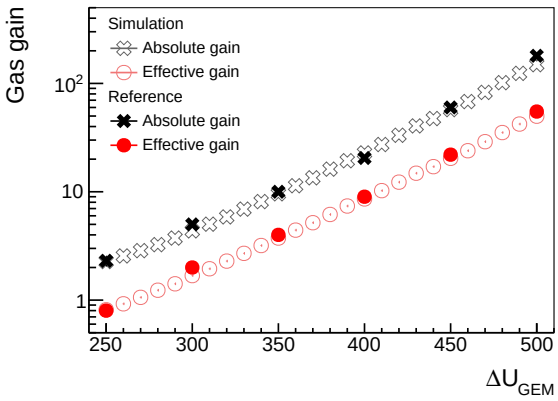

Figure A.2: The simulated gas gain is plot as a function of ΔU_{GEM}, with constant $E_{\text{drift}} = 2\,\text{kV}\,\text{cm}^{-1}$ and $E_{\text{ind}} = 3\,\text{kV}\,\text{cm}^{-1}$ using a Ar:CO_2 70:30 vol. % gas mixture and no Penning effect ($r_{\text{p}} = 0$). Due to losses of electrons at the GEM foil the effective gain is always smaller then the absolute gain. The simulation results fit the reference values. Reference values extracted from [Janssens, 2019]

Additionally to the effective gain, which is introduced in equation 3.1, the absolute gain is defined as

$$\text{absolute gain} = \frac{\text{number of all created electrons}}{\text{number of initial electrons}} \tag{A.1}$$

and both values are shown in figure A.2. Both, simulation and reference values, show the same results. The gas gain increases exponentially. Since there are electron losses in the GEM foil as visible in figure 3.4, the absolute gain is smaller than the effective gain. One relevant parameter for characterizing the performance of the detector in this thesis is the effective gain, as this provides an estimation of the number of electrons in the detector before the amplification process (as used in chapter 5.5.2). Therefore, the simulation results are compared to measurements, which are reported by [Janssens, 2019] and shown in figure A.3.

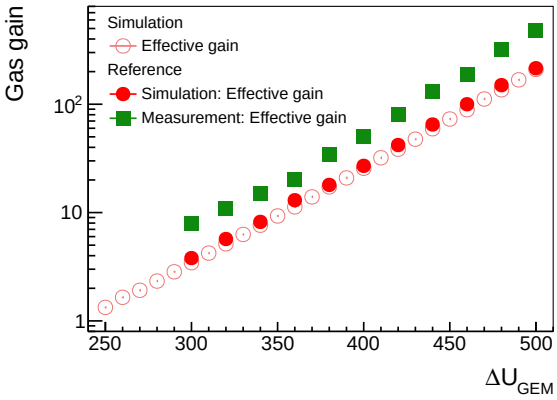

Figure A.3: Compared to figure A.2, here the Penning effect is included using r_p = 0.56 for Ar:CO_2 70:30 vol. % (see [Şahin et al., 2014]). The reference values are extracted from [Janssens, 2019]. While the simulation results agree, they indicate a factor 2 difference compared to the measurement.

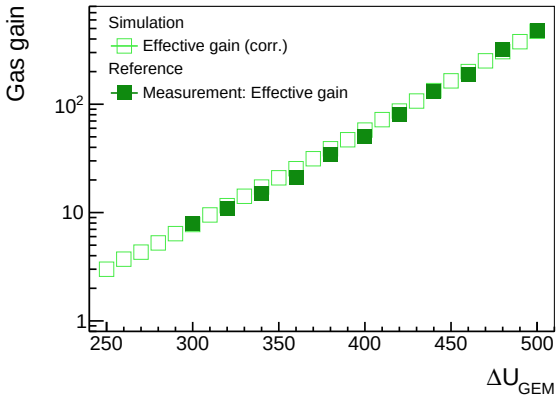

Figure A.4: Applying the factor of 2.25 ± 0.27 (from [Janssens, 2019]) as a correction to the simulated effective gain values from figure A.3, simulation and reference measurement show agreement.

Various papers like [Nemallapudi, 2012; Janssens, 2019] report a factor of about 2 discrepancy between simulation and measurement, as visible in figure A.3, that cannot be explained or resolved so far. Consequently, the simulation results are corrected by a factor of 2.25 ± 0.27 (from [Janssens, 2019]) to resolve this offset. As expected, the corrected simulation results and measurements are consistent with the inclusion of error intervals as shown in figure A.4.

Simulation Results

After verifying the simulation for a single-GEM detector, the gas is adapted to Ar:CO_2 93:7 vol. % using r_p = 0.42 (see [Şahin et al., 2014]), since the detectors in the measurements performed here are operated with this gas mixture. The dimension of the GEM foil and the electric fields stay constant. The resulting absolute and effective gain are shown in figure A.5. In order to estimate the real effective gain in the detector, it is multiplied with the correction factor, which can be seen in figure 3.5.

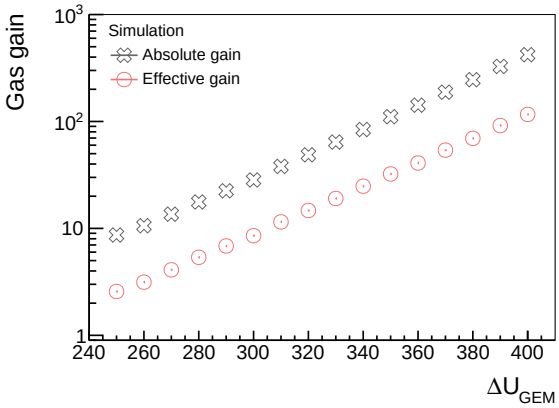

Figure A.5: Simulated absolute and effective gas gain in Ar:CO_2 93:7 vol. % as a function of the GEM voltage ΔU_{GEM} for a single-GEM detector. Due to the higher amount of Ar, which is responsible for gas amplification, the effective gain is about a factor 3 higher compared to figure A.3.

Triple-GEM Simulation

In this thesis the measurements are performed with a triple-GEM detector. In order to estimate the real effective gain of the detector by this simulation, first a verification simulation of a triple-GEM detector is performed. Then the parameters for the used detector setup are adjusted.

Verification

For verification of a triple-GEM detector (see figure 3.6) the simulation results are compared to the measurements reported by [Bachmann et al., 2002]. Therefore, the setup is adapted regarding parameters such as the drift region (3 mm) and the transport and induction region (1 mm each) as well as the corresponding electric fields $E_{\mathrm{drift}} = 2\,\mathrm{kV\,cm^{-1}}$ and $E_{\mathrm{ind}} = E_{\mathrm{trans1,2}} = 3.5\,\mathrm{kV\,cm^{-1}}$. The results shown in figure A.6 indicate a consistency between the corrected simulation and measurement.

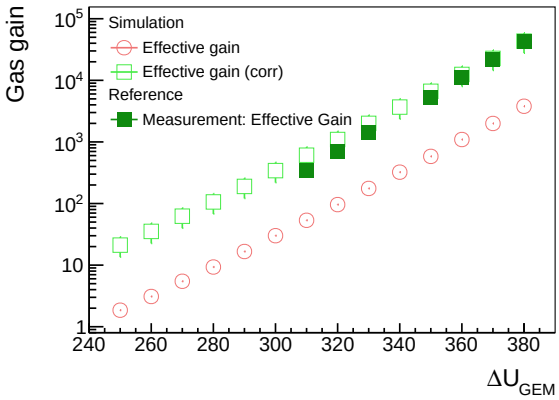

Figure A.6: The simulated and measured effective gas gain as a function of different GEM voltages, where ΔU_{GEM} is applied to each foil and the gas mixture Ar:CO_2 70:30 vol. % ($r_{\mathrm{p}} = 0.56$) is used. Since there are three amplification stages, the correction factor has to be adjusted to $(2.25 \pm 0.27)^3$. The corrected simulation values agree with the measurement results, but for lower GEM voltages the discrepancy slightly increases. Reference values taken from [Bachmann et al., 2002].

Simulation Results

The simulated measurement setup with the corresponding electric fields and the electron amplification process are shown in figure 3.7 and figure 3.8, respectively. The electrons start at y = 0.7 cm with an initial energy of 0.1 eV. They are randomly generated on an area of $1 \times 1\,\mathrm{cm}^2$ in x- and z-direction. The absolute and effective gain are shown in figure A.7, while the additional plots can be found in chapter 3.3, including the plot with the corrected effective gas gain, which is used for further analysis of the simulation results in this thesis.

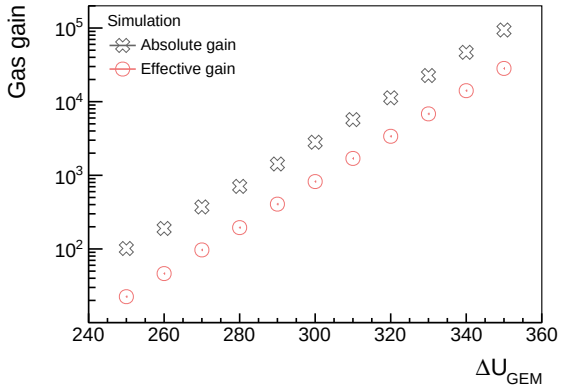

Figure A.7: For a triple-GEM detector filled with a gas mixture Ar:CO_2 93:7 vol. % (r_p = 0.42) the simulated effective gain for ΔU_GEM = 280 V is about 195.

Summary

For the single- and triple-GEM detector, the simulation provides a very good agreement with the results presented in other publications, which is a reasonable verification of the simulation. When comparing simulation and measurement results, a discrepancy of about 2 is reported. In order to achieve a valid estimate of the simulation, the simulation results are corrected by this offset.

Appendix B

Converter Layer Mounts

This mount and adapted versions of the design for the various converter layers are used for the measurements performed in chapter 5, chapter 8 and chapter 9.

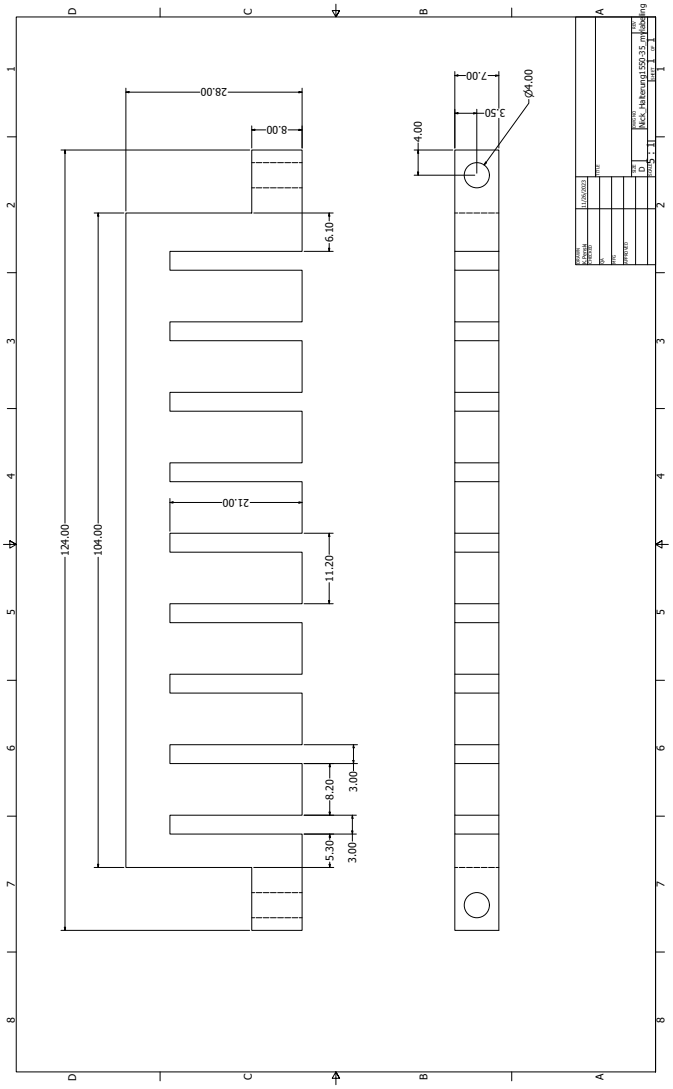

Figure B.1: The technical drawing of the converter layer mount used for the 1520 µm thick converter layers. Due to the additional SMD resistors the gap for inserting has to be larger. The center position of all gaps is the same for all mounts for the different layer thicknesses, but the gap is adapted. Provided by Nick Schneider as part of his master's thesis [Schneider, 2023], internal communication.

For thinner layers, which are utilized in chapter 8 and chapter 9, the gaps in the mount are adjusted to the layer thickness including the SMD resistors. It is ensured that the center of the converter layer positions remain unchanged for all setups.

For the tilted layer measurements from chapter 7 this mount in figure B.2 is used.

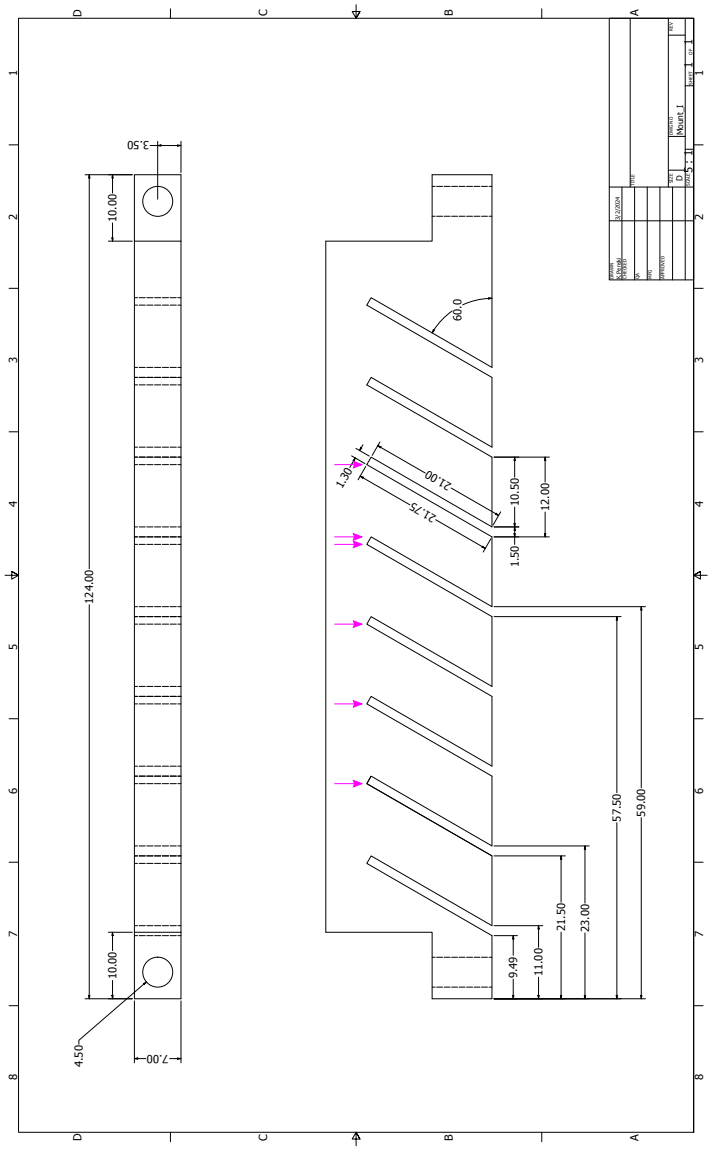

Figure B.2: Mount for the tilted layer setup: The positions of the layers for the multiple layer setup (chapter 7.3) are marked with a pink arrow, while the position of the single layer setup (chapter 7.2) is highlighted with two arrows.

Appendix C

Measurement: Detector Voltages and Environmental Parameter

Two different triple-GEM detectors are used for the measurements performed in this thesis, one with a small housing with a total height of about 5.5 cm from the anode to the cover and one with a large housing with a total height of 12 cm. Although the other dimensions, such as the distances of the transfer and drift regions, are about the same, differences can occur, for example, due to performance variations in the GEM foil. The pressure stabilization system is introduced in chapter 6 and is connected for all measurements discussed in subsequent chapters.

Chapter 5: Converter Layers for Photon Detection

All measurements in chapter 5 are performed with the detector with the large housing. The GEM voltages presented in Table 5.1 are applied. Since the detector is placed in the climate cabinet (see chapter 6.2), the measurements are performed at a constant temperature and relative humidity. However, the strong dependence of the measured frequency on the pressure is not taken into account (see chapter 6), since neither the MKS pressure system nor a monitoring device is implemented. The range of the environmental pressure of the measurement days is provided by [Meteorologisches Institut der Ludwig-Maximilians-Universität München, 2024]. Later comparisons show that the reported values are about 2–3 mbar higher than in the lab. Thus, these values are subtracted by 2.5 mbar. Except for the voltage scan of ΔU_{x} from figure 5.17, which is carried out at 961.0–966.2 mbar, all other measurements in chapter 5 are performed at 961.4–963.7 mbar.
The value of (962.5 ± 1.0) mbar is used for further calculations.

In chapter 5.5.2 the corrected effective gain $g_{\mathrm{eff,corr}}$ is needed. To extract this quantity for the measurement configuration from the simulation, a pressure-voltage calibration is performed, since pressure influences the gas gain in the GEM foil and thus the corrected effective gain $g_{\mathrm{eff,korr}}$. The simulated gain refers to a pressure of $p_2 = 1000$ mbar while the measurement is performed at $p_1 = (962.5 \pm 1.0)$ mbar with $U_1 = 280$ V. Applying equation 6.7, results in $U_2 = (283.7 \pm 0.1)$ mbar. U_2 is inserted in equation 3.2, providing $g_{\mathrm{eff,corr}} = 2858 \pm 20$ (error from equation not considered here).

Chapter 7: 3D Position Reconstruction

The measurements in chapter 7 have been performed after the measurements presented in chapter 8. Therefore, the values shown here are based on the settings in the next section and only the GEM-voltages are adapted for the different pressures according to equation 6.7. The values are presented in Table C.1.

Setup	p_1	U_1	p_2	U_2
Single layer	1017 mbar	286.0 V	1032 mbar	287.0 V
Multiple layers	1017 mbar	286.0 V	1035 mbar	288.0 V
Imaging	1017 mbar	286.0 V	997 mbar	284.0 V

Table C.1: The GEM voltages have to be adjusted to compensate for the different pressures. Here the voltages for the GEM1 and GEM2 foils are listed for the various converter layer types, while a 10 V higher voltage is applied to the GEM3 foil (see figure C.1).

Chapter 8: Material Optimization for High Photon Detection Efficiency

For the measurements in chapter 8 the large GEM detector is used, which is placed in the climate cabinet and is connected to the pressure stabilization system. Compared to chapter 5, the GEM3 foil has to be replaced. Although both foils should not differ in principle, they have to be operated at different GEM voltages (290 V instead of 280 V) to provide the same performance at a constant pressure (see figure C.1). The reason for this effect is not further investigated. All measurements in this chapter are carried out with this setup.

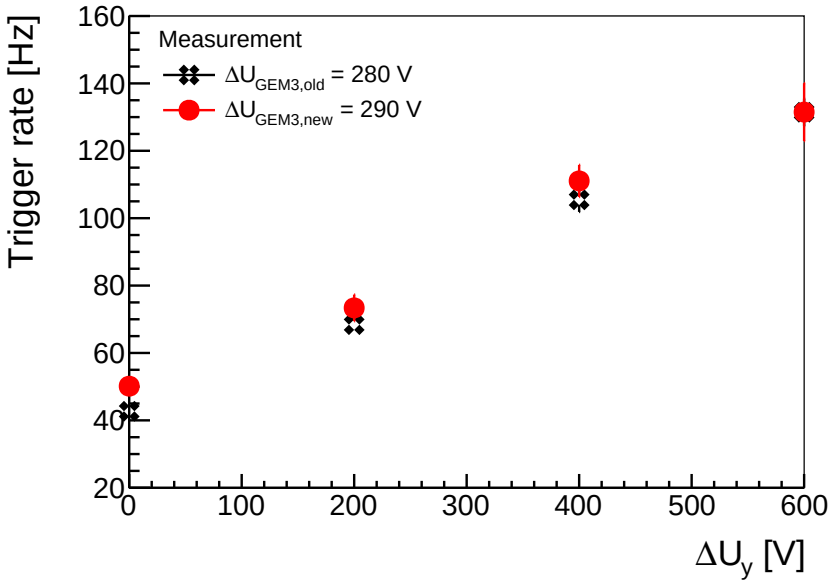

Figure C.1: A new GEM foil requires a higher voltage to achieve the same trigger rate.

In order to have the same amplification as in chapter 5 for different pressures, a pressure-voltage calibration has to be performed using equation 6.7. For $p_{=}$962.5 mbar, U_2 = 280 V and p_2 = 1017 mbar it results in $U_2 \approx 286$ V. The GEM voltages for the various layer types are presented in Table C.2, while ΔU_{ind} = 400 V, $\Delta U_{\text{trans1,2}}$ = 300 V and ΔU_{drift} = 100 V stay constant.

Naming	p_1	U_1	p_2	U_2
1520 + 41	1017 mbar	286.0 V	-	-
250 + 33	1017 mbar	286.0 V	1025 mbar	287.0 V
100 + 38	1017 mbar	286.0 V	1017 mbar	286.0 V
100 + 18	1017 mbar	286.0 V	1026 mbar	287.0 V
50 + 38	1017 mbar	286.0 V	1028 mbar	287.0 V
50 + 18	1017 mbar	286.0 V	1031 mbar	287.5 V

Table C.2: The GEM voltages have to be adjusted to compensate for the different pressures. Here the voltages for the GEM1 and GEM2 foils are listed for the various converter layer types, while a 10 V higher voltage is applied to the GEM3 foil.

Chapter 9: Detection Efficiency of a GEM Detector with Converter Layers for 511 keV Photons

The measurements in chapter 9 are performed using the GEM detector with the small housing and the voltages in Table C.3 are applied. Due to the measurement setup, the detector is not placed in the climate cabinet. The temperature in the laboratory varies between $(25.6 \pm 1.5)^\circ$ and the pressure provided by the pressure system fluctuates between (1030 ± 5) mbar over several days.

Variable	Value
ΔU_{ind}	400 V
$\Delta U_{\mathrm{trans1,2}}$	300 V
$\Delta U_{\mathrm{GEM1,2,3}}$	280 V
$\Delta U_{\mathrm{drift}}$	100 V
ΔU_{x}	0 V
ΔU_{y}	600 V

Table C.3: Voltages applied to the triple-GEM detector and the converter layers for the measurements carried out in chapter 9.

Appendix D

Simulation: Material Composition

Chapter 5: Converter Layers for Photon Detection

For the simulations in chapter 5 a homogeneous FR4 (ρ = 1.98 g cm^{-3}) composition is used, which differs from chapter 8.2.4. It is composed of 53 % glass fabric (ρ = 2.74 g cm^{-3}) and 47 % brominated epoxy resin (ρ = 1.13 g cm^{-3}). The glass fabric consists of 60.0 % SiO_2, 22.4 % CaO, 11.8 % Al_2O_3, 3.4 % MgO, 1.3 % TiO_2, 1.0 % Na_2O and 0.1 % Fe_2O_3. For brominated epoxy resin the chemical composition $C_{38}H_{40}O_6Br_4$ is utilized.

Chapter 8: Material Optimization for High Photon Detection Efficiency

In chapter 8.2.4, the substructure of the 250 + 33 FR4 layers is simulated. As shown in figure D.1 and figure D.2, neither the absorption nor the energy spectrum is affected by using the woven glass fabric embedded in brominated epoxy resin (see figure 8.9) instead of a homogeneous material with the same chemical composition. Since the homogeneous material is easier to implement in the simulation, it is used for the 1250 µm FR4 layer.

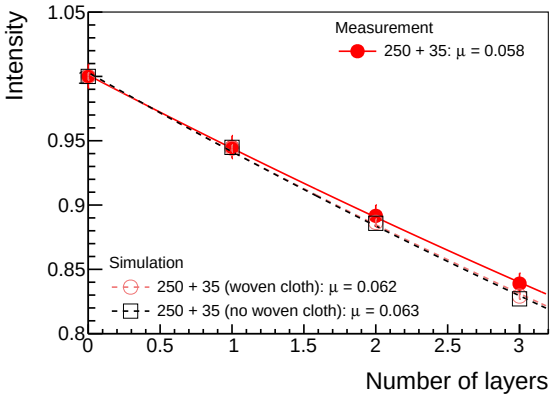

Figure D.1: The implementation of the woven glass fabric in the simulation does not change the absorption behavior compared to a homogeneous material approximation in FR4.

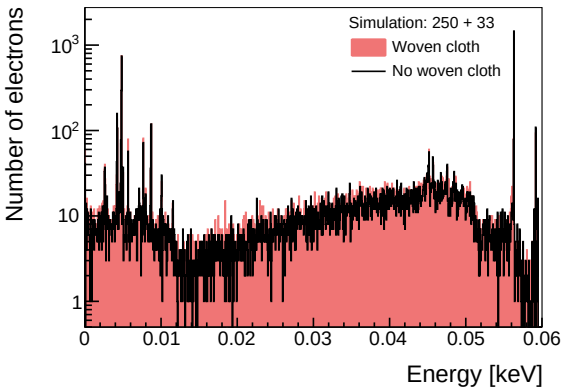

Figure D.2: The different material compositions (woven cloth or homogeneous material) of FR4 have no impact on the simulated energy spectrum.

Appendix E

Germanium Detector

The Germanium detector belongs to the class of semiconductor detectors. Due to its high efficiency and good energy resolution it is widely used as particle detector, mostly specialized in gamma ray spectroscopy. In this thesis the photon absorption measurements are performed using a HPGe detector. Its basic working principle, shown in figure E.1, is introduced here, following [Leo, 1995] and [Lutz, 2007], where more detailed information can be found.

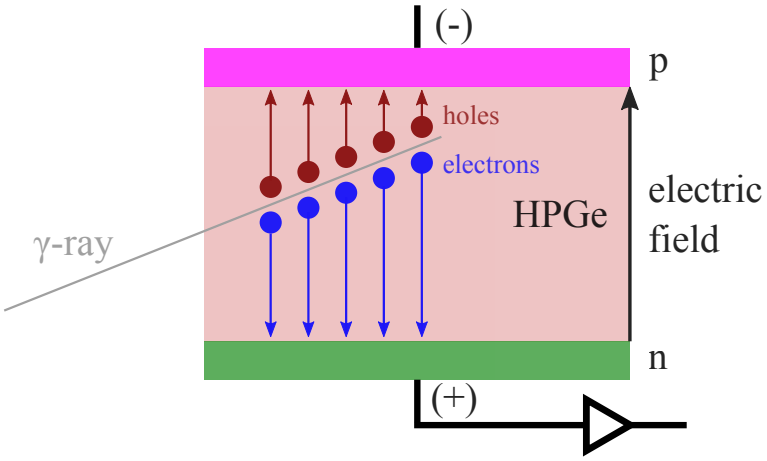

Figure E.1: A photon enters the HPGe detector and interacts with the crystal, creating electron-hole pairs. They are separated by an external electric field and migrate to the electrodes. The collected electron charge is measured and amplified to produce a signal that is directly proportional to the deposited photon energy.

An incoming photon interacts with the HPGe crystal according to the processes described in chapter 2.2. Similar to the electron-ion pairs generated on the gas of MPGDs, electron-hole pairs are produced in HPGe detectors. The number of pairs is thereby proportional to the deposited photon energy. For the creation of one electron-hole pair by ionization in Ge an energy of 2.96 eV is necessary. Furthermore, semiconductor detectors usually run at low temperatures of around 77 K to minimize thermal noise, which is achieved by cooling the crystal with liquid nitrogen. An external electric field is applied to separate the electron-hole pair and guide them efficiently to the corresponding electrodes. Consequently, a measurable current pulse is created by the electrons, which is amplified and read out. The resulting pulse height directly correlates with the photon energy, providing an excellent energy resolution.

Appendix F

Calculation: Expected Trigger Rate for Coincidence Setup

For an estimation, the expected coincidence trigger rate between both scintillation detectors is calculated.

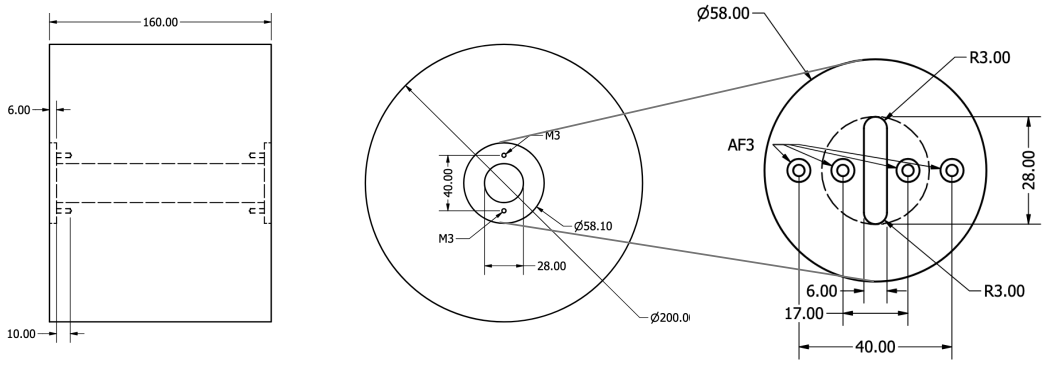

Figure F.1: Technical drawing of the complete brass cylinder (left figure) used for shielding the ^{22}Na particle source. It has a diameter of 20 cm. The source is located in the centre of the cylinder, which has two apertures on the left and right (middle figure). On top of these openings there is an additional cover with a slit (right figure), which determines the number of photons leaving the brass cylinder. The size of the slit is designed so that all converter layers in the GEM detector experience the same particle flux when the detector is placed directly in front of the cylinder. There is an additional opening in the cylinder with a diameter of 1 cm and its position is marked by the red line. Figures taken from [Dörfler, 2024].

The openings of the brass cylinder (see figure F.1) define the number of emitted photons. On the right side of the cylinder the NaI scinillation detector is positioned for detecting the 511 keV photons and on the top the $LaBr_3$ detector for measuring the 1275 keV photons. To estimate the coincident trigger rate, the solid angle Ω is calculated. It is defined as

$$\Omega = \frac{A}{r^2} \tag{F.1}$$

where A is the area and r the distance between the particle source and this area A. The opening at the right has an area of $A_{\mathrm{NaI}} = 6\,\mathrm{mm} \cdot 28\,\mathrm{mm} = 168\,\mathrm{mm}^2$ and on the top of $A_{\mathrm{LaBr_3}} = \pi(5\,\mathrm{mm})^2 = 78.5\,\mathrm{mm}^2$.
With a distance of $r_{\mathrm{NaI}} = 80\,\mathrm{mm}$, for the NaI detector this leads to a solid angle of

$$\begin{aligned}\Omega_{\mathrm{NaI}} &= \frac{A_{\mathrm{NaI}}}{r_{\mathrm{NaI}}^2} \\ &= \frac{168\,\mathrm{mm}^2}{(80\,\mathrm{mm})^2} \\ &= 0.026\,\mathrm{sr}\end{aligned} \tag{F.2}$$

This reduces the activity of the ^{22}Na particle source from $A_{\text{activity source}} = 3.2\,\mathrm{MBq}$ to

$$\begin{aligned}A_{\text{activity at NaI}} &= A_{\text{activity source}} \cdot \frac{\Omega_{\mathrm{NaI}}}{4\pi} \\ &= 3.2\,\mathrm{MBq} \cdot \frac{0.026\,\mathrm{sr}}{4\pi} \\ &= 6.6\,\mathrm{kBq}\end{aligned} \tag{F.3}$$

For the $LaBr_3$ detector in the same way the fraction of the solid angle Ω_{frac} with respect to the full sphere is calculated

$$\begin{aligned}\Omega_{\text{frac LaBr}_3} &= \frac{\Omega_{\mathrm{LaBr_3}}}{4\pi} \\ &= \frac{A_{\mathrm{LaBr_3}}}{4\pi(r_{\mathrm{LaBr_3}})^2} \\ &= \frac{78.5\,\mathrm{mm}^2}{4\pi(100\,\mathrm{mm})^2} \\ &= 6.25 \times 10^{-4}\end{aligned} \tag{F.4}$$

Using equation F.3 and equation F.4 and accounting for the intensity of 180 % for the 511 keV and of 100 % for the 1275 keV photons per decay, this results in an expected coincidence rate $f_{\text{coincidence}}$ of

$$\begin{aligned}f_{\text{coincidence}} &= A_{\text{activity at NaI}} \cdot \Omega_{\text{frac LaBr}_3} \cdot 1.8 \\ &= 6.6\,\mathrm{kBq} \cdot 6.25 \times 10^{-4} \cdot 1.8 \\ &= 7.4\,\mathrm{Hz}\end{aligned} \tag{F.5}$$

This coincidence rate does not account for the detection efficiency of each detector. It is typically between $\mathcal{O}(\varepsilon_{\text{detection}}) = 50$–$80\,\%$. Therefore, a coincidence rate between 2–5 Hz is expected.

Due to the additional lead shielding, the GEM detector has a distance of 14 cm to the aperture in the brass shielding. As the opening angle of the aperture is adapted to the GEM detector being placed directly in front of it, with a distance of 14 cm the last layer experiences a reduced particle flux compared to the first layer (see figure 9.11). The area of the particle flux A_{flux} is larger than the area of the converter layer $A_{\mathrm{layer}} = 20\,\mathrm{mm} \cdot 100\,\mathrm{mm}$ (which is the active area of the layer). Therefore, a certain proportion of the flux is undetectable due to the detector arrangement, reducing the measured detection efficiency of the GEM detector. To correct for this effect, the loss is calculated.
The GEM detector is placed on the left and thus has the same solid angle as NaI ($\Omega_{\mathrm{GEM}} = \Omega_{\mathrm{NaI}} = 0.026\,\mathrm{sr}$). It is assumed that all layers have the same detection efficiency $\varepsilon_{\mathrm{layer}}$, which adds up for 9 layer to the total detection efficiency $\varepsilon_{\text{detection (all)}} = 9 \cdot \varepsilon_{\mathrm{layer}}$. For $A_{\mathrm{flux}} > A_{\mathrm{layer}}$ the detection efficiency per layer reduces to

$$\begin{aligned} \varepsilon_{\text{layer (red)}} &= \frac{A_{\text{layer}}}{A_{\text{flux}}} \cdot \varepsilon_{\text{layer}} \\ &= \frac{20\,\text{mm} \cdot 100\,\text{mm}}{\Omega_{\text{GEM}} \cdot x^2} \cdot \varepsilon_{\text{layer}} \end{aligned} \tag{F.6}$$

where x is the distance from the layer to the source. The first layer has a distance of 277 mm to the source and the layers are placed with a distance of 11 mm to each other. With equation F.6, for all layers this leads to a total reduced efficiency of

$$\begin{aligned} \varepsilon_{\text{detection (red)}} &= \frac{20\,\text{mm} \cdot 100\,\text{mm}}{\Omega_{\text{GEM}}} \cdot \varepsilon_{\text{layer}} \cdot \sum_{i=0}^{8} \frac{1}{(277\,\text{mm} + i \cdot 11\,\text{mm})^2} \\ &= 6.9 \cdot \varepsilon_{\text{layer}} \end{aligned} \tag{F.7}$$

The reduced detection efficiency $\varepsilon_{\text{detection (red)}}$ has to be corrected by a factor of

$$\begin{aligned} f_{\text{correction}} &= \frac{\varepsilon_{\text{detection (all)}}}{\varepsilon_{\text{detection (red)}}} \\ &= \frac{9 \cdot \varepsilon_{\text{layer}}}{6.9 \cdot \varepsilon_{\text{layer}}} \\ &= 1.30 \end{aligned} \tag{F.8}$$

to obtain the actual efficiency. For the measurement in chapter 9.4, the measured efficiency has to be corrected by this factor.

Acknowledgments

At this point, I would like to thank all the people who supported me during my PhD. A special thanks to:

- Prof. Dr. Otmar Biebel for providing the opportunity to write this thesis under his supervision and for granting me the freedom and support to explore various aspects of this research project.
- Dr. Ralf Hertenberger for his supervision and valuable discussions over the past years, as well as his corrections and advice during the proofreading of my thesis.
- Prof. Dr. Wolfgang Dünnweber for being the second reviewer.
- Dr. Fabian Vogel, Dr. Christoph Jagfeld, and Dr. Alexander Lory for proofreading my thesis.
- I also thank the other (former) members of the working group, especially: Dr. Valerio D'Amico, Dr. Bernhard Flierl, Stefanie Götz, Dr. Maximilian Herrmann, Dr. Felix Klitzner, Eshita Kumar, Dr. Alexander Lory, Dr. Alexander Mann, Dr. Maximilian Rinnagel, Nick Schneider, and Dr. Chrysostomos Valderanis for their help and for creating an enjoyable atmosphere at work.
- My friends and family, especially my parents Astrid and Gerhard Penski, and my sister Verena Penski, for their support and understanding. Above all, my boyfriend Julius Kühne, who has encouraged and supported me more than ever in the last few months.